



Nonlinear hydrodynamic modelling of wave energy converters under controlled conditions

Giuseppe Giorgi

A thesis submitted for the degree of
Doctor of Philosophy

Faculty of Science and Engineering
Electronic Engineering Department
Maynooth University

Supervisor: **Prof. John V. Ringwood**
Head of the Department: Prof. Ronan Farrell

July 2018

Table of Contents

Abstract	v
Declaration of authorship	vi
Acknowledgement	vii
Acronyms	viii
List of symbols	ix
1 Introduction	1
1.1 Introduction	1
1.2 Motivation	4
1.3 Main objectives and contributions	6
1.3.1 List of publications	7
2 Review of nonlinear effects and modelling options	9
2.1 Motivation	9
2.2 Introduction	9
2.3 Main nonlinear effects in wave energy converters	11
2.3.1 The wave resource	11
2.3.2 Device	13
2.3.2.1 Froude-Krylov force	13
2.3.2.2 Diffraction and radiation forces	13
2.3.2.3 Viscous force	14
2.3.2.4 Parametrically excited motions	14
2.3.2.5 Sloshing	14
2.3.2.6 Slamming	14
2.3.2.7 Mooring system force	15
2.3.2.8 Relevance of nonlinear effects	15
2.3.3 Power take-off force	18
2.3.3.1 Air-turbines	20
2.3.3.2 High-pressure hydraulics	20
2.3.3.3 Direct drive	20
2.4 Nonlinear modelling approaches	20
2.4.1 CFD and SPH models	20
2.4.1.1 Computational fluid dynamics	21
2.4.1.2 Hydrodynamic modelling approaches for wave energy	22
2.4.1.3 Smoothed-Particles Hydrodynamics	22
2.4.2 Potential flow models	24

2.4.2.1	Linear potential flow model	24
2.4.2.2	Nonlinear potential flow models	25
2.4.2.3	Viscous effects in potential flow models	26
2.4.3	Models from data	27
2.4.3.1	Hammerstein/Wiener model	28
2.4.3.2	Feedback block-oriented model	29
2.4.3.3	Kolmogorov-Gabor Polynomial Model	30
2.4.3.4	Artificial neural networks	30
2.5	Discussion	31
2.6	Conclusion	35
2.6.1	Thesis contributions	35
3	Implementation of latching control in a CFD environment	37
3.1	Motivation	37
3.2	Introduction	37
3.3	Numerical Wave Tank	39
3.3.1	OpenFOAM	40
3.3.2	Implementation of latching control	40
3.4	Latching control	41
3.4.1	Latching control: an overview	41
3.4.1.1	Linear model approximation	42
3.4.2	Constant latching duration	43
3.4.3	Latching duration and natural period	45
3.4.3.1	Natural period	45
3.4.3.2	Free response tests	46
3.4.4	Alternative and adaptive latching durations	47
3.4.5	Case study	49
3.5	Results	53
3.6	Discussion	56
3.6.1	Comparison with linear model	56
3.6.1.1	3D case	56
3.6.1.2	2D case	56
3.7	Conclusions	58
4	Algebraic nonlinear Froude-Krylov force for heaving point absorbers	60
4.1	Motivation	60
4.2	Introduction	60
4.3	Modelling approaches	61
4.3.1	Linear model	62
4.3.2	Nonlinear Froude-Krylov force model	62
4.4	Algebraic solution	63
4.5	Case study	66
4.6	Validation and results	68
4.6.1	Validation of the Froude-Krylov force calculation	68
4.6.2	Results	70
4.7	Conclusions	73
5	Comparing heaving point absorbers and oscillating wave surge converters	76
5.1	Motivation	76
5.2	Introduction	76
5.3	Hydrodynamic models	77
5.3.1	Froude-Krylov term	78

5.3.1.1	Froude-Krylov torque for oscillating wave surge converters	78
5.3.2	Viscous drag term	80
5.3.2.1	Viscous drag force for heaving point absorbers	80
5.3.2.2	Viscous drag torque for oscillating wave surge converters	80
5.4	Case study	81
5.5	Results	82
5.6	Conclusions	88
6	Nonlinear hydrodynamic models in the computation/fidelity continuum	90
6.1	Motivation	90
6.2	Introduction	90
6.3	Hydrodynamic models	91
6.3.1	Potential theory-based (PoT) models	91
6.3.1.1	Froude-Krylov force modelling	92
6.3.1.2	Viscous drag modelling	94
6.3.2	Computational fluid dynamics (CFD) model	94
6.4	Case study	94
6.5	Results	96
6.6	Discussion	100
6.7	Conclusions	103
7	Consistency of viscous drag identification tests for wave energy applications	106
7.1	Motivation	106
7.2	Introduction	106
7.3	Flow around a wave energy converter	107
7.4	Identification techniques	108
7.4.1	Fully-submerged, fixed body, constant flow	110
7.4.2	Fully-submerged, prescribed motion, harmonic flow	111
7.4.3	Fully-submerged, prescribed motion, sawtooth flow	112
7.4.4	Floating, prescribed motion, harmonic flow	113
7.4.5	Floating, dynamic response	114
7.5	Conclusion	117
8	Relevance of pressure field accuracy for nonlinear Froude-Krylov force calculations	119
8.1	Motivation	119
8.2	Introduction	119
8.3	Wave theories	120
8.3.1	Regular waves	121
8.3.1.1	Linear Airy's wave theory	121
8.3.1.2	Wheeler's stretching method	123
8.3.1.3	Rienecker-Fenton wave theory	123
8.3.2	Irregular waves	124
8.3.2.1	Higher order spectral method	125
8.4	Regular wave results	126
8.4.1	Pressure profile	126
8.4.2	Pressure integral	128
8.5	Irregular wave results	131
8.5.1	Pressure profile	132
8.5.2	Pressure integral	137
8.6	Conclusion	138

9	Multi-degree of freedom nonlinear Froude-Krylov force models	140
9.1	Motivation	140
9.2	Introduction	140
9.3	Three-DoF nonlinear Froude-Krylov model	141
9.3.1	Algebraic integration	142
9.3.1.1	Cylinder section description	143
9.3.1.2	Disc section description	144
9.3.1.3	Cone section description	144
9.3.2	Numerical integration	147
9.3.3	Validation of modelling approach	149
9.3.3.1	Comparison with WAMIT	149
9.3.4	Comparison with tank tests	152
9.3.5	Parametric study	152
9.4	Six-DoF nonlinear Froude-Krylov model	156
9.4.1	Parametric resonance in wave energy converters	157
9.4.2	The CorPower-like device	158
9.4.2.1	Results for the CorPower-like device	159
9.4.3	The Wavebob-like device	163
9.4.3.1	Results for the Wavebob-like device	164
9.4.4	The SparBuoy-like device	168
9.4.4.1	Monochromatic waves results	170
9.4.4.2	Panchromatic waves results	174
9.5	Conclusions	178
10	Conclusions and future work	181
10.1	Future work	183
	Bibliography	184

Abstract

One of the major challenges facing modern industrialized countries is the provision of energy: traditional sources, mainly based on fossil fuels, are not only growing scarcer and more expensive, but are also irremediably damaging the environment. Renewable and sustainable energy sources are attractive alternatives that can substantially diversify the energy mix, cut down pollution, and reduce the human footprint on the environment. Ocean energy, including energy generated from the motion of wave, is a tremendous untapped energy resource that could make a decisive contribution to the future supply of clean energy. However, numerous obstacles must be overcome for ocean energy to reach economic viability and compete with other energy sources. Energy can be generated from ocean waves by wave energy converters (WECs). The amount of energy extracted from ocean waves, and therefore the profitability of the extraction, can be increased by optimizing the geometry and the control strategy of the wave energy converter, both of which require mathematical hydrodynamic models that are able to correctly describe the WEC-fluid interaction. On the one hand, the accuracy and representativeness of such models have a major influence on the effectiveness of the WEC design. On the other hand, the computational time required by a model limits its applicability, since many iterations or real-time calculations may be required. Critically, computational time and accuracy are often mutually contrasting features of a mathematical model, so an appropriate compromise should be defined in accordance with the purpose of the model, the device type, and the operational conditions. Linear models, often chosen due to their computational convenience, are likely to be imprecise when a control strategy is implemented in a WEC: *under controlled conditions*, the motion of the device is exaggerated in order to maximize power absorption, which invalidates the assumption of linearity. The inclusion of nonlinearities in a model is likely to improve the model's accuracy, but increases the computational burden. Therefore, the objective is to define a *parsimonious* model, in which only relevant nonlinearities are modelled in order to obtain an appropriate compromise between accuracy and computational time. In addition to presenting a wider discussion of nonlinear hydrodynamic modelling for WECs, this thesis contributes the development of a computationally efficient nonlinear hydrodynamic model for axisymmetric WEC devices, from one to six degrees of freedom, based on a novel approach to the nonlinear computation of static and dynamic Froude-Krylov forces.

Declaration of authorship

I, Giuseppe Giorgi, declare that this thesis titled ‘Nonlinear hydrodynamic modelling of wave energy converters under controlled conditions’ and the work presented in it are my own. I confirm that:

- This work was done wholly or mainly while in candidature for a research degree at this University.
- Where any part of this thesis has previously been submitted for a degree or any other qualification at this University or any other institution, this has been clearly stated.
- Where I have consulted the published work of others, this is always clearly attributed.
- Where I have quoted from the work of others, the source is always given. With the exception of such quotations, this thesis is entirely my own work.
- I have acknowledged all main sources of help.
- Where the thesis is based on work done by myself jointly with others, I have made clear exactly what was done by others and what I have contributed myself.

Date: _____

Signature: _____

Acknowledgement

First of all, I would like to thank my supervisor Professor John Ringwood for the advices he gave me on any matter relating not only my research work, but also my technical English writing and presentation skills.

I would like to thank the present and past members of COER, who have provided stimulating conversations and enjoyable collaborations, over the course of this research: Alain Ulazia, Alexis Mérigaud, Andrej Rössling, Christian Windt, Demián García-Violini, Francesco Paparella, Josh Davidson, Marina Garcia Abril, Markel Peñalba Retes, Nicolás Ezequiel Faedo, Paula Garcia-Rosa, Romain Genest, Simone Giorgi, Thomas Kelly, Victor José Ramos, and Yeraí Peña.

I would like to thank the French Embassy in Dublin for giving me the opportunity to spend some valuable time in École Centrale de Nantes for a PhD exchange of six weeks; consequently, I thank as well Jean-Christophe Gilloteaux, Alain Clément, Aurélien Babarit, and Lucas Letournel, for the precious discussions we had during my stay in Nantes.

I would like to thank Ann and Joanne, from the administration office, and John Maloco and Denis Buckley, from the technical staff, for their assistance during my stay at COER.

Acronyms

The list of the main recurrent acronyms used in the present thesis is the following:

WEC	Wave energy converter.
TRL	Technology readiness level.
TPL	Technology performance level.
CFD	Computational fluid dynamics.
SPH	Smoothed-particle hydrodynamics.
FK	Froude-Krylov.
HPA	Heaving point absorber.
OWSC	Oscillating wave surge converter.
PTO	Power take-off.
OPC	Oscillating pitching converter.
OWC	Oscillating water column.
RANS	Reynolds-average Navier-Stokes.
LES	Large eddy simulation.
DNS	Direct numerical simulation.
VOF	Volume of fluid.
SWENSE	Spectral Wave Explicit Navier-Stokes Equation.
NWT	Numerical wave tank.
BEM	Boundary element method.
HOS	Higher-order spectra.
RF	Rienecker-Fenton.
RAO	Response amplitude operator.
PoT	Potential theory-based models.
CoG	Centre of gravity.
SWL	Still water level.
NRMSE	Normalized root mean squared error.
FFT	Fast Fourier transform.
LFK	Linear Froude-Krylov.
NLR	Nonlinear restoring force.
NLFK	Nonlinear Froude-Krylov force.
VFK	Vertical body, algebraic nonlinear Froude-Krylov force calculation.
RFK	Rotated body, numerical nonlinear Froude-Krylov force calculation.

List of symbols

The list of the main recurrent symbols used in the present thesis is the following:

g	Gravitational acceleration.
ρ	Sea water density.
γ	Sea water specific weight.
t	Time.
φ	Velocity potential.
η	Free surface elevation.
H_w	Wave height.
a	Wave amplitude.
T_w	Wave period.
ω	Wave frequency.
λ	Wave length.
k	Wave number.
d	Water depth.
p	Pressure.
S	Wetted surface.
\mathbf{n}	Normal unity vector of the surface.
\mathbf{x}	Vector of states, composed of linear and angular positions.
(x, y, z)	Right-handed frame of reference, defined as (surge, sway, heave).
$(\mathbf{i}, \mathbf{j}, \mathbf{k})$	Triad of unity vectors of (x, y, z) .
(ϕ, θ, ψ)	Angular positions around (x, y, z) , defined as (roll, pitch, yaw).
(ϱ, ϑ)	Cylindrical coordinates.
(r, ϑ)	Polar coordinates.
\mathbf{M}	Inertial matrix of the body.
\mathbf{A}_∞	Infinity added mass matrix.
\mathbf{A}	Added mass matrix.
\mathbf{B}	Radiation damping matrix.
\mathbf{K}	Impulse response function.
\mathbf{G}	Hydrostatic stiffness matrix.
\mathbf{f}	Vector of generalized forces, composed of forces and torques.
\mathbf{F}	Force vector.
\mathbf{T}	Torque vector.
C_d	Drag coefficient.
A_d	Characteristic area.
V_0	Undisturbed flow velocity.
Re	Reynolds number.
KC	Keulegan-Carpenter number.

Introduction

1.1 Introduction

In the last two centuries, the energy demand of the industrialized world has exponentially grown, increasing concerns about future resource provision. Indeed, in the last decades, there is an affirmed awareness, both in the scientific community and public domain, of the depletion of traditional energy resources. The majority of the current energy consumption structurally relies on fossil fuels, whose increasing scarcity is making its price rise. Furthermore, dependences of nations on fuel supplies from other countries, due to an absence in the national territory, creates fragile international relationships, which may undermine their political and economic stability [1]. Most importantly, the exploitation of fossil fuels as a primary energy source causes emission of CO_2 in the atmosphere, which is contributing to world climate change and air pollution.

A growing alternative to fossil fuels is represented by renewable energy, which has seen a massive development in the last decades, especially in the form of photovoltaic, hydroelectric, and wind energy. The main, not negligible, advantage is that the resource is inherently free: it is just a matter of harvesting it, in an economically viable way. Policy makers and government institutions have put considerable effort into focusing industrial power towards the renewable energy sector. The European Council, in 2007, defined specific targets to face the energy problem, known as the ‘20 20 20 by 2020’, aiming to achieve, by the close to come year 2020, a 20% share of renewable energy (compared to 8.5% of 2005), a 20% reduction in greenhouse gas emission with respect to 1990 levels, and a 20% saving in energy consumption through energy efficiency [2]. Similarly, the ‘Roadmap 2050’ of the European Union (EU) states that nations within the EU should cut greenhouse emissions to 80% of 1990 levels, by 2050 [3].

Wave energy is a source of renewable energy which can diversify the energy mix, while increasing the renewable energy quota. Wave energy has an extremely high potential, since it is a densely concentrated form of solar energy. The sun, through radiation of 0.15 kW/m^2 energy density, generates temperature gradients in the air, therefore winds (increasing the energy density to 0.4 kW/m^2), which blows over the sea surface (increasing the energy density to 2.5 kW/m^2), generating the fetch and, after propagation with negligible energy loss, waves. Overall, total world wave energy is estimated to amount to around 2TW, which is of the same order of magnitude of the world’s electricity consumption (less than 10 TW) [4].

The amplitude and period of waves, and therefore their energy content, depend on the wind speed, the length of the fetch, and the sea-floor bathymetry. Large swell waves produced by north-westerly (northern hemisphere) and south-easterly winds (southern hemisphere) can travel very long distances with almost no loss of energy. As a result, high

levels of wave energy are typically experienced off western coasts of continents, and mainly concentrated between 40° and 60° latitudes, in both hemispheres, as shown in Fig. 1.1. Conveniently, in these regions, solar energy resources are scarcer than in the belt between 40° latitude south and north, so that wave energy may be a more accessible renewable energy resource.

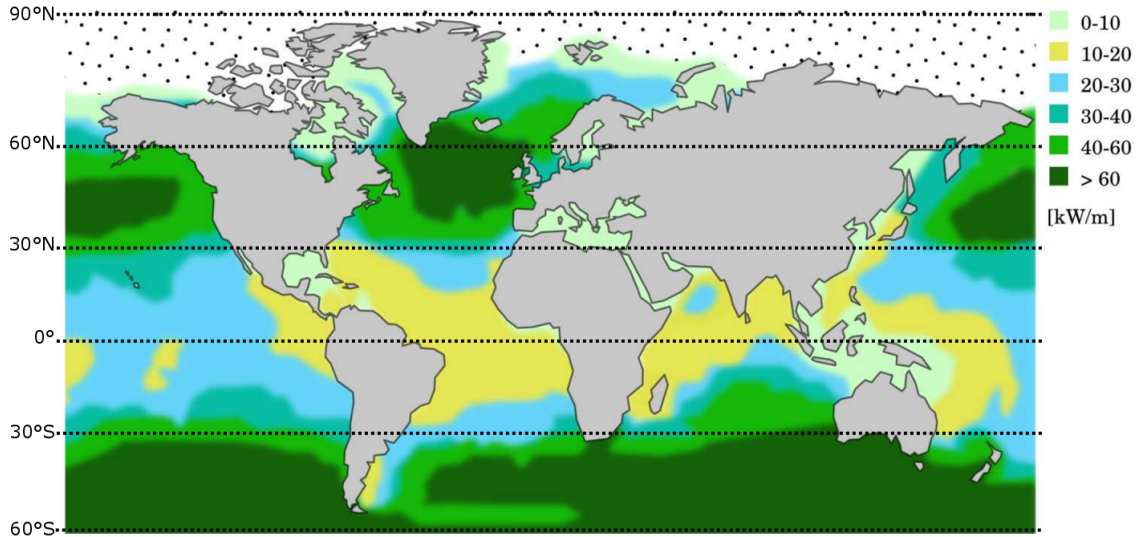


Figure 1.1: Average annual wave energy transport [kW/m], redrawn from [5].

Wave energy can be particularly advantageous in locations where other renewable energy sources are poor, or where the cost of traditional energy is relatively high; examples are islands not connected to the grid, locations with no reliable or conspicuous sun/wind energy resource, or without hydro power. Likewise, wave energy can be a solution in cases where energetic autonomy is required, such as offshore platforms, or power buoys.

Synergy between different renewable sources is a convenient way to cope with variability and availability of the resource, improving the quality of the electric energy produced. For example, offshore wind turbines and wave energy converters (WECs) may be installed on the same platform, taking advantage of the fact that wind and waves are often statistically uncorrelated, since they travel at different speeds, and waves may have travelled long distances, while winds are more local. Likewise, another way to exploit synergy is to install wave energy converters on already existing/planned marine structures. An example is the installation of oscillating water column in wave breakers, taking benefit from a shared investment and, therefore, generating energy at a lower cost.

Although wave energy has received worldwide attention since 1970s [6] (following the oil crisis), no WEC is commercially completed yet, since economic viability has not been reached. Furthermore, there is a striking absence of clear technology convergence, with over a thousand different concepts and patents proposed over the years. For the sake of comparison, when one thinks about the mature industry of wind energy, the established technology of the three-blade horizontal axis turbine comes into mind, while the young wave energy industry is populated by a plurality of extremely different WECs.

There are many reasons why wave energy is still mainly in research stage, rather than the commercial one, mostly related to the specific challenges and shortcomings of harnessing highly-concentrated wave power. Far from being exhaustive, a few important challenges are briefly discussed. Most importantly, the sea is a very hostile environment to live in; therefore, devices must be designed foremost for structural integrity, survivability, and longevity, according to the most extreme expected sea conditions, which are several times more severe than the operational ones. Hence, the device and its components are often oversized, with bigger and heavier components (more expensive), able to withstand

high ratios of maximum/average loads. Furthermore, due to potentially short and scarce time windows with mild weather conditions, accessibility of the WEC for maintenance is often an issue. Consequently, eventual long periods of production interruption may cause considerable financial loss, increasing the overall cost of energy. Another issue is related to relatively low quality short-term weather forecasts. While reliable for few days in advance, the accuracy of the prediction decreases on the hour-by-hour basis, and especially on the wave-by-wave time scale, which is crucial for power optimization control strategies. A further characteristic of the wave energy source is its variability, which has an impact on the low-end of the conversion chain: the electricity grid must be able to cope with low energy production periods, and high-voltage grid connection systems have to be designed to withstand large peaks of energy production, much larger than the average.

As a result, there is no mature technology yet, nor any strong convergence in the device design. In order to answer to the many challenges described above, different technological solutions have been adopted, which are dependent on the installation site, energy demand, weather conditions, market target and, most importantly, the inventors vision! Indeed, to date, there are over a thousand of essentially different WEC concepts. In order to evaluate the level of maturity of a technology, it is common practice to use the Technology Readiness Level (TRL) [7], which is a metric, ranging from 1 to 9, that defines how ready a technology is, directly associated with the commercial ability of the technology [8]. Most of the concepts are able to reach TRL 3, since relatively low investments are required, but very few reach TRL 6 or above.

Although the reasons for failure of most promising wave energy companies are varied, they often fall into the same global envelope. In fact, a common denominator of these failures, as pointed out in [8], is the rush to build the large/full scale device as soon as possible, involving massive capital investments, even though the trust on the overall performance is still low. Such a momentum, to rapidly escalate the size of the device, is often due to the investors' demand to have something tangible to show to stakeholders and the public domain. Unfortunately, since wave energy technology is still immature, with high levels of uncertainties and low industrial experience, it is extremely risky to accelerate the TRL growth before some performance requirements are met. Indeed, it is easier to make fundamental adjustments to the technology at an early stage of development (low TRL), working with small and cheap prototypes and mathematical models. Conversely, small changes at a high TRL are likely to require unacceptably large investments.

In order to visualize and systematically discuss differences in development strategies, in [8] a supplementary metric has been defined, called Technology Performance Level (TPL), ranging from 1 to 9, which measures how well a technology performs, directly associated with its economic ability. While the TRL is related to capital investment, the TPL is strictly related to cost of energy. In [8] it is roughly estimated that a 3-level increase in TRL corresponds to an order of magnitude increase in investment (starting from about 1 MEuro to reach TRL 3); similarly, a 3-level increase in TPL produces an order of magnitude decrease in cost of energy (starting from about 1 euro/ kW at TPL 3).

Considering the TRL-TPL matrix, two possible development paths are identified and discussed in [8], as shown in Fig 1.2. The first one, most common in the current wave energy industry, favours an initial increase of TRL, at low TPL, with a consequent increase of TPL, at high TRL. Such a trajectory is highly discouraged, while its inverse is proposed as optimal, with an initial increase of TPL, at low TRL, and consequent increase of TRL, at high TPL. The main advantage of the optimal trajectory is the flexible design at low TRL, made possible by the low financial and time investments requirements for fundamental modifications of the core technology. However, one of the challenges to actually succeed to push the TPL high at low TRL consists of the low reliability and trust on the mathematical models, and the difficulty to accurately foresee the behaviour and technical issues of the final device.

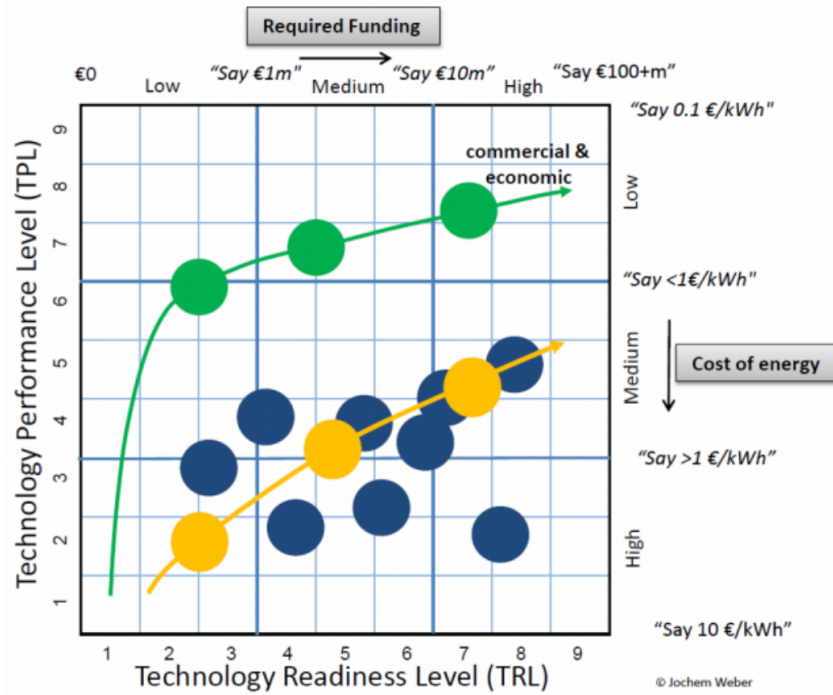


Figure 1.2: TRL-TPL realistic development paths. On the bottom, in blue and yellow, a characteristic subset of existing WEC technologies; on the top, in green, the optimal trajectory [8].

1.2 Motivation

The mandatory condition to make wave renewable energy sustainable is obtaining economic viability, therefore increasing the ratio between power produced and cost of energy. A key role in the quest of increasing power and decreasing costs is played by mathematical models. Mathematical models are essential to design every device feature, starting from the early stages of concept proof and preliminary design, all the way to final optimization and minor refinements. Furthermore, mathematical models are the main tool to estimate the response of the device, in terms of motion, power produced, and structural loads. Such information is used to evaluate how profitable the device is, or to verify if structural constraints, which permit operation in the power production mode, are respected, i.e. determine when the device must switch to survivability mode in order to survive to extreme events. Finally, mathematical models are often the core of the control strategy, which is the intelligent tuning of the device in order to maximize the power absorption, therefore increase the efficiency of the WEC.

On the one hand, it is desirable to have models with high accuracy, which guarantee reliable information, therefore effective design, motion/power/loads assessment, and control, whereas inaccurate models inherently generate poor performance. On the other hand, a modest computational time is often a fundamental requirement as well, especially in design optimisation and control processes. Combining the accuracy and the computational time demands is a challenging task since, usually, higher accuracy is paid for by additional computational burden.

Mathematical modelling of wave energy converters naturally germinates from traditional ocean engineering theory, where the use of linear models is commonplace. Indeed, the assumption of linearity, which is of small amplitude of motion of the body, is usually verified, since the objective in offshore applications is the stability of the structure. Conversely, the purpose of wave energy converters is to *exaggerate* the amplitude of motion, in order to maximize energy absorption. Such a magnification is usually imposed by

the control strategy, which tunes the system in chasing the maximum power conversion objective. Consequently, linear models for wave energy conditions, in the operational region, and therefore under controlled conditions, are potentially inaccurate, since the linear assumption is not respected.

However, the vast majority of mathematical models, in the wave energy field, are linear, mainly due to their computational convenience. In fact, including one or more nonlinear effects normally requires a non-negligible increase in model complexity and computational time, while generating accuracy improvements highly dependent on the device characteristics and operational conditions. Among the wide selection of modelling approaches, an appropriate one has to be chosen, according to the accuracy/computational time compromise requirement particular to the application the model is intended for. For preliminary studies, such as early stage concept development or approximate array calculations, low accuracy may be acceptable, while fast computation is mandatory. Fully-linear models are therefore widely used, since they can return reasonable results, rapidly. On the contrary, for survivability, extreme events, and loading studies, accurate results can be returned only by very complex and time consuming models such as, for example, fully-nonlinear CFD (computational fluid dynamics) or SPH (smoothed-particle hydrodynamics) models. In between, for power production assessment and model-based controller tuning and optimization, medium/high fidelity, with an acceptable computation time, is required to correctly define the parameters of a system and the predicted performance of a device, over a wide range of sea conditions. Furthermore, mathematical models for control applications must compute quickly enough to allow the control strategy to take action in real time.

Under the TRL-TPL matrix perspective of the optimal development path, mathematical models, which are simultaneously accurate and fast to compute, may facilitate a rise on the TPL scale, at low TRL values. Indeed, mathematical models are the main and more flexible developing tool at low TRLs. If accurate, they are more reliable, allowing the simulation of the actual dynamics of the system and, consequently, helping to increase the TPL, before going to large scale prototype testing. However, in order to have an important impact on the design, mathematical models have an important use in optimization studies; therefore, they have to be computationally viable. Furthermore, control strategies, which are potentially able to significantly increase the power absorption, therefore the TPL, are most effective if the mathematical model they are based on is accurate.

The aim of this thesis is to identify different relevant nonlinearities, for different devices, and in different wave conditions. A particular focus is put on controlled conditions, since they normally enhance nonlinear effects. Indeed, under uncontrolled conditions, nonlinearities are often negligible, and linear models are typically accurate. However, normal operation requires the implementation of a control strategy in order to increase power capture. On the other hand, extreme wave events fall beyond the scope of this study, since the device must turn into survival mode for self-preservation, and therefore is not producing energy.

In this thesis, novel mathematical models are designed, pursuing both accuracy and computational efficiency, in order to create models suitable for use in iterative design processes, or in control applications. Such models are referred to as “parsimonious”, meaning that only the most relevant nonlinearities are included, in a computationally efficient way, in order to describe the behaviour of the device in a fast but sufficiently accurate way. Therefore, a parsimonious model has a considerably higher accuracy than a linear model, at a reasonably low computational time, particularly allowing computation in real time (run time \leq simulated time). Similarly, a parsimonious model, in the power production region, should have an accuracy lower, but comparable, to fully-nonlinear models, but at a small fraction of the computational time.

1.3 Main objectives and contributions

The main objectives and novel contributions of this thesis are summarised as follows:

1. The main purpose of the present thesis is to critically discuss on the necessity of nonlinear hydrodynamic mathematical models for wave energy converters, and to propose novel approaches, which contribute to the advance of the state-of-the-art in the field. In order to do so, it is of paramount importance to draw a complete picture of available modelling techniques, up to date, with a particular focus on their strengths and weaknesses. **Chapter 2** provides a comprehensive review of nonlinear modelling approaches, and highlights some of the gaps in the literature this thesis purports to fill. Work published in [9, 10]
2. Despite the fact that active control strategies are one of the main causes of nonlinear behaviour of wave energy converters in nominal power production conditions, controllers are rarely, if ever, implemented into any fully-nonlinear CFD software. Therefore, the purpose of **Chapter 3** is to implement an active controller, in particular a latching control strategy, in the open source CFD software OpenFOAM. Such a CFD model is then used for accuracy benchmarking, and to discuss nonlinear effects, in Chapters 3 and 6. Work published in [11, 12, 13, 14].
3. Most wave energy converters are described by linear mathematical models, based on the main assumption of small amplitudes of motion. Notwithstanding the computational convenience, linear models can become inaccurate when large motions occur. Nonlinear hydrodynamic models implementing nonlinear calculation of Froude-Krylov (FK) forces are particularly well-performing for small devices, compared to the wavelength. Existing nonlinear FK models require, for geometry of arbitrary complexity, a spatial discretization and a time-consuming remeshing routine. However, model-based controllers require system dynamic models which can execute in real time. Therefore, **Chapter 4** proposes a computationally efficient representation of nonlinear static and dynamic Froude-Krylov forces, valid for any heaving axisymmetric point absorber. Work published in [13, 14, 15].
4. Nonlinearities are first and foremost device-specific. Two of the most common modes of oscillation of single degree of freedom wave energy converters are heave and surge, which are exploited, respectively, by heaving point absorbers (HPAs), and oscillating wave surge converters (OWSCs). **Chapter 5** purports to discuss major hydrodynamic differences between HPAs and OWSCs, taking into account nonlinear static and dynamic Froude-Krylov forces, and viscous drag forces, in order to highlight their very different contribution in building up the total hydrodynamic force. Work published in [16, 17].
5. The definition of a mathematical model is not straightforward and should take into account the specific application it is intended for. Two of the most important characteristics of a model are the computational time and the expected accuracy, which usually are mutually conflicting. The inclusion of nonlinearities potentially increases the model accuracy, but at a higher computational price. Considering a heaving point absorber with and without control, **Chapter 6** studies and compares nine different modelling options, eight of which are based on potential theory and consider nonlinear Froude-Krylov and viscous drag forces, while one is based on fully-nonlinear computational fluid dynamics. The value of including nonlinearities in the hydrodynamic model is discussed in relation to the computational cost of the eventual accuracy benefits, under a range of scenarios. Work published in [13, 14].

6. Viscous drag forces in mathematical models for wave energy converters is usually modelled by means of a term based on the Morison equation. Notwithstanding the importance of a reliable estimate of the drag coefficient in the Morison equation, much inconsistency and low trustworthiness is found in the literature, about both the values themselves, and the identification methods. **Chapter 7** seeks to discuss the inherent challenges to drag identification, specific to wave energy applications. Moreover, different identification techniques are implemented, evaluated and compared, with regard to the estimation of the drag coefficient for a floating heaving point absorber. Work published in [18].
7. One of the sources of nonlinearity in fluid-body interactions is the wave field itself. Different wave models exist, achieving a different compromise of accuracy and complexity. The impact of the accuracy of such wave theories strongly depends on the specific device (operating principle, power production region or survivability mode), and installation site (water depth, occurrences of each sea state in the scatter diagram of the installation site). **Chapter 8** evaluates the performance of different wave field representations, firstly in absolute terms and, secondly, in relation to the associated computation of nonlinear Froude-Krylov forces for different wave energy devices, in regular and irregular sea states. Work published in [19, 20].
8. Many real devices are likely to move in more than one degree of freedom; although simple and often effective, single degree of freedom models may neglect important effects. In particular, pitching instability and parametric resonance are highly nonlinear phenomena, with detrimental consequences on power production, and possibly the device integrity. Nonlinear Froude-Krylov models are able to appreciate such nonlinear effects, but usually at a high computational price. **Chapter 9** presents a computationally efficient approach to model nonlinear Froude-Krylov forces in many degrees of freedom; case studies are then considered, inspired by existing devices, namely the CorPower, the Wavebob, and the SparBuoy devices. Work published in [21, 22, 23, 24, 25, 26].

1.3.1 List of publications

- M. Penalba, G. Giorgi, and J. V. Ringwood, A Review of Non-Linear Approaches for Wave Energy Converter Modelling, in Proceedings of the 11th European Wave and Tidal Energy Conference, (Nantes), 2015.
- M. Penalba, G. Giorgi, and J. V. Ringwood, Mathematical modelling of wave energy converters: a review of nonlinear approaches, Renewable and Sustainable Energy Reviews, vol. 78, pp. 1188–1207, 2017.
- G. Giorgi and J. V. Ringwood, Implementation of latching control in a numerical wave tank with regular waves, Journal of Ocean Engineering and Marine Energy, vol. 2, no. 2, pp. 211–226, 2016.
- J. Davidson, C. Windt, G. Giorgi, R. Genest, and J. V. Ringwood, Evaluation of energy maximising control systems for wave energy converters using OpenFOAM. 2017.
- G. Giorgi and J. V. Ringwood, Computationally efficient nonlinear Froude-Krylov force calculations for heaving axisymmetric wave energy point absorbers, Journal of Ocean Engineering and Marine Energy, vol. 3, no. 1, pp. 21–33, 2017.
- G. Giorgi, M. Penalba, and J. V. Ringwood, Nonlinear Froude-Krylov Force Representation for Heaving Buoy Wave Energy Converters, in In Proceedings of the 3rd Asian Wave and Tidal Energy Conference, (Singapore), 2016.
- G. Giorgi and J. V. Ringwood, Nonlinear Froude-Krylov and viscous drag representations for wave energy converters in the computation/fidelity continuum, Ocean Engineering, vol. 141, no. April, pp. 164–175, 2017.

- G. Giorgi, M. Penalba, and J. V. Ringwood, Nonlinear hydrodynamic force relevance for different wave energy converter types, in Proceedings of the 3rd Asian Wave and Tidal Energy Conference, (Singapore), pp. 154–162, 2016.
- G. Giorgi and J. V. Ringwood, Comparing nonlinear hydrodynamic forces in heaving point absorbers and oscillating wave surge converters, *Journal of Ocean Engineering and Marine Energy*, vol. 4, no. 1, pp. 25–35, 2018.
- G. Giorgi and J. V. Ringwood, Consistency of viscous drag identification tests for wave energy applications, in 12th European Wave and Tidal Energy Conference, (Cork), 2017.
- G. Giorgi and J. V. Ringwood, Importance of nonlinear wave representation for nonlinear Froude-Krylov force calculations for wave energy devices, in 12th European Wave and Tidal Energy Conference, (Cork), 2017.
- G. Giorgi and J. V. Ringwood, Relevance of pressure field accuracy for nonlinear Froude-Krylov force calculations for wave energy devices, *Journal of Ocean Engineering and Marine Energy*, vol. 4, no. 1, pp. 57–71, 2018.
- G. Giorgi and J. V. Ringwood, Analytical Formulation of Nonlinear Froude-Krylov Forces for Surging-Heaving-Pitching Point Absorbers, in ASME 2018 37th International Conference on Ocean, Offshore and Arctic Engineering, (Madrid), 2018.
- G. Giorgi and J. V. Ringwood, Analytical representation of nonlinear Froude-Krylov forces for 3-DoF point absorbing wave energy devices, accepted in *Ocean Engineering*, 2018.
- G. Giorgi and J. V. Ringwood, A Compact 6-DoF Nonlinear Wave Energy Device Model for Power Assessment and Control Investigations, in press in *IEEE Transactions on Sustainable Energy*, 2018.
- J. Davidson, T. Kalmar-Nagy, G. Giorgi, and J. V. Ringwood, Nonlinear rock and roll - Modelling and control of parametric resonances in wave energy devices, in Proceedings of the 9th Vienna International Conference on Mathematical Modelling, (Vienna), 2018.
- G. Giorgi and J. V. Ringwood, Articulating Parametric Nonlinearities in Computationally Efficient Hydrodynamic Models, in Proceedings of the 11th IFAC Conference on Control Applications in Marine Systems, Robotics, and Vehicles, (Opatija), 2018.
- G. Giorgi and J. V. Ringwood, Parametric motion detection for an oscillating water column spar buoy., in Proceedings of the 3rd International Conference on Renewable Energies Offshore, (Lisbon), 2018.

Review of nonlinear effects and modelling options

2.1 Motivation

The objective of this thesis is to present a critical discussion on the need for nonlinear hydrodynamic modelling for wave energy converters, leading to the development of novel modelling approaches. Therefore, in order to define the current gaps in the state-of-the-art of the field, it is essential to draw a complete picture of available modelling techniques, up to date, focusing on their strengths and weaknesses. Hence, the motivation of the present chapter is to provide a comprehensive review of nonlinear modelling approaches, and to highlight some of the gaps in the literature this thesis purports to fill.

2.2 Introduction

The ultimate success, or at least feasibility, of the wave energy industry in providing an effective alternative to traditional energy supplies, as well as other renewable energy sources, strongly relies on the capability of reducing the ratio between costs and power production. In fact, the wave energy industry can economically justify its existence only by selling electricity at a price which is competitive within the energy market. It is therefore necessary to maximize the efficiency of the device, across the full range of sea states, while keeping costs low. Economic performance can be significantly assisted through the optimization of device intelligence, namely through energy maximizing control algorithms. Intelligent and precise control strategies can considerably improve the performance of any wave energy device (heaving point absorbers (HPAs) [27], oscillating pitching converters (OPC) [28] or oscillating wave surge converters (OWSC) [29]).

The fullest and most precise information on the wave energy system is imperative for the optimization of the device, and maximization of the generated power, which requires precise mathematical models able to accurately reproduce the behaviour of a device in real sea conditions. Mathematical models are crucial, for example, for power production assessment, simulation of device motion, estimation of structural loads, and model-based control strategies. Wave energy converters (WECs) are, nonetheless, commonly designed and studied by numerical models inherited by the offshore engineering industry. Due to the wide range of diverse sea states and conditions that any device operating in the ocean needs to face, different operational modes are used: power production mode, activated within a range of sea-states for which the device is able to produce power, without compromising its integrity; and survival mode, activated during extreme sea conditions, in order to avoid structural damage. Similar procedures are also applied in offshore engineering,

where nonlinear behaviour is assumed to be important during extreme conditions, but not during normal operation mode.

However, in contrast to traditional offshore engineering applications, WECs are designed to maximise power absorption, and to experience large motions, by encouraging the device to oscillate as much as possible, for which control strategies are used. Large motions are, therefore, usual for wave energy devices, so that nonlinear dynamics may appear, not only within the survival mode (which is obvious, due to the highly nonlinear behaviour of the device under extreme conditions), but also during power production mode. Accordingly, linear approaches, originally created for traditional offshore engineering applications, may not be accurate in reproducing the behaviour of WECs, when large motions occur. Thus, as illustrated in Fig. 2.1, a typical scenario, valid for wave energy applications, is divided into three different regions: a linear region, a nonlinear region, and a highly nonlinear region. In such a scenario, nonlinear models would also be essential within the *nonlinear region* of the power production mode.

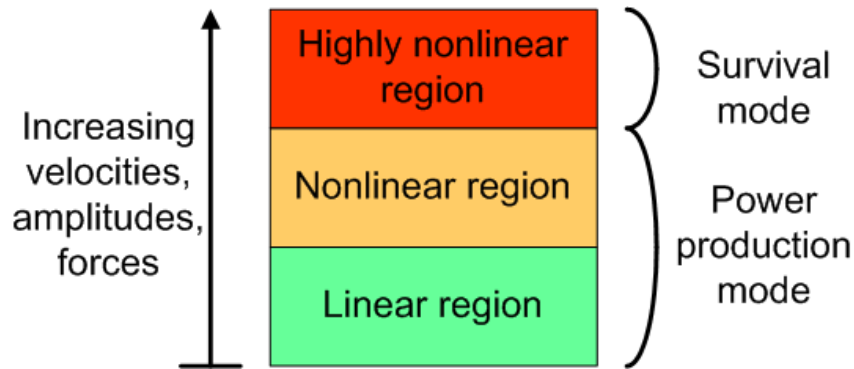


Figure 2.1: Different operating regions for wave energy devices

Although WECs are likely to work in nonlinear regions, the vast majority of mathematical models utilised so far are linear, due to both computational convenience and simplicity, and to some historical inertia to change the modelling approach that serves the standard ocean engineering applications so well. However, with increasing maturity of the wave energy field, progressively diverting from the traditional ocean engineering field, the possible need for nonlinear models is widely acknowledged, and nonlinear approaches are becoming more and more common. The present chapter of the thesis proposes an overview of existing modelling options, with a critical view on their advantages and disadvantages. Most importantly, depicting the complex canvas of existing mathematical models also serves the purpose of identifying the gap, which this thesis purports to fill.

Thus, the present chapter is divided into two different sections: Sect. 2.3 identifies different nonlinear effects involved in wave-device interaction, and critically analyses the relevance of such nonlinear effects for different WECs, while Sect. 2.4 considers different modelling approaches that describe such nonlinear effects: nonlinear physics-based models (Navier-Stokes, and smoothed-particle hydrodynamics), different versions of potential flow models (partly-, weakly-, and fully-nonlinear methods), and data-based models are reviewed.

Since relevant nonlinear dynamics may vary with the characteristics of each WEC type, the appropriate modelling approach for each WEC may also vary. Therefore, the most suitable modelling solution for each kind of WEC is suggested, in order to efficiently fulfil their different requirements. In order to provide a broader perspective of the nonlinear effects present in wave energy converter dynamics, nonlinearities of the incoming wave trains and the power-take off (PTO) systems are, in addition, briefly addressed. Therefore, Sect. 2.5 presents a critical comparative study of the different modelling approaches examined, and their applicability/suitability for different WECs.

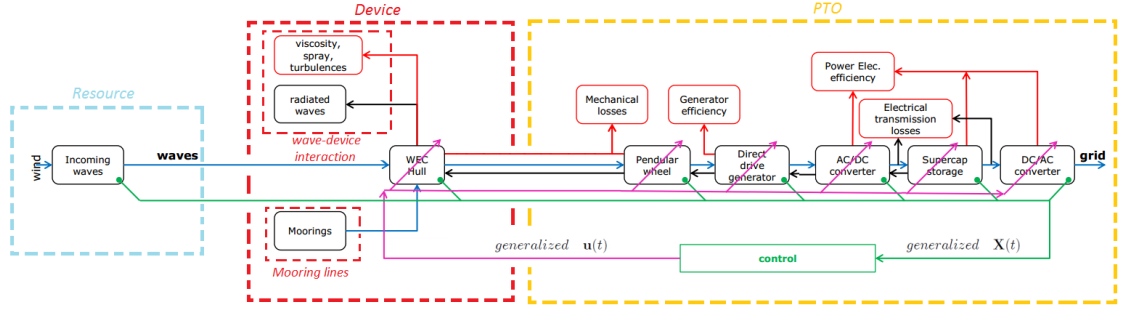


Figure 2.2: Block diagram of different modelled components of the SEAREV device, modified version of the diagram in [34]

2.3 Main nonlinear effects in wave energy converters

The origin of nonlinear hydrodynamic effects has been demonstrated to be very diverse, but three main sources can be identified: the *resource* or incoming wave (modelling nonlinear incoming waves [30]), the *device* (different nonlinear effects resulting from the wave-device interaction, such as viscous effects [31], the variation of the wetted surface due to the motion of the body [32], or mooring lines [33]) and the *power take-off* system (nonlinear dynamics within the PTO system [27]).

Fig. 2.2 illustrates the various components and driving forces for a general WEC. The diagram has been divided into three main aspects: the resource (the wave) in light blue on the left, the device (and wave-body interaction) in red in the middle, and the power take-off system in yellow on the right. The three groups (resource, device, and PTO) are described in the following subsections 2.3.1, 2.3.2, and 2.3.3, respectively.

2.3.1 The wave resource

Incoming waves, as a direct result of the wind, can be represented in many different ways, from linear monochromatic waves, where waves are basically adjustable (amplitude and frequency) sinusoidal signals, to irregular and fully nonlinear (including viscous effects) waves in three dimensions, simulated in a numerical wave tank. For the case of regular waves, Fig. 2.3 illustrates the appropriate wave theory to be used, as a function of the wave height, wave period, and water depth.

Because the focus of this thesis is on devices operating in the power production mode, only waves that are suitable for power production are considered, avoiding extreme, highly nonlinear, waves. Therefore, defining a region of the wave theory diagram under which power can be harvested is useful. However, operational conditions of WECs are highly device-dependent. For each device, data from open ocean tests can be used to determine the upper boundary of the power production region, in relation to the location characteristics (water depth). Fig. 2.3 shows such an upper boundary for three different devices, the *Oyster* (near-shore) [35], and the *Pelamis* (off-shore) WECs [36], deployed at the European Marine Energy Centre (EMEC), and the *Sea Power* device (off-shore) [37], deployed at the Atlantic Marine Energy Test Site (AMETS), giving a reasonable representation of different WEC types and location characteristics. Hence, an approximate *power production mode operation area*, the blue area in Fig. 2.3, is defined.

This *power production mode application area* suggests that Stokes water waves [38] up to the third order should be considered in intermediate and deep water waves. Stokes' theory, nevertheless, breaks down in shallow water [38], where an alternative is the Cnoidal theory, providing waves with sharper crests and flatter troughs. [38] shows that a fifth-order expansion of Stokes' and Cnoidal theories is of acceptable accuracy almost every-

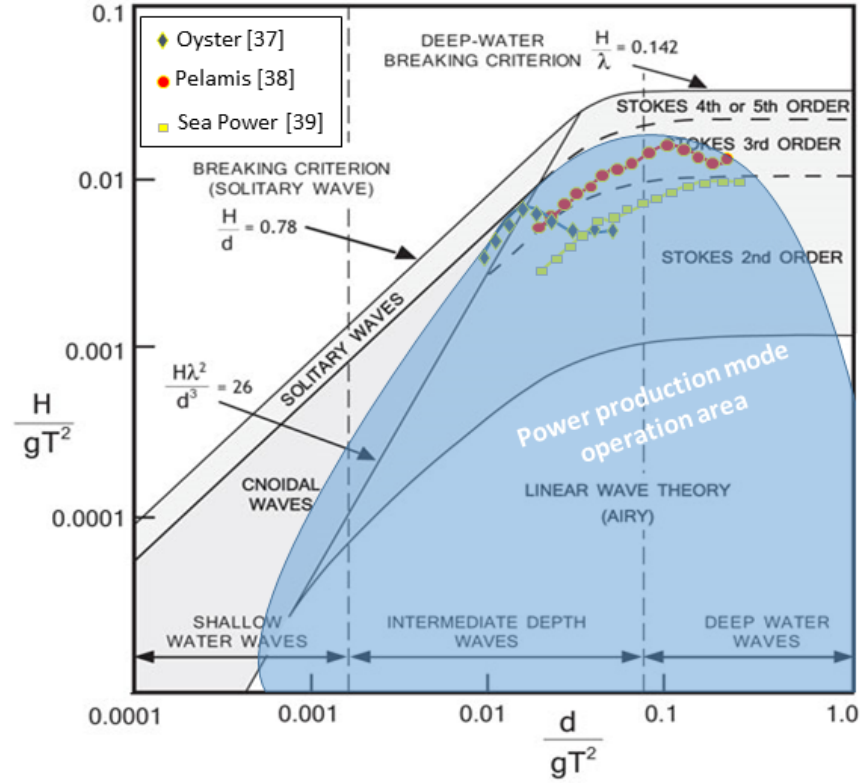


Figure 2.3: Wave theory diagram with the application area for power production in wave energy [9]. Markers based on data published in [35] for Aquamarine, in [36] for Pelamis, and in [37] for Sea Power

where within the range of validity of each theory, but very high-order expansions are required to get really accurate results. Expansions up to the fifth order largely cover the *power production mode application area*. Rienecker and Fenton presented an efficient, but numerical, method [38], where equations are solved by Newton’s method and coefficients are calculated numerically by solving fully nonlinear equations. On the other hand, artificial modifications of linear theory are sometimes employed, in order to reduce the errors of linear wave theory, but preserving its simplicity. One effective approach is Wheeler stretching [39], which stretches the dynamic pressure profile, obtained with linear Airy’s theory, so that the total pressure on the free surface matches the atmospheric pressure. **Chapter 8** of this thesis discusses the relevance of the accuracy of the incoming wave pressure field representation, in the context of nonlinear hydrodynamic force calculations, considering Airy’s theory, Wheeler stretching, and Rienecker-Fenton waves.

However, regular (monochromatic) wave theories do not represent real waves since, in the ocean, two consecutive waves are never identical. Therefore, irregular wave theories are used to reproduce a real sea-state. The most established way of describing real sea-states is via Fourier analysis of records taken in different sites. These records are used to create a wave spectrum for real locations, giving the distribution of wave energy among different wave frequencies, or wave-lengths, on the sea surface. Various idealized spectral modes are used in ocean engineering and oceanography, such as the Pierson-Moskowitz [40], the JONSWAP [41], the Bretschneider [42] models, or the Ochi-Hubble [43] model able to describe a multi-peak spectrum.

Another alternative is to use a high order spectral (HOS) method, for simulating nonlinear propagation of free-surface waves [30], using a spectral expansion and the Fourier transform, together with a modified Taylor series expansion, in order to compute the Dirichlet to Neumann map on the free-surface. **Chapter 8** also takes a HOS method into

account for the comparison of different incoming wave theories, for computing nonlinear hydrodynamic forces.

While Fourier analysis and spectral methods are well established, other methods may provide more insight into the wave physics, especially in non-stationary and highly nonlinear conditions. [44] presents a method, for which the key part is the empirical mode decomposition (EMD), allowing the decomposition of any data set, no matter how complicated, into a finite and small number of intrinsic mode functions that admit Hilbert transforms. The main advantage is the definition of an instantaneous frequency, varying in time, which retains physical meaning in a more compact decomposition using different time scales.

2.3.2 Device

In order to analyse nonlinear effects of a device, time domain models are usually required. Equation (2.1) represents all the forces acting on a wave energy device, without specifying the way they interact

$$\mathbf{M}\ddot{\mathbf{x}}(t) = \mathcal{F}(\mathbf{f}_{FK}(t), \mathbf{f}_D(t), \mathbf{f}_R(t), \mathbf{f}_{vis}(t), \mathbf{f}_{PTO}(t), \mathbf{f}_{moor}(t), \mathbf{f}_{add}(t)) \quad (2.1)$$

where \mathcal{F} is a generic nonlinear function, \mathbf{M} is the inertial matrix of the device, \mathbf{x} is the state vector, \mathbf{f} the generalized force vector, composed of forces (F) and torques (T), \mathbf{f}_{FK} the Froude-Krylov force, \mathbf{f}_D the diffraction force, \mathbf{f}_R the radiation force, \mathbf{f}_{vis} the viscous force, \mathbf{f}_{PTO} the force acting on the structure due to the power take off (PTO) system, \mathbf{f}_{moor} the force due to the mooring lines, and \mathbf{f}_{add} the force corresponding to any other additional force, such as drift, wind, tidal, or other body-water interactions.

The following subsections analyse the different forces acting on the device, and the nonlinear dynamics resulting from the wave-device interaction.

2.3.2.1 Froude-Krylov force

The Froude-Krylov (FK) force is the load due to the undisturbed incident pressure field, acting on the wetted surface of the body. It is generally divided into static ($\mathbf{f}_{FK_{st}}$), and dynamic ($\mathbf{f}_{FK_{dy}}$) components. The static part represents the relation between gravity and buoyancy forces, while the dynamic part represents the force due to the time-varying part of the pressure of the incident wave train.

Linear codes compute the FK force over the mean surface of the body, while nonlinear computation requires the integration of the incident wave pressure and the hydrostatic pressure over the *instantaneous* wetted surface, at each time step. Different techniques to compute nonlinear FK forces are presented in Sect. 2.4.2.2. The linear representation of FK forces loses accuracy when analysing large relative motions between the free-surface elevation and the device motion, when the wetted surface varies considerably over time.

2.3.2.2 Diffraction and radiation forces

The diffraction force is the load associated with the action of the diffracted wave. Such a disturbance is introduced into the wave system by the presence of the floating body, and is defined for a body fixed in position, subject to incoming waves. The dynamic FK force, together with the diffraction force, makes up the total wave excitation force acting on a floating body. According to [45], assuming a linear diffraction term is a reasonable approximation to the excitation force if the body is small in comparison to the wavelength.

The radiation force, on the other hand, is the hydrodynamic force associated with the motion of the floating body in calm water. In general, a linear representation for

the radiation force is reasonably good for devices which are much smaller than the wavelength, as in the case of the diffraction force [32]. However, a more precise computation of diffraction-radiation terms is possible, as shown in Sect. 2.4.2.2.

2.3.2.3 Viscous force

In the traditional offshore industry, in which hydrodynamic models have been mainly based on linear potential flow theory, viscous losses are considered relevant for structures that are small compared to the wave amplitude. Since offshore structures are, in general, relatively large (e.g. offshore oil and gas platforms or ships), viscous losses are minor losses, except for localized effects, such as vortex shedding generation around sharp edges. However, wave energy converters are generally small devices, especially point-absorbers, and so viscous effects may be relevant.

2.3.2.4 Parametrically excited motions

Any object floating in the ocean, e.g. ships or WECs, may experience the parametric amplification of roll/pitch motions, caused by time-varying system parameters, and non-linear coupling of at least two degrees of freedom. Such a coupling appears when the incident wave has a frequency approximately twice the resonance roll/pitch frequency. This highly-nonlinear effect is often described, qualitatively, as a Mathieu-type instability [46]. Parametric instability is related to geometrical characteristics of the floating object caused, for long spars, by the dynamic variation of the metacentre position, as a consequence of the heave motion. When the metacentre height becomes negative during the simulation/experiment, the device becomes unstable, causing large roll/pitch motion amplitudes.

In the particular case of wave energy converters, parametric coupling represents a mechanism for internal excitation, and diverts energy from the degree of freedom where the energy is harvested, to a secondary one, generating parasitic motions and, consequently, power losses. The phenomenon of parametrically excited motions has been identified in wave energy converters when testing devices in real wave tanks [46, 47, 48]. Since, it is related to a loss of hydrodynamic stability in situations of large displacements, nonlinear potential models including nonlinear Froude-Krylov forces, such those presented in Sect. 2.4.2.2, are able to predict the phenomenon. **Chapter 9** of this thesis develops a computationally efficient, multi-degree of freedom, nonlinear FK force model, and uses it to effectively describe parametric resonance, in pitch and roll, of different existing devices.

2.3.2.5 Sloshing

When a liquid is enclosed in a container, and the liquid is provided with a free-surface within that container, slosh dynamics refer to the movement of the liquid within the container, which can severely affect the system dynamics [49]. The sloshing phenomenon has been much studied in ships and trucks transporting liquids, and is highly nonlinear. Hence, sloshing must be studied using fully nonlinear methods that include viscous effects, described in Sect. 2.4.1.

Sloshing effect can only appear in very specific WECs, where sea water can be considered to be enclosed. Hence, the sloshing effect is effectively restricted to oscillating water column devices, or specific concepts with an internal fluid tank, which can be used as a passive control device.

2.3.2.6 Slamming

Slamming is the impact of an object in the ocean onto the free surface, which is typical in those wave energy converters that raise from the free surface, and subsequently impact

it. Impact events are very typical under extreme conditions, which are beyond the scope of this thesis, but can also appear when operating in power production mode, especially in devices where energy is extracted by means of a rotation motion, e.g. hinged flaps. Slamming is a highly nonlinear phenomenon that requires wave tank experiments or fully nonlinear modelling methods. The key variables of a slamming event are the pressure magnitude, the duration of the event, and the spatial distribution [50].

2.3.2.7 Mooring system force

Since floating WECs are subject to drift forces due to waves, currents, and wind, they have to be kept on station by moorings. The offshore industry uses many different configurations, for different offshore applications. Nonlinear effects in mooring lines seem, in general, to be much more significant in the case of slack moorings than in the case of tightly moored devices [33]. [51] presents an approach for slack mooring lines, where cables are modelled as catenary lines by means of a quasi-static representation, where the nonlinear behaviour of a mooring line is clearly demonstrated for surge motion. Similar approaches are used in [52], for a slack mooring system, and in [33], for tightly moored systems, to articulate nonlinear mooring forces. However, quasi-static approximations cannot cover important dynamic effects, such as cable inertia, viscous drag forces, or effects due to slowly varying forces. [53] presents some measurements where the relevance of the dynamic effects is demonstrated by comparing experimental results with two different simulations: a simulation run with the fully-dynamic software OrcaFlex [54], and a quasi-static simulation presented in [55].

2.3.2.8 Relevance of nonlinear effects

The diversity of WEC concepts, based on very diverse working principles, makes the idea of a general mathematical model extremely difficult. Therefore, it is useful to group all the diverse concepts, in order to identify the main nonlinear effects relevant to each group. Based on the device working principle, and motion characteristics, with special attention paid to the relevance of different nonlinear effects, the following classification is considered:

- Oscillating Water Column converter (OWC)
- Heaving Point-Absorber (HPA)
- Oscillating Pitching Converter (OPC)
- Oscillating Wave Surge Converter (OWSC)

Overtopping devices are omitted, since overtopping itself is an extremely nonlinear phenomenon and essential effects, such as green water or breaking waves, can only be analysed by using fully nonlinear codes. The most important nonlinear effects of each WEC group are analysed in the following paragraphs.

Oscillating water column converter Nonlinear FK forces are an important factor, since the variation of the entrained water mass in the chamber depends on the relative motion between the device structure and the free-surface, so that the pressure of the water mass inside the chamber and the absorbed power can be more accurately computed by nonlinear FK force models [56]. In addition, and related to nonlinear FK forces, parametrically excited motions can appear in floating OWCs, as shown in [57], causing large motion amplitudes in pitch and roll. The Mathieu-type instability turns the desirable heave motion into an inconvenient pitch or roll motion, negatively impacting energy harvesting. A floating OWC is presented in **Chapter 9**, as an applicative case study for the

nonlinear FK force model proposed in this thesis, highlighting the ability of the model to articulate parametric resonance.

Viscous effects are also important in OWCs. In onshore located fixed OWCs, where waves have normally already broken, waves arrive at the chamber with high components of turbulence, and generate shedding vortices around the outer wall of the chamber. A similar phenomenon appears in the case of floating WECs, although waves are not broken yet. The behaviour of the free surface inside the chamber during the cycle is, therefore, highly nonlinear. Hence, linear approaches may under- or over-estimate the pressure differential in the chamber, since they commonly assume the water column acting as a simple piston.

Furthermore, especially in the case of floating OWCs, where a partially empty tank is moving, a sloshing effect may appear, resulting in significant variations of the fluid behaviour inside the chamber. Dynamic forces caused by liquid sloshing cannot currently be captured by seakeeping software and, therefore, fully-nonlinear modelling approaches are necessary. The sloshing phenomenon in floating structures creates a non-uniform force field in the chamber, with direct consequences on the whole body dynamics and stability, as seen in [58].

Heaving point absorber Linear computation of Froude-Krylov forces can be accurate for small motions, or even for situations where the device behaves as a wave follower, but loses accuracy when the relative motion between the device and the free-surface increases. In fact, when the relative motion between the device and the free-surface is large enough, for example, when the device resonates due to a control strategy, the influence of the nonlinear Froude-Krylov force on the dynamics of the system becomes important [59].

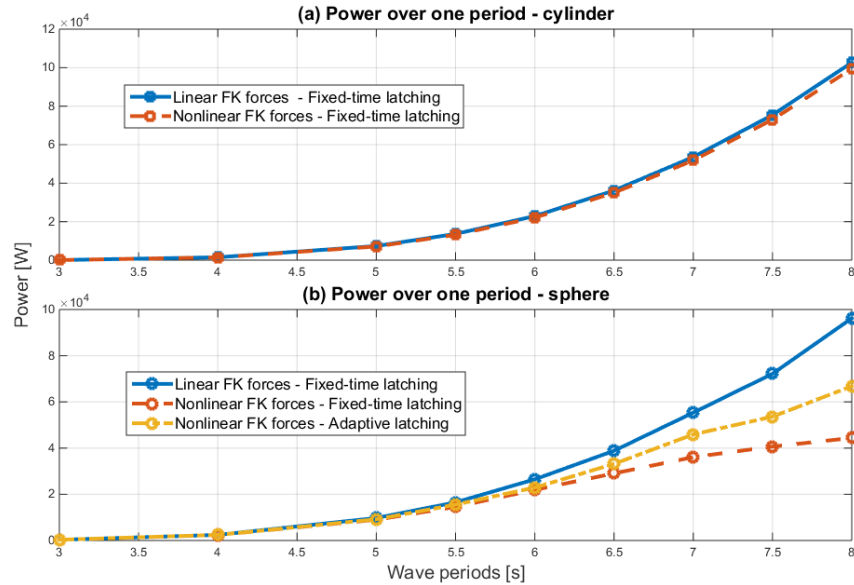


Figure 2.4: Power absorption for a cylinder and a sphere with linear and nonlinear computation of FK forces, with a latching control strategy [59]

There is, however, a geometric factor to be considered. Nonlinear Froude-Krylov effects can be important in cases where the cross-sectional area is non-uniform, such as a sphere, while the linear model representation appears to be reasonable for the case where the cross-section is uniform. Figure 2.4 illustrates the power overestimation of the models with linear FK forces, the loss of performance of control strategies based on linear models, and the geometric factor of FK forces.

Parametrically excited motions must be considered in HPAs with more than one degree of freedom. Self-reacting devices, where coupling between different modes is important, are highly sensitive to the nonlinear coupling of heave, and roll or pitch. [46] clearly

demonstrates that nonlinear heave, roll and pitch coupling occurs for large motion amplitudes, and that the nonlinear FK model is able to predict parametric resonance, validating the model against experimental tests in a wave tank. Inspired by the WEC in [46], a self-reacting two-body HPA is considered in **Chapter 9**, where a novel, computationally advantageous, nonlinear FK force model is shown able to similarly describe the parametric excitation phenomenon.

Viscous effects appear to have a low influence in small heaving point absorbers [60]. Vortex shedding is generated by the motion of the body relative to the surrounding fluid, but such shedding is not powerful enough to produce significant changes in the behaviour of the body and its power production capacity, if the achieved velocities are not too high. However, in the presence of an aggressive control strategy, such as latching control, viscous effects may become more relevant. Furthermore, some two-body HPAs use a damping plate attached to the bottom of the central floater, which enhances the vortex shedding process, changing the hydrodynamic properties by introducing extra damping (viscous damping) and increasing the added-mass [61].

Oscillating pitching converters In wave tank experiments, highly nonlinear behaviour, such as parametric roll and slamming, are found for the OPC SEAREV device [62], as illustrated in Fig. 2.5, highlighting the poor performance of the linear model in such conditions.

In the same way as HPAs, the computation of nonlinear FK forces is crucial for OPCs in order to predict the parametrically excited modes [62]. In addition, fast and large motions, typical in OPCs, encourage the formation of vortex shedding and other viscous effects which, consequently, become important. Furthermore, the characteristic pitching motion with large amplitude leads to highly nonlinear slamming events, that dissipate energy and limit the amplitude of the motions.

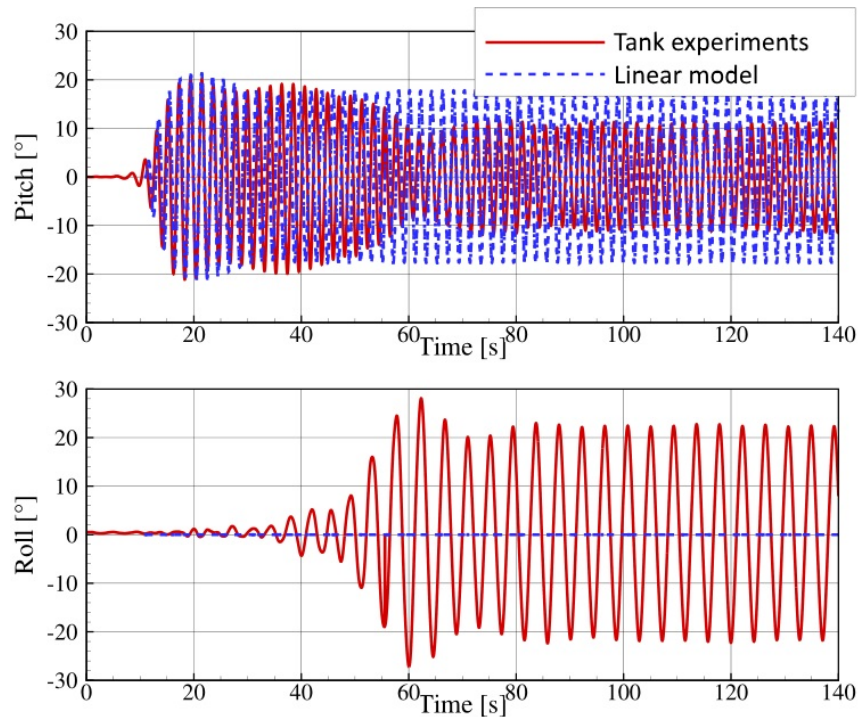


Figure 2.5: Nonlinear behaviour of the SEAREV device at large motions: (a) pitch motion (where the power is extracted), and (b) parametric roll, modified from [62]

Such nonlinear behaviour can only be predicted by fully nonlinear models, including

viscosity effects. Indeed, the viscous model needs to be suitably adapted to capture such behaviour.

Oscillating wave surge converters Radiation, diffraction, and viscous drag forces are prevalent, due to the typical large dimension of OWSCs. The fact that radiation and diffraction are dominating in OWSCs suggests that the impact of nonlinear radiation and diffraction may not be negligible, as happens with OWCs, HPAs, or OPCs. Unfortunately, no study was found in the literature that confirms or refutes the relevance of nonlinear radiation/diffraction forces in OWSCs. However, in **Chapter 5** of this thesis, a comparative study is proposed, between HPAs and OWSCs, using nonlinear FK forces and viscous drag forces. Considering how the total hydrodynamic force is partitioned into its subcomponents, it is concluded that the main excitation mechanism is the FK force in HPAs, while it is the diffraction force in OWSCs; likewise, viscous forces are relatively larger in OWSCs compared to HPAs.

Different studies have analysed viscous effects in surging devices and important nonlinear behaviour, such as the slamming phenomenon, has been observed. Turbulent vortices around surging converters are normally strong, and have a significant impact on motion and power absorption [31], as shown in Table 2.1.

Table 2.1: Viscous effects and their relevance for HPAs and OWSCs, in terms of annual power production (APP), from [60] and [31].

WEC type	Energy output	Without viscous term	With viscous term
HPA	APP	58 kW	56 kW
OWSC	APP	114 kW	74.4 kW

Slamming characteristics have been studied in [63], demonstrating the need to satisfactorily capture the slamming phenomenon in OWSCs, to accurately predict the behaviour of the device. Slamming events in WECs are still barely explored events, and more investigation is required to fully understand, for example, the cause of the sudden plunge of the water level in front of the device prior to the impact. In addition, due to the slamming phenomenon, a water jet is created as the device re-enters the water [63]. This water jet travels up the face of the flap and is finally ejected when the flap enters the water.

Summarizing the discussion provided in Sect. 2.3.2.8, Table 2.2 presents a comparative study of the impact of nonlinear effects on different WEC types. The relevance of the FK, radiation/diffraction, and viscous forces is evaluated for each WEC type. In addition, particular nonlinear effects that are likely to be important in each WEC-type are given.

2.3.3 Power take-off force

Different PTO systems are under development for wave energy devices, such as turbine transfer PTO (with air or sea-water as the working fluid), high-pressure hydraulic systems, or direct drives. With the exception of direct drive, all PTO systems convert the energy of the waves into electric power in two stages.

In many studies, PTO systems are modelled as a linear spring and damper in parallel, or even just as a single linear damper, consciously avoiding nonlinear effects, which does not mean the relevance of nonlinear effects in PTO systems is low. [71] studies all the different aspects, from the wave to the grid, where all kind of PTO systems and their characteristics are analysed, including losses and efficiencies.

Different sources of the nonlinearities for each type of PTO system are identified in Subsections 2.3.3.1 to 2.3.3.3.

Table 2.2: A comparative study of the impact of different nonlinear effects on different WEC types.

WEC-type	Reference WEC	Particular effects	Relevance of nonlinear effects		
			Froude-Krylov	Radiation/Diffraction	Viscosity
OWC	Mutriku [64] SparBuoy [65]	Breaking waves	<i>High</i> : essential to account for the time-variant entrained water mass in the chamber and predict parametrically excited motions.		<i>High</i> : crucial to predict the vortex shedding at chamber walls, behaviour of the free-surface in the chamber (sloshing phenomena) and highly turbulent broken waves.
		Sloshing Parametric excitation			
HPA	Wavestar [66] CETO [67] PowerBuoy [68]	Parametric excitation	<i>High</i> : crucial under large relative motions, for reproducing devices' behaviour, including parametrically excited motions.	<i>Negligible</i> : nonlinear radiation and diffraction effects are negligible for devices much smaller than the wavelength.	<i>Low</i> : viscous effects are low in general, but may become important with particularly aggressive control strategies, and for HPAs with damping plates.
OPC	SEAREV [69]	Parametric excitation Slamming	<i>High</i> : essential to predict parametrically excited motions.		<i>High</i> : crucial to predict the vortex shedding on the edges and slamming events.
OWSC	Waveroller [70]	Slamming	<i>Low</i> : the contribution of FK forces is low in OWSCs.	<i>N/A</i> : although dominated by radiation and diffraction forces, the relevance of nonlinear effects is not proven.	<i>High</i> : crucial to predict the vortex shedding on the sides of the flaps and slamming events.

2.3.3.1 Air-turbines

Different turbines for OWC converters are under development, including the Wells turbine which is “clearly the most frequently proposed and/or used air turbine to equip OWC plants” [72]).

Among the different options to model different air turbines in the literature, the turbine induced damping, studied in [73], suggests a linear relationship between chamber pressure and air mass flow for Wells turbines, and a nonlinear relation for self-rectifying impulse turbines. The main nonlinear effects in air turbines are the air compressibility in the chamber and the losses, which should be carefully included in order to get accurate results.

2.3.3.2 High-pressure hydraulics

High-pressure hydraulic systems are highly nonlinear systems, particularly suitable for slow motions, either in translation or rotation, linked to large forces or moments, respectively. A high-pressure hydraulic system consists of a hydraulic cylinder, valves, accumulators, a hydraulic motor, and hoses to connect the different components.

In order to consider different nonlinear effects in different components of the hydraulic circuit, the model should consider friction and fluid inertia forces, fluid compressibility in the cylinder [74], pressure losses in the hoses [75], time-varying gas volume and pressure in the accumulators (including compressibility of the fluid) [76], and compressibility and friction losses on the motor and valves (leakages) [76].

2.3.3.3 Direct drive

A direct drive linear generator generally consists of three parts: the armature, the translator, and a set of springs attached between the seabed and the armature. [77] describes different available concepts, such as the linear permanent magnet synchronous machine, the linear air-cored permanent magnet synchronous machine, and the slot-less tubular permanent magnet synchronous machine.

[78] describes different forces, some of which can lead to nonlinear behaviour, that are involved in the operation within the machine: the interaction of the two sets of magnets, electromagnetic damping due to the current carrying coils, and other forces due to different losses, such as eddy currents in armature and translator, saturation and reactive field losses, and losses due to proximity effects.

2.4 Nonlinear modelling approaches

A critical classification of the existing modelling approaches for wave-device hydrodynamic interaction is presented in this section. This classification is organised as follows: first of all, the physical theory the models are based on is presented and, secondly, the way in which nonlinear effects are treated is considered. Hence, the main existing models are divided into three groups (*Navier-Stokes and smoothed-particle hydrodynamics*, *potential flow models*, and *models from data*), discussed in Sects. 2.4.1, 2.4.2, and 2.4.3, respectively. Note that, although other fully-nonlinear models exist, such as the Lattice Boltzman Method (LBM) [79], CFD and SPH currently cover the vast majority of applications in the wave energy field [80].

2.4.1 CFD and SPH models

CFD (computational fluid dynamics) and SPH (smoothed-particle hydrodynamics) models are both fully nonlinear models, and the main difference between the two options is the

domain discretization method: mesh-based in CFD, and mesh free in SPH, which uses an array of particles to form the spatial domain.

The behaviour of the fluid is analysed by solving a set of differential equations, known as the Navier-Stokes equations. The fundamental basis of all fluid problems is governed by the transfer of mass, momentum, and heat, described by the following equations [81]: the continuity equation (2.2), the equation of motion (2.3), and conservation of energy (2.4):

$$\frac{\partial \rho}{\partial t} + \nabla \cdot (\rho \mathbf{u}) = 0 \quad (2.2)$$

$$\frac{\partial \mathbf{u}}{\partial t} + (\mathbf{u} \cdot \nabla) \mathbf{u} = -\frac{1}{\rho} \nabla p + \bar{\mathbf{F}} + \frac{\mu}{\rho} \nabla^2 \mathbf{u} \quad (2.3)$$

$$\rho \left(\frac{\partial \epsilon}{\partial t} + \mathbf{u} \cdot \nabla \epsilon \right) - \nabla \cdot (K_H \nabla T) + \rho \nabla \cdot \mathbf{u} = 0 \quad (2.4)$$

where ρ is the fluid density, \mathbf{u} the velocity vector, p the pressure field, $\bar{\mathbf{F}}$ the external force per unit mass, μ the fluid viscosity, ϵ the internal energy, K_H the heat conduction coefficient, and T the temperature.

However, equations (2.2), (2.3), and (2.4), cannot generally be solved analytically, so numerical discretization is necessary to obtain a solution. For this purpose computational codes are employed, simplifying and discretizing the Navier-Stokes equations. The nature of the phenomenon to be simulated, the computation capacity of the computing machine, and/or the fidelity requirements, drive the decision between the numerous approaches available.

In the case of wave energy, wave tank experiments or real-sea tests can be implemented in numerical wave tanks [82]. These simulations have been used for decades in offshore and ocean engineering for fluid-body interaction analysis.

2.4.1.1 Computational fluid dynamics

CFD numerically solves the Navier-Stokes equations by discretizing space and time domains. The main issue when modelling WECs using CFD, with respect to other CFD applications, is the presence of a free-surface. Specific free-surface modelling techniques have been developed, which can be classified into two main categories [83]: fitting methods (also known as tracking methods), and capturing methods. The tracking method models the free surface as a sharp boundary, while the interface-capturing method includes water and air in the mesh, adopting either the volume of fluid (VOF) method, or the level-set formulation. Free surface capturing methods are more common in hydrodynamic applications, mainly because, since no remeshing is required, they gain in robustness.

In wave energy, especially in full-scale real devices, the flow is considered turbulent, suggesting the use of the Reynolds decomposition of the fluid velocity, which consists of decomposing instantaneous quantities into time-averaged and fluctuating quantities. Therefore, the Navier-Stokes equations become Reynolds-Averaged Navier-Stokes (RANS) equations, giving approximate time-averaged solutions to the Navier-Stokes equations. RANS is the most widely used method, due to the higher computational requirements of other methods, like the large eddy simulation (LES), or the direct numerical simulation (DNS).

In order to produce a closed system of solvable equations, RANS equations require a turbulence model. The two most common models are the two-equation $k - \epsilon$ model, and the $k - \omega$ model, where k refers to the turbulent kinetic energy in both models, and the second term refers to the dissipation rate of the turbulence kinetic energy (ϵ), or the turbulence frequency (ω). The $k - \epsilon$ model is more robust and computationally

cheaper, but performs poorly under severe pressure gradients, while the $k - \omega$ model shows superior performance under adverse pressure gradients and separation, although separation is typically exaggerated and predicted too early. Shear stress transport (SST- $k - \omega$) turbulence models have also been suggested : the SST- $k - \omega$ model is a hybrid model using a transformation of the $k - \varepsilon$ model into a $k - \omega$ model in the near-wall region, and the standard $k - \varepsilon$ model in the fully turbulent region far from the wall [84]. A comparative study of different turbulence models can be found in [85].

NWT simulations implemented in CFD codes have some advantages and drawbacks, when compared to real wave tank tests, but both appear to be essential in the process towards an optimal WEC design. NWT simulations avoid both the complexity and costs of building a real prototype, and scale effects [86], as full scale devices can be numerically simulated. In addition, reflection effects from tank walls can be controlled effectively and a large variety of situations can be implemented with different incident waves or forces applied to the device. [87] presents the main advantages and drawbacks of using CFD methods in the design process of a WEC, with the main weakness being the high computational requirement.

2.4.1.2 Hydrodynamic modelling approaches for wave energy

In general, CFD codes are very general codes used for many and varied applications where fluid flows are considered. Nevertheless, other models specifically created for analysing wave-structure interactions are also available. This review describes two of these specific models: the *Spectral Wave Explicit Navier-Stokes Equation (SWENSE)*, developed by the Hydrodynamic and Ocean Engineering group of the Ecole Centrale de Nantes (ECN), and the *IH2VOF* model, developed at IH Cantabria.

The SWENSE approach based on RANS equations combines the advantages of potential and viscous solvers, by solving each physical problem with the appropriate tool: the propagation of the waves with the potential flow solver, and the diffraction-radiation problem with the viscous solver [88]. Hence, the simulation is divided into two different steps, where undisturbed incident waves are analysed by a nonlinear spectral scheme based on potential flow theory, while the computation of the nonlinear viscous flow uses the free surface RANS solver ICARE [89], which adopts the tracking method to model the free surface. The coupling of the potential and viscous solvers is implemented by incorporating incident flow parameters as forcing terms into the modified RANS equations.

The IH2VOF model was initially created for coastal structures, and includes realistic second order wave generation and active wave absorption. It solves the 2-D wave flow by the resolution of the volume-averaged Reynolds-averaged Navier-Stokes (VARANS) equations, based on the decomposition of the instantaneous velocity and pressure fields and the $k - \varepsilon$ equations.

2.4.1.3 Smoothed-Particles Hydrodynamics

The SPH method is a purely Lagrangian meshless interpolation method, that can approximate continuous field quantities, and their derivatives, by using discrete sample points, called smoothed particles. These discrete elements, or particles, are transported with the local velocity, carrying information of the field, such as mass, pressure, or density. In order to define continuous fields, using discrete samples, smoothing kernel functions (or weighting functions) are used, which specify the contribution of a typical field variables at any position. For example, with reference to the scheme in Fig. 2.6, the pressure at any position (r) depends on the pressure of all the particles within a radial distance h , also known as the smoothing length.

The contribution of all the particles, within this radial distance, to a property of the central particle is not the same. This contribution is weighted relative to the distance

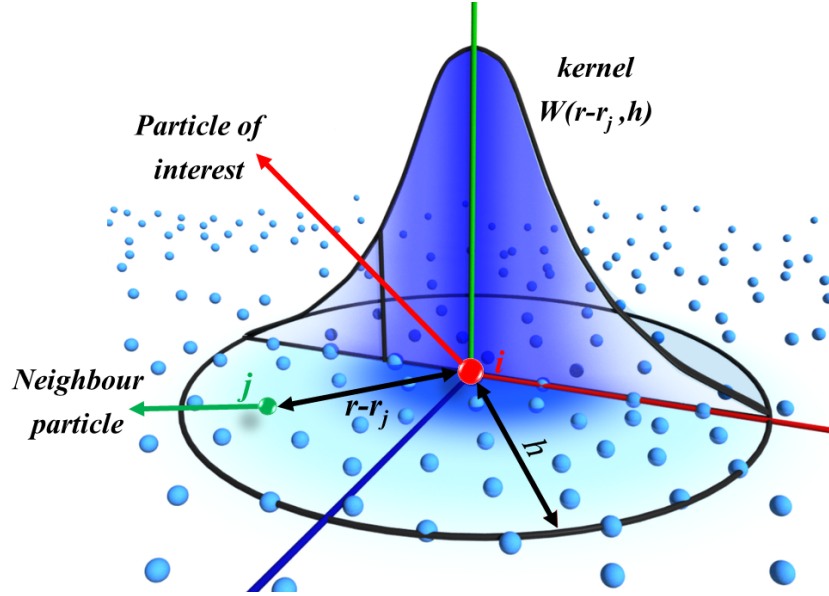


Figure 2.6: The principle of the SPH kernel function, modified from [90].

between the analysed particle and the contributor particle ($r - r_j$) and their density. This is mathematically governed by the kernel function, illustrated in Fig. 2.6. As a consequence, the field variable is known at a discrete set of points (N) within this radial distance and can be defined as follows:

$$A(r) = \sum_j^N \frac{m_j}{\rho_j} A(r_j) W(r - r_j, h) \quad (2.5)$$

where $A(r)$ could be any field variable at any position r , N is the number of particles, m the mass and ρ the density associated with the particle, and W is the kernel function.

One of the main advantages of SPH simulation, over CFD, is the perfect conservation of mass, which is an issue for CFD solvers when the free surface is modelled. In fact, in a SPH simulation with a free-surface, the fluid consists of a constant number of particles with a constant mass (particle mass is a user defined parameter), implying that mass conservation is guaranteed. Hence, the total force acting on each particle is specified, which can be divided into internal (pressure or viscosity), and external (gravity or buoyancy) forces. External forces can arise from the presence of a wave energy device, a rigid floating body in the vast majority of the cases, which can be included in the SPH model as a set of extra particles. The particles that form the WEC are similar to the particles that form the boundary walls. The individual forces on the different particles of the floating body are summed to represent a total force and moment at the centre of gravity of the body.

Furthermore, SPH outperforms CFD, in terms of fidelity, when particularly large body motions are present since, in CFD, it is challenging to adapt the spatial mesh discretization without losing accuracy. It follows that most of the studies using SPH in wave energy applications are focused on extreme events, where SPH can have significantly greater fidelity than CFD. Nevertheless, when SPH has been implemented to study WECs' behaviour under operational conditions, results show good agreement with experimental results, and CFD. However, SPH simulations are still about one order of magnitude slower than CFD solvers, therefore they are used only when CFD models are not able to produce reliable results, especially with floating bodies under extreme events.

2.4.2 Potential flow models

Potential flow models, also known as boundary element methods (BEMs), are based on the potential theory method, where the velocity flow is described as the gradient of the velocity potential. Under the assumptions of inviscid fluid, and irrotational and incompressible incident flow, the velocity potential can be split into three different parts: the undisturbed incident potential (ϕ_i), the diffracted potential (ϕ_D), and the radiated potential (ϕ_R). The incident, diffracted, and radiated potentials, added together, form the total potential of the incident flow (ϕ_{tot}).

Thus, the pressure (p) of the total incident flow, acting on the body, can be obtained by deriving the total potential in Bernoulli's equation, as follows:

$$p = -\rho gz - \rho \frac{\partial \phi_{tot}}{\partial t} - \rho \frac{|\nabla \phi_{tot}|^2}{2} \quad (2.6)$$

where z is the position of the body, and $p_{st} = -\rho gz$ the hydrostatic pressure.

Following the division of the incident flow potential into three parts, the Bernoulli equation (2.6) can also be given as follows,

$$p = -\rho gz - \rho \frac{\partial \phi_i}{\partial t} - \rho \frac{|\nabla \phi_i|^2}{2} - \rho \frac{\partial \phi_D}{\partial t} - \rho \frac{|\nabla \phi_D|^2}{2} - \rho \frac{\partial \phi_R}{\partial t} - \rho \frac{|\nabla \phi_R|^2}{2} + \quad (2.7)$$

$$- \rho \nabla \phi_i \nabla \phi_R - \rho \nabla \phi_i \nabla \phi_D - \rho \nabla \phi_D \nabla \phi_R$$

Equation (2.7) represents the pressure acting on the floating body, where nonlinearities are present in the form of quadratic and second-order radiation-diffraction terms. Analysing wave-structure interactions, the governing equation, based on Newton's equation, for the example of translation motion, is given as:

$$m\ddot{\mathbf{x}} = \mathbf{F}_g - \int_{S(t)} p \mathbf{n} dS \quad (2.8)$$

where \mathbf{F}_g is the gravity force, \mathbf{n} the unity vector, normal to the time-varying wetted surface $S(t)$.

2.4.2.1 Linear potential flow model

Linear potential flow models are based on the assumption of small motion and small wave steepness. Therefore, the wetted surface is considered constant (the mean value is used) for the linear model, while the instantaneous wetted surface is calculated at each time-step for the partially nonlinear model. As the pressure acting on the body is divided as shown in (2.7), Newton's equation (2.8) develops into (2.9), for the linear case, and into (2.10) for the partially nonlinear case.

Apart from computing the pressure over the mean wetted surface, the quadratic terms of (2.7) are neglected in the linear case, and so the governing linear equation develops into

$$m\ddot{\mathbf{x}} = -\mathbf{G}\mathbf{x} - \int_{-\infty}^{\infty} \mathbf{K}_{ex}(t-\tau)\eta(0,0,\tau)d\tau - A_{\infty}\ddot{\mathbf{x}} - \int_{-\infty}^{\infty} \mathbf{K}_R(t-\tau)\dot{\mathbf{x}}(\tau)d\tau \quad (2.9)$$

where $\eta(0,0,\tau)$ is the free surface elevation $\eta(x,y,t)$ computed in the origin, \mathbf{K}_{ex} is the excitation force kernel, which comprises diffraction and dynamic FK forces, and \mathbf{G} is the hydrostatic stiffness matrix, that describes the balance between the gravity force and the hydrostatic pressure force. The radiation force is expressed as a convolution product, based on Cummins' equation, where A_{∞} is the added mass at infinite frequency, and \mathbf{K}_R the radiation impulse-response function.

2.4.2.2 Nonlinear potential flow models

Partially nonlinear model A partially nonlinear model is essentially a modest extension of the linear model, which uses the linear model as a framework, and describes one or more terms in a nonlinear fashion. Two main extensions are found in the literature, where the first extension considers nonlinear Froude-Krylov forces, and the second one allows a more precise computation of radiation-diffraction forces [91, 92].

The first improvement of the linear model includes nonlinear FK forces, calculated by integrating the undisturbed incident pressure, shown in (2.7), neglecting quadratic and second order terms, over the instantaneous wetted surface. In this first extension, static and dynamic FK forces are summed into the instantaneous FK force, while other forces, such as radiation or diffraction forces, remain linear and are computed separately. The resulting dynamic equation, for translation motion, is represented as:

$$m\ddot{\mathbf{x}} = \mathbf{F}_g - \int_{S(t)} (p_{st} + p_{dy}) \mathbf{n} dS - \int_{-\infty}^{\infty} \mathbf{K}_D(t-\tau) \eta(0, 0, \tau) d\tau - A_\infty \ddot{\mathbf{x}} - \int_{-\infty}^{\infty} \mathbf{K}_R(t-\tau) \dot{\mathbf{x}}(\tau) d\tau \quad (2.10)$$

where K_D is the diffraction force kernel, and p_{dy} is the dynamic pressure, computed by applying the Bernoulli equation to φ_i .

Computing nonlinear FK forces, for a geometry of arbitrary complexity, requires discretization of the geometry, by means of a mesh over the body surface. The efficacy of the nonlinear computation of Froude-Krylov forces is, however, extremely sensitive to an accurate estimation of the instantaneous wetted surface, as mesh panels on the free-surface interface can be partly submerged, and partly out of the water, leading to a misestimation of the instantaneous wetted surface. Two main strategies to accurately estimate the wetted surface, at each time-step, are presented in the literature. While [62] uses a very fine mesh, taking into account only those cells below the instantaneous free-surface at each time-step, [91] uses a remeshing routine, modifying those cells of the mesh which are partly submerged and partly out of the water.

Both approaches are computationally expensive, making the nonlinear FK force model much slower than the linear one, and limiting the scope of applicability of such a method. It is worth stressing out that the bottleneck for computational time is the meshing/remeshing routine, needed, at each time step, in order to consider only the instantaneous wetted surface. One of the objectives of this thesis is to overcome such a problem, defining, for a certain class of body geometries, computationally efficient, mesh-less analytical approaches. Indeed, while, for a geometry of arbitrary complexity, a mesh-based approach is the only option, for axisymmetric or prismatic devices, a convenient parametrization is definable, as further explained in **Chapters 4 and 9** of this thesis.

A further extension of linear models purports to improve the computation of radiation and diffraction forces. While, in the linear approach, time derivative and second order terms are neglected, in this approach a Taylor expansion of such quantities around the mean position of the body is considered [91].

The first extension (nonlinear FK model) considerably improves the results by considering nonlinear FK forces, while the second extension (second order radiation and diffraction) makes little difference, at least for devices considerably smaller than the wavelength, as discussed in Sect. 2.3.2.8. However, the second extension requires a recalculation of the hydrodynamic parameters at each sampling instant, resulting in a high computational overhead.

Weakly nonlinear model While the partially nonlinear models' objective is to improve the linear one, the approach pursued by the so called weakly nonlinear models is to simplify the fully nonlinear formulation. A perturbation expansion of the equations describing the

interactions between waves and structure is performed with respect to the wave steepness ka , where k is the wave number and a is the wave amplitude, and the boundary conditions are approximated by their Taylor expansion. The perturbation method solves for the lowest degree of steepness, and uses the results as an input for the higher degree terms. Typically a second order approximation is used, where the (linear) solution in ka is used to solve for $(ka)^2$. Different codes which use a second order approximation are able to more effectively describe the diffraction and the excitation problem [93].

An alternative approach to simplify the fully-nonlinear problem is the weak-scatterer approximation [94], which assumes the perturbation potential (composed of the radiation and diffraction potentials) small compared to the incident potential. Such an approximation is valid for bodies whose characteristic dimension is much smaller than the wave length. The boundary value problem is then solved iteratively on the exact free surface elevation and the instantaneous wetted surface.

Fully nonlinear model When sea conditions exceed the power production mode, any simplification of the complete model becomes unacceptable, and the only way to describe the response of the device in extreme conditions is to consider all nonlinearities. Notwithstanding that, in the potential flow framework, viscosity is not included, as well as effects like green water, slamming or sloshing, due to the resolution of the fully-nonlinear problem and the exact instantaneous boundary conditions, with no simplifying assumption, very accurate results are achievable, even with large waves [95].

Weakly nonlinear and fully nonlinear potential flow models are both at an early stage of development, so further research is necessary to extract more definitive conclusions. [96] presents a comparison of weakly and fully nonlinear models, analysing a fully submerged cylinder, concluding that both methods give good agreement in the hydrodynamic coefficients. Although the low complexity of the problem is recognised (a fully submerged cylinder), it remarks that expectations have been met with both methods.

2.4.2.3 Viscous effects in potential flow models

Viscous effects are completely neglected by linear potential flow models, as the fluid is considered inviscid. However, their relevance has been discussed in Sect. 2.3.2.8, suggesting viscous effects should be externally included. Viscous losses depend, linearly and/or quadratically, on the velocity of the device with respect to the fluid. In wave energy applications, a quadratic relation is commonly assumed, and viscosity is modelled as an additional Morison-like term [60], shown in (2.11), based on the Morison equation [97],

$$\mathbf{F}_{vis} = -\frac{1}{2}\rho A_d C_d (\dot{\mathbf{x}} - V_0) |\dot{\mathbf{x}} - V_0| \quad (2.11)$$

where A_d is the characteristic area of the device, perpendicular to the flow, C_d is the drag coefficient, and V_0 is the undisturbed flow velocity.

The Morison equation was introduced in the 50s, for describing forces on cables of oil platforms and, afterwards, has been applied in the wave energy field, to describe viscous effects. Though several decades have passed, there is still some inconsistency in the literature about drag coefficient values for wave energy applications. In addition, there is no consensus with regard to which drag coefficient estimation technique should be used. Consequently, a common issue with the implementation of a Morison-like term is the choice of the drag coefficient. **Chapter 7** of this thesis presents further discussions on causes and consequences of the uncertainty in the selection of C_d , mainly related to the particularly challenging application the wave energy converter usually is. Some considerations for identification experiments and coefficient choice are presented, such as the advice to overestimate C_d , rather than underestimating it, and the notion of an “equivalent drag coefficient” is proposed.

2.4.3 Models from data

The complexity of certain physical systems is so high that it is difficult to create a model which explicitly takes the physics of the system into account. In such cases, a possibly more viable approach is to base the model on input/output data of the system, rather than trying to include all the governing equations in the model. System identification is used to determine the model, utilizing statistical methods to create a mathematical description of the dynamic systems, from measured data.

Every identification method consists of

- Conducting a series of representative tests on the system,
- selecting a series of representative data of the system to be reproduced, for training and validation,
- determining the structure of the model (model type and order, nonlinear terms, etc.),
- defining the fitting criteria,
- using numerical optimisation to identify the system parameters, and
- validating the identified model.

Thus, there are three key elements in system identification: the representative data, the model structure and the identification algorithms.

Using representative data of the system dynamics, that entirely covers the whole range of frequencies/amplitudes the system is likely to deal with, is crucial. In the particular case of hydrodynamic applications, such data can be obtained from wave tank experiments [98]. However, extracting representative data from wave tank experiments may be problematic, because it is not always easy to isolate the required data, due to the limitations on the range of excitation signals, or the tank wall reflections. Data can also be extracted from numerical wave tank simulations, implemented in BEM or CFD codes [99].

Numerical wave tank simulations have certain advantages compared to experimental tests, because intermediate variables, such as excitation force, can be measured. In addition to this access, measurements are accurate in NWT simulations, since there is no measurement noise, as in experimental tests. Furthermore, reflection effects can be effectively limited and controlled, through appropriate controls on the numerical set up (mesh and wave absorption techniques). In fact, the effectiveness of wave absorption should be assessed for each numerical wave tank.. Moreover, NWT simulations are fully non-linear simulations, so the results generally show good agreement with the experimental tests. The main disadvantages of NWT simulations are the computational requirement, as mentioned in Sect. 2.4.1, and the uncertainty of the results accuracy, without proper validation.

In order to generate adequate data for the identification of model parameters, various experiments can be carried out to provide data of different characteristics. The simplest possible experiment is the free decay test (no external input), where the fundamental dynamic parameters of the system, such as natural frequency, can be identified. A test with input waves (free surface elevation as input) is another possibility, where the output can be body motion, position and/or velocity, or excitation force. An external force (e.g. PTO force), can also be used as input, with the device motion as the measured output [99]. In the case of an input wave test, the input signal is limited by different factors, e.g. wave steepness, while, in input force tests, one has total freedom over the choice of the excitation signal shape. Finally, prescribed motion tests can also be used, where the

device is forced to follow a predetermined path, while measuring the fluid force on the device.

Once the data is generated, the structure of the model must be determined, which is the key point in order to create a representative model. The majority of system identification techniques are based on discrete-time models [100], which can be of very diverse form. The choice of the mode structure essentially depends on the features of the system. If the system to be reproduced is considered linear, an autoregressive with exogenous input (ARX) model may be suitable, where only n_a and n_b need to be specified in (2.12).

$$y(k) = \sum_{i=1}^{n_a} a_i y(k-i) + \sum_{i=0}^{n_b} b_i u(k-n_d-i) \quad (2.12)$$

where $y(k)$ and $u(k)$ are the output and input, respectively, at the discrete time k .

However, the ARX model cannot capture nonlinear behaviour, and is therefore excluded. In order to capture nonlinear effects, nonlinear autoregressive with exogenous input (NARX) models are suggested [101], where the current output depends on the past (and future if the system is non-causal, $n_d < 0$) output values and the input values. Figure 2.7 illustrates a general block diagram for NARX models, where n_a and n_b represent the order of the model, and n_d the input delay.

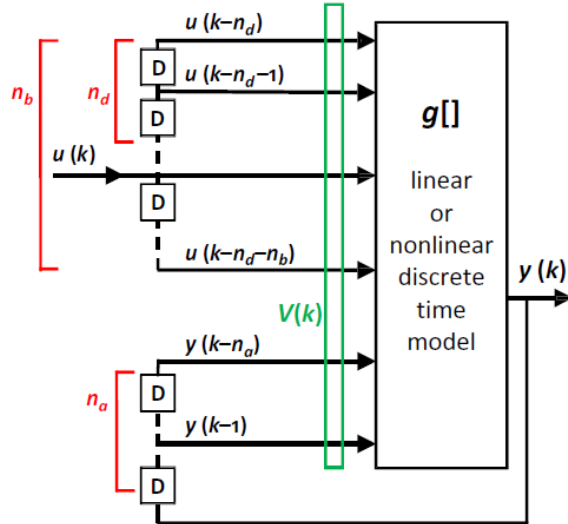


Figure 2.7: Block diagram of a general NARX discrete-time model.

There are several possibilities of model structures, $g[]$ in Fig. 2.7, from a structure based on the knowledge of the physical principals of the system (grey-box), to a structure completely ignorant of these principals (black-box) [100]. Apart from the model structure, the way to analyse nonlinearities (the form), and its complexity, need also to be selected.

Some model structures for nonlinear modelling of wave energy converters, and their capabilities, are presented in the following subsections.

2.4.3.1 Hammerstein/Wiener model

Nonlinear input/output relationship can be modelled by using a simple nonlinear static block ($r()$), which be used in combination with a linear ARX model, obtaining a nonlinear model structure. Depending on the number of static blocks, and their configuration, different model structures can be formed.

In the Hammerstein model, a nonlinear static block is connected in cascade with a linear ARX block, as illustrated in Fig. 2.8 (a). As a consequence, the relationship

between the input and output is given by the product of $s(k)$ and the steady-state gain of the ARX model [102]:

$$y(k) = \sum_{i=1}^{n_a} a_i y(k-i) + \sum_{i=0}^{n_b} b_i r(u(k-n_d-i)) \quad (2.13)$$

A Wiener model is regarded as the dual of Hammerstein model [103], with the order of the two block inverted, and both are considered grey-box models, since they combine a partial theoretical structure with data to complete the model.

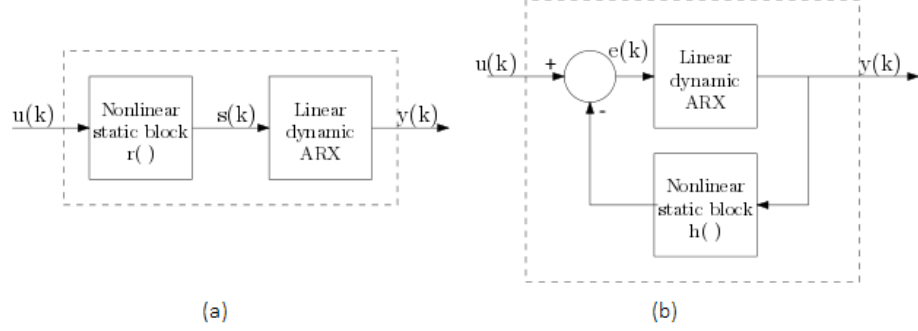


Figure 2.8: Hammerstein (a), and feedback block-oriented (b) model structure diagrams, modified from [9]

2.4.3.2 Feedback block-oriented model

In the case of the feedback block-oriented model, illustrated on the right side of Fig. 2.8, the structure is characterized by a negative feedback [102], where the static nonlinear block ($h()$) is placed in the feedback path, between the output and the input. Feedback block-oriented models are also a grey-box models, and the nonlinear input/output relationship is given as follows,

$$y(k) = \sum_{i=1}^{n_a} a_i y(k-i) + \sum_{i=0}^{n_b} b_i e(k-n_d-i) \quad (2.14)$$

where

$$e(k) = u(k) - h(y(k)) \quad (2.15)$$

The Hammerstein/Wiener and feedback block-oriented models are nonlinear in their input/output relationship, but linear in the parameters. [104] uses a Hammerstein and a feedback block-oriented model for a heaving device, using an external force as input. The heaving device is a vertical cone, which in theory implies, at least, a nonlinear restoring force. In addition, NWT simulations provide data where the body motion is large enough to exhibit nonlinear effects.

Apart from the parameters of the ARX model component in Fig. 2.8, the static block must be identified. In [104], the static block for the Hammerstein and feedback block-oriented models is identified using a predefined motion experiment in a NWT, slowly moving the device from fully submerged to a fully dry position, and measuring the fluid force. Moving the device sufficiently slowly, the measured fluid force is assumed to be a hydrostatic force. Hence, a physical interpretation for the static block is possible in both models. For the Hammerstein model, $r()$ can be interpreted as the inverse of the restoring force, while in the feedback block-oriented model, $h()$ is the negative of the restoring force.

Besides the Hammerstein and feedback block-oriented models, an ARX model is studied on the data containing significant nonlinear behaviour in [104]. While the ARX model

is unable to capture the nonlinear behaviour, which is to be expected, both the Hammerstein and the feedback block-oriented models show excellent agreement in reproducing the asymmetrical steady-state response. In this specific example, the feedback block-oriented model performed particularly well.

2.4.3.3 Kolmogorov-Gabor Polynomial Model

The Kolmogorov-Gabor Polynomial (KGP) model is a black-box model that uses polynomial nonlinearities to describe the input/output relationship of the data [101]. Despite the nonlinear input/output relationship, the KGP model is linear in the parameters, as shown in (2.16), which allows fast identification.

$$\begin{aligned}
y(k) = & \sum_{i=1}^{n_a} a_{i1}y(k-i) + \sum_{i=1}^{n_b} b_{i1}u(k-n_d-1) + \dots \\
& + \sum_{i=1}^{n_a} a_{ip}y^p(k-i) + \sum_{i=1}^{n_b} b_{ip}u^p(k-n_d-1) + \sum_{i=1}^{n_a} \sum_{j=0}^{n_b} c_{ij}y(k-i)u(k-n_d-j) + \dots \quad (2.16)
\end{aligned}$$

where p is the highest polynomial order and a_{ij} , b_{ij} , and c_{ij} are the model parameters. Because the KGP model is a black-box model, the parameters have no physical meaning.

[105] studies a heaving floating body with a KGP model, using data from NWT tests. The cross product terms, involving u and y in (2.16), are removed to avoid instability, and a polynomial order (p) of 2 is selected. The agreement with the NWT data is good, both in training and validation. Structures with higher polynomial orders are found to improve the results on the training data, but reduce the performance on the validation data, suggesting overfitting. A linear ARX model is also studied on the same data in [105], showing very similar performance to the KGP model, which indicates that the data employed probably does not include much nonlinear behaviour. Significantly, the excitation in this case comes only from a wave input (no PTO/external input).

2.4.3.4 Artificial neural networks

Artificial Neural Networks (ANNs) are systems of interconnected simple artificial nodes, that consist of sets of adaptive weights plus a nonlinear activation function and are capable of approximating nonlinear functions of their inputs. The adaptive weights specify the connection strengths between neurons.

There exist several types of ANNs structures, used in different applications. The model suggested in [99] is a multilayer perceptron (MLP) ANN, which is a black-box model with a nonlinear input/output relationship, nonlinear in the parameters. This latter characteristic makes it different from any other model structure suggested in this section, and makes the identification process difficult, since local minima can be found in the parameter optimization problem.

Hence, through the modelling procedure, different conditions, such as the number of layers, the number and type of neurons in each layer, or the delayed input and output values, must be determined to define the required structure of the ANNs. The complexity of a MLP model is determined by the the order of the model and by the number of neurons in each hidden layer. Assuming two hidden layers, the input/output relationship is given as follows:

$$y(k) = \sum_{i=0}^{n_2} \omega_i^{(out)} \Psi_i \left(\sum_{j=0}^{n_1} \omega_{ij}^{(2)} \Psi_j \left(\sum_{l=0}^{n_v} \omega_{jl}^{(1)} v_l(k) \right) \right) \quad (2.17)$$

where $\omega_i^{(out)}$, $\omega_i^{(1)}$, and $\omega_i^{(2)}$ are the unknown parameters of the output, the first, and second layers, respectively, and Ψ_i is the activation function. The role of this activation function in an ANN is to produce a nonlinear decision boundary via nonlinear combinations of the weighted inputs. In [99] a tansigmoidal activation function is chosen to provide global support and a smooth interpolation.

[99] uses a NWT model to generate data, where three identification tests are performed: one with purely wave excitation (irregular sea-state), and two types of direct force inputs (chirp and random amplitude random period (RARP)). When identifying the parameters for a model relating free surface elevation to device motion (wave excitation input), because the relationship between the two is noncausal, an additional step to measure the noncausal advance must be taken.

Results of the ANN model for the wave excitation input show very good agreement on the training data, but loses performance in the validation test, similarly to the overfitted KGP model in [105]. The degradation in validation performance is seen by the authors as a consequence of the nonlinear optimization with many local minima, which demonstrates the complexity associated with the nonlinear identification of ANN models.

The performance of the models presented in this section, regardless of the model structure, is limited to the data the models are identified from, so that the scope of validity of the models relies heavily on the data they are trained on.

A comparative study of all the nonlinear approaches analysed in Sect. 2.4 is shown in Table 2.3, where the fluid and hydrodynamic models, the expected accuracy, and computational cost, and the main advantages or drawbacks of each method are evaluated. It should be noted that all the characteristics are not applicable to all the methods, e.g. the ANN model does not use any fluid or hydrodynamic model, which is denoted with the *N/A* (not applicable) abbreviation. In addition, the capabilities of models from data are still untapped, due to the lack of a complete validation. Therefore, the accuracy column in Table 2.3 reads *N/I*, which means not enough information is available.

2.5 Discussion

The different modelling approaches evaluated in Sect. 2.4 show the ability to deal with different nonlinear effects, and their relevance is demonstrated to vary with the WEC type in Sect. 2.3.2.8. Thus, a model that efficiently deals with a relevant nonlinear effect can be chosen for each WEC type. However, the selection of an efficient modelling approach includes an additional essential variable: model purpose. All the possible purposes of a mathematical model in wave energy, e.g. power production assessment, model-based control, optimization, simulation of device motions, or structural analysis, can be divided into two groups, with a distinguishing dominant requirement: computational cost vs. fidelity (accuracy). Fig. 2.9 illustrates the compromise between computation and fidelity of the modelling approaches described in Sect. 2.4.

Models for power production assessment, model-based control or optimization, require a low computation time (with a reasonable fidelity), since a large number of cases need to be studied. In the case of model-based control, apart from the computation, the structure of the model is also important, with the additional requirement to turn the model into a control calculation. The red dashed line in Fig. 2.9 represents the limit of the maximum affordable computation for models with low computation requirements.

In contrast, models for device behaviour simulation or structural analysis require high fidelity, because they are crucial in the final device design process, which is one of the key cost drivers for WECs. CFD models are most commonly used in this context, in spite of their high computation requirements. A solution to reduce computation costs, without losing fidelity, can be the combined potential flow-CFD approaches.

Table 2.3: A comparative study of the different numerical modelling approaches for wave energy converters evaluated in Sect. 2.4.

Modelling Approach	Fluid model	Hydrodynamic model	Accuracy	Computation	Main Advantages	Main Drawbacks
Navier-Stokes SPH	CFD	Viscous fluid	RANS	++++	Flow field considered entirely	Computationally expensive
	SWENSE IHVOF		RANS	++++	Lower computation for CFD-similar fidelity	Dynamic mesh complexity
	SPH	N/A*	SPH	++++++	Meshless approach	Computationally prohibitive
Potential flow	Partially nonlinear		Linear BEM Instantaneous FK	++/+++	Computationally beneficial	Viscous effects neglected
	Weakly nonlinear	Perfect fluid	Nonlinear BEM	+++	Nonlinear boundary conditions	Computationally expensive
	Fully nonlinear		Nonlinear BEM	+++	All potential-flow nonlinearities included	Viscous effects neglected
	Viscous drag	Empirical viscosity	Linear/Nonlinear BEM	Improves inviscid BEMs	Same as BEM	Drag coefficient uncertainty
Models form data	Hammerstein				Linear in parameters	Model rigidity
	Feedback block-oriented	N/A*	N/A*	N/I** (data dependent)	Physical meaning available (Grey-box)	
	KGP				Linear in parameters	No physical meaning (Black-box)
	ANN				Model flexibility	Nonlinear in parameters No physical meaning (Black-box)

*N/A means not applicable.

**N/I means not enough information for evaluation.

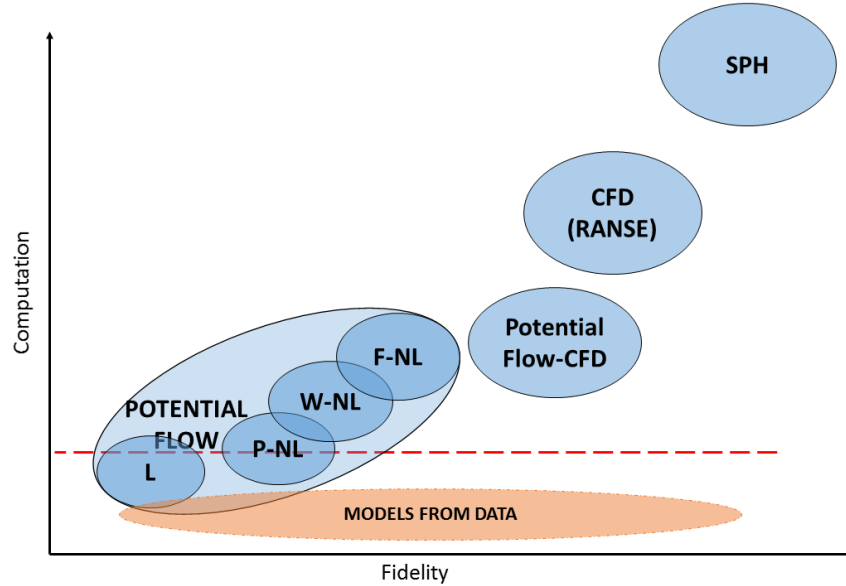


Figure 2.9: The computation/fidelity compromise of the different modelling approaches evaluated in Sect. 2.4. **L** means linear, **P-NL** means partially-nonlinear, **W-NL** means weakly-nonlinear, and **F-NL** means fully-nonlinear. The red dashed horizontal line represents the affordable computation limit for models with low computation requirements.

In the case of OWCs, viscosity effects appear to be significantly more important than potential flow nonlinearities. The predominant viscosity effects, the separation and vortex generation at the front wall, combined with the two-phase problem, makes the CFD approach ideal for high fidelity studies of OWCs. Fixed OWCs are relatively easy to model in CFD, since a 2D model can be sufficiently accurate, and especially because no dynamic mesh is required. 3D models may provide an additional marginal accuracy, with respect to 2D models, but the computation cost substantially increases from 2D to 3D simulations. Floating OWCs include a further difficulty: the dynamic mesh. The motion of the device makes the use of a dynamic mesh indispensable, which complicates the simulation, and further increases the computational time.

In HPAs, except those with damping plate, the relevance of viscous effects is demonstrated to be generally low, as shown in Table 2.2, so potential flow nonlinearities become dominant. Therefore, nonlinear potential flow approaches are a suitable solution. Due to the fact that nonlinear radiation and diffraction appear to be negligible [32], and the main nonlinear effects arise from nonlinear Froude-Krylov forces [46], partially nonlinear approaches suit ideally, which are also convenient in terms of computational requirements. CFD approaches provide marginally higher fidelity [106] compared to potential flow models, but the excessive additional computation cost is hardly justified by the differences in the results.

OPCs are in between OWCs and HPAs, where both potential flow nonlinearities and viscous effects are equally important. In fact, [62] demonstrates that a partially nonlinear potential flow model is able to predict parametric excitation, but not the correct motion amplitude. Therefore, [62] suggests a code that combines a nonlinear potential flow method to account for the incident wave, and a CFD (RANS) model for the scattering and viscous effects. Hence, the computational time is reduced, while the fidelity of the results is substantially improved. Note that HPAs with damping plates may be considered as OPCs, due to the higher relevance of viscous effects, compared to HPAs without a damping plate [107].

Finally, OWSCs appear to be dominated by viscous losses and radiation/diffraction forces. [31] suggests viscous losses may be dominant for bottom-hinged OWSCs, with a

power loss of over 30% due to viscous effects. However, [108] concludes that the Oyster OWSC is diffraction dominated. The highly nonlinear, though typical, slamming events in OWSCs [109], added to the above mentioned relevance of viscous losses and radiation/diffraction forces, suggest that CFD approaches, that consider the whole nonlinearity of the flow field, may be ideal. CFD codes have often been used to model OWSCs using 2D [109], and 3D simulations [110], provided with dynamic mesh capabilities, giving good agreement with experimental tests.

Table 2.4: Suggested modelling approaches for models with high fidelity requirements.

High fidelity <i>(Simulation of device behaviour/Structural analysis)</i>	
OWC	CFD ^{***}
HPA	Partially nonlinear potential theory with viscous drag ^{**}
OPC*	Partially nonlinear potential theory combined with CFD
OWSC	CFD ^{***}

*OPCs in this table include self-reacting HPAs with damping plates.

**While CFD provides marginally better fidelity than partially nonlinear potential theory, the excessive additional computation cost demanded is hardly justified by the differences in the results.

*** The additional computation of SPH models can be justified under specific (extreme) conditions in OWCs or OWSCs, but not in models for WECs operating in the power production mode.

Apart from HPAs, with the exception of HPAs with a damping plate, the relevance of the nonlinear effects presented in Sect. 2.3.2.8 suggests the need for CFD models, either CFD alone or combined with potential flow methods, as shown in Table 2.4. Despite the constant improvement in the computational power of computers, and the refinement of CFD approaches, CFD is still a computationally expensive solution, and is far from the affordable limit, the red horizontal dashed line, in Fig. 2.9. Therefore, alternative less accurate, but faster, solutions are necessary for models with low computation requirements.

As shown in Fig. 2.9, the only approaches within the affordable computation region, delimited by the red dashed line, are the linear and partially nonlinear potential flow models, and the models from data. The latter approaches (data-based models) can be highly interesting with really low computation requirements and potentially able to provide high fidelity results. However, models from data are still in an early stage of development regarding wave energy and, as a consequence, the real capabilities of data-based models are still unknown. That is the reason why the *models from data* box is shown in a different colour in Fig. 2.9.

Hence, despite the different requirements presented in Sect. 2.3.2.8 for each WEC type, the modelling possibilities are reduced to two options: linear and partially nonlinear potential flow models. In the benchmarking study carried out in [111], different devices are evaluated using linear potential flow with viscous drag, which is the most commonly used approach in the literature. However, including nonlinear Froude-Krylov forces by means of the partially nonlinear potential flow approach is recommendable for all the WECs, except for OWSCs, for which the relevance of nonlinear FK forces is determined to be negligible. Viscous drag can be included in all the cases, since no extra computation cost is required. Suggested modelling approaches for models with low computation requirements are shown in Table 2.5, for each WEC type.

Table 2.5: Suggested modelling approaches for models with low computation requirements.

Low computation <i>(Power assessment/Model-based control/Optimization)</i>	
OWC	Partially nonlinear potential theory with viscous drag
HPA	Partially nonlinear potential theory with viscous drag
OPC*	Partially nonlinear potential theory with viscous drag
OWSC	Linear potential theory with viscous drag

*OPCs in this table include self-reacting HPAs with damping plates.

2.6 Conclusion

Due to a wide variety of devices and the lack of a predominant concept to focus on (compared, for example, to the 3-bladed horizontal-axis turbine typical in the wind industry), mathematical modelling of wave energy converters becomes highly device-dependent, where each concept has particular modelling requirements.

Linear models cover the vast majority of the WEC models documented in the literature, mainly due to the appealing computational requirements. However, the relevance of nonlinear effects has been demonstrated in the literature for a wide variety of WECs, especially under controlled conditions. Although nonlinear effects may be highly device-dependent, a classification based on the relevance of nonlinear effects is given in the present chapter, suggesting a specific modelling approach for each WEC type. However, most of the nonlinear approaches require high computational resources, which may be incompatible with the purpose of the model.

Considering the different model purposes in wave energy, two dominant requirements have been identified: computational time, and fidelity. The dominant requirement for models for power production assessment, optimization, or model-based control, is low computation (with a reasonable accuracy), while models for simulation of the device behaviour, or structural analysis, over short timescales, require high fidelity, and can afford higher computations. Hence, modelling approaches have been suggested for different purposes and WEC types.

In the case of models with high fidelity requirements, CFD models are the most suitable option, either CFD alone or coupled to a potential flow model, for all the WEC types except for heaving points absorbers, for which nonlinear potential theory appears to be sufficiently accurate. SPH methods have some benefits compared to CFD, but can be computationally prohibitive.

In contrast, models with low computational requirements are necessarily based on potential flow methods, either linear or partially-nonlinear, due to the excessive computational costs of fully nonlinear approaches. Models from data, such as KGP or ANN models, appear to be promising alternatives, but they are still in an early stage of development.

2.6.1 Thesis contributions

Having discussed, in some detail, the state-of-the-art of nonlinear mathematical modelling for wave energy devices, it is possible to highlight several areas where further investigation is needed, which are undertaken by the author in the course of the PhD research, and compose the heart of the present thesis:

1. The relevance of nonlinearities is highly dependent on the operational region, therefore on the control strategy. Indeed, the main purpose of the controller is to enlarge the amplitude of motion, in order to maximise the power capture. In this thesis it is

repetitively shown that, while linear models are sufficiently accurate under uncontrolled conditions, they perform poorly when control is implemented. Therefore, in order to have a correct understanding of the mathematical model’s performance, it is mandatory to consider the response of the device under *controlled conditions*.

2. Following comment (1), the lack of an active control strategy in common CFD simulation was noted. Therefore, as discussed in **Chapter 3**, a latching control strategy routine has been implemented in the open source CFD software OpenFOAM. Differences between accuracy in controlled and uncontrolled conditions are then analyzed, discussing their implication on the optimization of the control parameters itself.
3. However, the main focus of this thesis is to create computationally efficient, but sufficiently accurate, nonlinear models. Therefore, the class of partially-nonlinear potential flow models has been taken into consideration. In the sub-class of nonlinear Froude-Krylov force models, the novelty proposed in this thesis consists of a convenient parametrization of the wetted surface, applicable to axisymmetric WECs, which can achieve the same accuracy as existing mesh-based approaches, but at a fraction of the computational time. Such a method is described in **Chapters 4 and 9**, for the single-, and multi-degree of freedom cases, respectively.
4. Since nonlinearities are very device specific, the relative importance of the components of the total hydrodynamic force, experienced by HPAs and OWSCs, is considered in **Chapter 5**. Linear radiation and diffraction, nonlinear FK, and viscous drag forces are taken into account, showing that HPAs are FK-dominated, while OWSCs dynamics is mainly governed by diffraction and radiation efforts, with non-negligible viscous effects.
5. Considering a HPA, with and without latching control applied, several different nonlinear FK models, with and without viscous drag effects, are studied in **Chapter 6**. The performance of each model is evaluated in terms of computational time and accuracy, using CFD simulation as a validation and accuracy benchmark.
6. The challenges, specifically associated to the wave energy field, of determining an appropriate viscous drag coefficient are addressed in **Chapter 7**. Pros and cons of different identification tests are discussed, along with suggestions on how to appropriately define the testing conditions, and finally select a drag coefficient, introducing as well the notion of an “equivalent drag coefficient”.
7. The relevance of nonlinear representation of the incoming wave pressure field, in relation to FK force calculations, is examined in **Chapter 8**, considering Airy’s theory, Wheeler stretching, Rienecker-Fenton waves (for regular waves), and HOS (for irregular waves). A particular focus is put on the compromise between accuracy and complexity of the resulting pressure field representation and, most importantly, the computed nonlinear FK forces, for HPAs and OWSCs.
8. Multi-degree of freedom nonlinear FK models are presented in **Chapter 9**, and applied to WECs inspired by real wave energy devices (the Corpower, the Wavebob, and the Sparbuoy). In particular, it is highlighted how such nonlinear models are able to appreciate parametric roll motion, in a computationally efficient way.

Implementation of latching control in a CFD environment

3.1 Motivation

Hydrodynamic nonlinearities in wave energy converters are enhanced by large amplitudes of motion, relative to the free surface elevation. Within the operational region, apart from natural resonance conditions, WECs without an active control strategy usually behave as wave followers, with small relative motion excursions, hence mostly linear behaviour. However, implementation of active controllers is important, if not imperative, in real WECs attempting to be economically viable, since the controller increases the power absorption across the whole range of wave conditions. Therefore, nonlinear models, formulated in this thesis, are tested under controlled conditions, and their fidelity is measured by means of comparison against accuracy benchmarks. Codes based on the solution of the fully-nonlinear Navier-Stokes equations, such as CFD software, are believed to be extremely accurate, as discussed in Chapter 2. Therefore, they can be effectively used as “gold-standard” benchmarks, in order to evaluate the performance of other mathematical models. However, up to the date of the work proposed in this chapter, no active control strategy has ever been directly coded into any CFD software. Therefore, the purpose of this chapter is to implement an active controller, in particular a latching control strategy, in the open source CFD software OpenFOAM. Thanks to the open source framework, it was possible, firstly to access and modify the source code of the program, and then to make the latching control strategy available to the public. In this chapter, a case study is also considered, in order to discuss nonlinear effects.

3.2 Introduction

For several countries around the world, the exploitation of ocean wave power may constitute a significant contribution to the diversification of the energy production scenario, increasing the portion of sustainable and renewable resources [112, 113, 114]. However, in most cases, wave energy converters are not yet efficient enough to be economically competitive in the renewable energy market. An important role in the achievement of the economic viability is played by the control strategy, able to double the energy harvested [115].

On the other hand, the ability of the controller to magnify power absorption is extremely sensitive to the ratio of wavelength to device size [116]. A small device tends to have a larger absorbed-power increase than a big device, so its performance gains more benefits from the inclusion of the controller. In order to maximize the power extracted,

a WEC must effectively convert energy in a range of frequencies as wide as possible. For heaving point absorbers, for example, the resonance frequency of the WEC is usually quite pronounced, and the response amplitude rapidly decays for frequencies away from resonance. Indeed, the main aim of the control strategy is to address the sea state variability, and significantly enlarge the amplitude of motion, especially at frequencies far from the resonance peak. The most common control strategies for linear WEC models are based on a form of complex-conjugate [117] or reactive [118] control, which returns the optimal conditions, in the frequency domain, to maximize energy absorption, as shown in [45]. On the other hand, examples of time domain approaches are given by latching [119, 115, 120], and methods based on numerical optimization [121, 122].

Regardless of which particular model-based control strategy is adopted, a comprehensive model of the system is required, and the performance of the controller is highly dependent on the model accuracy. The simplest and most common choice is to linearize the system, implicitly assuming small amplitudes of motion. However, under controlled conditions, the motion may be exaggerated and, as a consequence, the relevance of nonlinearities increases.

In absence of control, the only external action comes from the waves, whose steepness is physically limited, as shown in [123]. The resulting wave excitation force is smooth and largely without high frequency components. Conversely, the controller acts directly on the device with an arbitrary force, limited only by the structural constraints of the system. An example is latching control, which imposes a discrete on/off force. [92] implements latching control with both a linear and a partially nonlinear hydrodynamic model, and shows how the predicted power output, and the optimal control calculations, are affected by presence/absence of nonlinear terms. While linear and nonlinear models produce similar WEC motion in the uncontrolled case, the motions diverge when control is applied. Specifically, nonlinearities become relevant when the sharp exciting force of the controller directly influences the dynamic envelope of the device, leading to, among other effects, an asymmetric response.

An accurate evaluation of the performance of the controller, as well as a validation of the results of the simulations, may be achieved through experimental tests, in the sea, or in wave tanks [12]. [124] tests latching on an axisymmetric floating body in a wave tank, and the implementation of the control increased the power captured up to 4.3 times. A comparison between a simulation and tank tests is reported by [125], where a latching control strategy is applied in a wave tank to the SEAREV device. The controller increased the energy production up to ten times with regular waves, from 50% to 86% with irregular waves.

Unfortunately, experimental tests are not widely performed, because they are time consuming, expensive, and require both a device, usually scaled, and a wave tank. A more feasible evaluation tool is represented by a numerical wave tank (NWT), that implements a real tank in a CFD environment. The application of the Navier-Stokes equations permits the inclusion of all the nonlinearities, while the numerical domain makes the simulation of the full scale device possible, hence avoiding scale effects. On the other hand, CFD has several drawbacks, among which the most relevant are: expensive large clusters needed to perform the computation in a reasonable time, long setup time and the expertise required to produce reliable results, as well as long computational time for each simulation.

Nowadays, in wave energy applications, numerical wave tanks are mainly used to evaluate fluid-structure interaction on one or more floating bodies in operational conditions, to test survivability in extreme conditions [126], to quantify viscous effects in order to identify the terms of the Morison equation and model an equivalent viscous force [31], or to provide data for system identification techniques [127]. Even though experimental results demonstrate the impact of the controller on the system's dynamics, a *real time control* study in a NWT is missing. This chapter addresses this absence of a control strategy in a CFD

environment, implementing latching in the open source software OpenFOAM[®]. Rather than focusing on a nonlinear control algorithm, which could be based on the mathematical formulation of [128], the objective of the work in this chapter is to show that a real time controller in CFD is implementable, and to highlight the prominence of nonlinear WEC behaviour under controlled conditions, which leads to a significant difference between optimal latching duration for linear and nonlinear WEC simulations. In particular, the focus is on nonlinearities deriving from the *wave-body interaction*, therefore only linear waves are analysed.

Likewise, additional PTO damping has not been included since, even without a PTO, the system is already damped enough to avoid unacceptably large oscillations; it will be shown that the maximum oscillation achieved (0.028 m) is just the 22% of the device radius (see Fig. 3.11, or Table 3.3). Moreover, without PTO damping, the only control parameter to be optimized is the latching duration, making the control problem easier. With no PTO, there is no power extraction, so the sole objective of the optimization is to exaggerate the amplitude of oscillation. Nevertheless, [129] shows that, for latching control in a linear system with regular waves, maximization of the amplitude of oscillation is as effective as the maximization of the power extracted.

The remainder of the chapter is organized as follows: Sect. 3.3 presents the mathematical and computational description of the software's structure, while Sect. 3.4 shows the control choices available in the proposed latching algorithm. In Sect. 3.5, results are presented and, in Sect. 3.6, comparisons are drawn between CFD simulations and linear simulations. In Sect. 3.7, some conclusions and final remarks are presented.

3.3 Numerical Wave Tank

Numerical wave tanks are computer implementations, in either two or three dimensions, of physical wave tanks [130]. Having a numerical facility brings several advantages over a real tank: a more cost-effective evaluation of motion and power capture, passive access to individual hydrodynamic forces (e.g. restoring or viscous forces) and status variables (e.g. pressure or velocity) in every point of the fluid domain, implementation of ideal constraints and restraints, and no scale effects. Several drawbacks also exist, among which the most relevant by far is the high computational time, typically 1000 times greater than the simulation time [99]. Furthermore, the setup of a spatial mesh, which ensures a reasonable compromise between computational time and accuracy, requires time and experience.

The fluid dynamics in CFD are ruled by the Navier-Stokes differential equations [81]. Under the incompressibility assumption, only the equations for transfer of mass (3.1) and momentum (3.2) are utilized:

$$\nabla \cdot \mathbf{u} = 0 \tag{3.1}$$

$$\rho \frac{\partial \mathbf{u}}{\partial t} + \rho \mathbf{u} \cdot \nabla \mathbf{u} = -\nabla p + \nabla \cdot \mathbf{T} + \rho \mathbf{g} \tag{3.2}$$

where \mathbf{u} is the fluid velocity, ρ is the fluid density, p is the pressure, \mathbf{g} is the acceleration due to gravity and \mathbf{T} is the stress deviator tensor, given by.

$$\mathbf{T} = \mu[\nabla \mathbf{u} + (\nabla \mathbf{u})^T] \tag{3.3}$$

where μ is the dynamic viscosity.

The CFD software discretizes the time and space domains in order to form a system of linear algebraic equations. The software utilized in this work is the open source OpenFOAM, version 2.3.

3.3.1 OpenFOAM

The development of NWTs in OpenFOAM is a rich research topic, and numerous research theses and reports are available [131, 132]. In the wave energy field, OpenFOAM has been used to simulate wave energy converters in operational conditions [133, 134], and under extreme events [135].

The wave generation application is called *wave2Foam*, and was created as an extension of the built-in *interFoam* [136]. The free surface elevation is described by an interface-capturing method, known as volume of fluid (VOF) [137]. Within the tank, there are three different zones: in the middle region, dynamics are purely governed by the Navier-Stokes equations; hence, this is the actual experimental area of the tank. Upwave, there is the wave generation zone, where the required wave profile is gradually imposed on the fluid domain. Downwave, there is the absorption zone, where waves are gradually erased to avoid reflections. Figure 3.1 shows the generic configuration of a numerical wave tank, where the curved profiles in the generation and absorption zones represent the proportion with which the wave profile is imposed on the fluid domain.

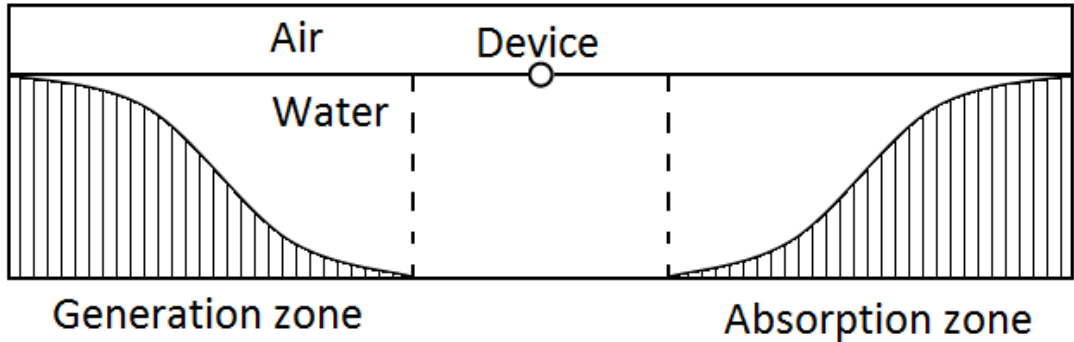


Figure 3.1: Scheme of a Numerical Wave Tank implemented in OpenFOAM using *waveFoam*.

A further development of the wave generation application is called *waveDyMFoam*, based on the built-in *interDyMFoam*, which allows the presence of a floating body, thanks to a dynamic mesh that moves and deforms according to the body motion. In Version 2.3 of OpenFOAM, the introduction of the *sixDoFRigidBodyMotion* solver considerably improves the mechanism taking care of the movement of the body, and the consequent deformation of the surrounding mesh. Moreover, constraints and restraints are more reliable and efficient than in the previous versions.

The main reason for the choice of OpenFOAM, instead of other CFD software, is its flexibility and open source availability. Besides the undeniable attraction of being cost-free, the greatest value is the possibility to access and modify the source code, which allows a deep understanding and total control over the calculations performed by the software. OpenFOAM is written in C++, which makes straightforward the insertion of a new customized subroutine into the main structure of the software. Indeed, new compatible applications are easy to create, making the software flexible and adaptable to user's needs. In Sect. 3.3.2, the basics steps required to implement a new application are explained, as well as the instructions to download, compile, and use the latching control application.

3.3.2 Implementation of latching control

The proposed control algorithm is relised as a customized version of the built-in *sixDoFRigidBodyMotion*, which can be found in the source code folder of OpenFOAM. The

original application’s task is to apply Newton’s second law of dynamics, integrating all forces acting on the body surface, eventually including external restraints, to calculate and update both linear and rotational acceleration, velocity, and position. Furthermore, if present, constraints are analytically imposed, directly setting to zero the displacement in the blocked degree of freedom. Note that, in the *sixDoFRigidBodyMotion* solver, applying a constraint means to *forbid* the motion in a particular direction, and not to impose a maximum allowable displacement/velocity. In previous versions of OpenFOAM, constraints were *indirectly* obtained by adding a counteracting force against the resulting force in the direction of the blocked degree of freedom. Even though such an approach is theoretically valid, the numerical finite accuracy can cause a defective constraint.

Since a basic latching control essentially acts on the device by means of restraints (PTO force, proportional to velocity) and constraints (locking mechanism), *sixDoFRigidBodyMotion* is suitable as the backbone of the new application, implementing the real-time control algorithm. The user can either code his/her own control algorithm, or download the ready-to-use latching control algorithm available in [138]. Details about the control strategy features and options are provided in Sect. 3.4, while practical instructions are given in the user manual in [138]

3.4 Latching control

After a brief overview of latching control, given in Subsection 3.4.1, the strategy actually implemented in the proposed control algorithm is revealed. Subsection 3.4.2 describes the basic logic of the new source code. Subsection 3.4.3 highlights a nonlinear behaviour of the natural period, with relevant consequences on the latching strategy, leading to an expansion of the control algorithm, explained in Subsection 3.4.4. Finally, in Subsection 3.4.5, a case study is presented, along with a description of some issues related to the CFD simulation environment.

3.4.1 Latching control: an overview

The purpose of a latching control strategy is to force the velocity into phase with the excitation force. An on/off PTO force is applied by means of a latching system, in order to minimise phase difference between the velocity and the incoming wave excitation force. Referring to Fig. 3.2, the device is locked at times t_1 , t_3 , and t_5 , at the extrema of displacement, namely when the velocity is zero, and released at times t_2 and t_4 , after a latched duration T_L . The two latching durations, upper position $t_2 - t_1$, and lower position $t_4 - t_3$, may, in certain cases, be chosen to be different [139].

If the wave is regular and monochromatic, with period T_w , the natural period T_n of the device is known and, if damping effects are negligible, the control variable T_L is optimally calculated [140] as:

$$T_L = \frac{t_5 - t_1}{2} - (t_5 - t_4) = \frac{T_w}{2} - \frac{T_n}{2} \quad (3.4)$$

Equation (3.4) implicitly suggests that the latching control strategy best suits conditions in which the wave period is longer than the device natural period, with $T_L > 0$. Conversely, another control strategy, called declutching, is able to control devices facing an incoming wave with period smaller than the device natural period [141].

The appearance of, and requirement for, the natural period in equation (3.4) presents several issues. While, in a linear case, the natural period is a well known and an univocal concept, the presence of nonlinearities, or large amplitudes of motion, makes it ambiguous to define. Subsection 3.4.3 focuses on the variability of the natural period, and the consequences on the choice of the latching duration. Furthermore, equation (3.4) is exact only

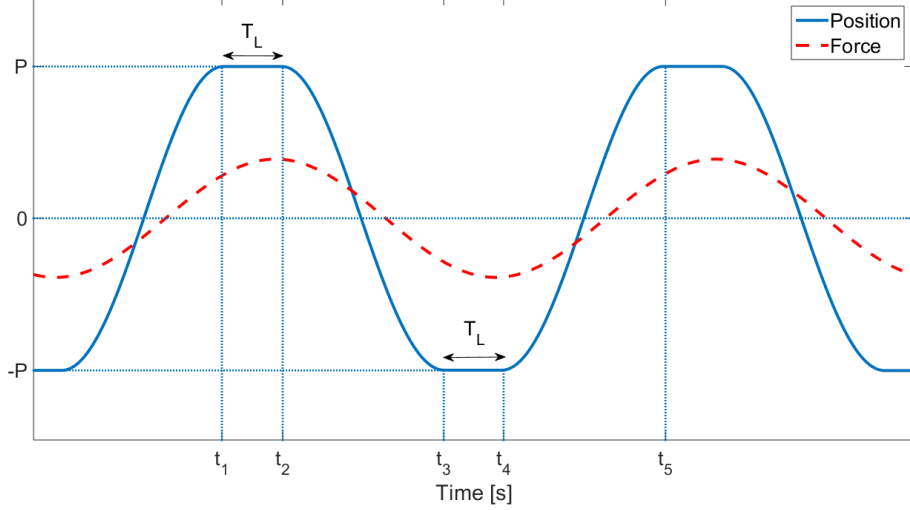


Figure 3.2: Latching calculations to put position and force in phase. Latching instants at extrema of position P and -P: t_1 , t_3 and t_5 ; latching duration: T_L ; unlatching instants: t_2 and t_4 .

if damping is absent or negligible. In the presence of damping, the natural period should be substituted by the damped natural period, which approaches the natural period as the damping goes to zero. Section 3.4.1.1 shows the linear hydrodynamic model approximation of the system, and proposes a model order reduction to estimate the influence of the damping on the natural period.

Finally, if the sea state is characterized by polychromatic waves, the requirement of phase accordance between velocity and excitation force becomes blurred, so the optimization criterion is not well defined [142]. Different targets can be pursued, such as the synchronization of the velocity and excitation peaks [143], or the maximization of the absorbed power [115].

3.4.1.1 Linear model approximation

The linear equation of motion for a single degree of freedom floating body, as in [144], is defined in the frequency domain as:

$$\{-\omega^2[M + A(\omega)] + j\omega B(\omega) + G\}z(j\omega) = f_{ex}(\omega), \quad (3.5)$$

where M is the mass, $A(\omega)$ the added mass, $B(\omega)$ the radiation damping, G the hydrostatic stiffness, $f_{ex}(\omega)$ is the wave excitation force, and z the vertical degree of freedom, for example. The hydrodynamic parameters $A(\omega)$ and $B(\omega)$ are calculated by solving the potential problem using the BEM open source software NEMOH.

For the purposes of real-time control, a time domain formulation is needed, obtained by applying Cummins equation [145]:

$$(M + A_\infty)\ddot{z}(t) + \int_{-\infty}^{\infty} K_R(t - \tau)\dot{z}(\tau)d\tau + Gz(t) = f_{ex}(t) \quad (3.6)$$

where A_∞ is the infinity frequency added mass asymptote, and the kernel K_R of the convolution term is the impulse response of radiation damping function. The calculation of K_R and A_∞ is facilitated by Ogilvie's relationships [146]:

$$K_R(t) = \frac{2}{\pi} \int_0^{\infty} B(\omega)\cos(\omega t)d\omega, \quad (3.7)$$

$$A_\infty = \lim_{\omega \rightarrow \infty} A(\omega). \quad (3.8)$$

Finally, since the direct computation of the integral in (3.6) is expensive, the convolution term can be replaced by a state space representation [147], as showed by [148]. In this way, the whole dynamic problem becomes a computationally efficient set of first order differential equations. The identification of a state space model is performed using the toolbox provided by [149], which automatically selects a proper order, hereafter called n , to approximate the convolution integral. Therefore, the overall dynamical system order of the system (3.6) becomes $2+n$.

However, since the oscillatory behaviour of a floating object resembles the dynamics of a simple constant mass-damper-spring system, [150] proposes a second order approximation, namely reducing the radiation damping state space approximation order to zero, i.e. the complete system order to two. The reduction is reasonable if the system is described by a dominant pole pair. The evaluation of the relevance of each order is made by means of the Hankel singular values of the complete system σ_i , which are used to quantify the energy content of each order i [151]. If arranged in descending order, namely $\sigma_1 \geq \sigma_2 \geq \dots \geq \sigma_{n+2}$, the second order approximation is reliable if $\sigma_2 \gg \sigma_3$.

The second order system approximation presents a constant damping term, so equation (3.6) can be rearranged to match the standard second order dynamical system:

$$\ddot{z} + 2\zeta\omega_n\dot{z} + \omega_n^2z = 0, \quad (3.9)$$

where $\zeta < 1$ is the damping ratio and $\omega_n = \frac{2\pi}{T_n}$ is the natural frequency. Notwithstanding the approximation introduced, the advantage of the order reduction is the possibility to analytically evaluate the effect of the damping on the system dynamics. Since the damped natural frequency is defined as

$$\omega_d = \omega_n\sqrt{1 - \zeta^2}, \quad (3.10)$$

it is smaller than the natural frequency. Consequently, the presence of damping reduces the ideal optimal latching duration:

$$T_L = \frac{T_\omega}{2} - \frac{T_L}{2} = \frac{T_\omega}{2} - \frac{T_n}{2\sqrt{1 - \zeta^2}} \quad (3.11)$$

The approximation error introduced by equation (3.4) is proportional to the damping factor of the non-reduced system, which is not as explicitly accessible as in the standard second order differential equation (3.9). The second order reduction may be of assistance if the whole system is clearly second-order-dominant, namely if the approximation introduced by the order reduction is negligible. Since every case should be assessed for second order dominance, it is not possible to give to the method a general validity. Therefore, T_L is not always exactly definable, and T_n is used instead, mindful that the actual optimal T_L will be smaller, accordingly to the damping factor of the system.

3.4.2 Constant latching duration

The basic latching control algorithm applies to devices subject to monochromatic waves, and utilizes a constant latching duration, which is equal for both positive and negative peaks. Conversely, alternative and adaptive latching duration options are available to deal with nonlinear dynamics, as further explained in Sect. 3.4.4.

The control algorithm allows the user to choose which degree of freedom the latching control should be applied to, either in *surge* (x -axis), *sway* (y -axis), or *heave* (z -axis) motion. The conventional right-handed coordinate system assumes the incoming wave to

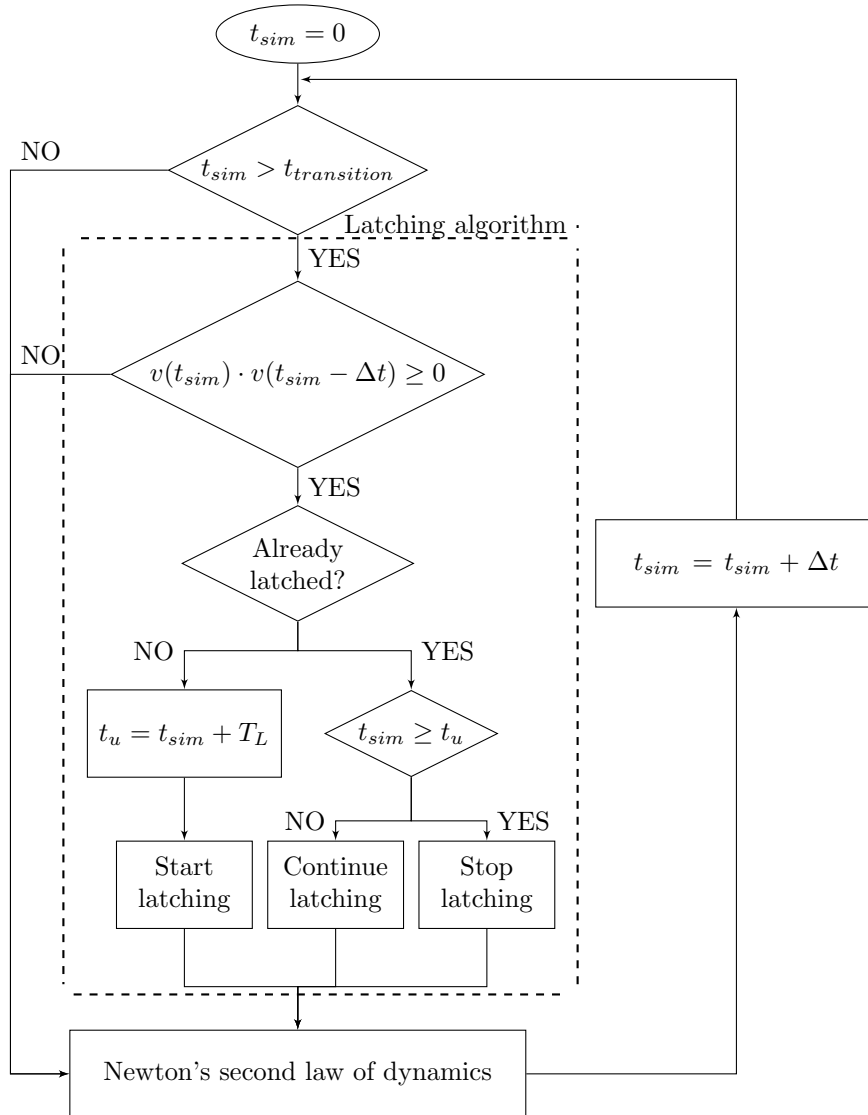


Figure 3.3: Constant latching duration control strategy. Simulation time: t_{sim} ; time step: Δt ; transition time: $t_{transition}$; velocity: v ; latching duration T_L ; unlatching instant: t_u .

travel along the x - *axis*, gravity acting on the negative direction of the z - *axis*, and the y - *axis* oriented according to the right-hand-rule.

In order to be effective, the controller must be able to detect when the latching conditions are verified, and actually lock the motion for as long as required by the latching controller. The innovation introduced by the new control algorithm is the dynamical use of constraints, as defined in Sect.3.3.2, to perform the latching act: instead of being applied just at the beginning of the simulation, constraints in the controlled degree of freedom are imposed when the body is latched, and removed when the body is released. The timing with which the controller intervenes is defined by the control strategy, whose logic is showed in the flowchart in Fig. 3.3.

The algorithm applies Newton's second law of dynamics at every time step Δt of the simulation time t_{sim} , and updates the state variables of position, velocity, and acceleration. Prior to the application of Newton's law, the control algorithm sets the constraints, accordingly to the latching status.

Initial conditions normally assume the floating body to be in quiet equilibrium in the numerical wave tank at the still water level (SWL). When the simulation starts, waves are gradually created in the generation zone, and travel towards the device which, in turn, begins to move. Hence, the control loop is bypassed for a transition time $t_{transition}$, defined by the user, to allow the device motion to reach a steady free response.

Then, the latching condition of zero velocity at the extrema of displacement needs to be verified. Due to numerical precision, a null velocity is very unlikely, so the multiplication between the values in two successive time steps ($v(t_{sim}) \cdot v(t_{sim} - \Delta t)$) is checked instead: in the case of an extremum, the product will be either negative or null. Furthermore, when the body is latched, the velocity is exactly set to zero, so the null-multiplication-condition is verified as well. Consequently, it is important to asses whether the body has just reached the peak, or it was already locked in the extremum from the previous time step, i.e. whether or not the body was latched in the last iteration. At the very first sample point that the controller locks the device, the unlatching instant t_u is defined by adding the latching duration to the simulation time. The body is kept in position until the latching duration has elapsed, then is freed to escape from the extreme position.

Summing up, in order to use the latching control algorithm, the user should declare the *type* of latching control (constant, alternative, or adaptive), the *degree of freedom* (surge, sway, or heave) where latching is applied, the value of *latching* duration, and *starting* time.

3.4.3 Latching duration and natural period

The main important parameter to choose to perform latching control is the latching duration. If the incoming wave is monochromatic, equation (3.4) achieves optimal latching control, as long as the natural period of the controlled device is known, and the damping term ζ is negligible. If damping is not negligible, then (3.11) can be used instead. Unfortunately, the definition of a unique characteristic natural period is not straightforward, if the linear assumption of small motion is not made, as explained in Sect. 3.4.3.1. Since the amplitude of the motion is exaggerated by the latching control, the small motion hypothesis is generally invalid.

3.4.3.1 Natural period

In dynamics, the natural period (or frequency) describes how fast the undamped body oscillates, if displaced from an equilibrium position, and set free to move. The natural frequency is calculated from the inertia and the stiffness terms of the equation of motion. Equation (3.5) shows the frequency dependence of the added mass $A(\omega)$ and damping term $B(\omega)$, while the mass M and the stiffness G are constant.

Actually, equation (3.5) is accurate only in a range of motion around the equilibrium, small enough to consider the wetted body surface constant. The added mass (which is the mass of water accelerated by the body motion, therefore depending on the submerged portion of the body), and the hydrostatic stiffness (which depends on the cross section piercing the water), both depend on the instantaneous wetted surface, with the notional dependence shown by $A(x(t))$ and $G(x(t))$ in (3.12), respectively. The natural period, which is defined, in linear conditions, as a time-invariant characteristic of the body, is not a proper descriptor under large motion conditions. A new quantity, called the *instantaneous natural period*, is defined in (3.12), which returns the natural period relative to the actual submerged portion of the body, at each time instant. Hence, the instantaneous natural period is able to capture the nonlinear relation between the natural period and the motion of the body.

$$T_n(x(t)) = 2\pi\sqrt{\frac{M + A(x(t))}{G(x(t))}}. \quad (3.12)$$

Furthermore, the instantaneous *damped* natural period (T_L), also depends on the radiation, and eventual viscous, damping in the system. In Sect. 3.4.3.2, a free decay time series, from CFD simulation, is used to appreciate the range of variability of the *instantaneous* natural period.

3.4.3.2 Free response tests

The natural period is a description of the dynamical behaviour of a body left free to move from a position of non-equilibrium. Therefore, a reliable measurement of the actual natural period can be obtained from a free decay test, performed either in a real, or numerical, tank. While, in a linear analysis, essentially inaccurate assumptions are used to *calculate* the natural period, here it is directly *measured* from the time series, which is inclusive of all nonlinearities.

During the evolution of the free decay, both the amplitude and the frequency are changing in time. For the sake of simplicity, the two variables are separated, so that:

$$x(t) = X(t)\sin(\omega_n(t)t + \phi) \quad (3.13)$$

The natural period is defined as the time lag between two successive homologous points on the t-x plot (referring to points of equal displacement, a period apart) of the harmonic function. Since, in a free decay test, the amplitude is not constant, there is not a continuous set of homologous points; therefore, it is only possible to sample the natural period at extrema or zero-crossings. While a discrete description of the instantaneous natural period is valuable, a more precise and continuous trend is required to understand how nonlinearities gradually modify the dynamics, as the amplitude varies. Hence, in order to spot all the couples of consequent homologous points, equation (3.13) needs to be normalized, i.e. divided by the envelope that connects the absolute value of all the peaks and troughs of the free decay signal. Such an envelope is shown in Fig. 3.4.

As an example, the instantaneous natural period has been calculated for a semisubmerged sphere with radius and draft of 0.125m, with the center of gravity at the free surface height. A heave free decay is simulated in a CFD environment, starting with the center of gravity displaced to -0.1m. The resulting instantaneous natural period variations in time are shown via the solid line in Fig. 3.4. In the same graph, the envelope of the free decay time series is drawn using a dotted line, along with the separate indication for peaks and troughs.

As time elapses, the amplitude of the free decay decreases and the natural period becomes shorter, until it matches the linear natural period, represented by the horizontal dashed line. The transition toward the asymptote of 0.69s is smooth, with a maximum

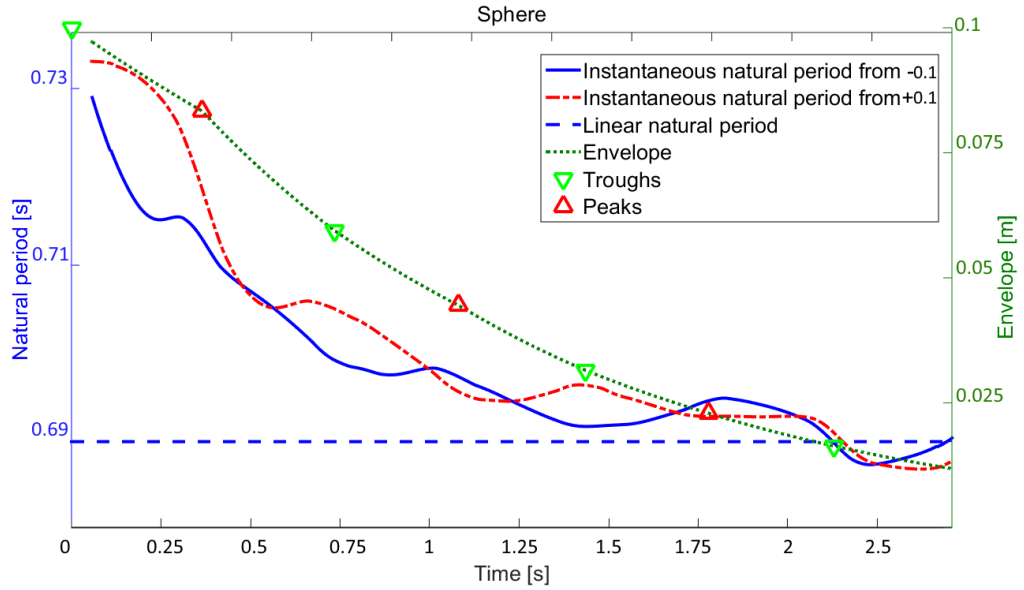


Figure 3.4: Instantaneous natural period for a CFD heave free decay test of a sphere with radius of 0.125m.

variation of about 7%, from the highest value of 0.74s, that occurs for an amplitude around 0.1m. Note a systematic alternation of concavity and convexity, respectively, occurring at the peaks and troughs of the free decay displacement. As a consequence, it is possible to infer that, at equal amplitude, the natural period is relatively longer at positive displacement (above the SWL), than at negative (below the SWL). Indeed, at the right hand side of Fig. 3.4, where the steepness of the curve is less, the variability of the natural period between peaks and troughs is more evident. Further insight can be had by simulating a free decay from a symmetric initial condition, namely starting from 0.1m, instead of -0.1m. The resulting instantaneous natural period, shown with the dash-dot line in Fig. 3.4, follows the same average trend, but with a symmetric alternation of concavity and convexity, which confirms that at equal magnitudes of motion, the natural period is different inside and outside the water. The discrepancy between peaks and troughs becomes smaller as the amplitude decreases. The principal effect responsible for the different natural periods at peaks and troughs is the asymmetric action of the viscous forces, since the body is surrounded by two fluids, mainly water at troughs and mainly air at peaks, with very different viscous coefficients.

Finally, as far as the constant latching duration algorithm is concerned, the instantaneous natural period analysis allows a more effective selection of the latching period. A reasonable forecast of the amplitude of motion acquirable, for example, through a linear simulation, can point to the zone of the envelope in which the body will oscillate under control. Consequently, the corresponding natural period, pertinent to the particular point in the envelope, allows the selection of a more suitable latching duration.

3.4.4 Alternative and adaptive latching durations

Following the discussion about the variability of the natural period, in Sect. 3.4.3.2, the correct choice of the latching duration is not obvious. Since the instantaneous natural period is always longer than that for the linear case, equations (3.4) or (3.11) lead to a shorter latching period. The optimal latching duration is not clearly defined, since it depends on the amplitude of the motion which, in turn, depends on the latching duration itself. Moreover, the asymmetric behaviour between peaks and troughs adds a further

degree of complexity. The present control algorithm proposes two options to partially overcome the issues of the non-constant natural period: *alternative* and *adaptive* latching control strategies.

The *alternative* latching control aims to provide more flexibility to the control algorithm, allowing the definition of two different latching periods for peaks and troughs. An instantaneous natural period analysis of a free decay test, as in Fig. 3.4, may be of assistance to the selection of such different latching periods. Since the natural period at peaks is longer than at troughs, typically the latching duration should be shorter at positive extrema.

The second option available is *adaptive* latching control, which is an optimization tool, loosely based on extremum-seeking control, used to find out the latching period that maximizes the amplitude of oscillation of the controlled body. A similar approach has already been applied in [92] to overcome the uncertainty of the latching duration, due to the use of a partially nonlinear model.

The optimization loop is based on the assumption of the existence and uniqueness of an optimal point, which is the only maximum of a convex performance function. As explained in Sect. 3.4.3.2, the presence of nonlinearities *decreases* the optimal latching duration. On the other hand, a null value for the latching period implies an absence of control, which is implicitly not optimal, unless the natural period is the same as, or larger than, the wave period. The uniqueness of the optimal solution is not straightforward to prove, but a comparison with the linear case can bring confidence: constant latching duration control has been implemented in a linear simulation model with several latching periods, in order to draw the performance curve in Fig. 3.5.

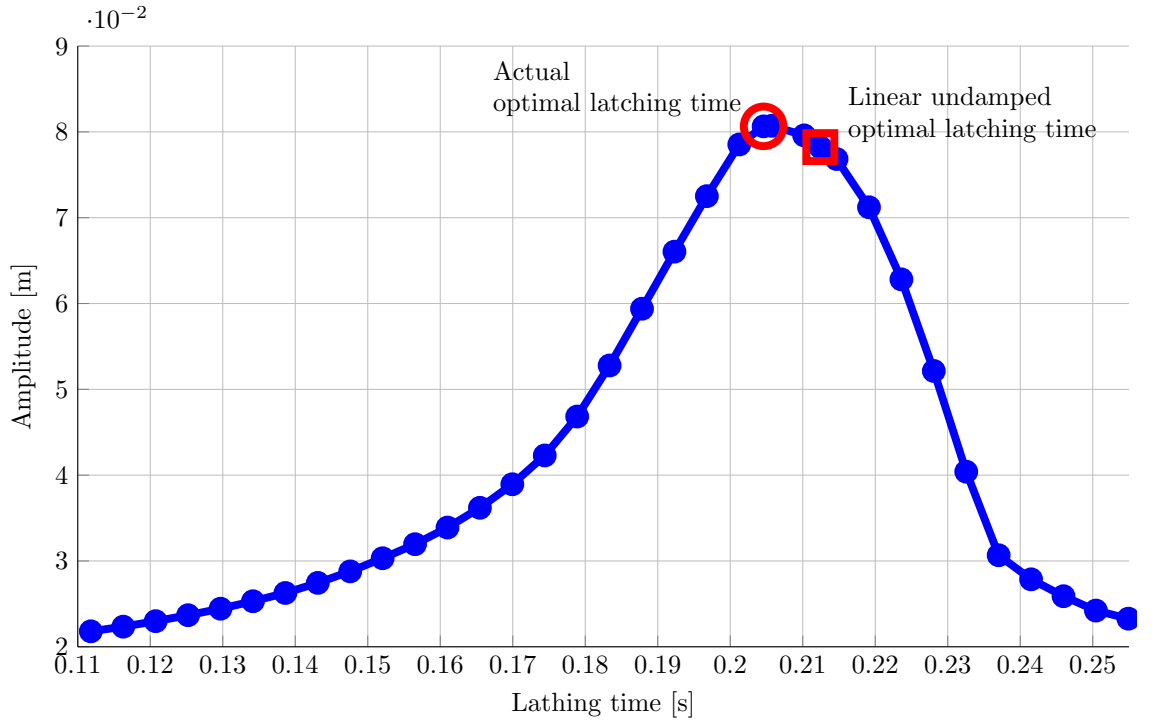


Figure 3.5: Performance curve of latching control using a linear simulation for a sphere with radius of 0.125m.

The graph in Fig. 3.5 validates the assumption of uniqueness of the optimal point in a linear model, equal to 0.205s, corresponding to an equivalent natural period of 0.709s. The optimal latching duration is highlighted by a circle marker on the top of the convex curve of Fig. 3.5. Moreover, the square marker represents the linear undamped approximation, calculated with equation (3.4). As expected, the damping makes the actual optimal

latching duration smaller than the undamped, in this case 3.8% smaller.

Model order reduction, using the Hankel singular values as estimators of the significant order of the system, proposed in Sect. 3.4.3.1, has been applied to approximate the linear model with a second order differential equation, and evaluate the damped natural frequency. The ratio of the second and third order Hankel singular values, about 43, is large, but not enough to give absolute confidence in the reduction. Indeed, the method was successfully applied in [150] to geometries with ratios ranging between 230 and 3204. Nevertheless, the reduction suggests a value of damping factor ζ of about 0.1, which, in turn, makes the damped natural period rise from 0.693s to 0.698s.

The calculation of the optimal latching duration, in the linear case, is made possible by the low computational cost of the simulations. A similar approach, in CFD, is not feasible, due to the huge computational effort required by each simulation. The approach pursued by the adaptive control algorithm is to tune the latching period, within one simulation run, aiming at maximizing the displacement of the body. The first latching duration is an educated guess based, for example, on the linear, or the instantaneous, natural period. When latching is applied, the amplitude gradually increases, either monotonically or with an intermediate maximum, and stabilizes to a steady value. As the amplitude changes, the period of motion adapts accordingly and, after a transient, stabilizes, matching the forcing wave period. Likewise, when a modification to the latching duration is carried out, both the amplitude, and the response period, experience a transient, that ultimately leads to a steady state. Clearly, the transient is longer when latching is applied for the first time, than when the latching period has been adapted. The adaptive algorithm's task is to wait for the steady state to occur, then update the latching period in order to increase the response of the device, taking into account records of previous modifications.

The adaptive latching duration control strategy, shown in Fig. 3.6, is a combination of the constant latching duration control strategy, shown in Fig. 3.3, and an algorithm for updating the latching duration: the *latching duration update* algorithm (see Fig. 3.6) calculates the latching duration, which is used by the *latching algorithm*.

The adaptive strategy is divided into two phases: it first identifies when the period and amplitude are stable, then modifies the latching duration. The steadiness is achieved when the motion period matches the wave period, and the amplitude is constant, both within the percentage tolerances, set either by the user, or by default. Once the transient has elapsed, the stable value of the amplitude is recorded, and compared with the last stable value in memory, in order to ascertain whether the last modification of the latching duration increased the stable amplitude. Assuming the convexity of the performance function, similar to Fig. 3.5, the latching duration is progressively reduced, with a certain step ΔT_L , as long as the performance improves. Conversely, a deterioration occurs if the maximum has been exceeded, so the direction of search is reversed and the step is halved to refine the quest.

3.4.5 Case study

In order to demonstrate the performance of the latching control algorithm, and to highlight the strengths and weaknesses of the CFD implementation, a case study is presented. CFD simulations are carried out in both 3D and 2D, hence the body is, respectively, a sphere (3D simulations) and a circle (2D simulations) of radius 0.125m, and draft of 0.125m. The shape of the floater is inspired by the Wavestar device, and its dimensions correspond to the 1:20 prototype scale [66]. The device is constrained to move in the heave direction. The incoming wave is a linear harmonic function, with a constant amplitude and period, in order to clearly show nonlinear effects, and the action of the adaptive latching algorithm. The wave amplitude is 0.015m, such that the oscillation of the body is comparable to its dimension, highlighting nonlinearities. The wave period is 1.118s, longer than the natural

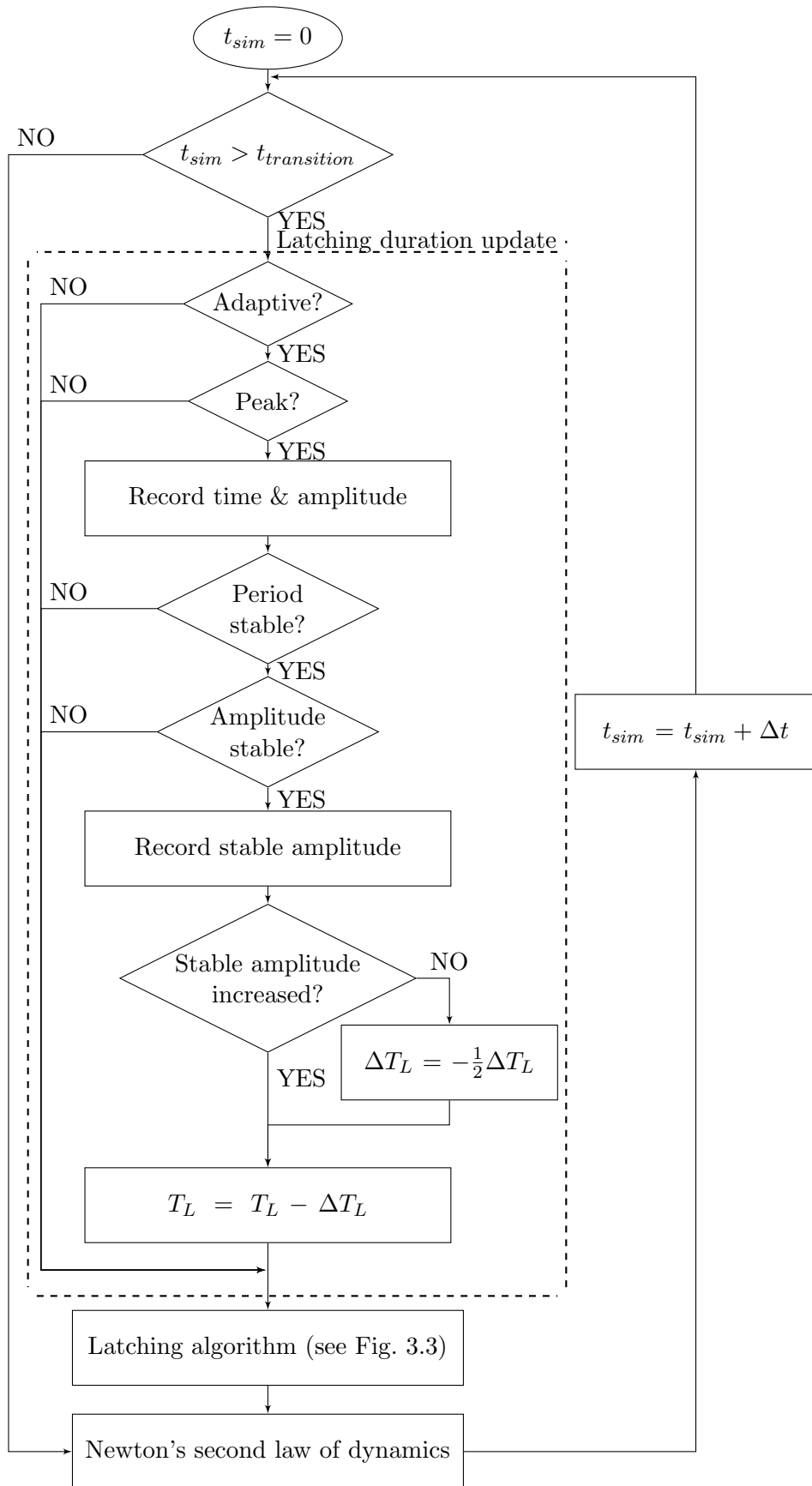


Figure 3.6: Adaptive latching duration control strategy. Latching duration: T_L ; latching duration increment: ΔT_L

period of both the sphere and the circle, which are between 0.671s and 0.894s, allowing latching to be an effective controller, as explained in Sect. 3.4.1.

A schematic representation of the device within the numerical wave tank is given in Fig. 3.1. For all the details concerning the CFD implementation in OpenFOAM, such as the numerical wave tank, the mesh, the solver, the boundary conditions etc., refer to [152]. Key information are listed in Table 3.1, with reference to the 3D simulation case. The cell count refers to the body region, where a constant cell size is implemented, while elsewhere constant grading is applied. The simulation time is obtained with 24 cores, each one carrying an Intel Xeon E5-2695 2.4 GHz processor. The method used for quantifying the reflection coefficient uses the time signal of three probes, arranged with a certain spacing. Using a least squares approach, the method is able to separate incident and reflected wave spectra. The reflection coefficient is defined as the ratio between incident and reflected waves [153].

Table 3.1: Tank characteristics for the 3D simulation: cells per wave length (CPL), cells per wave height (CPH), time step (Δt), wave period (T_w), propagating along the x direction, with z vertical.

Spatial discretization:	
dx	200CPL
dy	50CPL
dz	10CPH
Temporal discretization:	$1400\Delta t/T_w$
Run time / computational time	$5 \cdot 10^3$
Reflection coefficient	2%

Due to the small characteristic length of the device, the Reynolds number is about $2 \cdot 10^4$ and the flow is assumed to be laminar, although turbulences and vortex shedding may occur. However, the choice of a laminar solver for point absorbers within this range of Reynolds numbers is common practice in the wave energy field [80].

The boundary conditions of the 3D numerical wave tank are summarized in Table 3.2. Taking advantage of the symmetry of the problem, only half of the tank is simulated. The names of the boundaries are self-explanatory while the four fields that need to be defined are the phase fraction (α), the velocity U , the dynamic pressure ($p_d = \frac{1}{2}\rho|U|^2$), and the displacement of the cells (pointDisplacement). The phase fraction α ranges from 0 (only air) to 1 (only water).

Table 3.2: Boundary conditions for the 3D numerical wave tank using OpenFOAM 2.3.

	α	U	p_d	pointDisplacement
Front	symmetryPlane	symmetryPlane	symmetryPlane	symmetryPlane
Back	zeroGradient	fixedValue (0)	zeroGradient	fixedValue (0)
Inlet	waveAlpha	waveVelocity	zeroGradient	fixedValue (0)
Outlet	waveAlpha	waveVelocity	zeroGradient	fixedValue (0)
Bottom	zeroGradient	fixedValue (0)	zeroGradient	fixedValue (0)
Atmosphere	inletOutlet	pressureInletOutletVelocity	totalPressure	fixedValue (0)
Sphere	zeroGradient	movingWallVelocity	fixedFluxPressure	calculated

The names of the boundaries refer to version 2.3 of OpenFOAM [154]. Calling Φ the general field (either α , U , p_d , or pointDisplacement), the boundary conditions are the following:

- symmetryPlane: it defines the boundary as a symmetry plane.
- fixedValue (0): it sets Φ to zero.

- zeroGradient: normal gradient of Φ is zero.
- waveAlpha: input wave surface elevation determined by waves2Foam [136].
- waveVelocity: input wave velocity determined by waves2Foam [136].
- inletOutlet: zeroGradient in case of outflow, fixedValue (0) in case of inflow.
- pressureInletOutletVelocity: a zeroGradient condition is applied for outflow while for inflow U is evaluated from the flux.
- totalPressure: total pressure $p_T = p_0 + \frac{1}{2}\rho|U|^2$ is fixed, where p_0 is the reference pressure and ρ is the density; when U changes, p_0 is adjusted accordingly.
- movingWallVelocity: the normal of the patch value is replaced so that the flux across the patch is zero.
- fixedFluxPressure: the pressure gradient is adjusted such that the flux on the boundary is that specified by the velocity boundary condition.
- calculated: the displacement of the cell is calculated according to the Newton's second law of dynamics.

In the case of a 2D simulation, which is a one-cell thick 3D simulation, the boundary condition for every field of the boundary front and back is signalled as ‘empty’. As a result, the third dimension is neglected during the calculations.

Generally, the definition and meshing of the computational domain has major consequences for the success and quality of the simulation. The most relevant issues related to a controlled floating object are analyzed. The risk of failure due to over-deformation of the cells is particularly important when control is applied, since numerous large-amplitude motions, caused by the controller, stress the whole mesh around the device. On the other hand, the accuracy of the generated waves depends both on the cell dimension at the free surface elevation, and on the size of the generation and absorption zones. A rule of thumb is that the generation zone has to be between two and three times the wave length. In the present case study, the wave length is 1.95m, which means at least 3.9m for the generation zone. The resulting mesh is presented in Fig. 3.7. As described in detail in [152], the central region contains a high-density mesh, that horizontally stretches with distance away from the device. Furthermore, the free surface region presents a high density mesh in the vertical direction. A boundary layer of finer mesh has been added around the floater in order to correctly describe viscous effects. The thickness of the boundary layer has been determined using the Blasius solution [155], resulting in a total thickness of 7.6mm, divided into ten grid points.

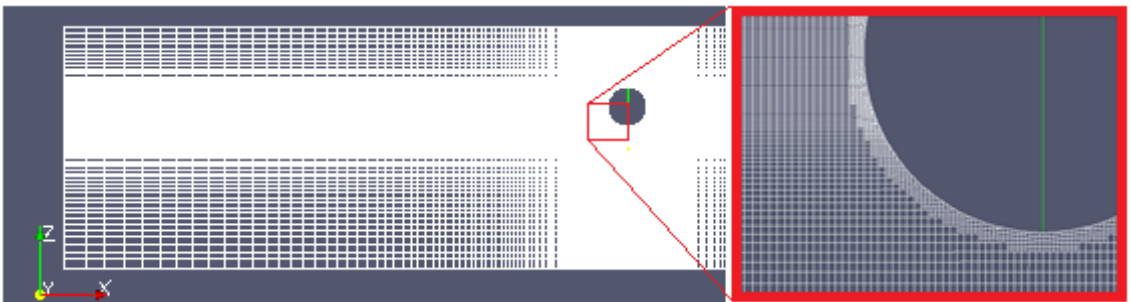


Figure 3.7: Computational mesh of the numerical wave tank domain. Central region with high density mesh; free surface region with high vertical density mesh.

Clearly, the biggest impact on the computational load is the number of dimensions simulated, namely two or three, where the third dimension is horizontal and perpendicular to the incoming wave direction. The 2D-boundary conditions are such that all the equations are solved within the $x - z$ plane. As a consequence, the equivalent three-dimensional counterpart is a cylinder of infinite length along the third dimension.

In the simulations performed for this work, on identical computing hardware, the simulation time required by a 3D simulation is approximately 500 times greater than its 2D equivalent. In absolute terms, 60s of 3D simulation typically requires in the region of several days or weeks of computation. Such a long time is prohibitive for running a wide range of diverse simulations. Therefore, the main focus is on the 2D simulations, since the shorter computational time facilitates a change in several parameters, with subsequent analysis of the behaviour of the control algorithm. Section 3.5 shows the performance of the constant and adaptive latching duration control, applied to the two-dimensional case study. However, one single 3D latching simulation, along with other 2D simulations, has been used in Sect. 3.6 for validation against a linear model.

3.5 Results

The results of the 2D case study are presented. By means of the free decay analysis, described in Sect. 3.4.3.2, the instantaneous natural period has been found to range between 0.827s and 0.783s. A basic constant latching duration control is applied, with a latching duration of 0.145s, corresponding to a nonlinear natural period of 0.827s. The resulting time trace is shown in Fig. 3.8.

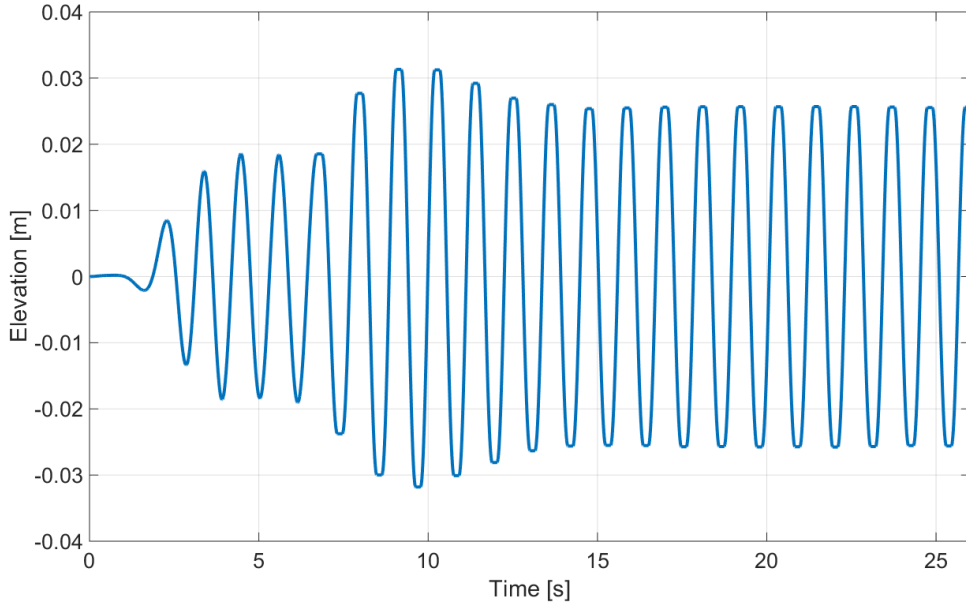


Figure 3.8: Constant latching duration control of a circle of radius 0.125m using a 2D CFD simulation, with regular wave (height: 0.015m, period: 1.118s) and latching duration of 0.145s.

The controller is activated after 6.5s, in order to wait for the wave to arrive and reach steady-state motion, following the initial transient. When latching is applied, the amplitude increases, reaches a maximum, and decreases toward a stable value. The improvement in amplitude achieved by the controller in this case is approximately 38%.

In the steady response, before latching is applied, the period of motion is identical to that of the wave. When latching is applied, the motion period suddenly increases, and

then is forced to match the excitation period again. Figure 3.9 shows the evolution of the period against the number of peaks after the beginning of the latching.

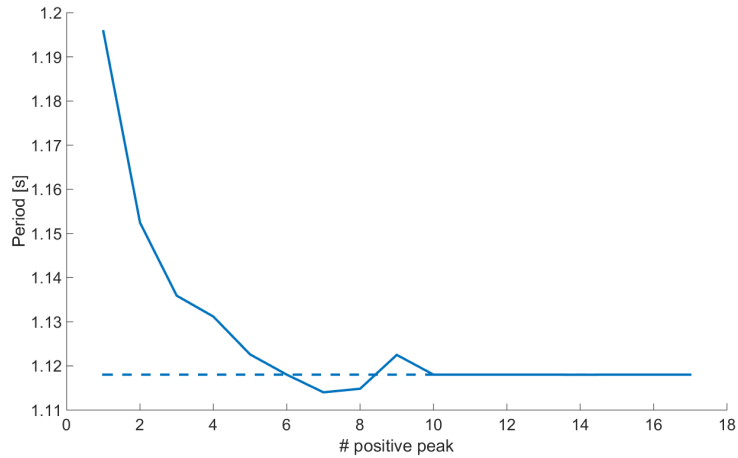


Figure 3.9: Evolution of the period of motion of the response in Fig. 3.8 when latching control is applied. The horizontal axis represents the number of peaks from the beginning of latching.

The adaptive latching duration control calculation, shown in Fig. 3.6, is now applied, initialised with a latching duration of 0.145s, corresponding to the nonlinear natural period of 0.827s. After 9 modifications of the latching duration, the resulting optimum point is identified at 0.1146s, leading to an amplitude increment of 49%. Fig. 3.10 shows the progression of the optimization: the vertical bars indicate the modification steps of the latching duration, while the line graph represents the corresponding stable amplitude achieved. The horizontal axis shows the simulation time when the stable amplitude is reached. Note that, in order to define the latching duration with a four-digit resolution, the simulation time step must be smaller or equal to 0.0005s.

As a first step, the latching duration is decreased, because the nonlinear natural period is longer than the linear one. Then, as long as the stable amplitude increases, the latching duration is decreased. Conversely, every time the stable amplitude decreases, the search of the optimal latching duration is reversed and refined. The graph in Fig. 3.10 shows that the optimization algorithm effectively converges.

The foundations of the adaptive algorithm are built on the hypothesis of convexity of the performance curve, assuming the full nonlinear CFD to behave similarly to the linear case, shown in Fig. 3.5. In order to validate such an assumption, the performance curve has been reconstructed, using several constant latching duration simulations, at different latching periods, as shown in Fig. 3.11.

As expected, the performance trend presents a unique peak, occurring for the same latching period indicated by the adaptive algorithm. Moreover, the optimal latching duration, for the CFD fully-nonlinear model, is smaller than the optimal latching duration for the linear model. The markers in Fig. 3.11 also highlight the amplitude achieved using the linear natural period (0.783s) for the computation of the latching duration (0.168s). Finally, using the instantaneous natural period (0.827s), i.e. latching duration of 0.145s, produces a larger response than using the linear natural period, validating the approach of the instantaneous natural period analysis. Table 3.3 summaries amplitudes and percentage improvements obtained with the three choices of latching duration, namely computed using the linear natural period, using the nonlinear instantaneous natural period, or optimized with the adaptive algorithm. Table 3.3 shows that the controller efficiency is quite sensitive to the latching duration, making the physical implementation problematic.

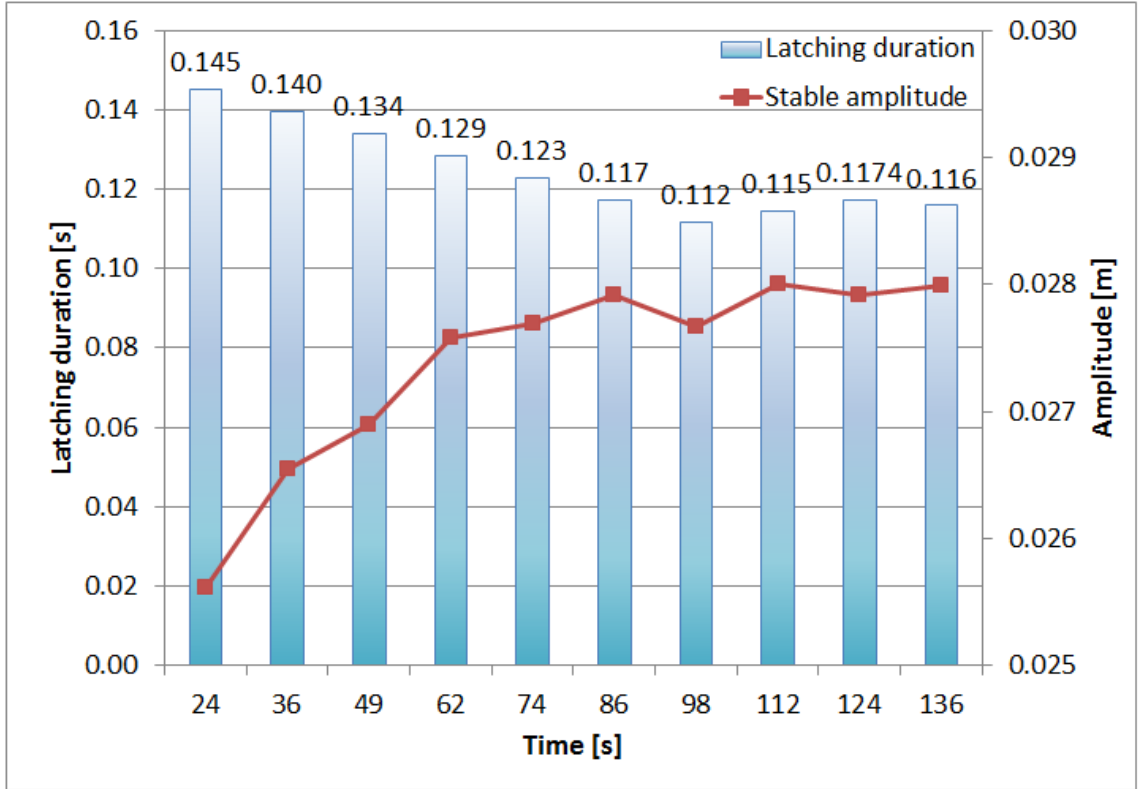


Figure 3.10: Iterations of the adaptive latching duration control algorithm: the horizontal axis represents the simulation time when the stable amplitude is reached and a modification of the latching duration is performed.

Table 3.3: Latching control performance using a two dimensional CFD simulation for a circle of radius 0.125m. The percentage improvements refer to the unlatched case.

Latching duration [s]	Amplitude [m]	Improvement
0	0.013	-
0.168	0.019	8%
0.145	0.026	38%
0.1146	0.028	49%

For example, a 15% relative difference in latching duration from 0.168s to 0.145s causes a 30% decrease in amplitude. Previous work has studied the sensitivity to the latching duration [47], which is mainly due to the sharp edges and abrupt modifications of the control force signal. Note that controllers, other than latching, may implement a similar force characteristic [156]. Implementing the exact latching duration in a real device can be quite difficult, due to the delay between the instant when latching is commanded, and the instant when the latching system actually locks the device. Various strategies have been tested in order to mitigate such difficulties: [157] utilizes the threshold unlatching criterion, while [125] advances the latching/unlatching instants to cover the latching system response delay. However, it has to be noted that the time scales, examined in this study, are commensurate with a small scale prototype. Larger devices have slower dynamics, which eases the implementation of a latching control strategy.

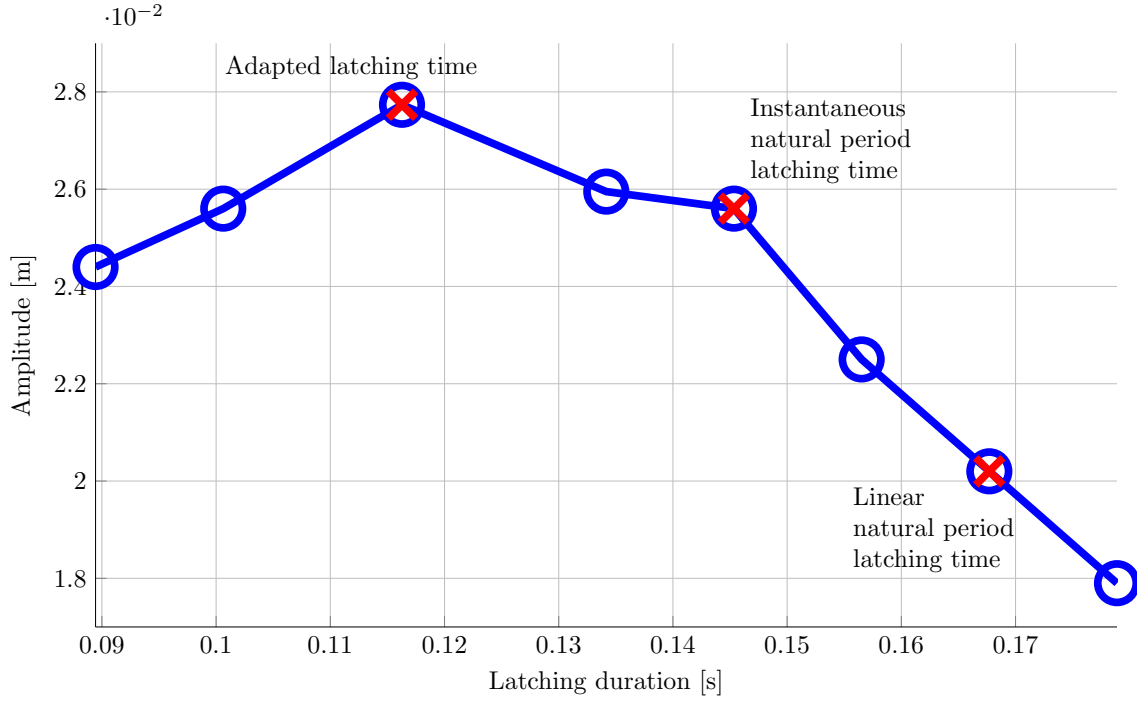


Figure 3.11: Performance curve of latching control using a two dimensional CFD simulation for a circle of radius 0.125m.

3.6 Discussion

The implementation of latching control in a CFD NWT is valuable in being able to include all nonlinear effects, and produce more realistic results than could be achieved from a linear model. Nevertheless, the characteristic high computational cost [99] makes an extensive application prohibitive, especially at an early design stage. On the other hand, a more suitable use is to provide a benchmark to validate and evaluate the results of linear or partially nonlinear simulation models, eventually defining a range of reliability in which the linear model is acceptable. Indeed, Sect. 3.6.1 compares the results of a linear model with a CFD NWT model.

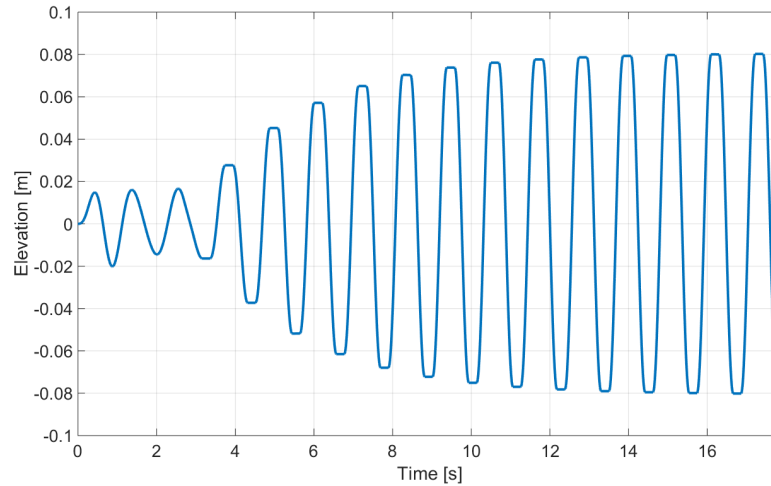
3.6.1 Comparison with linear model

3.6.1.1 3D case

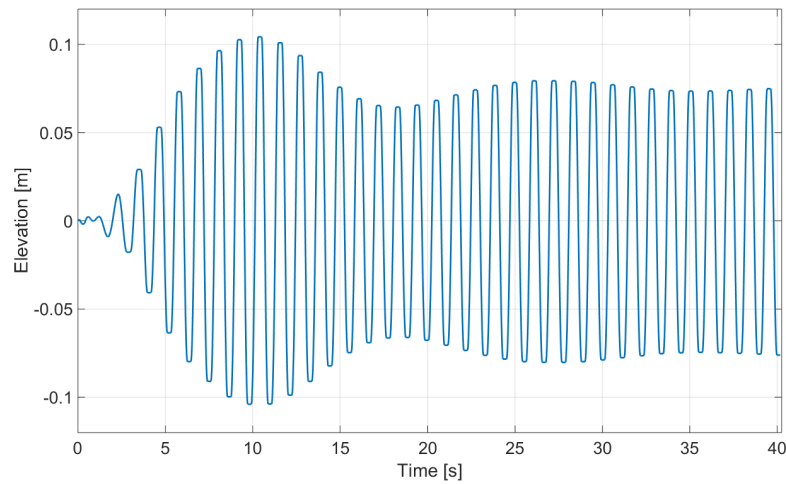
The 3D case study has been simulated in CFD, in order to make a comparison with the linear simulation model. The latching duration has been chosen as 0.205s, matching the linear optimal latching duration, shown in Fig. 3.5. The resulting linear and CFD time traces are shown in Figs. 3.12a and 3.12b, respectively.

The first evident difference is in the transient shape: while the linear simulation shows a monotonic growth towards the steady value, the CFD time series presents an oscillatory behaviour, with a visible maximum and minimum, before stabilizing. Following the transient, the steady amplitude of motion in CFD is 0.074m, smaller than the 0.084m from the linear model. Furthermore, the transient in CFD lasts about 33s, 3 times longer than in the linear simulation, which reaches the steady state in less than 11s. As the amplitude experiences a transient, there is also a transient of the period of motion, shown in Fig. 3.13.

3.6.1.2 2D case



(a) Linear model simulation.



(b) 3D CFD simulation.

Figure 3.12: Constant latching duration control of a sphere of radius 0.125m, with regular wave (height: 0.015m, period: 1.118s) and latching duration of 0.205s.

Sect. 3.5 shows several two-dimensional results that can be compared. Since the hydrodynamic matrices needed for the linear simulations are computable only for 3D geometries, a direct comparison requires the BEM software to simulate an infinitely long cylinder. From a practical point of view, a cylinder is considered infinitely long when a variation of length doesn't produce a variation of response. Indeed, considering progressively longer cylinders, from 0.25m to 2.5m, Fig. 3.14 shows the asymptotic trend of the response amplitude operator (RAO), defined as the magnitude of the transfer function between the surface elevation and the displacement of the body, hence the ratio between the maximum body displacement and wave amplitude.

Therefore, control has been applied to the longest horizontal cylinder in Fig. 3.14 (length of 2.5m), for which the asymptote is reached. The relative improvements, with respect to the unlatched motion, are summarized in Table 3.4. As in Sect. 3.4.4, for the sphere, the actual optimal latching duration is smaller than for the linear approximation, respectively 0.132s and 0.168s. The relative difference in latching duration is about 21.3%, considerably greater than the 3.8% for the sphere. The larger discrepancy for the cylinder is consistent with the higher damping that an infinite long cylinder provides to the system.

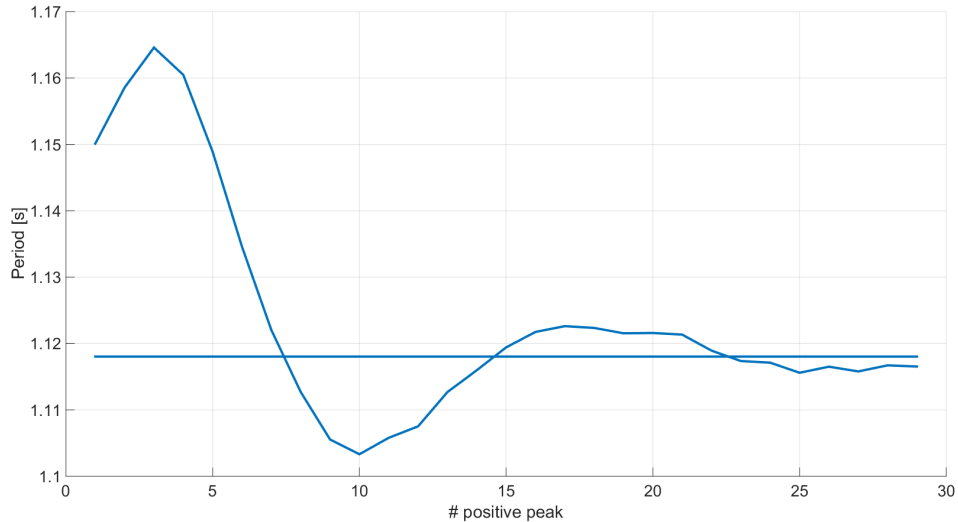


Figure 3.13: Decay of the period of motion of the response in Fig. 3.12b when latching control is applied. The horizontal axis represents the number of peaks from the beginning of latching.

Table 3.4: Comparison between latching performances in linear and CFD simulations. The percentage improvements refer to the unlatched case.

Latching duration [s]	Linear improvement	CFD improvement
0.168	30%	8%
0.145	57%	38%
0.132	62%	40%
0.1146	56%	49%

The presence of viscous losses and nonlinearities causes, for all latching durations, that the improvements in CFD simulations are considerably lower than in simulations with the linear model. Overestimation of the amplitude in the linear model leads to an overoptimistic prediction of the power captured under control. Notwithstanding the importance of accurate prediction of the motion, the key feature to highlight is the different optimal latching duration. While the best linear performance occurs for a latching duration of 0.132s, with an improvement of 62%, the CFD simulation shows a lower improvement of 49% at a smaller latching duration of 0.1146s.

As far as the controller is concerned, the main purpose of the simulation model is to calculate the optimal latching duration for the *real device*. An inaccurate simulation model is not only unable to effectively predict the response, but also points to a latching duration which, even though optimal for the simulation model, is suboptimal for the real device. Since the CFD model is more accurate than the linear model, the main advantage of having the latching control algorithm implemented in CFD is to indicate a latching duration that better suits the real device.

3.7 Conclusions

The controller performance and parameters are closely related to the simulation model and its accuracy. The reliability, as well as the complexity, of a model depends on the ability to describe nonlinear behaviour. The simplest and computationally lightest model is linear, while CFD is able to include all the nonlinearities, but with a huge computational

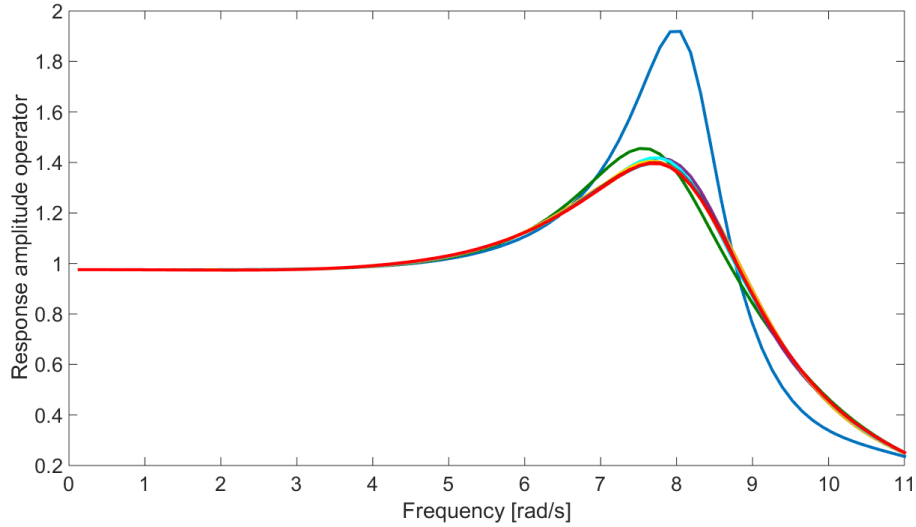


Figure 3.14: Response amplitude operators of horizontal cylinders with 0.125m radius and length ranging from 0.25m to 2.5m.

load. The fact is that nonlinearities are magnified by the control, which exaggerates the amplitude of motion, and applies abrupt forces directly to the device. While linearization may be acceptable with the uncontrolled device, it becomes an unacceptable oversimplification when control is applied. Nevertheless, to date, control has not been applied in a CFD environment. In this work, latching control has been implemented in the CFD open source software OpenFOAM.

Results confirm that basing the latching control calculations on a linear model is misleading and suboptimal. Primarily, the amplitudes calculated by the linear model are too optimistic, leading to an overestimation of power extraction. Moreover, the optimal latching duration indicated by the linear model fails to maximize the performance of the real device. Indeed, the optimal latching duration depends on the natural period, which is not constant and unique, as in the linear approximation. In contrast, the nonlinear natural period is extended by the damping of the system, and varies with the displacement of the device. An optimization tool has been coded in CFD, in order to find the actual optimal latching duration, which is smaller than the latching duration computed using a linear model.

This chapter provides some preliminary results, in order to show the capabilities of the proposed latching control strategy, and to provide some evidence of nonlinear behaviour, under controlled conditions, which help to articulate the need for models more accurate than a linear one. However, a more detailed analysis of nonlinear effects, their relevance under controlled/uncontrolled conditions, and their impact on the operational space and control optimization, is provided in Chapter 6; 3D CFD simulations are extensively used as an accuracy benchmark, in order to evaluate the performance of several nonlinear models, in terms of fidelity and computational time. In particular, a set of such nonlinear models is based on a novel approach for nonlinear Froude-Krylov force calculation, detailed in Chapter 4.

Algebraic nonlinear Froude-Krylov force for heaving point absorbers

4.1 Motivation

Most wave energy converters are described by linear mathematical models, based on the main assumption of small amplitude of motion. Despite the computational convenience, linear models can become inaccurate when large motions occur. Chapter 3 shows how important nonlinearities are, especially under controlled conditions. Chapter 2 argues that nonlinear hydrodynamic models implementing the nonlinear calculation of Froude-Krylov forces are particularly well-performing for devices that are small in horizontal dimension relative to the wavelength. However, existing nonlinear FK models require, for geometries of arbitrary complexity, a spatial discretization and a time-consuming remeshing routine. However, model-based controllers require dynamical system models which can execute in real time. Therefore, this thesis proposes a computationally efficient representation of nonlinear static and dynamic Froude-Krylov forces, valid for any heaving axisymmetric point absorber.

4.2 Introduction

In wave energy applications, the accuracy of the mathematical model of a wave energy device is crucial to simulate the correct motion, and to reliably assess power production, as well as to design model-based controllers, which depend, explicitly or implicitly, on the mathematical model of the system to determine the control parameters. Usually, the model is linear and based on the Cummins equation [145], with hydrodynamic parameters calculated using boundary element methods. Despite the simplicity and the computational convenience of a linear model, the hypotheses under which the linear model is valid are quite restrictive, in particular the assumption of small motion.

As the purpose of a wave energy converter is to exaggerate motion, in order to maximize power production, nonlinearities may become important, and linear models may become relatively inaccurate. While the computational effort usually increases considerably with the number, and the complexity, of nonlinearities included in the model, the gain in accuracy depends on the relevance of each nonlinear effect for a particular device. For heaving point absorbers, the most relevant nonlinear component of the hydrodynamic force is the Froude-Krylov force, which is the integration of the incident pressure over the wetted surface.

While, in a linear approach, the FK force is computed over the constant mean wetted surface, in a nonlinear approach the pressure is integrated over the *instantaneous* wetted

surface, which, for geometry of arbitrary complexity, requires significant additional computational effort, since it implies the use of either a very fine mesh [62] or an automatic remeshing routine for the wetted surface [91]. Such nonlinear solutions return more accurate results, but at a computational price too high to be compatible with the real-time requirement of model-based controllers. This chapter proposes a *computationally efficient* algebraic calculation of the nonlinear FK force, valid for *axisymmetric heaving* point absorbers. Note that such devices normally satisfy the condition of rotational symmetry because they are normally designed to be non-directional (i.e. to be equally efficient at absorbing waves from any direction).

A purely algebraic calculation of nonlinear FK forces is achievable for axisymmetric point absorbers, constrained to move in heave only, as exemplified by the Wavestar device [158], or for axisymmetric point absorbers operating mainly in waves that are long with respect to the device diameter, where the pitch motion is negligible. In the case of combined heave and pitch motion, no algebraic solution exists, and the FK integral has to be solved numerically, as further discussed in Chapter 9.

In this chapter, three different methods are implemented and compared:

- (a) a linear hydrodynamic model,
- (b) a nonlinear Froude-Krylov model, using a remeshing routine to compute the instantaneous wetted surface, and
- (c) a nonlinear Froude-Krylov model, using the algebraic solution of the Froude-Krylov force integral.

The linear, remeshing, and algebraic approaches, are used to simulate the motion of a heaving sphere, with its centroid at the still water level; linear monochromatic waves are considered, in order to highlight nonlinearities deriving from the FK force only, at each individual wave frequency. The chosen geometry is a sphere, which has a cross-sectional area (CSA) varying with the instantaneous draught of the device, and likely to emphasize the nonlinearity of the FK force. In order to maximize power production in each wave condition, latching control is implemented, which is a discrete controller that locks the device motion at its extrema, for an appropriate latching duration, so that the amplitude of motion is exaggerated [119]. As a consequence, the wetted surface experiences greater changes, exaggerating the relevance of nonlinearities. The performance of methods (a), (b), and (c) (linear, remeshing nonlinear FK, and algebraic nonlinear FK, respectively) is compared in terms of amplitude of motion, optimal control parameters, power production, and computational time.

4.3 Modelling approaches

As discussed in Sect. 2.4.2, assuming the fluid to be inviscid, and the flow to be incompressible and irrotational, it is possible to write down the equation of motion, based on the velocity potential, decomposed in FK, diffraction, and radiation components. Several sources of nonlinearities are present: quadratic terms in the Bernoulli equation, nonlinear incident potential flow, and time-varying wetted surface. While the quadratic terms are assumed negligible [32], and only linear waves are considered, the wetted surface is modelled as either constant or variable, leading to a linear or nonlinear representation of Froude-Krylov forces, respectively, resulting in linear and nonlinear Froude-Krylov hydrodynamic models. Radiation and diffraction forces are assumed to be linear in both models: [45] shows that diffraction effects are negligible when the device dimension is considerably smaller than the wave length; likewise, [159] shows that radiation nonlinearities are negligible for floating bodies that are small compared to the wavelength. [32]

implements both nonlinear Froude-Krylov, and nonlinear radiation and diffraction forces, for a heaving point absorber, showing that the response of the device is mainly affected by nonlinear FK forces, while nonlinear radiation and diffraction forces have minor effects on the system dynamics. Furthermore, [91] and [160] use real tank experiments, with the SEAREV device and the Wavestar device, respectively, to validate a nonlinear Froude-Krylov model with a linear radiation and diffraction term, showing a significant improvement in accuracy, with respect to a fully linear model, and good agreement with the experimental measurement.

4.3.1 Linear model

The linear approach assumes a small amplitude and steepness of the wave, thus the potential problem is linearized, and solved around the equilibrium position of the device. Therefore, the mean wetted surface (S_M) is considered for the computation of linear FK forces. Recalling Sect. 2.4.2.1, the equation of motion in heave (z), with linear hydrodynamics, is:

$$M\ddot{z} = \underbrace{-Gz}_{F_{FKst}} - \underbrace{\int_{-\infty}^{\infty} K_{ex}(t-\tau)\eta(0,0,\tau)d\tau}_{F_{ex}=F_{FKdy}+F_D} - \underbrace{A_{\infty}\ddot{z} - \int_{-\infty}^{\infty} K_{rad}(t-\tau)\dot{z}(\tau)d\tau}_{F_R} - F_{PTO} \quad (4.1)$$

where:

- F_{FKst} is linearly described by the hydrostatic stiffness G ;
- F_{ex} is represented by the convolution product between the excitation impulse-response function (IRF) K_{ex} and the free-surface elevation $\eta(x, y, \tau)$ in the origin;
- F_R is represented by the added mass A_{∞} and the convolution product between the radiation IRF K_R and the velocity \dot{z} , based on Cummins equation [145];
- F_{PTO} represents the PTO force.

The added mass and the impulse response functions are calculated by the time domain BEM software ACHIL3D [161]. The radiation convolution term, which is computationally expensive to compute directly, is replaced by its state space representation [148].

4.3.2 Nonlinear Froude-Krylov force model

While the linear model uses the constant mean wetted surface S_M , the nonlinear FK model computes the Froude-Krylov forces, considering the exact instantaneous wetted surface $S(t)$, namely integrating the fluid pressure over the actual submerged portion of the body, as it moves through the water:

$$F_{FK} = F_{FKst} + F_{FKdy} = F_g - \iint_{S(t)} (p_{st} + p_{dy}) n_z dS \quad (4.2)$$

where n_z is the vertical component of the normal unity vector \mathbf{n} , since F_{FK} is computed only in the heave direction. Note that both static and dynamic Froude-Krylov forces depend on the instantaneous wetted surface, which depends both on the incident wave elevation *and* the displacement of the body. The remaining force components of (4.1) are computed linearly: the radiation force is described as in the Cummins equation, while the diffraction force is represented by the convolution product between the diffraction impulse-response function (K_D), and the free surface elevation η :

$$F_D = - \int_{-\infty}^{\infty} K_D(t - \tau) \eta(\tau) d\tau \quad (4.3)$$

While, in the linear model, the diffraction force is computed together with the dynamic Froude-Krylov force, by means of the excitation IRF (K_{ex}), in the nonlinear FK model, the diffraction force is calculated independently through the diffraction IRF (K_D).

For an arbitrary device geometry, the computation of the integral in (4.2) is performed by discretizing the surface of the body with a finite mesh, and summing up the forces generated by the pressure acting on the area of each plane panel. At each time step, as the body moves, an automatic (computationally expensive) routine remeshes the partially submerged panels around the free surface, and updates the instantaneous wetted surface. A detailed description of the remeshing routing can be found in [91].

In contrast, this chapter shows an algebraic solution to the pressure integral in (4.2), valid for any axisymmetric geometry, subject to deep water linear waves, achieving the same results of a mesh-based nonlinear FK model, but with considerable computational savings, as discussed in Sect. 4.6. Details of the pressure integral calculations are provided in Sect. 4.4.

4.4 Algebraic solution

The algebraic calculation of the integral in (4.2) requires the explicit definition of the pressure p , the infinitesimal surface element $\mathbf{nd}S$, and the limits of integration. The pressure is obtained by applying Airy's wave theory for mono-directional waves, in infinite water depth conditions:

$$p(x, z, t) = \rho g a e^{kz} \cos(\omega t - kx) - \rho g z \quad (4.4)$$

where x is the direction of wave propagation, z is the vertical direction (positive upwards), a is the wave amplitude, k the wave number, and ω the wave frequency.

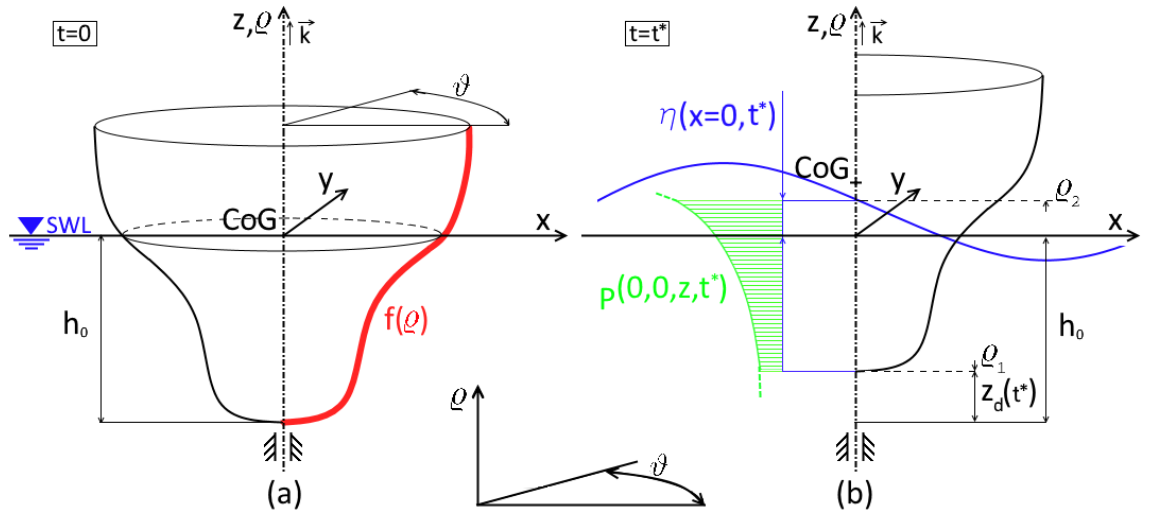


Figure 4.1: Axisymmetric heaving device with generic profile $f(\rho)$: The figure on the left shows the rest position, with the center of gravity at the still water level (SWL) and draft h_0 ; the figure on the right shows the free surface elevation η , and the device displacement z_d after a time t^* . The pressure is integrated over the wetted surface, between ρ_1 and ρ_2 .

As shown in Fig. 4.1, the geometry is assumed to be axisymmetric, with a fixed vertical axis, so that it is possible to describe its surface in parametric cylindrical coordinates:

$$\begin{cases} x(\varrho, \vartheta) = f(\varrho) \cos \vartheta \\ y(\varrho, \vartheta) = f(\varrho) \sin \vartheta \\ z(\varrho, \vartheta) = \varrho \end{cases}, \quad \vartheta \in [0, 2\pi) \wedge \varrho \in [\varrho_1, \varrho_2] \quad (4.5)$$

Table 4.1 shows some examples of profiles of revolution $f(\varrho)$, using cylindrical coordinates in (4.5).

Considering the canonical basis, given by radial and tangent unit vectors, \mathbf{e}_ϱ and \mathbf{e}_ϑ , respectively, the infinitesimal surface element $\mathbf{n}dS$ becomes:

$$\mathbf{n} dS = \mathbf{n} \|\mathbf{e}_\varrho \times \mathbf{e}_\vartheta\| d\varrho d\vartheta = \mathbf{n} f(\varrho) \sqrt{f'(\varrho)^2 + 1} d\varrho d\vartheta \quad (4.6)$$

Finally, the point absorber is constrained to move in heave only (along the unit vector \mathbf{k} of the z -axis); therefore, only the vertical component (p_z) of the pressure is taken into account:

$$p_z = p \cdot \langle \mathbf{n}, \mathbf{k} \rangle = \left\langle \frac{\mathbf{e}_\varrho \times \mathbf{e}_\vartheta}{\|\mathbf{e}_\varrho \times \mathbf{e}_\vartheta\|}, \mathbf{k} \right\rangle = p \cdot \frac{f'(\varrho)}{\sqrt{f'(\varrho)^2 + 1}} \quad (4.7)$$

Combining equations (4.4) to (4.7) with (4.2), the magnitude of the Froude-Krylov force in the vertical direction becomes:

$$\begin{aligned} F_{FK_z} &= \int_0^{2\pi} \int_{\varrho_1}^{\varrho_2} p(x(\varrho, \vartheta), z(\varrho, \vartheta), t) f'(\varrho) f(\varrho) d\varrho d\vartheta \\ &= \int_0^{2\pi} \int_{\varrho_1}^{\varrho_2} (\rho g a e^{k\varrho} \cos(\omega t - k f(\varrho) \cos \vartheta) - \rho g \varrho) f'(\varrho) f(\varrho) d\varrho d\vartheta \end{aligned} \quad (4.8)$$

Referring again to Fig. 4.1, with h_0 the draft at equilibrium, $z_d(t)$ the vertical displacement of the body, and $\eta(t)$ the free surface elevation of the undisturbed incident flow at $x = 0$, the instantaneous wetted surface is defined by the following limits of integration:

$$\begin{cases} \varrho_1 = z_d(t) - h_0 \\ \varrho_2 = \eta(t) \end{cases} \quad (4.9)$$

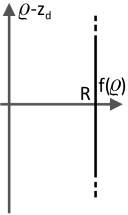
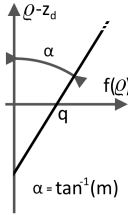
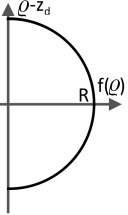
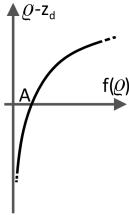
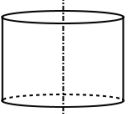
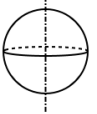
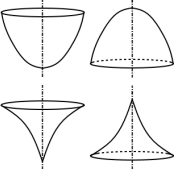
The expression for the pressure in (4.4) is still not directly integrable because of the x -dependence of the argument of the cosine. Two solutions are available:

- The long wave approximation, which assumes that the wave length λ is considerably longer than the characteristic dimension of the device, so the dependence of the pressure on x is negligible, or
- a McLaurin expansion of the cosine term.

In Sect. 4.6.1 it is shown that, while both methods are accurate for long waves, only the McLaurin expansion method (using just three terms of the expansion) is able to return accurate results, for all wave conditions.

The integral in (4.8) can be solved for any profile $f(\varrho)$, defined either as a polynomial function of order zero (cylinder), one (cone), or higher, as an arc of a circumference (portion of a sphere), or as an exponential. Table 4.1 summarizes results, for a variety of common geometries, under the long wave approximation.

Table 4.1: Solution of the integral of the vertical component of static and dynamic pressure under the long wave approximation for axisymmetric devices with different profiles of revolution: vertical line (cylinder), oblique line (cone), arc of circumference (sphere), and exponential profile.

Vertical line	Oblique line	Arc of circumference	Exponential profile
$f(\varrho) = R$ 	$f(\varrho) = m(\varrho - z_d) + q$ 	$f(\varrho) = \sqrt{R^2 - (\varrho - z_d)^2}$ 	$f(\varrho) = Ae^{B(\varrho - z_d)}$ 
Cylinder		R	
	$f(\varrho)$	R	
	$\int_0^{\varrho_2} \int_0^{\varrho_1} p_{st_z} d\varrho d\vartheta$	$-\pi R^2 \rho g \varrho_1$	
	$\int_0^{\varrho_2} \int_0^{\varrho_1} p_{dy_z} d\varrho d\vartheta$	$\pi R^2 \rho g a e^k \varrho_1 \cos \omega t$	
Cone		$m(\varrho - z_d) + q$	
	$f(\varrho)$	$m(\varrho - z_d) + q$	
	$\int_0^{\varrho_2} \int_0^{\varrho_1} p_{st_z} d\varrho d\vartheta$	$-2\pi \rho g m \left[m \frac{\varrho^3}{3} + (q - mz_d) \frac{\varrho^2}{2} \right]_{\varrho_1}^{\varrho_2}$	
	$\int_0^{\varrho_2} \int_0^{\varrho_1} p_{dy_z} d\varrho d\vartheta$	$-\frac{2\pi}{k} \rho g a m^2 \cos \omega t \left[\left(\frac{q}{m} - \frac{1}{k} - z_d + \varrho \right) e^{k\varrho} \right]_{\varrho_1}^{\varrho_2}$	
Sphere		$\sqrt{R^2 - (\varrho - z_d)^2}$	
	$f(\varrho)$	$\sqrt{R^2 - (\varrho - z_d)^2}$	
	$\int_0^{\varrho_2} \int_0^{\varrho_1} p_{st_z} d\varrho d\vartheta$	$-2\pi \rho g \left[\frac{\varrho^3}{3} + z_d \frac{\varrho^2}{2} \right]_{\varrho_1}^{\varrho_2}$	
	$\int_0^{\varrho_2} \int_0^{\varrho_1} p_{dy_z} d\varrho d\vartheta$	$-\frac{2\pi}{k} \rho g a \cos \omega t \left[\left(z_d + \frac{1}{k} - \varrho \right) e^{k\varrho} \right]_{\varrho_1}^{\varrho_2}$	
Exponential profile		$Ae^{B(\varrho - z_d)}$	
	$f(\varrho)$	$Ae^{B(\varrho - z_d)}$	
	$\int_0^{\varrho_2} \int_0^{\varrho_1} p_{st_z} d\varrho d\vartheta$	$-\pi \rho g A^2 \left[\left(\varrho - z_d - \frac{1}{2B} \right) e^{2B(\varrho - z_d)} \right]_{\varrho_1}^{\varrho_2}$	
	$\int_0^{\varrho_2} \int_0^{\varrho_1} p_{dy_z} d\varrho d\vartheta$	$2\pi \rho g \frac{A^2 B}{2B+k} a e^{-2Bz_d} \cos \omega t \left[e^{(2B+k)\varrho} \right]_{\varrho_1}^{\varrho_2}$	

4.5 Case study

The relevance of nonlinear Froude-Krylov forces, and hence the difference between linear and nonlinear FK models, becomes important when the instantaneous wetted surface significantly differs from the mean wetted surface. Two major conditions for this situation are as follows:

- (a) the device has a nonuniform cross sectional area (CSA), and
- (b) the device does not behave as a wave follower, namely its displacement z_d is significantly different from the wave surface elevation η .

Note that condition (b) results in significant variations in wetted surface of the WEC. Therefore, as shown in Fig. 4.2, the device is chosen to be a sphere of 2.5m radius, with the center of gravity coincident with the geometric center, and a natural period of 3.17s. The dimension of the sphere is chosen to be comparable with common existing wave energy converters, such as the Wavestar WEC [158]. The device is constrained to heave only, and is tethered to the seabed with a linear damper, which acts as a PTO, in combination with a latching mechanism.

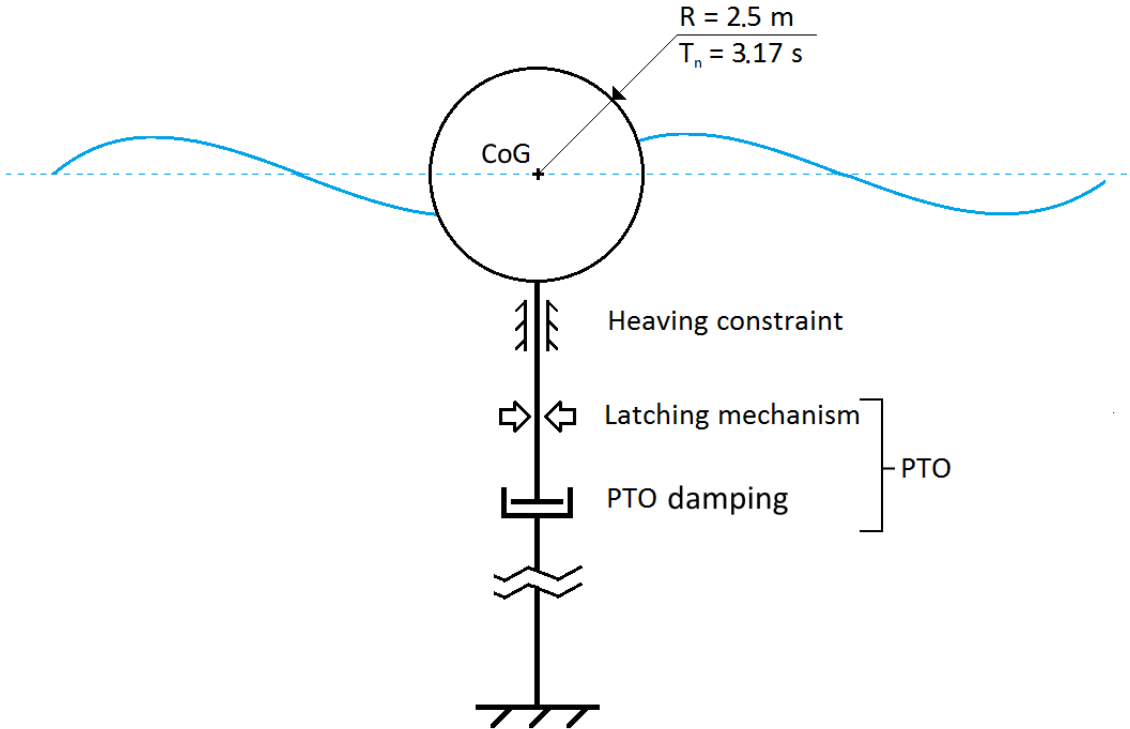


Figure 4.2: Case study: spherical device (radius $R = 2.5\text{m}$, 3.17s natural period T_n) constrained to heave with PTO linear damper and latching mechanism, subject to deep water linear waves.

The hydrodynamic coefficients have been calculated using the boundary element method (BEM) solver WAMIT [162]. In order to avoid significant errors, and to achieve high accuracy in the definition of the hydrodynamic coefficients, a very large number of both panels (1600), and wave frequencies ω (600, equally spaced, with a 0.03rad/s step) have been used. As a comparison, note that [111] performs a convergence study for the same geometry (half submerged sphere of 5m diameter), using 140 and 300 panels. The resulting added mass and radiation damping coefficients are shown in Fig. 4.3.

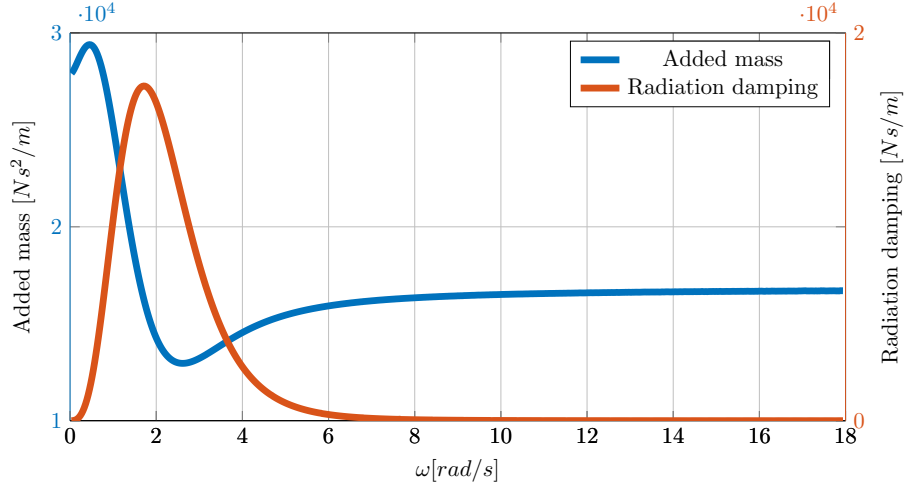


Figure 4.3: Added mass and radiation damping for the heaving floating sphere of 2.5m radius, using the boundary element method solver WAMIT [162].

Table 4.2: Wave conditions: Linear monochromatic deep water waves according to Airy’s theory. Wave lengths have been normalized with respect to the buoy diameter $D = 5m$

Wave periods [s]	T_w	3	4	5	6	7	8	9	10
Normalized wave lengths	λ/D	2.8	5.0	7.8	11.2	15.4	20.0	25.2	31.2
Wave heights [m]	H_w								
for $H_w/\lambda = 0.006$		0.08	0.15	0.23	0.34	0.46	0.60	0.76	0.94
for $H_w/\lambda = 0.012$		0.17	0.30	0.47	0.67	0.92	1.20	1.52	1.87
for $H_w/\lambda = 0.018$		0.25	0.44	0.69	1	1.36	1.78	2.25	2.78

In order to focus only on nonlinearities related to FK forces, linear waves based on Airy’s theory are used, assuming a small steepness H_w/λ [123], defined as the ratio between the wave height H_w , and the wavelength λ . Waves are chosen to be monochromatic, in order to analyze the response of the device at each different frequency independently, with wave periods T_w chosen to cover common sea states experienced by a point absorber wave energy device in deep water conditions [158]. Since FK nonlinearities are caused by changes in the instantaneous wetted surface, which depends on the intersection between the free surface elevation and the body position, the higher the wave steepness, the greater the relevance of FK nonlinearities. Therefore, three different wave steepness indices are considered (0.006, 0.012, and 0.018), where 0.018, the highest steepness allowed in linear wave theory [123], generates the most significant nonlinear response. The comparison is carried out at constant steepness, for different wave periods, in order to have the same (scaled) wave profile and, consequently, a fair comparison. The resulting wave conditions are summarised in Table 4.2.

A brief introduction to optimal complex conjugate control and latching control of a wave energy converter is now outlined. The main objective of a WEC is to maximize the energy captured by the PTO system. Considering the force-to-velocity model of a WEC, in the frequency domain, and for a linear system, [45] obtains:

$$\frac{V(\omega)}{F_{ex}(\omega) + F_{PTO}(\omega)} = \frac{1}{Z_i(\omega)}, \quad (4.10)$$

where $Z_i(\omega)$ is the intrinsic impedance of the system, $V(\omega)$ is the device velocity, $F_{ex}(\omega)$ is the wave excitation force, and $F_{PTO}(\omega)$ is the control force. The condition for optimal energy absorption is derived by [45], and is referred to as *complex conjugate control*, since

the external impedance added by the PTO is required to be the complex conjugate of the intrinsic impedance:

$$Z_{PTO}(\omega) = Z_i^*(\omega) \quad (4.11)$$

Meeting the condition in (4.11) is equivalent to realizing an optimal velocity profile as

$$V^{opt}(\omega) = \frac{F_{ex}(\omega)}{2R_i(\omega)}, \quad (4.12)$$

where $R_i = 1/2(Z_i + Z_i^*)$ is the real part of Z_i . As a consequence, R_i is a real function, so the velocity profile is in phase with the excitation force. Therefore, the optimal complex conjugate control imposes a condition over both the amplitude *and* the phase of the velocity. A simpler approach is a *phase-only* control strategy, such as latching, which pursues only phase matching between the velocity and the exciting force, without considering the amplitude. Latching is a discrete example of phase control, meaning that an on/off PTO force is applied, usually by means of a braking system, in order to eliminate align maxima of the velocity and the incoming wave excitation force.

Therefore, a latching control system is implemented to improve the power capture of the WEC, in each wave condition. Moreover, especially at frequencies far from resonance, the latching control system prevents the device behaving like a wave follower, thus exaggerating the amplitude of motion and, consequently, FK nonlinearities [92]. Latching control is a common solution for point absorbers, thanks to its straightforward implementation in a real device and its good power capture performance [119, 115].

As discussed in Chapter 3, the performance of the latching control strategy is very sensitive to the choice of the latching duration, which is not trivial when nonlinearities are significant. In the nonlinear FK model, since the cross sectional area changes during the motion of the WEC, the hydrostatic stiffness and, consequently, the damped natural period are not constant. Moreover, it has already been shown that, even in the linear case, an algebraic solution to the power optimization problem of both the PTO damping coefficient (B_{PTO}) and the latching duration (T_L) is not possible [163, 142]. Therefore, the optimal pair of control parameters, T_L and B_{PTO} , that maximizes the power output, is calculated iteratively for each wave condition. Since the optimization procedure uses the results of the nonlinear FK model simulations, such a latching control strategy effectively becomes a nonlinear model-based control.

4.6 Validation and results

4.6.1 Validation of the Froude-Krylov force calculation

It is first necessary to evaluate the correctness of the algebraic results of the pressure integral in (4.2). The static part of the FK integral can be validated against an alternative method to calculate the nonlinear static FK force, namely considering the balance between the weight of the device, and the weight of the volume of fluid V_{wet} , instantaneously displaced by the device in calm water. As expected, these two methods return exactly the same results.

On the other hand, the static FK force calculated with the remeshing routine approach is about 2% less than that calculated with the algebraic approach. The main reason for the difference is the actual geometry simulated: while the algebraic solution is based on an ideal sphere, the remeshing routine model is based on a discretized geometry, which rounds down the wetted surface and, consequently, V_{wet} . In fact, the nonlinear stiffness approach, based on the same discretized geometry, gives better agreement with the remeshing approach. Note that while the non-ideal geometric approximation is assessable only for the static part, it affects both the static and the dynamic FK forces. Finally, note that the meshing

Table 4.3: Percentage difference between the results of the remeshing routine approach and the algebraic dynamic Froude-Krylov force, estimated using either the long wave or the McLaurin approximation, for different wave steepness indices (0.006, 0.012, 0.018).

Steepness:		Long wave approximation			McLaurin approximation		
		0.006	0.012	0.018	0.006	0.012	0.018
T_w [s]	λ/D						
3	2.8	19.7%	20.0%	20.3%	0.9 %	1.2 %	1.4 %
4	5.0	10.7%	11.0%	11.2%	1.3 %	1.4 %	1.5 %
5	7.8	5.7%	5.9%	5.9%	1.6 %	1.5 %	1.5 %
6	11.2	3.5%	3.6%	3.6%	1.7 %	1.7 %	1.7 %
7	15.4	2.5%	2.6%	2.8%	1.6 %	1.7 %	1.8 %
8	20.0	2.1%	2.2%	2.4%	1.8 %	1.9 %	2.1 %
9	25.2	1.9%	2.1%	2.3%	1.8 %	2.0 %	2.2 %
10	31.2	1.8%	2.0%	2.2%	1.8 %	2.0 %	2.2 %

and BEM software (Achil3D) used for the mesh-based approach were not available at the time of this study, so it was not possible to perform a convergence study on the geometry discretization. However, it has to be expected that the 2% error would decrease if a finer mesh were used.

The algebraic dynamic FK force can be calculated using either the long wave approximation or the McLaurin expansion, as discussed in Sect. 4.4. Within the expansion, all the sine terms in equation (4.13) integrate to zero, so only the cosine terms contribute to the algebraic solution. Using only the first three terms (i.e. the long wave approximation, plus a further two terms of the expansion), an acceptable accuracy is achieved for all wave conditions in Table 4.2, including the shortest wave. While the results in Table 4.1 refer to the long wave approximation, equation (4.13) shows the algebraic solution of the dynamic FK integral for a sphere, using the first three terms of the McLaurin approximation.

$$\begin{aligned}
 F_{FK_{dyz}}^{Mc} = & \int_0^{2\pi} \int_{\varrho_1}^{\varrho_2} (\rho g a e^{k\varrho} (\cos \omega t + k f(\varrho) \cos \vartheta \sin \omega t - \frac{k^2 f(\varrho)^2 \cos \vartheta^2}{2} \cos \omega t) f'(\varrho) f(\varrho) d\varrho d\vartheta = \\
 & - \frac{2\pi}{k} \rho g a \cos \omega t \left[e^{k\varrho} (z_d + \frac{1}{k} - \varrho) \right]_{\varrho_1}^{\varrho_2} + \\
 & - \frac{\pi}{2} k \rho g a \cos \omega t \left[e^{k\varrho} (z_d R^2 - z_d^3 + \frac{R^2 - 3z_d^2}{k} - \frac{6z_d}{k^2} - \frac{6}{k^3}) \right]_{\varrho_1}^{\varrho_2} + \\
 & - \frac{\pi}{2} k \rho g a \cos \omega t \left[e^{k\varrho} (\varrho (3z_d^2 - R^2 + \frac{6z_d}{k} + \frac{6}{k^2}) - \varrho^2 (3z_d + \frac{3}{k}) + \varrho^3) \right]_{\varrho_1}^{\varrho_2}
 \end{aligned} \tag{4.13}$$

Table 4.3 shows the percentage difference between the dynamic FK force, calculated using the two algebraic methods (long wave and McLaurin approximations), and the remeshing routine approach. As for the static FK force, the dynamic force is always smaller in the remeshed approach, mainly because of the discretized geometry approximation. For long waves, the two algebraic methods significantly overlap, and the small difference with the remeshing approach is mainly due to the geometric approximation. Conversely, when short waves are considered, only the McLaurin method is effective. Finally, in addition to a dependence on the wave length, the relative error slightly increases when the wave steepness increases.

4.6.2 Results

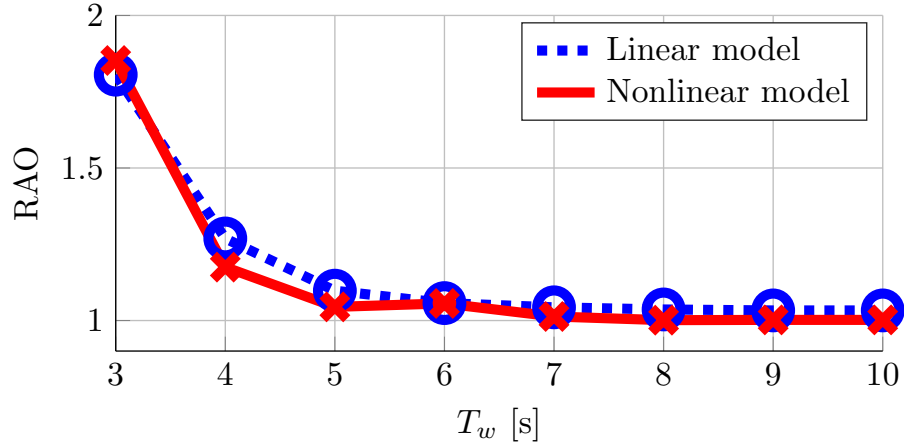
Section 4.6.1 shows that, notwithstanding the differences introduced by the geometry approximation, the results of the algebraic approach are essentially the same as the remeshing routine approach. Table 4.4 shows that the computational time of the algebraic nonlinear model is similar to the linear model, while the remeshing routine is several times slower. It is important to highlight that the remeshing approach is coded in Fortran, while the linear and algebraic models are implemented in Matlab, which is between one and two orders of magnitude slower than lower-level coding languages, such as C or, indeed, Fortran [164]. Despite being written in a slower language, the fact that the algebraic approach still computes much faster than the remeshing approach further supports its merit as a computationally efficient method.

Table 4.4: Normalized computational time of each nonlinear FK model relative to the linear model.

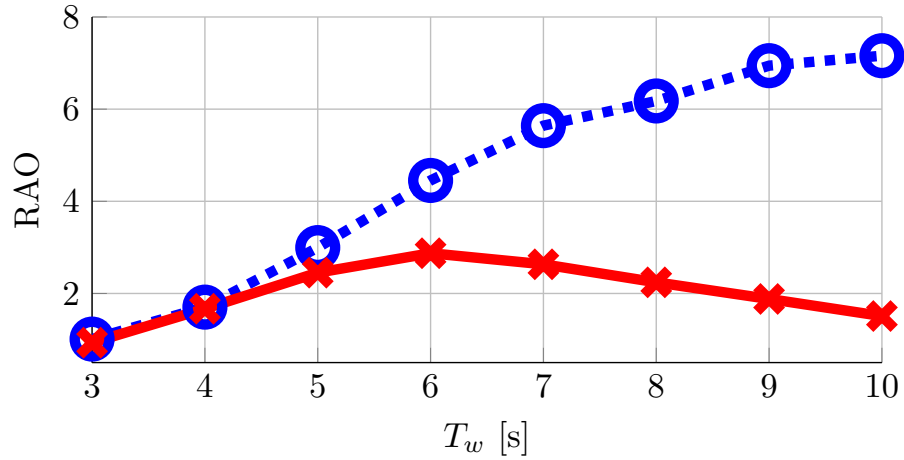
		Normalized computational time
Algebraic method	Long wave approximation	1.35
	McLaurin approximation	1.65
Remeshing method		5.15

Hereafter, referring to Table 4.2, only the highest wave steepness (0.018) is considered to compute the response of the device, as it generates the most significant nonlinear behaviour. The difference in the amplitude of motion between the linear and nonlinear FK models is analyzed through the response amplitude operator (RAO), which is defined as the ratio between the peak response of the device and the wave amplitude. Figure 4.4a shows that, without the controller, the responses of the linear and nonlinear FK models are very similar. The motion of the device is amplified at frequencies close to resonance, though the corresponding wave heights are small. On the other hand, the device acts like a wave follower for larger waves at frequencies far from resonance. In both cases, the variation of the instantaneous wetted surface is limited, therefore nonlinearities have little relevance. In contrast, the influence of nonlinearities is enhanced when latching control increases the relative motion between the device and the wave. Consequently, as shown by the RAO in Fig. 4.4b, the linear model significantly overestimates the response of the device for large wave periods, when the wave height is larger.

Comparing Figs. 4.4a and 4.4b, it is evident that the impact of nonlinear FK forces is enhanced by the control strategy since, as shown in Fig. 4.5, the controller magnifies the amplitude of motion with respect to the free surface elevation and, as a consequence, exaggerates the change in instantaneous wetted surface. Without control, the linear and nonlinear models significantly overlap in performance, since the relative displacement is small. Conversely, when control is applied, the relative displacement is augmented, and the linear model diverges from the nonlinear one. Nevertheless, the finite geometry of the floater imposes a physical limit, since a relative displacement larger than the draught would mean that the body is completely out of the water. In such a situation, all hydrodynamic forces should be null, so the body is pulled back into the water by gravity. On the contrary, all hydrodynamic forces in the linear model are computed with respect to the mean wetted surface, and are therefore unrealistic when large motions occur. In contrast, the nonlinear FK model takes into account the instantaneous wetted surface, giving realistic FK forces, while the diffraction force is calculated as in the linear model. As a result, the linear model crosses the physical threshold (relative displacement larger than the draught), and it becomes unrealistic for a wave much smaller than for the nonlinear FK model. Note that it is physically possible for the device to clear the water, due to inertial effects, i.e.



(a) Uncontrolled conditions.



(b) Controlled conditions.

Figure 4.4: Response amplitude operator (RAO) of linear and nonlinear models, (a) without and (b) with latching control.

the residual velocity the body has when clearing the water.

The relative comparison between linear and nonlinear models strongly depends on the device geometry. In the case of the sphere, the nonlinear FK forces are smaller than the linear FK forces, because the area of the intersection, between the instantaneous wetted surface and the free surface elevation, is always smaller than the CSA at the still water level. If a cylinder were considered, nonlinear and linear FK forces would be essentially the same [92]. Conversely, if the CSA increases as the device moves away from the mean position, the nonlinear FK forces would be larger than the linear forces. However, in general, all existing point absorbers have a diameter which decreases with draft, and the vast majority are broadly spherical or cylindrical. In general, if the area increases with draft, the normal to the surface would be upwards; eventually, the normal must change sign and point downwards as the draft increases. The consequence is that the Froude-Krylov forces on the surface would partially cancel out, generating a small resulting force on the device. Clearly such a situation is not suitable for floating wave energy converters, since the main objective is to excite the body, rather than stabilize it.

For each wave condition, the optimal latching control parameters B_{PTO} and T_L are defined iteratively, facilitated by the low computational cost of both models. Figure 4.6 shows an example of the power graph used to identify the point of maximum power generation. The resulting optimal profiles of the control parameters, for each wave condition,

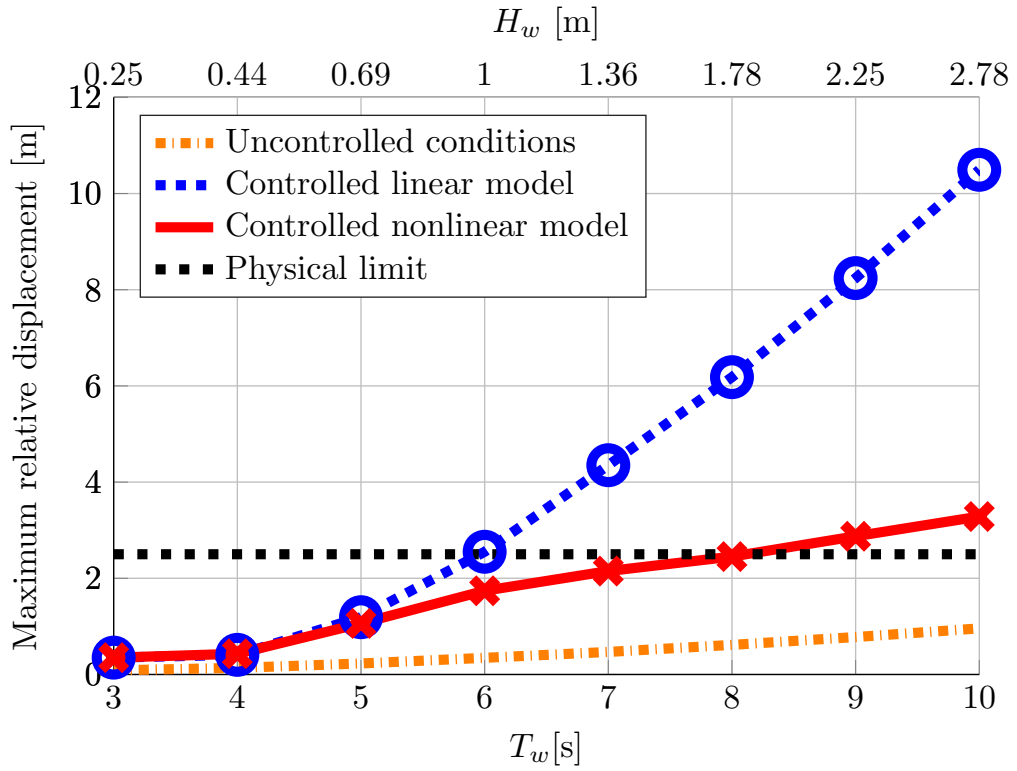


Figure 4.5: Maximum relative displacement between the vertical displacement of the floater and the free surface elevation for linear and nonlinear model under uncontrolled and controlled conditions. The physical limit represents the relative displacement equal to the draft.

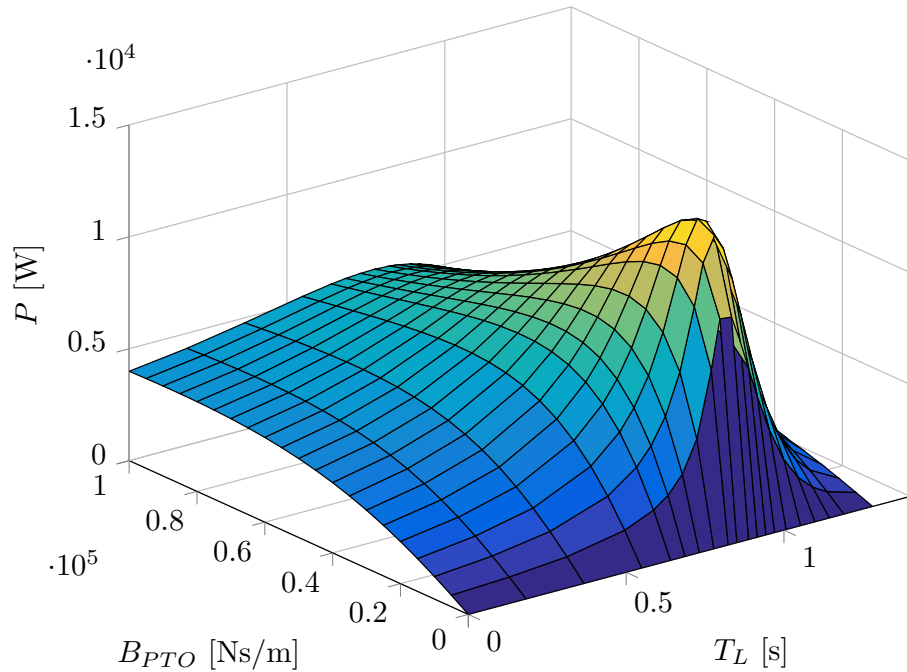


Figure 4.6: Power, P , generating using different control parameters (damping coefficient B_{PTO} and latching duration T_L), using the nonlinear model for the wave with period T_w of 5s.

are presented in Figs. 4.7 and 4.8. In the linear model, the progressive reduction of the optimal damping, as T_w increases, depends on the reduction in the radiation damping term of the sphere at low frequencies [45]. Conversely, the optimal B_{PTO} for the nonlinear model increases. As a consequence, the damped natural period T_d of the nonlinear model is longer, and the optimal latching duration is consequently shorter. Figure 4.8 presents the algebraic optimum for the nonlinear model (dash-dot red line), computed using (3.11) with the optimal B_{PTO} from Fig. 4.7. Note that the natural period T_n , used in (3.4), is accurate only for small amplitudes of motion, since it is calculated from the mean cross-sectional area. On the other hand, the variations in instantaneous wetted surface considered in the nonlinear model result in a longer natural period and, consequently, a shorter optimal latching duration (solid red line).

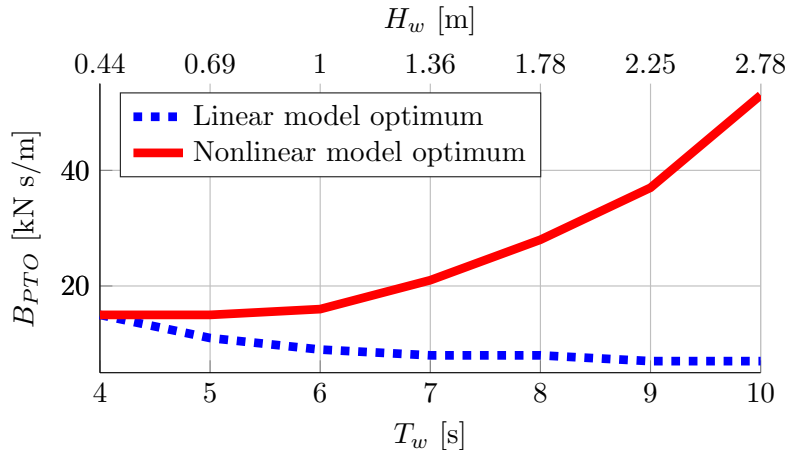


Figure 4.7: Optimal profiles of PTO damping coefficients B_{PTO} for linear and nonlinear models, for waves with period T_w .

Figure 4.9 shows the mean power extracted by the WEC using the optimal control parameters. Consistent with the RAO in Fig. 4.4b, the linear model overestimates the motion of the wave energy device, leading to an overly optimistic power production assessment.

4.7 Conclusions

Previous work [32, 92] shows that nonlinear Froude-Krylov forces are likely to be the dominant source of nonlinearities for heaving point absorbers with non-uniform cross sectional area, under controlled conditions. This chapter proposes an algebraic formulation for nonlinear static and dynamic FK forces, valid for any axisymmetric heaving wave energy converter. An alternative method using a remeshing of the surface is used to validate the algebraic approach; despite considerable computational savings, the nonlinear FK forces are computed to be virtually identical to the remeshing method.

From the comparison between linear and algebraic nonlinear models, applied to a spherical point absorber, subject to linear regular waves, the following conclusions are drawn:

- Nonlinear FK forces are relevant only when the instantaneous wetted surface experiences substantial variation. Under latching control conditions, the amplitude of motion is exaggerated, and the behavior as a wave follower is prevented. Other control philosophies (apart from latching) might likewise exaggerate the body motion relative to the free surface elevation, causing significant changes in the nonlinear FK forces [156].

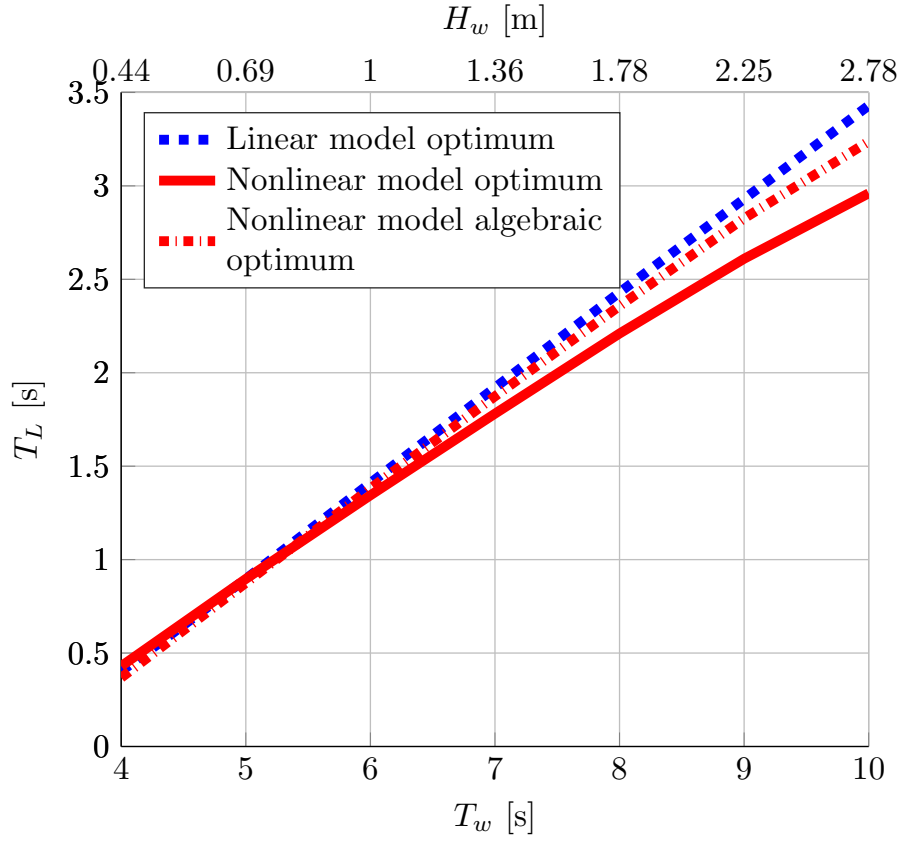


Figure 4.8: Optimal profiles of latching durations T_L for linear and nonlinear models, for waves with period T_w . The algebraic optimum for the nonlinear model refers to the application of (3.4) with the optimal damping in figure 4.7.

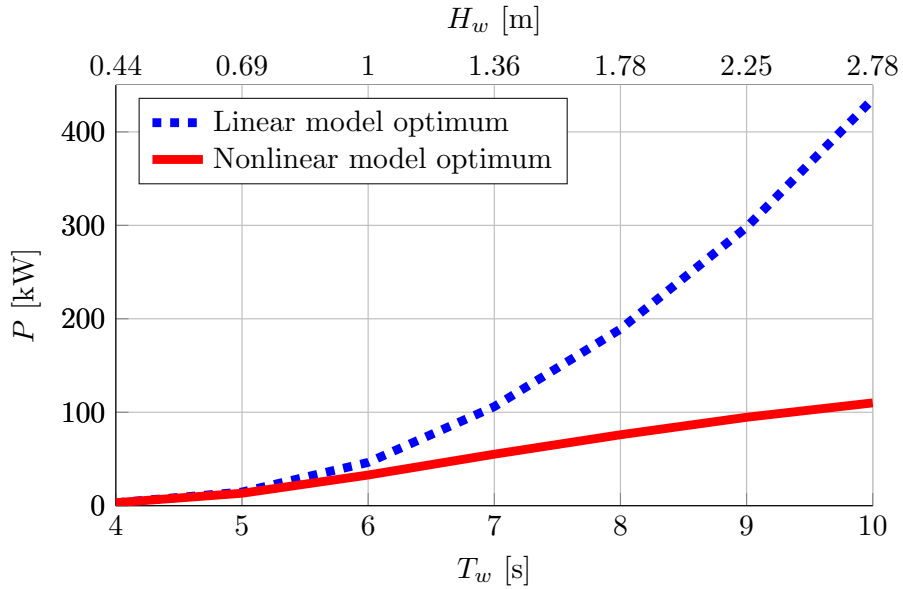


Figure 4.9: Optimal power extracted using linear and nonlinear models.

- Nonlinearities affect the choice of optimal latching control parameters: the optimal B_{PTO} , according to the nonlinear model, is considerably higher than the one computed with the linear model. Furthermore, the damped natural period is longer in the nonlinear model, due to both higher damping and changes of the instantaneous

cross sectional area, so the optimal latching duration T_L is smaller.

- The linear model leads to an overly optimistic power production assessment.

Comparing heaving point absorbers and oscillating wave surge converters

5.1 Motivation

Hydrodynamic nonlinearities are first and foremost device-specific, as discussed in Chapter 2. The construction of parsimonious models requires the modelling, in a computationally efficient way, of only relevant nonlinearities, so that the increase in complexity is justified by a significant gain in accuracy. Even though the relative relevance of a particular nonlinear effect is highly dependent on the application, operational conditions, and the type of control applied, the main driving factor is the operating principle of the device, hence the way it interacts with the incoming wave. Two of the most common modes of oscillation of single degree-of-freedom wave energy converters are heave and surge, which are exploited, respectively, by heaving point absorbers (HPAs), and oscillating wave surge converters (OWSCs). This chapter purports to discuss the major hydrodynamic differences between HPAs and OWSCs, taking into account nonlinear static and dynamic Froude-Krylov forces, and viscous drag forces, in order to highlight their very different contributions in building up the total hydrodynamic force.

5.2 Introduction

Wave energy converters are often classified based on the operating principles they use to absorb energy from ocean waves. Such operating principles refer to the modes in which the device oscillates, due to the action of the waves. Two of the most common modes are heave and surge, which are exploited, respectively, by heaving point absorbers and oscillating wave surge converters.

Due to differences in geometry, characteristic dimension, and degree of freedom (DoF), very different fluid-structure interaction mechanisms govern the motion of such devices; therefore, major hydrodynamic differences exist between HPAs and OWSCs [165]. Nevertheless, the same linear model structure is commonly utilized, in order to define a mathematical model for the physical system. Unfortunately, the linearising assumption of small motion is critically challenged when a control strategy is included which, with the aim of increasing the power capture, magnifies the motion of the device, consequently increasing the relevance of nonlinearities.

Given different hydrodynamic characteristics of HPAs and OWSCs, different nonlinear forces may be less or more relevant, depending on the device operating principle. Likewise, scaling properties of such nonlinear forces may be different, according to the type of device. Scalability of nonlinear forces is particularly important when tests with prototypes are

used to predict the performance of the device at full scale. Candidates, to incorporate significant nonlinear effects into the WEC model, appear to be Froude-Krylov forces, and viscous drag forces, while the linear formulation of diffraction and radiation forces is normally assumed to be accurate enough, especially when the characteristic length of the device is much smaller than the wave length [45, 159].

Chapter 4 provides a method for computing nonlinear FK forces for HPAs, which can be easily extended to OWSCs, as shown in Sect. 5.3. Viscous drag forces are usually included in the model by means of a Morison-like term [166, 31]. This chapter attempts to develop *parsimonious* hydrodynamic models for HPAs and OWSCs by combining, as appropriate, linear and nonlinear hydrodynamic forces in a boundary-element formulation, and considering both prototype and full scale models. Indeed, including nonlinearities may increase the model accuracy, but at an additional computational burden. A model is parsimonious if it describes only relevant nonlinearities, in the attempt to realize the best compromise between model fidelity and computational cost. Crucially, parsimony dictates that OWSC and HPA models differ in model structure.

5.3 Hydrodynamic models

This chapter compares two single-DoF devices, as shown in Fig. 5.1: a heaving point absorber, which is constrained to translate in the vertical direction only, and an oscillating wave surge converter, which pitches around a hinge, with angle θ . Illustrations of the HPA and the OWSC are shown in Fig. 5.1, where the dimensions refer to a likely full scale size.

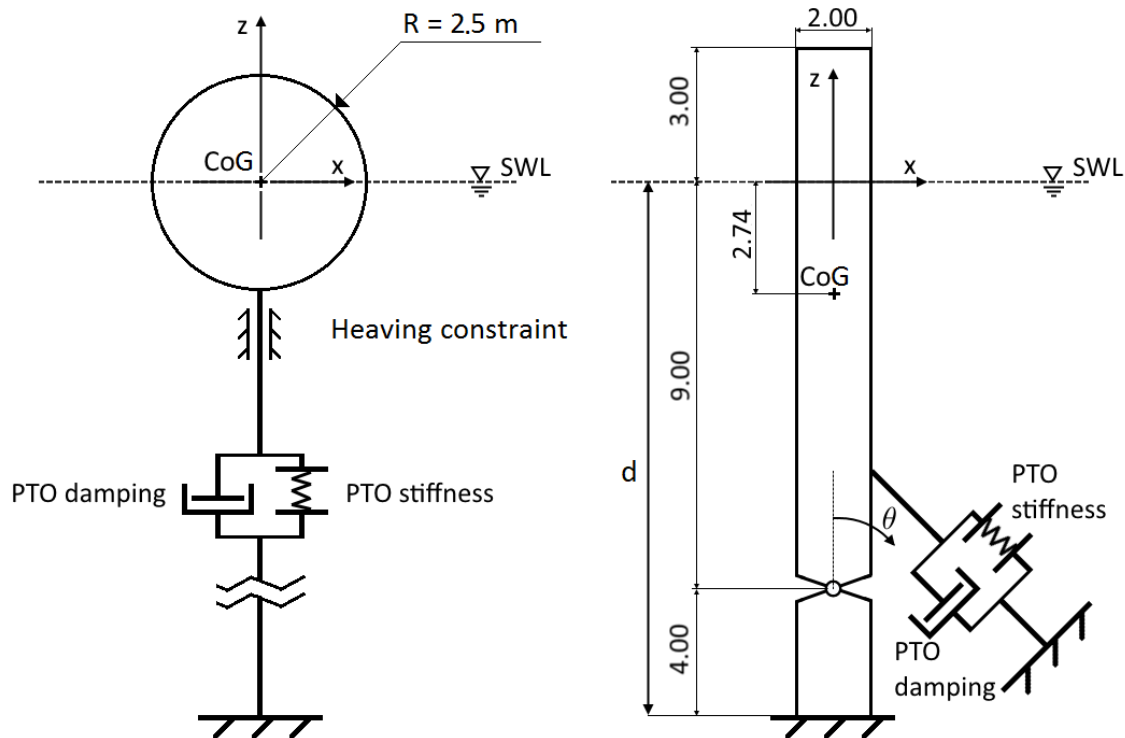


Figure 5.1: Full-scale devices under study: On the left, a spherical heaving point absorber, in deep water, with radius R of 2.5m, with the centre of gravity CoG at the still water level (SWL); on the right, a prismatic oscillating wave surge converter, hinged at 4m from the sea bottom, and piercing 3m from the SWL when at rest. Both devices have a power take-off (PTO) system with a damping and a stiffness term. The PTO representation for the OWSC is simply conceptual, since the actual PTO operates on the rotational quantities of θ and $\dot{\theta}$.

Under the assumption of an inviscid fluid, and irrotational and incompressible incident flow, Newton's second law of dynamics can be applied [32], so that, for the HPA:

$$m\ddot{\mathbf{z}}(t) = \mathbf{F}_g - \iint_{S(t)} p(t) \mathbf{n} dS + \mathbf{F}_{PTO}(t), \quad (5.1)$$

while, for the OWSC:

$$I\ddot{\boldsymbol{\theta}}(t) = \mathbf{L}_g \times \mathbf{F}_g - \iint_{S(t)} p(t) \mathbf{l} \times \mathbf{n} dS + \mathbf{T}_{PTO}(t), \quad (5.2)$$

where m and I are, respectively, the mass of the HPA and the pitching inertia of the OWSC, \mathbf{F}_g is the gravity force, $\|\mathbf{L}_g\|$ the distance between the centre of gravity of the OWSC and the hinge, S the submerged surface, p the pressure of the fluid on the body surface, and \mathbf{n} the vector normal to the infinitesimal surface dS , which is at a distance $\|\mathbf{l}\|$ from the hinge, in the case of the OWSC. Finally, the power take-off system applies a force (\mathbf{F}_{PTO}) on the HPA and a torque (\mathbf{T}_{PTO}) on the OWSC.

Applying linear potential theory, as in Chapter 4, and adding a viscous drag term, one obtains, for the HPA:

$$m\ddot{\mathbf{z}} = \mathbf{F}_{FK} + \mathbf{F}_D + \mathbf{F}_R + \mathbf{F}_{vis} + \mathbf{F}_{PTO}, \quad (5.3)$$

while, for the OWSC:

$$I\ddot{\boldsymbol{\theta}} = \mathbf{T}_{FK} + \mathbf{T}_D + \mathbf{T}_R + \mathbf{T}_{vis} + \mathbf{T}_{PTO}, \quad (5.4)$$

where \mathbf{F} and \mathbf{T} are the force and torque applied to the HPA and OWSC, respectively, and the subscripts FK , D , R , vis , and PTO refer to FK, diffraction, radiation, viscous drag, and PTO, respectively. Diffraction and radiation terms are computed linearly, as explained in Chapter 4.

5.3.1 Froude-Krylov term

The FK force is divided into two parts, static and dynamic, where the static FK force is the balance between the gravity force, and the integral over the wetted surface of the static pressure p_{st} , while the dynamic FK force refers to the integral over the wetted surface of the dynamic pressure p_{dy} . The integral is nonlinearly computed over the instantaneous wetted surface of both devices, considering the instantaneous intersection between each body and the free surface elevation. The solution of the nonlinear FK integrals for HPAs is presented in Chapter 4, while Sect. 5.3.1.1 describes how nonlinear FK forces are computed for OWSCs.

5.3.1.1 Froude-Krylov torque for oscillating wave surge converters

While HPAs are usually employed in deep water conditions, OWSCs are bottom-hinged devices; therefore, the pressure formulation in intermediate-depth water conditions needs to be used:

$$p(x, z, t) = -\rho g z + \rho g a \cos(\omega t - kx) \frac{\cosh(k(z+d))}{\cosh(kd)} \quad (5.5)$$

where d is the water depth.

The static and dynamic pressures simultaneously act perpendicularly to the front and rear surfaces of the OWSC, which have opposite normals, generating, as a consequence, opposite torques. The torque due to the pressure on each side of the OWSC is computed as the outer product between the resulting force \mathbf{F}_{FK} and its distance \mathbf{L}_{FK} from the hinge:

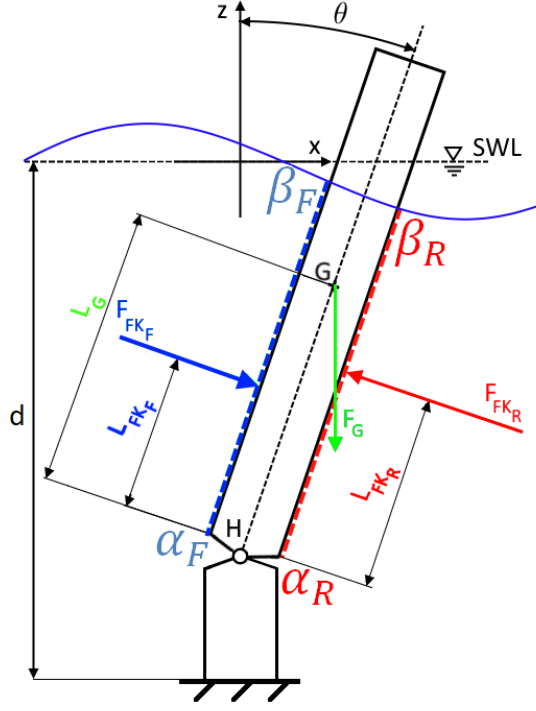


Figure 5.2: Scheme for nonlinear Froude-Krylov force calculation for an oscillating wave surge converter. The static and dynamic pressures act on the front and rear surfaces of the flap, delimited by α_F and α_R at the bottom, and β_F and β_R at the intersection between the free surface and the body.

$$\mathbf{F}_{FK_F} = - \int_{-\frac{W}{2}}^{\frac{W}{2}} \int_{\alpha_F}^{\beta_F} p \mathbf{n} \frac{dx dy}{\sin \theta} \quad (5.6a)$$

$$\mathbf{L}_{FK_F} = \frac{1}{\mathbf{F}_{FK_F}} \int_{-\frac{W}{2}}^{\frac{W}{2}} \int_{\alpha_F}^{\beta_F} p \mathbf{l} \times \mathbf{n} \frac{dx dy}{\sin \theta} \quad (5.6b)$$

$$\mathbf{F}_{FK_R} = - \int_{-\frac{W}{2}}^{\frac{W}{2}} \int_{\alpha_R}^{\beta_R} p \mathbf{n} \frac{dx dy}{\sin \theta} \quad (5.6c)$$

$$\mathbf{L}_{FK_R} = \frac{1}{\mathbf{F}_{FK_R}} \int_{-\frac{W}{2}}^{\frac{W}{2}} \int_{\alpha_R}^{\beta_R} p \mathbf{l} \times \mathbf{n} \frac{dx dy}{\sin \theta} \quad (5.6d)$$

where F and R subscripts refer to the front and rear surface, respectively, and the infinitesimal area of the flap, rotated by an angle θ , is $dS = \frac{dx dy}{\sin \theta}$. The limits of integration are defined by W , which is the width of the flap along the y axis, and by α_F , α_R , β_F , and β_R , which define the surface on which the pressure is acting, as shown in Fig. 5.2. If the body is piercing the water, β_F and β_R are the submerged lengths of the flap; if the device becomes fully submerged (when large motions occur), β_F and β_R are the extremities of the flap.

The total FK torque is the sum of the torque due to gravity, and the torques due to the static and dynamic pressures on the front and rear surfaces:

$$\mathbf{T}_{FK} = \mathbf{L}_g \times \mathbf{F}_g + \mathbf{L}_{FK_F} \times \mathbf{F}_{FK_F} + \mathbf{L}_{FK_R} \times \mathbf{F}_{FK_R} \quad (5.7)$$

5.3.2 Viscous drag term

5.3.2.1 Viscous drag force for heaving point absorbers

The viscous drag force calculation is based on the Morison equation [97], which takes into account the shape of the device via the drag coefficient C_d , the size of the floater via the characteristic area A_d , and the relative velocity between the velocity of the floater $\dot{\mathbf{z}}$ and the vertical component \mathbf{V}_{0_z} of the undisturbed flow velocity [111]:

$$\mathbf{F}_{vis} = -\frac{1}{2}\rho C_d A_d |\dot{\mathbf{z}} - \mathbf{V}_{0_z}| (\dot{\mathbf{z}} - \mathbf{V}_{0_z}) \quad (5.8)$$

Note that the characteristic surface area A_d is the projection of the instantaneous wetted surface onto the plane normal to the flow. Therefore, as the the instantaneous wetted surface is considered, A_d changes as the device pierces the water during its motion, considering for simplicity the vertical movement of the buoy as the main direction of the relative flow.

The value of the drag coefficient C_d can be estimated for simple geometries by using the Keulegan-Carpenter number (KC), which is a dimensionless quantity defined as the ratio between drag and inertia forces, acting on a body in an oscillatory fluid flow [167]. In case of sinusoidal motion, the KC number can be computed as:

$$KC = 2\pi \frac{A}{L_c} \quad (5.9)$$

where A is the amplitude of motion and L_c is the characteristic length scale, which is equal to the diameter, in the case of a sphere. The motion of the HPA and the diameter of the floater are of the same order of magnitude, which means that the KC number is about 2π so, according to [168], C_d can be taken equal to 1. However, it is worth pointing out that such a method for estimating the drag coefficient is subject to some uncertainty, which could be assessed through a sensitivity analysis, as shown by [111]. In fact, there are several issues related to drag coefficient identification techniques, which are specifically discussed in Chapter 7.

5.3.2.2 Viscous drag torque for oscillating wave surge converters

As in Sect. 5.3.2.1, the drag torque is computed by applying the Morison equation [97]. However, since the device is rotating, the relative linear velocity between the body and the fluid is progressively changing, while moving away from the hinge. Furthermore, since intermediate water depth conditions are used, the fluid velocity is changing significantly with depth, due to the proximity of the bottom. Therefore, the wetted surface of the flap is equally divided into $N_s = 10$ horizontal sections, and the total viscous torque \mathbf{T}_{vis} is computed as follows [111]:

$$\mathbf{T}_{vis} = \sum_{i=1}^{N_s=10} \mathbf{L}_i \times \left(-\frac{1}{2}\rho C_d A_{d_i} |\mathbf{V}_i - \mathbf{V}_{0_i}| (\mathbf{V}_i - \mathbf{V}_{0_i}) \right) \quad (5.10)$$

where \mathbf{L}_i is the distance from the centre of the i^{th} slice to the hinge, and $\mathbf{V}_i = L_i \dot{\boldsymbol{\theta}}$ is its velocity. As in Sect. 5.3.2.1, the instantaneous wetted surface is similarly taken into account. The number of sections N_s has been chosen equal to 10, in order to have a reasonable balance between computational time and accuracy. On the one hand, the higher the number of divisions, the smaller the width of each section, the smaller the variation of the velocities with respect to the centre of the section, and the higher the accuracy of the computation. On the other hand, the computational time is directly proportional to the number of sections.

The amplitude of motion of the top of the flap is likely to be of the same order of magnitude of the wave amplitude, which results in a Keulegan-Carpenter number less than one. According to [169], the drag coefficient for a plate in oscillatory flow at low KC is $C_d = 7.8KC^{-\frac{1}{3}}$, so C_d has been taken as 8. Although a pitching flap presents different types of viscous losses (e.g. water sliding along the surface of the paddle), the plate approximation is generally accepted [111]. However, significant sensitivity analyses are usually performed. In particular, starting with a nominal $C_d = 8$, and applying variation from zero to twice the nominal value of the drag coefficient, [108] shows that the resulting power output varies from +30% ($C_d = 0$) to -4% ($C_d = 16$). It follows that overestimations of the drag coefficient have little impact on the power absorption, consistent with the results obtained in Chapter 7.

5.4 Case study

Fig. 5.1 shows the geometries and full-scale dimensions of the HPA and the OWSC, which have been inspired, respectively, by the Wavestar HPA [66] and the Oyster 2 OWSC [170]. One of the inherent differences between HPAs and OWSCs is that OWSCs must be installed near shore, whereas HPAs may be installed either near- or off-shore. Therefore, in order to highlight such a difference, related to the operating principle, deep water conditions are chosen for the HPA.

The HPA is a sphere of radius $R=2.5\text{m}$, with the geometric and gravity centre at the SWL, designed to work in deep water conditions, constrained to heave (z), and tethered to the seabed through a PTO mechanism, composed of stiffness and damping terms.

The OWSC is a rectangular prism, with dimensions according to the section shown in Fig. 5.1 and width W of 26m. The position of the centre of gravity CoG (2.74m below the SWL), the mass (150000kg), and the inertia around the hinge ($8.12 \cdot 10^6 \text{kgm}^2$), as well as all the dimensions, have been taken from [111]. The flap rotates around the hinge with angle θ , and a PTO with rotational stiffness and damping terms is implemented. Note that the PTO representation in Fig. 5.1 is simply conceptual, since the actual PTO operates on the rotational quantities θ and $\dot{\theta}$.

Incident regular waves are used, in order to study hydrodynamic forces at each individual frequency. Wave periods T_w range from 5s to 15s, with a 1s step, while wave heights H_w range from 0.5m to 3m, with a 0.5m step. Note that some of the considered wave conditions (at large H_w and small T_w) have a steepness too large to be appropriately described by linear Airy's theory, as assumed in Sect. 5.3. However, the objective of this chapter is to focus on the comparative wave-structure interactions due to *different WEC operating principles*, which is facilitated by the use of identical input wave conditions.

The response of the device is analyzed under controlled conditions, since the action of the controller enlarges the amplitude of motion, and increases the relevance of nonlinearities. In order to facilitate as close a comparison as possible, the controller structure has been chosen to be the same for both the HPA and the OWSC. Therefore, reactive control is applied, which tunes the stiffness and damping parameters of the PTO, K_{PTO} and B_{PTO} , respectively, in order to maximize power absorption for each wave condition. No controller parameter constraints are imposed in the power optimization strategy, so that the K_{PTO} may take negative values, for example, in the case where the device resonance frequency is less than the predominant wave frequency. Furthermore, no constraints are imposed on either device displacement, velocity, or PTO force. Simulations show that reactive control is effective for both the HPA and the OWSC, as it achieves the objective of increasing power absorption, compared to the case where the PTO acts just as a linear damper (uncontrolled condition).

The prototype model dimensions have been obtained by applying Froude similarity since, in wave energy applications, gravity and inertial forces are dominant [171]. Accord-

ing to Froude similarity, the dimensionless Froude number (Fr), which is the square root of the ratio between inertial and gravity forces, is kept constant. The scaling ratio (s) has been chosen equal to 1 : 20 for both the HPA and OWSC, consistent with the prototype scale of the Wavestar [76], and Oyster [172] devices.

The PTO coefficients, K_{PTO} and B_{PTO} , have been chosen in order to optimize the power absorption of the full-scale device. These control parameters have been scaled down for the prototype model, according to Froude similarity. Note that, due to nonlinearities, such PTO parameters may be suboptimal for the small-scale device. Nevertheless, in real applications, the objective is to maximize power absorption of the full-scale device, rather than the small-scale one. Furthermore, Froude-scaling the PTO coefficients facilitates the comparison between small and full scale models since, with scaled PTO parameters, differences in the response (displacement, velocity, and forces) are due to nonlinearities only.

Likewise, the same drag coefficient has been used for the small and full scale models. In general, C_d depends on the type of flow around the device; therefore, it is influenced by the Reynolds number (Re), which is the dimensionless number defined as the ratio between inertial and viscous forces. Froude-scaling ensures the same Fr number, implying a different Re number instead. Nevertheless, it is assumed that the main contribution to drag forces is flow separation, associated with the inertia of the flow field, which is largely preserved under Froude similarity. Consequently, retaining the same C_d for small and full scale devices is considered as a good first approximation. However, as for the PTO parameters, having the same drag coefficient makes the comparison more even, since differences arise from the model structure only, rather than from differently scaled coefficients.

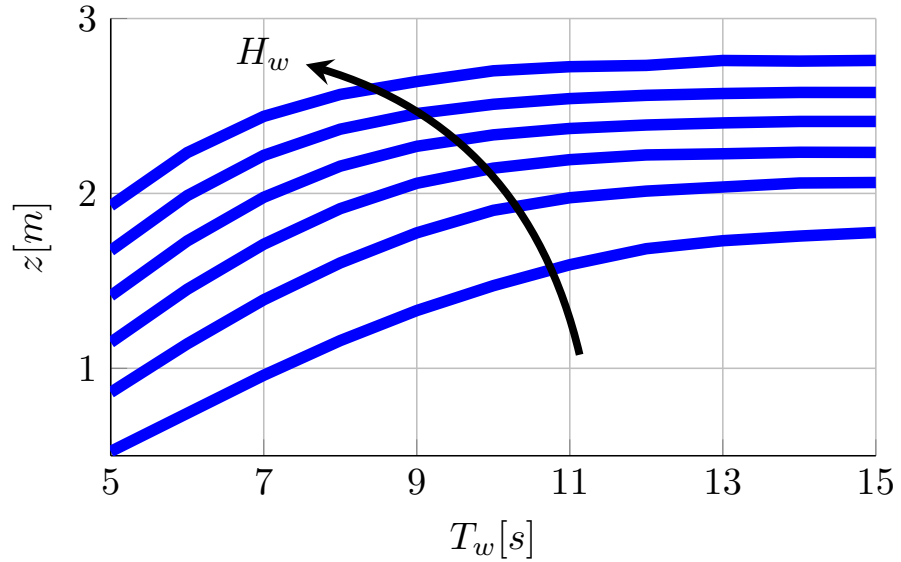
5.5 Results

The responses of the HPA and OWSC, at full scale, are shown in Fig. 5.3, which presents the maxima of the vertical/angular displacements, computed once the transient has elapsed.

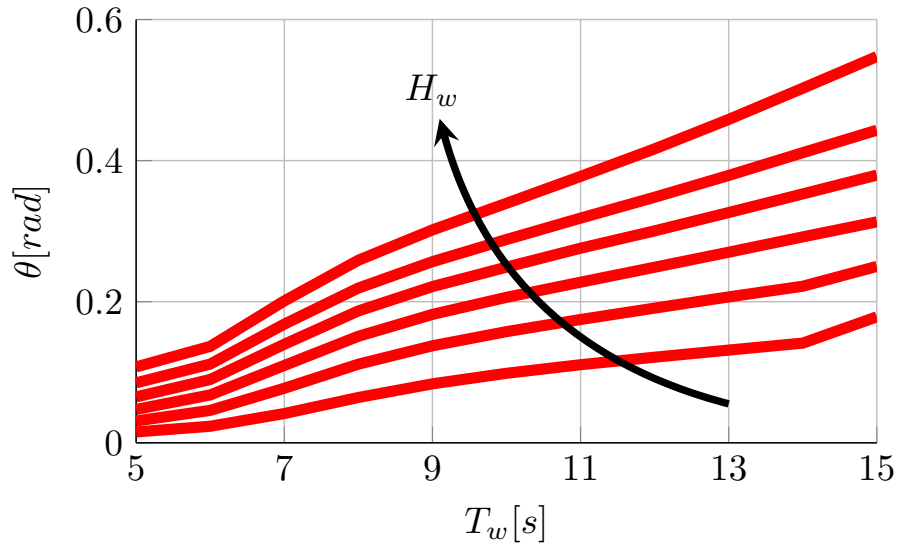
The main differences between the HPA and the OWSC arise from the comparative relevance of each of the hydrodynamic forces in each of the devices. Figures 5.4a and 5.4b show the amplitude of the static FK (FK_{st}), dynamic FK (FK_{dy}), diffraction (D), radiation (R), and viscous drag (vis) forces and torques under controlled conditions, for the HPA and the OWSC, respectively, using a regular wave of $T_w = 10s$ and $H_w = 1.5m$. Due to nonlinearities, forces may be, in general, asymmetric; therefore, the force amplitude has been defined as half of the variation from peak to trough. Finally, both model scales have been plotted together, in Fig. 5.4: results obtained with the prototype model have been scaled up (scale ratio s), with a factor s^3 for the forces of the HPA, and s^4 for the torques of the OWSC. Forces and torques obtained with the prototype scale are identified by the subscript p , whereas f indicates the full scale model.

Overall, the nonlinear static FK term, which is the restoring force that pulls the device back into the equilibrium position, is by far the largest component in HPAs. While the dynamics of the HPA are dominated by static and dynamic FK forces, in the OWSC, the major hydrodynamic action is due to diffraction and radiation forces.

The components related to wave excitation are the dynamic FK force and the diffraction force. Figure 5.4 shows that HPAs are mainly excited by the dynamic FK force while, in OWSCs, diffraction forces are the most important wave excitation mechanism. Radiation damping and viscous drag are the dissipative terms of the hydrodynamic force, with a notional linear and quadratic dependence on the velocity of the device, respectively. While in HPAs, dissipation terms are very small compared to the FK components, in OWSCs radiation and viscous drag are predominant.



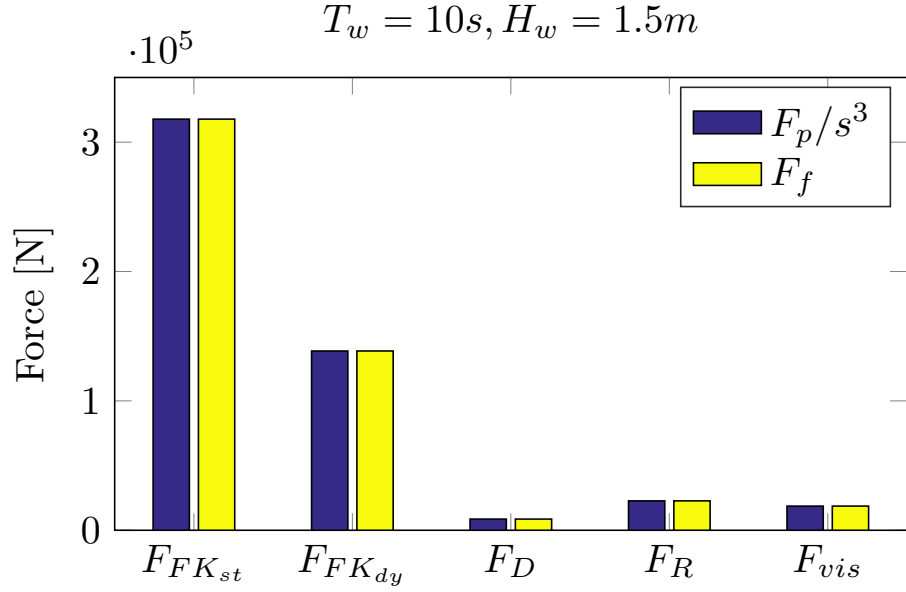
(a) Heaving point absorber.



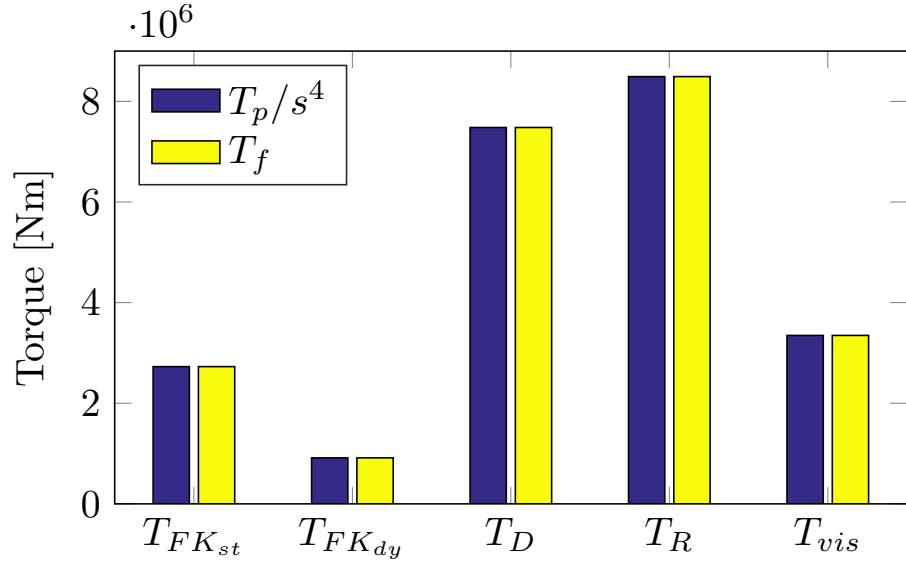
(b) Oscillating wave surge converter.

Figure 5.3: Maxima of the steady state response for the heaving point absorber, (a), and the oscillating wave surge converter, (b). The wave height increases in the direction pointed by the arrow.

Comparing small and full scale models, it is clear that all forces and torques are perfectly scalable, meaning that nonlinear FK and viscous drag models are insensitive to scaling, for both the HPA and the OWSC. Consequently, as far as the nonlinear model structure is concerned, it is equivalent to consider small or full scale, as long as the same model parameters are chosen. However, even though the nonlinear model structure is scale-independent, the values of the model parameters, in particular the viscous drag coefficient, may vary between different scales. Indeed, [173] shows that the power captured during experimental tests for an OWSC, at prototype scale, is 7% greater, relative to full scale. Figure 5.4 suggests that such a difference is *not* due to the inherent structure of nonlinear forces, but may be attributed to different flow conditions at different scales, resulting in different values of the drag coefficient. Furthermore, note that the drag formulation with the Morison-like term is an approximation and changes of scale are likely to influence its suitability: [174] shows that, apart from change in viscosity, there are different effects that



(a) Heaving point absorber.



(b) Oscillating wave surge converter.

Figure 5.4: Full-scale total hydrodynamic force (F) and torque (T) decomposition into static FK (FK_{st}), dynamic FK (FK_{dy}), diffraction (D), radiation (R), and viscous drag (vis), according to the prototype (p) and full scale (f) model, using a regular wave of period T_w 10 s and height H_w 1.5 m.

discriminate between full and small scale OWSCs (e.g. separation of bubbles at full scale, vortices at small scale).

Following scalability considerations, only the full scale devices will be discussed hereafter.

Differences between the hydrodynamic forces, experienced by the HPA and the OWSC, are not only due to their amplitudes, as shown in Fig. 5.4, but also on the phase with which they are acting on the body. Notwithstanding the clear notion of phase between quasi-harmonic signals, a rigorous definition of phase is available only for sinusoidal signals. Nevertheless, a predominant phase Φ can be defined, using the delay at which the cross-correlation function has its maximum. Such phases are computed for all forces F (and torques T), with respect to the free surface elevation η , as follows:

$$\Phi = \frac{2\pi}{T_w} \operatorname{argmax}_{\tau} \left\{ \int_{-\infty}^{\infty} F^*(t) \eta(t + \tau) dt \right\}, \quad (5.11)$$

where F^* denotes the complex conjugate of the force (or torque), and τ the time lag between signals.

For all the hydrodynamic forces, such a phase difference is used to construct a phasor, whose length is equal to the exponential of the ratio between the amplitude of the force and the total hydrodynamic force. The phasor graphs for the HPA and the OWSC are shown in Figs. 5.5 and 5.6, respectively. The reason for scaling the length of the phasor with an exponential is to compress the differences between the amplitudes of the different forces, facilitating comparative plotting.

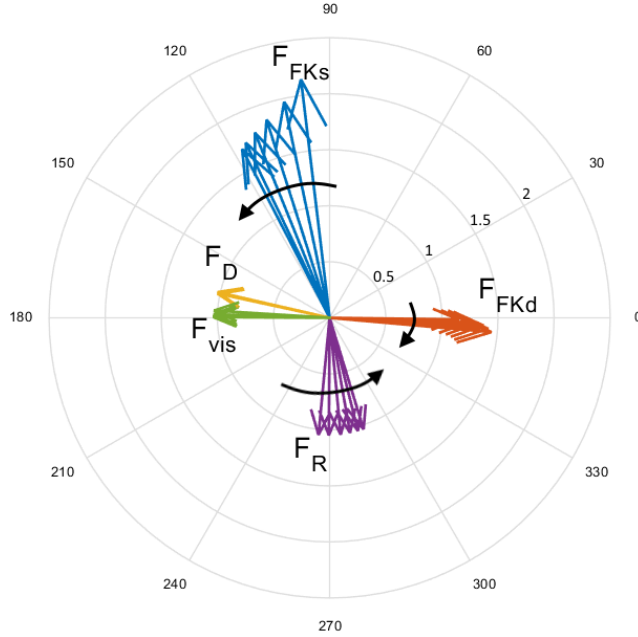


Figure 5.5: Phasor graph for the HPA, for a wave period $T_w = 10s$, and 6 heights H_w from $0.5m$ to $3m$, increasing in the direction of the curved arrows.

In order to highlight the effect of nonlinearities, Figs. 5.5 and 5.6 are drawn for waves with the same period $T_w = 10s$, and 6 heights H_w from $0.5m$ to $3m$. Indeed, if the model was fully-linear, the phase of each force would depend only on the wave frequency, and would be independent of the wave height. On the contrary, nonlinear forces show a phase *drift* causing, in turn, a phase shift in position and velocity. Therefore, due to nonlinearities, as the wave height increases, the phasors are rotating in the direction indicated by the curved (black) arrows in Figs. 5.5 and 5.6.

In fact, the only phasor that is not rotating is the diffraction one, which is linear, and does not depend on the response of the device. On the other hand, notwithstanding that the radiation force is linear, the radiation phasor is rotating, since it depends on the velocity. Finally, FK and viscous drag phasors are rotating both due to their nonlinear nature, and their dependence on displacement and velocity.

Nevertheless, the rotation of the dynamic FK phasor is relatively small, since it depends mainly on the free surface elevation. Conversely, static FK and radiation phasors rotate in the same direction, due to the large dependence on position and velocity, respectively; in fact, since position and velocity are roughly 90 degrees out of phase, they rotate with a consistent phase difference, so static FK and radiation phasors rotate accordingly.

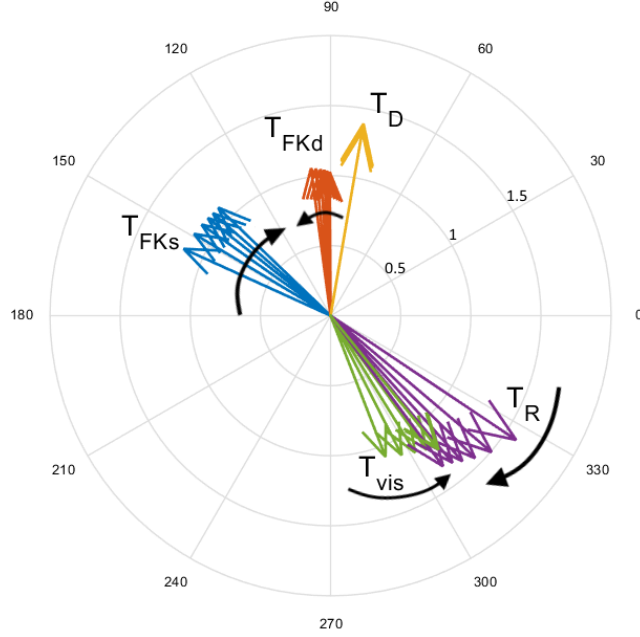


Figure 5.6: Phasor graph for the OWSC, for a wave period $T_w = 10s$, and 6 heights H_w from $0.5m$ to $3m$, increasing in the direction of the curved arrows.

Table 5.1: Phase range of the phasors in Figs. 5.5 and 5.6, and correspondent phase difference.

$H_w[m]$	HPA		OWSC		Difference	
	0.5	→ 3	0.5	→ 3	0.5	→ 3
$\Phi_{FK_s}[deg]$	97	→ 117	156	→ 136	-59	→ -19
$\Phi_{FK_d}[deg]$	359	→ 355	90	→ 98	269	→ 257
$\Phi_D[deg]$	167	→ 167	80	→ 80	87	→ 87
$\Phi_R[deg]$	265	→ 287	326	→ 307	-62	→ -20
$\Phi_{vis}[deg]$	179	→ 176	291	→ 309	-112	→ -132

Finally, the viscous drag phasor rotation is quite small for the HPA and relatively large for the OWSC, consistent with the relative importance of the viscous drag term in each device. Note that, in the OWSC, the phasors of the two dissipative terms, namely radiation and viscous drag forces, are counter-rotating as the wave height increases. Furthermore, the phase difference between the radiation and viscous drag phasors decreases for larger wave amplitudes; consequently, a more constructive interaction is achieved, making the total loss larger.

Comparing the phasor graphs of the HPA and the OWSC, in Figs. 5.5 and 5.6, respectively, it can be noted that the phasors of each hydrodynamic force component rotate in the opposite direction (the FK_s phasor, for example, is rotating counter-clockwise for the HPA, but clockwise for the OWSC). Moreover, the range of phases of each phasor is different between the HPA and the OWSC (the HPA FK_s phasors, for example, are between 97 and 117 degrees, while the OWSC FK_s phasors are between 136 and 156 degrees). Table 5.1 tabulates the bounding phase values for each force component, namely at the smallest and largest wave height, as well as the phase difference between the HPA and OWSC.

In order to have a more complete description of the relevance of nonlinearities in HPAs and OWSCs for all wave conditions considered, the FK ratio is defined as the ratio between

the amplitude of FK forces/torques (static plus dynamic) and the total hydrodynamic force/torque. Likewise, the viscous drag ratio is defined as the ratio between the amplitude of the viscous drag force/torque, and the total hydrodynamic force/torque.

FK and viscous drag ratios are shown, respectively, in Figs. 5.7 and 5.8, where each line corresponds to a constant wave height. The HPA exhibits FK ratios from 0.81 to 0.96, showing that FK forces constitute the largest part of the total hydrodynamic force. On the other hand, FK ratios for the OWSC are considerably smaller, ranging from 0.09 to 0.36. Nevertheless, both the HPA and the OWSC show a similar trend: the FK ratio increases with the wave period T_w , while it is independent of the wave height H_w .

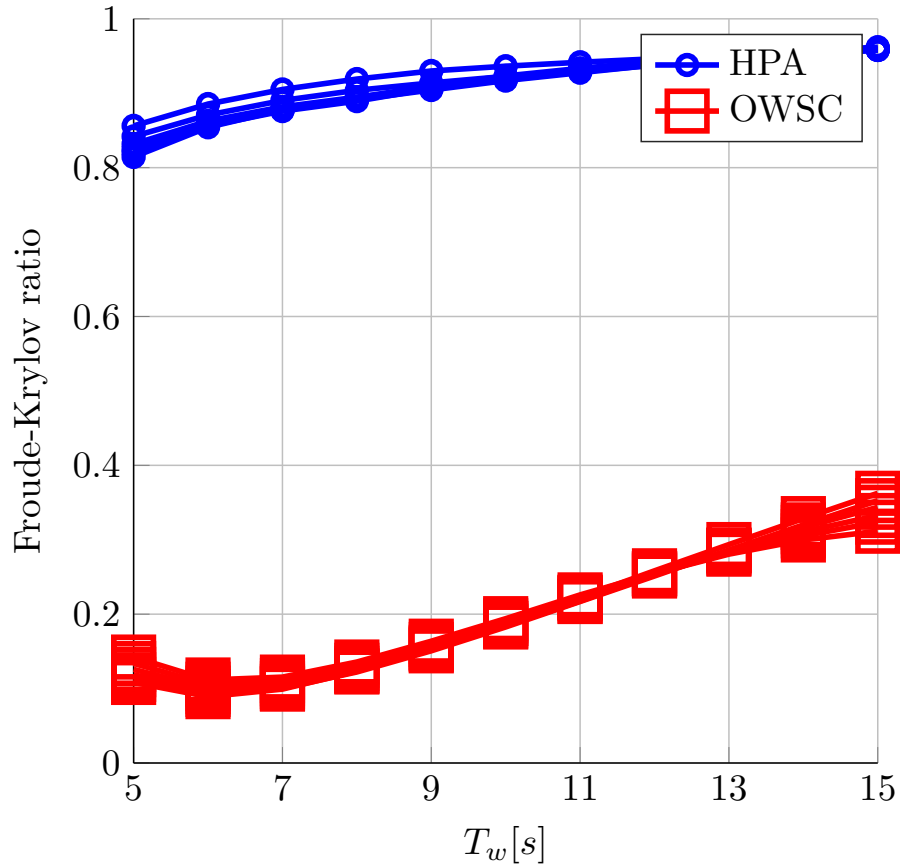


Figure 5.7: Froude-Krylov force ratio, defined as the ratio between the FK force (static and dynamic) and the total hydrodynamic force. Each line corresponds to constant wave height, ranging from 0.5m to 3m with a step of 0.5m.

The viscous drag ratio, in Fig. 5.8, shows a completely different trend, compared to Fig. 5.7. The viscous drag ratio of the HPA experiences little dependence on either wave period or height, especially at larger periods, and exhibits a general slightly negative slope of the curves; since the FK forces are dominating the device dynamics, as shown in Fig. 5.7, the variations in viscous drag force have little impact on the overall hydrodynamic force, so the viscous drag ratio remains quite small (between 0.01 and 0.06). Furthermore, the negative slope suggests that the increase in viscous drag force is even smaller than the increase in FK force. On the other hand, the viscous drag ratio for the OWSC shows a strong dependence on both wave period and height. Moreover, the curves are clearly distinct because of the large values the viscous drag ratio assumes, highlighting its relevance with respect to the total hydrodynamic force.

It is useful to gather the information contained in Figs. 5.7 and 5.8 in a single compact graph, shown in Fig. 5.9, in order to highlight the essential differences between HPAs and

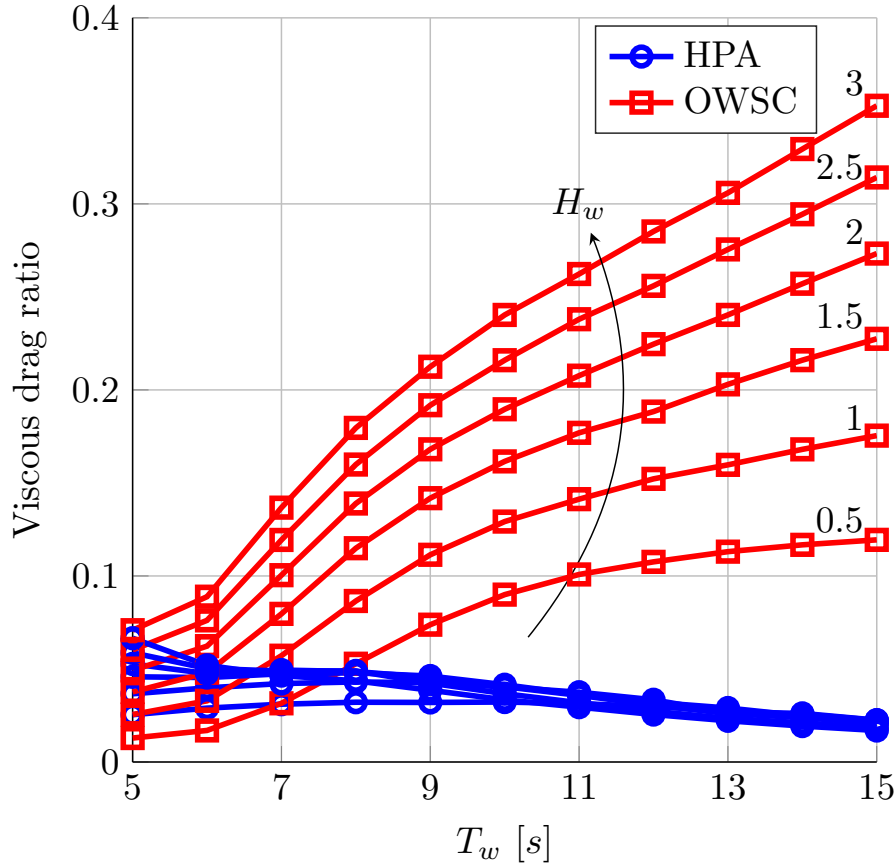


Figure 5.8: Viscous drag ratio, defined as the ratio between the viscous drag force and the total hydrodynamic force. each line corresponds to constant wave height (shown at the right hand side), ranging from 0.5m to 3m with a step of 0.5m. The wave height increases in the direction pointed by the arrow.

OWSCs, and the relative importance of nonlinear FK and viscous drag effects. As shown by the arrows in Fig. 5.9, the cloud of points for each device presents different trends at constant wave heights H_w , increasing from left to right, with the wave period T_w increasing upwards along each line.

The cloud of points for the HPA is compact and shows little dependence on different wave heights and periods, occupying a small area at the top left corner of the graph at high FK ratios (greater than 0.8), and low viscous drag ratios (smaller than 0.07). On the contrary, a completely separate region of the graph in Fig. 5.9 is occupied by the OWSC, located at low FK ratios (lower than 0.4), and viscous drag ratios up to 0.35. The OWSC points are widely spread, showing a strong sensitivity to both wave period and height.

5.6 Conclusions

This chapter deals with major hydrodynamic differences existing between heaving point absorbers, and oscillating wave surge converters. The relative amplitude and phase of each hydrodynamic force component is investigated, using nonlinear models for Froude-Krylov and viscous drag forces. A particular focus is placed on the importance of nonlinearities; on the one hand, the sensitivity of scaling to hydrodynamic nonlinearity is examined, when a prototype scale model is used to predict the full scale model performance; on the other hand, the relevance on nonlinear forces is discussed, with respect to the total hydrodynamic force.

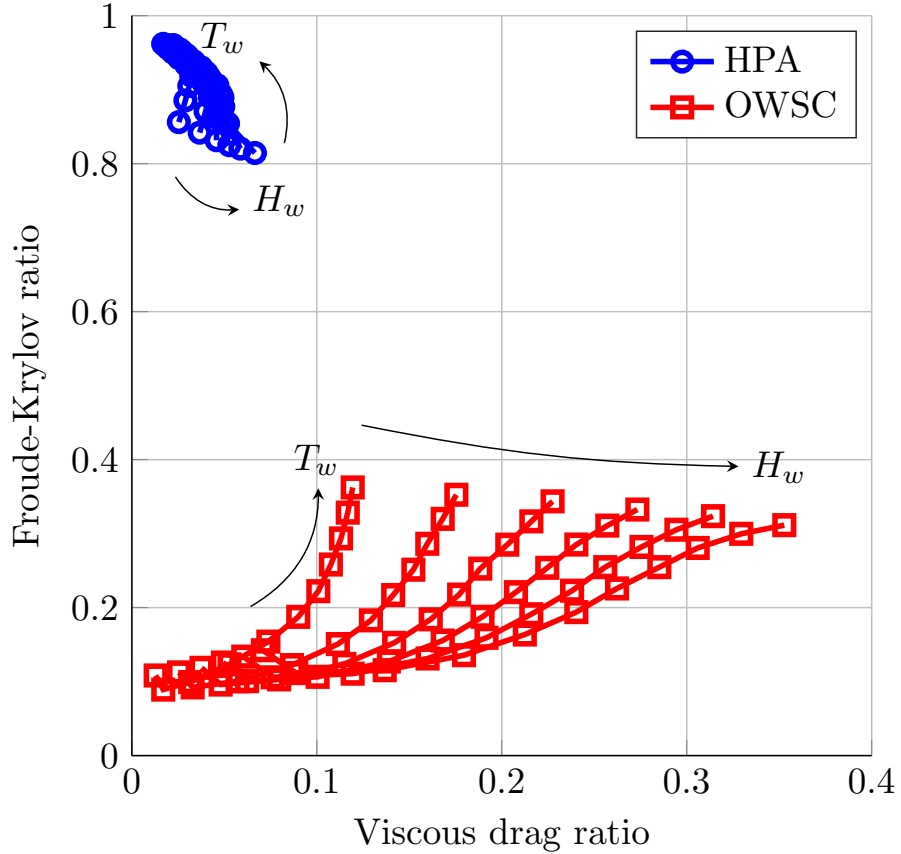


Figure 5.9: Froude-Krylov ratio versus viscous drag ratio, defined as in Figs 5.7 and 5.8, respectively. Every line has a constant wave height, ranging from 0.5m to 3m with step 0.5m, increasing from left to right, with wave period T_w , ranging from 5s to 15s with step 1s, increasing upwards along each line.

From Fig. 5.4, it is clear that the mathematical formulation of nonlinear Froude-Krylov and viscous drag forces is device scale invariant. Therefore, eventual differences between experimental tests at prototype and full scales are not due to the inherent structure of the nonlinear forces, but may be attributed to different flow characteristics, which impact the model parameters (namely C_d).

Nonlinearities also affect the phase with which the force components acts on the devices since, for a constant wave frequency, the phasors of the forces are rotating, as the the wave height increases.

Nonlinear forces show different relevance in HPAs and OWSCs. Viscous drag effects in HPAs are small compared to other forces, while they are significant in OWSCs. The most important hydrodynamic force in HPAs is the nonlinear FK force, while the magnitudes of diffraction and radiation forces are relatively small. Moreover, the dynamic FK force is the main wave excitation mechanism in HPAs, since the diffraction force is negligible. On the contrary, the dynamics of OWSCs are mainly driven by diffraction and radiation forces, while the dynamic FK force is relatively low.

Consequently, the relevance of nonlinear FK forces in HPAs appears to be considerably larger than the viscous drag force, since FK forces cover 81% to 96% of the total hydrodynamic force. Such percentages remain consistent for different wave heights and periods. Conversely, the relative relevance of nonlinear FK forces and viscous drag in OWSCs is quite sensitive to wave parameters. Aside from variability, FK forces are, in general, significantly more important in HPAs than in OWSCs, while viscous drag becomes much more relevant in OWSCs than HPAs.

Nonlinear hydrodynamic models in the computation/fidelity continuum

6.1 Motivation

The definition of a model structure, and its parametrisation, is not straightforward, and should take into account the specific application it is intended for. Two of the most important characteristics of a model are the computational time and the expected accuracy, which usually are mutually conflicting. The inclusion of nonlinearities potentially increases the model accuracy, but at a higher computational price. Considering a heaving point absorber with and without control, this chapter studies and compares nine different modelling options, eight of which are based on potential theory, including nonlinear Froude-Krylov and viscous drag forces, while one is based on fully-nonlinear CFD. The value of including nonlinearities in the hydrodynamic model is discussed in relation to the computational cost of the eventual accuracy benefits, under a range of scenarios. Therefore, this chapter purports to evaluate the performance of the different modelling options discussed in previous chapters.

6.2 Introduction

Chapter 4 introduced a novel modelling approach for computationally efficient computation of static and dynamic FK forces for axisymmetric devices. However, it is not the case that such a model is always the best candidate: numerous possible approaches to modelling are available, and the choice of an *appropriate* model needs to take into account specific requirements demanded by the intended application of the model itself, taking particular care of the compromise between expected accuracy and computational time. For preliminary studies, such as early stage concept development or approximate array calculations, low accuracy may be acceptable, while fast computation is mandatory. Fully-linear models are therefore widely used, since they require minimal set-up and generally execute at high speed. Conversely, for survivability, extreme events, and loads studies, accurate results can be returned only by very complex and time consuming models such as, for example, fully-nonlinear CFD models. In between, for power production assessment and model-based controller tuning and optimization, medium/high fidelity, with an acceptable computation time, is required to correctly define the parameters of the system and the predicted performance of the device, over a wide range of sea conditions. Furthermore, mathematical models for control applications must compute quickly enough to allow the control strategy to take action in real time.

The focus of the chapter is on the power production region (medium/high fidelity) of a

small heaving sphere, operating under the application of a latching control strategy. Note that, in the unlikely situation that no control is implemented, linear models are normally quite accurate for small heaving WECs, which are characterized by a high and peaky resonance frequency: usually operating in sea states at frequencies lower than resonance, such devices behave, in absence of a control strategy, as wave followers, and nonlinear models are not likely to produce any significant advantage. Nevertheless, the purpose of real-world deployed WECs is to maximize power capture; such an objective is pursued by the control strategy. Commonly, control strategies, such as latching control, seek the objective of increasing power absorption by increasing the motions amplitude and, consequently, the relevance of nonlinearities. When such control strategies are employed, it is expected that nonlinear models are able to considerably improve the fidelity of the model fit, at an additional computational cost, which depends on the complexity of the specific nonlinear model.

This chapter seeks to evaluate the performance of a wide range of nonlinear models, relevant to heaving point absorbers WECs, in terms of accuracy and computational cost, in order to define a continuum in the *computation/fidelity space*, from fully-linear to fully-nonlinear models. HPAs are chosen, for which nonlinear FK force calculations are relevant, as discussed in Chapter 5. In total, nine different implementations of prominent nonlinearities in the equations of motion are considered; while one model is based on fully-nonlinear CFD software, the remaining eight models are based on different implementations of Froude-Krylov (FK) and viscous drag forces (four FK force modelling options, multiplied by two viscous drag modelling options). Since CFD is fully-nonlinear, CFD results are taken as a “gold standard” benchmark, in order to validate the other models, and compare their accuracy. Note that CFD can be used as accuracy benchmark in the power production region (the scope of this chapter), while SPH should be preferred in case of extreme events and survivability conditions [80]. In fact, thanks to the meshless approach, SPH is able to handle very large motion and spray effects more effectively than CFD. However, drawbacks of SPH simulations are noisy velocity (thus pressure) signals, challenging free surface tracking, and difficulties in accurately capturing near body regions [80].

6.3 Hydrodynamic models

Eight of the nine hydrodynamic models have their foundations in potential theory (PoT), described in Chapter 2. Different options, for modelling of FK and viscous drag forces, described respectively in Sects. 6.3.1.1 and 6.3.1.2, discriminate between each of the models considered here. A summary of the different models is presented in Table 6.1. The final model, used as somewhat of a gold standard, is based on the application of the Navier-Stokes equations (CFD), which are described in Chapter 3.

6.3.1 Potential theory-based (PoT) models

The theoretical background for the application of the velocity potential theory is discussed in Chapter 2, Sect. 2.4.2. Consequently, it is possible to formulate the equation of motion for a heaving point absorber, as in (2.10), as:

$$m\ddot{\mathbf{z}} = \mathbf{F}_{FK_{st}} + \mathbf{F}_{FK_{dy}} + \mathbf{F}_D + \mathbf{F}_R + \mathbf{F}_{PTO} \quad (6.1)$$

As with the analysis in Chapter 4, radiation and diffraction forces are *assumed* linear; such an assumption, is reasonable for devices much smaller than the wavelength [45]. Furthermore, Chapter 5 shows that radiation and diffraction forces are much smaller than FK forces for HPAs, and so are less relevant in altering the dynamics of the body.

Table 6.1: Summary of the 8 potential theory-based (PoT) models considered in this Chapter, where \circ and \bullet stand, respectively, for linear and nonlinear representation of the static FK force ($F_{FK_{st}}$) and dynamic FK force ($F_{FK_{dy}}$), and absence/presence of the viscous drag force (F_{Vis}), as defined in Sect. 6.3.

	PoT models	$F_{FK_{st}}$	$F_{FK_{dy}}$	F_{vis}
1	LFKnoD	\circ	\circ	\circ
2	NLRnoD	\bullet	\circ	\circ
3	NLFKanoD	\bullet	\bullet	\circ
4	NLFKrnoD	\bullet	\bullet	\circ
5	LFKD	\circ	\circ	\bullet
6	NLRD	\bullet	\circ	\bullet
7	NLFKaD	\bullet	\bullet	\bullet
8	NLFKrD	\bullet	\bullet	\bullet

Different approaches for FK force modelling are proposed in Sect. 6.3.1.1, considering (or not) the instantaneous wetted surface for the static and dynamic pressure integrals. Progressively, Sect. 6.3.1.2 deals with the eventual inclusion of viscous effects in the dynamical equation of the system. Each one of the eight resulting models will be labeled by two indices: the first one refers to the FK force modelling mode, namely linear FK (LFK), nonlinear restoring (NLR), re-meshing nonlinear FK (NLFKr), and algebraic nonlinear FK (NLFKa); the second one indicates the absence (noD) or the inclusion (D) of a viscous drag term.

Note that improving the accuracy of the mathematical description of the different components of the PoT model, by means of different implementation of FK force models and eventually including viscous drag effects, does not necessarily produce more accurate results. In fact, given the number of force components in equation (6.1), different modelling errors sources are present, which may add up (increasing the total error), or subtract (decreasing the total error). When two (or more) modelling errors partially cancel out, a “mitigation” effect is achieved, as described in Sect. 6.3.1.1.

6.3.1.1 Froude-Krylov force modelling

Differences between the proposed modelling options for FK force representation consider how the instantaneous wetted surface is, or is not, taken into account in the calculation of the static and dynamic FK forces. Therefore, differences in the computed force depend on the relative displacement (z_{rel}) between the device position (z_d) and the free surface elevation (η), as discussed in Chapter 4. In particular, a significantly different behavior can be observed in the extreme (unrealistic) situation when the relative displacement is larger than the physical dimension of the device, namely when the body is clear of the water surface. Such a situation is not uncommon, when fully-linear models of heaving WECs under latching control are considered, as shown in Fig. 4.5. Given the absence of any fluid-structure interaction, the physically correct answer when the body is completely out of the water would be a restoring force equal to the weight of the device (independent of the body position) and a null excitation force.

Linear Froude-Krylov force (LFK) According to the fully-linear representation of FK forces, the mean wetted surface is considered for both static, and dynamic, pressure integrals, as discussed in Sect. 4.3.1. Therefore, the hydrostatic stiffness G is used, which, in the heave degree of freedom, is proportional to the cross-sectional area at the still water level (A_{SWL}):

$$\mathbf{F}_{FK_{st}} = -Gz = -\rho g A_{SWL} z \quad (6.2)$$

Note that such a restoring force assumes the device to be an infinitely long vertical prism, namely with constant cross-sectional area and always piercing the water. Consequently, the restoring force linearly increases with displacement, irrespective of the actual change in body shape and cross sectional area.

The excitation impulse response function is used for the calculation of the dynamic FK and diffraction forces, as shown in (4.1); the excitation force is calculated with reference to the mean wetted surface, irrespective of the body position. Consequently, when the body is completely out of the water, the excitation force continues to exert an effort on the body but, at the same time, the restoring force is linearly increasing with the displacement, so the two modelling errors counteract and a “mitigation” effect is achieved.

Nonlinear restoring force (NLR) For the nonlinear restoring force model (NLR), as shown in Fig. 6.1, the integral of the *static* pressure *only* (as opposed to static and dynamic pressure) is computed over the instantaneous wetted surface $S(t)$: alternatively to the approach proposed in Chapter 4, the static FK integral can be solved by describing $S(t)$ as the closed surface S_c minus the horizontal surface S_{WP} , as shown in [175]. S_{WP} is defined as the intersection between the body and the horizontal plane at a free surface elevation η . Consequently, $\mathbf{F}_{FK_{st}}$ can be computed as follows:

$$\mathbf{F}_{FK_{st}} = \mathbf{F}_g - \left(\iint_{S_c} p_{st} \mathbf{n} dS - \iint_{S_{WP}} p_{st} \mathbf{n} dS \right) \quad (6.3)$$

Applying Gauss’s divergence theorem to the integral over the closed surface S_c , equation (6.3) becomes:

$$\mathbf{F}_{FK_{st}} = \mathbf{F}_g + (\rho g V_{sub} - \rho g \eta A_{WP}) \mathbf{k} \quad (6.4)$$

where V_{sub} is the submerged volume enclosed by S_c , and A_{WP} is the area of S_{WP} . Note that the computation of $\mathbf{F}_{FK_{st}}$ according to (6.3) and (6.4) is an alternative but equivalent approach to the one discussed in Chapter 4. However, (6.4) can be applied to $\mathbf{F}_{FK_{st}}$ only, while Chapter 4 provide a method applicable to both $\mathbf{F}_{FK_{st}}$ and $\mathbf{F}_{FK_{dy}}$. On the other hand, as shown in Fig. 6.1, (6.4) can be applied to any arbitrary geometry, while the approach of Chapter 4 only to axisymmetric bodies.

The nonlinear restoring force is smaller than the linear one, in cases such as a sphere, where A_{WP} is smaller than A_{SWL} , and reaches a plateau when the body is completely out of the water. However the excitation force is linear; therefore, there is no “mitigation” effect, and amplitudes larger than the linear model are expected.

Nonlinear Froude-Krylov forces (NLFK) For the nonlinear FK models (NLFK), both static and dynamic pressures are integrated over the instantaneous wetted surface, either through a mesh-based approach [91], or through algebraic calculation, as discussed in Chapter 4. The mesh-based approach is identified by the NLFKr label, since it requires a computationally expensive re-meshing routine, while the algebraic approach is identified by the NLFKa label. Note that, in case of an axisymmetric heaving device, the re-meshing (NLFKr) and algebraic (NLFKa) approaches return identical results, albeit at a different computational cost.

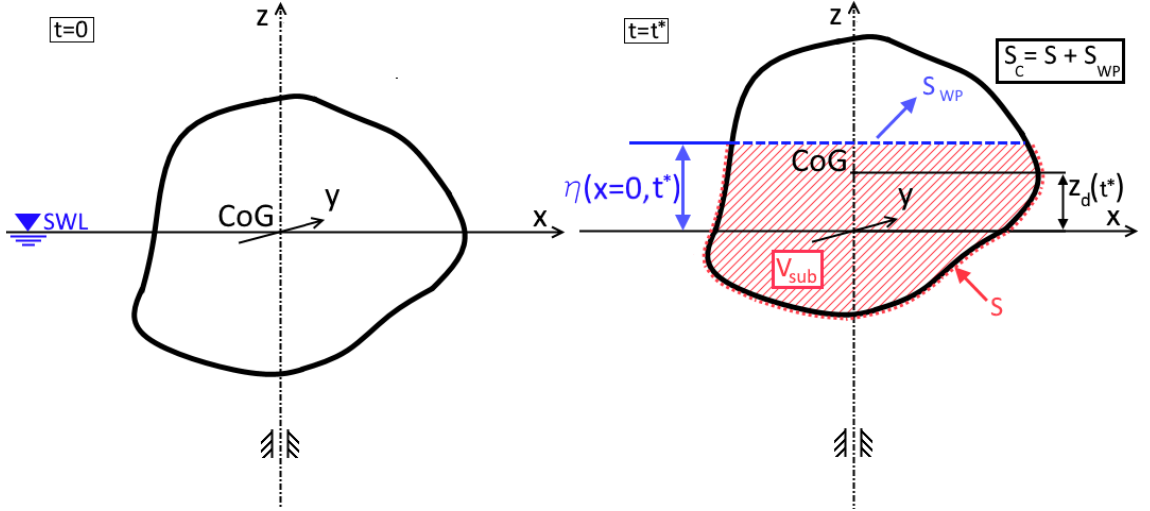


Figure 6.1: Generic heaving device: the figure on the left shows the rest position, with the center of gravity CoG at the still water level (SWL); the figure on the right shows the free surface elevation η and the device displacement z_d after a time t^* . The closed surface S_c surrounds the submerged volume V_{sub} , which is upper limited by the water plane surface S_{WP} .

6.3.1.2 Viscous drag modelling

Viscous effects are included through a Morison-like term, as in (5.8) in Chapter 5:

$$\mathbf{F}_{vis} = -\frac{1}{2}\rho C_d A_d |\dot{\mathbf{z}} - \mathbf{V}_{0z}| (\dot{\mathbf{z}} - \mathbf{V}_{0z}) \quad (6.5)$$

However, there are major issues in selecting a representative drag coefficient, which are discussed in detail in Chapter 7.

6.3.2 Computational fluid dynamics (CFD) model

The fully-nonlinear model is implemented in a numerical wave tank (NWT) using the open-source CFD software OpenFOAM [154]. A detailed description of the CFD approach and the NWT setup is given in Chapter 3.

High fidelity is expected from this modelling approach, since all nonlinear effects are included. Consequently, results obtained through CFD simulation are taken in this study as a fidelity benchmark to evaluate the results obtained with the other models. However, drawbacks of the CFD model are its complexity and computational speed. In addition to a computational time several orders of magnitude higher than PoT models, correct design of the NWT dimensions, mesh structure and parameters requires significant effort and experience, often relying on an exhaustive trial and error process.

6.4 Case study

The models presented in Sect. 6.3 are used to simulate the response of a heaving sphere in deep water conditions, as shown in Fig. 4.2. The geometry of the body is chosen as a sphere, since cylinders present linear static FK forces, as shown in (6.2) and discussed in Sect. 6.3.1.1. On the contrary, significant nonlinearities in FK forces are mainly excited by non-uniform cross sectional area in the direction of motion [92]. The diameter of the sphere is chosen as 5m, as the one used in previous chapters. Added mass and radiation damping are shown in Fig. 4.3 in Chapter 4.

A second order Runge-Kutta method with a constant time step (0.01s) is used to solve the equation of motion (6.1) in the time domain. The time step is chosen following a convergence study (using several time steps between 0.2s and 0.001s) based on the free response amplitude operator which, in the time domain, is defined as the ratio between the simulated displacement of the device and free surface elevation, with B_{PTO} equal to zero and the latching mechanism inactive. The RAO, computed in the frequency domain, according to [162], is used as a benchmark for the convergence. Note that the fully-linear model is used for the convergence study, since results obtained in the frequency domain are inherently linear. Fig. 6.2 shows the resulting RAO, computed both in the time and frequency domain. The amplitude of motion of the floater is likely to be of the same order of magnitude as the characteristic length (the diameter) of the device, resulting in a KC number of about 2π and, according to [168, 111], a drag coefficient C_d of unity is appropriate.

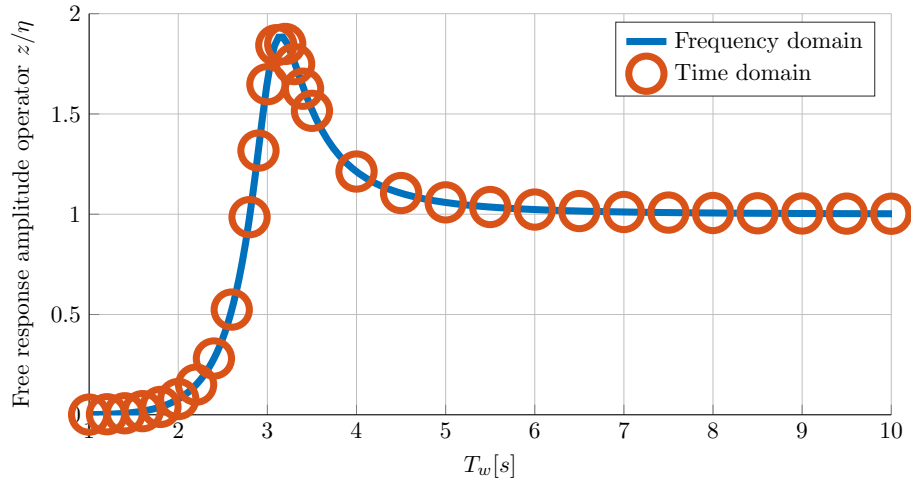


Figure 6.2: Free response amplitude operator for the floating sphere in Fig. 4.2, computed both in the frequency (benchmark) and time domain, with B_{PTO} equal to zero. After a convergence study in the time domain, the time step is chosen equal to 0.01s, and the two RAOs are significantly overlapping.

A set of regular waves is considered, in order to analyze the frequency and amplitude effects, independently. 24 wave conditions are considered, whose heights range from 0.5m to 2m, with a 0.5m step, and periods ranging from 5s to 10s, with a 1s step. The free surface elevation in the NWT is generated through waves2Foam [136], which implements numerical generation and absorption zones, which gradually blend the required wave profile into the numerical domain. Consequently, the actual wave profile obtained depends on many factors, among which the most important are the length of the domain, and the size of the mesh. Therefore, the free surface elevation at the position of the body is measured by running a simulation without the body, using a two-dimensional section of the NWT. In practice, the measured free surface elevation can be slightly different from the harmonic profile required. In order to provide the most accurate comparison of model performance, the PoT models take the actual wave profile, measured in CFD, as an input.

Real wave energy applications are likely to benefit from the implementation of a controller, which magnifies the amplitude of motion, in order to increase power absorption. For the purpose of this study, latching control has been chosen, since it is a simple discrete strategy, particularly able to induce high relative fluid/device velocities relative displacements and, therefore, likely to reveal differences between various modelling approaches. Results are compared with the uncontrolled case (resistive damping PTO), in order to highlight how nonlinearities are excited by the action of the controller.

Latching control requires the definition of only two parameters, namely the PTO damping coefficient (B_{pto}) and the latching duration (T_L). The same PTO damping has been chosen for all models, set equal to the radiation damping $B(\omega)$, at the wave frequency, according to the linear optimal energy absorption condition [45]. The zero-threshold criterion [176] is applied for release instant selection, following a zero-crossing in the excitation force. Note that, still following the objective of establishing a level field of comparison, the zero-crossing of the linear excitation force is considered for all the models, so that the release time is the very same for each model.

As a remark, note that the objective is not to optimize the power capture, but rather to have an identical control strategy for each model configuration. Indeed, Chapter 4 shows how the *optimal* PTO damping coefficient and latching duration are significantly different, when nonlinearities are included.

6.5 Results

The response amplitude operator is studied, with and without latching control applied, for different T_w and H_w , comparing the (fully-linear) LFKnoD model to the NLFKaD model, as shown in Fig. 6.3. On the one hand, without control, LFKnoD and NLFKaD curves overlap, due to the negligible impact of FK and viscous nonlinearities. In fact, the uncontrolled RAO is close to unity, and almost constant, so the floating sphere tends to behave as a wave follower, with a consequent small relative motion with respect to the free surface elevation.

In contrast, the latching control strategy exaggerates the amplitude of motion, increasing the relevance of FK and viscous nonlinearities. Consequently, the fully-linear model significantly overestimates the response of the device relative to the NLFKaD model. Furthermore, the NLFKaD model is represented by different curves at different H_w , decreasing as H_w increases, highlighting that such nonlinear effects become more important as the wave energy content increases.

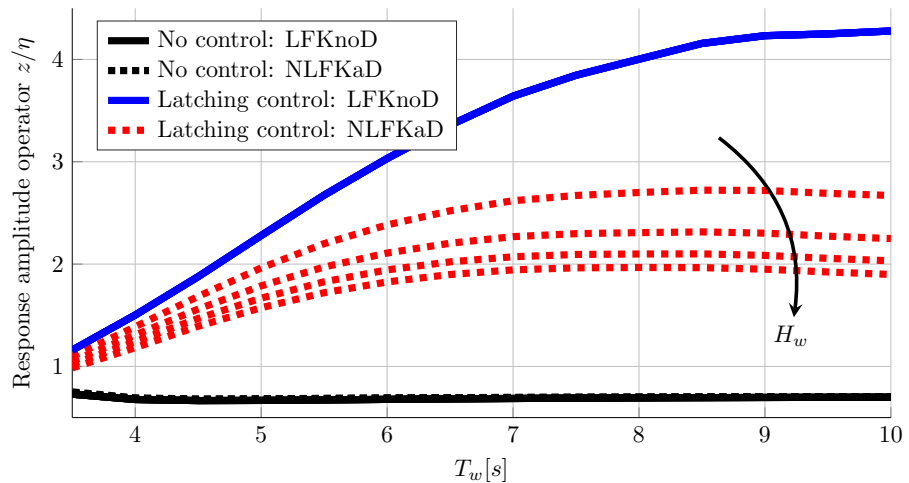


Figure 6.3: Response amplitude operator, with and without latching control, considering LFKnoD and NLFKaD models.

The accuracy of the results obtained with the PoT models is evaluated against the CFD results. Considering one period of the steady state response, an error index is defined, for each model j , through the normalized root mean squared error (NRMSE) of the vertical displacement z_j , as follows:

$$NRMSE_j = \frac{1}{\overline{z_{CFD}}} \sqrt{\frac{\sum_{t_i=t_0}^{t_0+T_w} (z_{CFD}(t_i) - z_j(t_i))^2}{n}} \quad (6.6)$$

where n is the number of time samples, and $\overline{z_{CFD}}$ is the difference between the maximum and minimum values of the displacement in the CFD model.

Figure 6.4 shows the error indices for all wave conditions and models, with latching control. For each wave period and height, six sets of bars are grouped together, three in the horizontal direction, and two in the vertical direction. The three bar sets represent the FK force modelling options, respectively, from left to right: linear (LFK), nonlinear restoring (NLR), and nonlinear FK force (NLFK). Note that the two modelling options for the nonlinear FK force (re-meshing (NLFKr) and algebraic (NLFKa) approaches) return exactly the same results, with different computational times, so they are represented with the same bar, for brevity. For each FK force modelling option, the upper bar is without drag (noD), whereas the lower one includes drag (D). In interpreting the results shown in Fig. 6.4, consider that the final total accuracy is a consequence of several interacting modelling errors, which may add up or cancel out, as discussed in Sect. 6.3.1.

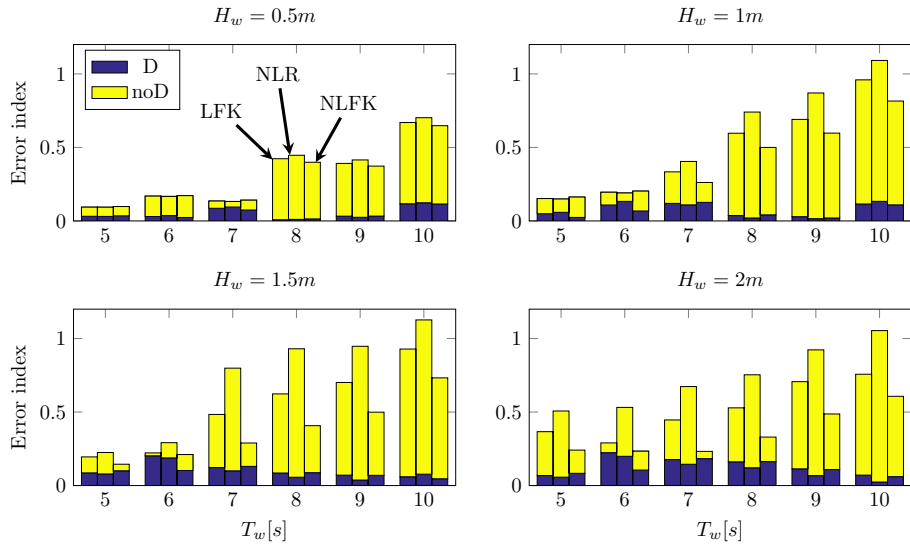


Figure 6.4: Error index, as defined in equation (6.6), for different wave heights H_w and periods T_w . For each wave, six bars are grouped together: according to the notation in Sect. 6.3, three in the horizontal direction, from left to right, for FK force modelling options (LFK, NLR, NLFK) and two in the vertical direction for the absence (noD, on the top) or presence (D, on the bottom) of viscous drag in the model.

Overall, it is clear that the inclusion of viscous drag in the model significantly reduces the error in the resulting estimation of displacement, regardless of the FK force modelling option. In general, when viscous drag is implemented, errors are quite low for all the wave conditions considered. Furthermore, when drag is modelled, the differences between different FK force models is also relatively small. The reason of such a reduction in differences between FK models is that viscous drag is restraining the device motion to such an extent that the variations in instantaneous wetted surface are also limited, making nonlinear FK force modelling less relevant.

Conversely, when drag is not implemented, considerable differences between FK force models (and larger errors) may arise for more energetic waves (large periods and/or heights). Furthermore, since the nonlinear restoring force model (NLR) loses the “mitigation” effect, described in Sect. 6.3, larger errors are consistently obtained, compared to

the linear model. Overall, the accuracy of the results is largely attributed to the implementation of the FK force *only* if viscous damping is absent, under controlled conditions. A more detailed discussion about the reasons why viscous drag is more important than nonlinear FK force, and the way in which the dynamics of the device are changed by such nonlinearities, is presented in Sect. 6.6.

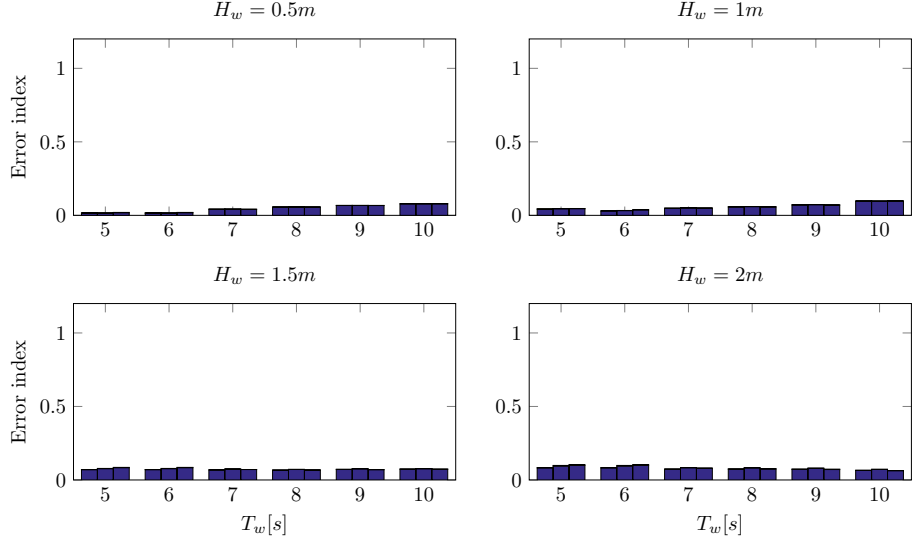


Figure 6.5: Error index as in Fig. 6.4, but without latching control.

As in Fig. 6.4, Fig. 6.5 shows the error indices without control applied, for all the wave conditions considered. Comparing Fig. 6.5 with Fig. 6.4, it is clear that lower errors are obtained in the uncontrolled case. Furthermore, differences between the models are negligible since, as expected, the absence of a control strategy results in small relative motion, with consequent weak nonlinearities. Consequently, for the uncontrolled case, linear models return approximately the same results as nonlinear models, but with a lower computational price. Section 6.6 shows how the control strategy prevents the device from behaving as a wave follower since, in the absence of control, relative body/fluid displacement and velocity are small.

The error index is not the only quality indicator to evaluate the performance of the models. Including nonlinearities in the model has a complexity and computational cost. Ultimately, the computational speed of a model has to be evaluated with respect to real time; therefore, the ratio between the computational time t_{comp} , and the simulated time t_{sim} , is considered.

For PoT models, a second order Runge-Kutta scheme is implemented in Matlab, on a machine with an Intel(R) Xeon(R) CPU (E5-1620 v3 @ 3.50GHz) processor, with 16.0 GB RAM and Windows 7 Professional 64 bit. CFD calculations are performed on a high-performance computing cluster, made available by the Irish Centre for High-End Computing (ICHEC) [177]. Each core of the machines in ICHEC carries an Intel Xeon E5-2695 2.4 GHz processor, and several nodes can be used, each one with 24 cores. For the purpose of this study, simulations used from 24 to 192 cores, according to the computational domain and simulation time, in order to meet the 72 hours time limit imposed by ICHEC. In order to have a fair comparison, computational times have been scaled linearly, as if only one core was used, therefore introducing an up-scaling factor of about 1-2 order of magnitudes, between 24 and 192. Note that an error is introduced since, in general, the computational time does not scale linearly with the number of processors used. The time ratio-error index couples, for the nine models and 24 wave conditions considered, are plotted in Fig. 6.6.

Each point is identified by two concentric markers: the outer marker indicates which

of the four FK force modelling options is used, while the inner one indicates the presence/absence of viscous drag. The cloud of points for each model is fitted with an ellipse, in order to define a clear region in the graph. Since the CFD model is the benchmark model, the resulting error, by definition, is zero; therefore, it is represented with a line, and no markers are used.

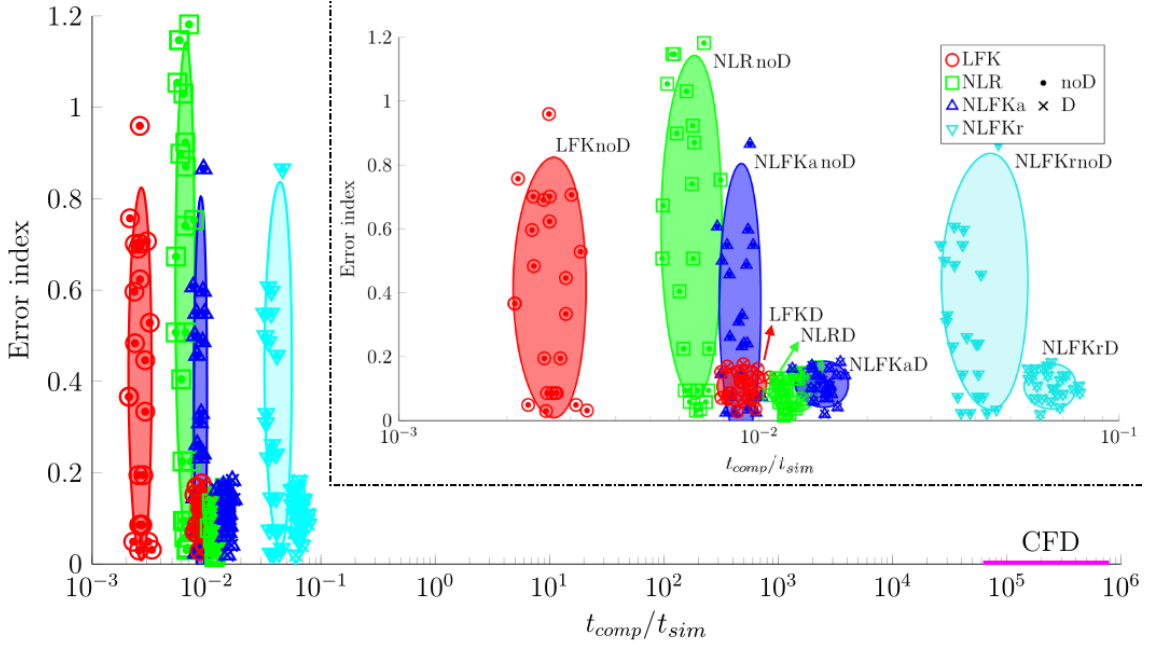


Figure 6.6: Error index, as defined in equation (6.6), plotted against the ratio between computational time t_{comp} and simulation time t_{sim} . For each wave, two concentric markers are used: according to the notation in Sect. 6.3, the outer marker indicates which of the four FK force modelling options while the inner one indicates the presence/absence of viscous drag. For each model, the cloud of points has been fitted with an ellipse.

As expected, the CFD computational time is several orders of magnitude longer than the other models, requiring from 10^5 to 10^6 seconds to perform one second of simulation (using the same comparative hardware capabilities as the other models). As a result of the logarithmic scale of the horizontal axis, PoT models are squeezed to the left hand side of Fig. 6.6.

Consistent with Fig. 6.4, Fig. 6.6 demonstrates that NRMSE for models without viscous drag are much larger than when viscous drag is included. Furthermore, errors in the linear model are smaller than in the nonlinear restoring force model, but larger than in the nonlinear FK force model. With regard to the computation time ratio, the nonlinear restoring force and algebraic nonlinear FK force models are up to an order of magnitude slower than the linear FK models. On the other hand, the re-meshing approach model (NLFKr) returns identical errors to the algebraic model (NLFKa), but at computational time almost an order of magnitude larger. Finally, the inclusion of viscous drag increases the computational time of each of the four FK models, but in a more pronounced way for the linear model, than for the others. The mean value and the relative standard deviation for the computational times of each PoT model have been summarized in Table 6.2.

As already mentioned in Chapter 4, it is important to highlight that the NLFKr model is implemented in Fortran, which is a language likely to be between one and two orders of magnitude faster than Matlab, which is used for all the other PoT models. Therefore, the relative computational times of PoT models, shown in Fig. 6.6 and Table 6.2, are potentially reducible, if lower level coding languages are employed, in particular considerably increasing the gap between NLFKa and NLFKr.

Table 6.2: Mean and relative standard deviation of computational time for each PoT model, as shown in Fig. 6.6. Note that all models are coded in Matlab, except for NLFKnoD and NLFKnoD, which are coded in Fortran, inherently one or two order of magnitude faster than Matlab.

$\log(t_{comp}/t_{sim})$	Mean $\cdot 10^{-3}$	Relative standard deviation
LFKnoD	2.63	12.7%
NLRnoD	6.43	9.7%
NLFKanoD	8.90	7.9%
NLFKnoD	38.1	10.4%
LFKD	9.06	8.1%
NLRD	12.1	6.9%
NLFKaD	15.5	7.1%
NLFKnoD	65.0	9.8%

6.6 Discussion

The relevance of FK and viscous nonlinearities, for the floating sphere considered in this study, depends mainly on the amplitude of the device motion with respect to the free surface elevation. In the uncontrolled case, small relative motions around the free surface are obtained, with resulting low impact of FK and viscous nonlinearities. Consequently, nonlinearities are enhanced by the control strategy, whose main effect is to considerably enlarge the relative motion between the floater and the free surface. In particular, when no control is applied, the device behaves as a wave follower, since the relative displacement is not significant. Figure 6.7 shows a graphical representation of the device motion, obtained with the CFD model, with and without control applied: Figs. 6.7a and 6.7b show, respectively, the peak and bottom position of the floater without control, while Figs. 6.7c and 6.7d show, under controlled conditions, the peak and bottom position, respectively, at the unlatching instant. Without control, the center of the body is approximately at the free surface elevation height; therefore, the floater behaves as a wave follower, and nonlinearities are negligible. On the contrary, when control is applied, a larger amplitude of motion, and significant variations in the instantaneous wetted surface, arise.

Figure 6.8 shows the complete operational space (relative displacement and relative velocity) of the steady state response of the device, for an example of a regular wave, with and without control applied. Nonlinearities in FK forces depend on the variation in the instantaneous wetted surface, and therefore on the relative displacement between the device and the free surface elevation. Likewise, viscous drag forces have a quadratic dependence on the relative velocity. It is clear that the action of the controller considerably enlarges the operational space and, consequently, the relevance of nonlinearities. Indeed, only one curve is presented for the uncontrolled case, since the response is largely the same, irrespective of which model is used. On the other hand, the fully-linear and fully-nonlinear models, which are presented for the controlled case as two extreme representative implementations, show large differences in the simulated response, highlighting how nonlinearities are enhanced by the controller.

However, the device is normally working under controlled conditions, since the objective is to increase power absorption. Indeed, one of the most fundamental outputs of a simulation is the estimation of power production. Under controlled conditions, neglecting to model viscous drag effects may cause a significant overestimation of power production, leading to overly optimistic expectations. Figure 6.9 shows the ratio between the power estimation according to the linear and the fully-nonlinear models, while Table 6.3 tabulates the ratio for all the models. The ratio presented in Fig. 6.9 varies between 1 and 4.45, and the overall trend is increasing with both wave height and period, as more energetic

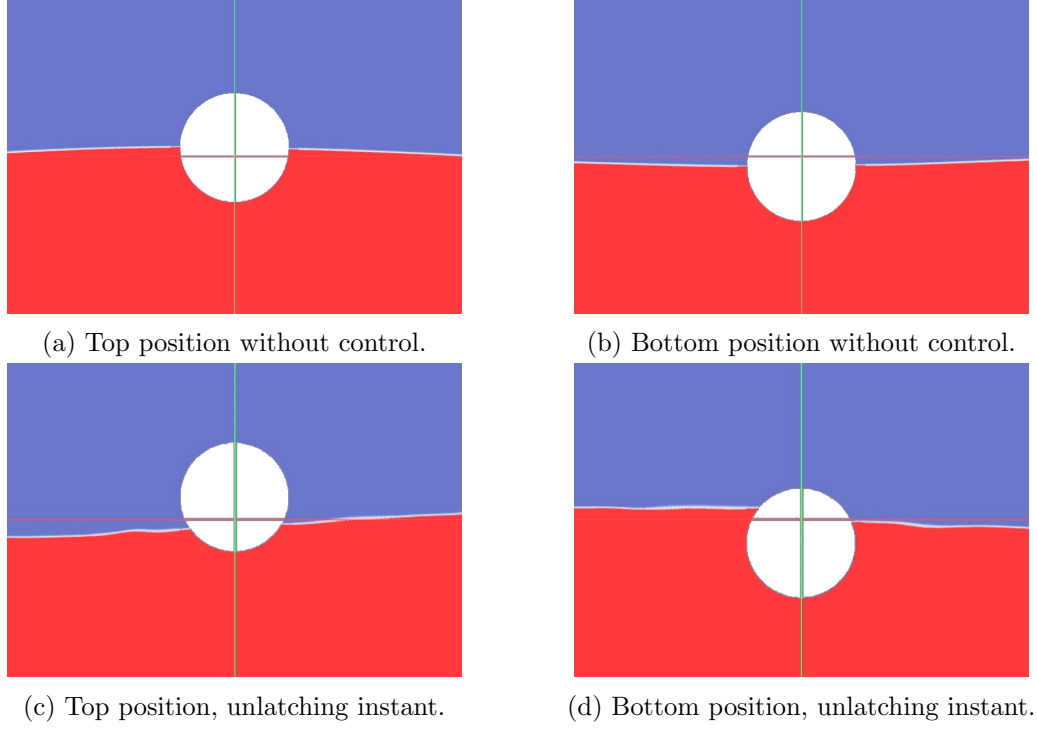


Figure 6.7: Screen-shots of CFD simulations with and without control applied [14].

waves cause larger oscillations. The translucent plane in Fig. 6.9 corresponds to a unity power ratio, which is the fidelity benchmark.

Overall, Table 6.3 confirms the trend shown in Figs. 6.4 and 6.9. Additional information, that is clear from Table 6.3, is that the ratio for the models with drag, especially those with additional nonlinear FK force, are relatively low (which is good) but quite variable, and can be even less than unity. Such a trend suggests that the drag coefficient, which would allow the best fit with the CFD model and, consequently, ensure a unity power ratio, is variable, and lower than the drag coefficient chosen according to [111]. Such an issue is further analysed in Chapter 7.

A closer look at how nonlinear FK and viscous drag forces influence the dynamics of the device can give further insight into the relevance of each nonlinearity, and the way they interact with each other. Figure 6.10 shows nonlinear FK and viscous drag forces, for one period of the periodic response, under the action of one sample regular wave. The

Table 6.3: Ratio between the predicted power outputs according to each of the potential theory-based models and the fully-nonlinear (CFD) model.

P/P_{CFD}	$H_w[m]$												
	0.5			1			1.5			2			
5	1.02	1.02	1	1.13	1.15	1.04	1.55	1.61	1.34	2.16	2.65	1.55	No drag
	0.79	0.79	0.78	0.67	0.68	0.65	0.83	0.84	0.79	0.99	1.03	0.90	Drag
6	1.06	1.07	1.03	1.28	1.32	1.14	1.63	1.80	1.24	1.84	2.70	1.11	No drag
	0.64	0.64	0.63	0.60	0.60	0.58	0.62	0.63	0.58	0.60	0.62	0.54	Drag
7	1.21	1.22	1.17	1.96	2.11	1.69	2.52	4.13	1.78	2.38	3.25	1.46	No drag
	0.71	0.72	0.70	0.75	0.76	0.73	0.77	0.79	0.72	0.68	0.70	0.62	Drag
8	2.22	2.28	2.12	2.92	3.31	2.46	3.08	4.83	2.25	2.74	3.59	1.72	No drag
	1	1.01	0.99	0.95	0.96	0.92	0.87	0.90	0.83	0.71	0.75	0.67	Drag
9	2.10	2.16	2.03	3.31	3.86	2.81	3.35	5.32	2.54	3.42	4.38	2.23	No drag
	0.95	0.96	0.94	1.00	1.03	0.98	0.90	0.93	0.86	0.82	0.87	0.78	Drag
10	3.10	3.19	2.99	4.45	5.22	3.84	4.39	6.85	3.41	3.54	4.90	2.60	No drag
	1.29	1.30	1.27	1.29	1.33	1.26	1.13	1.18	1.09	0.93	0.99	0.89	Drag
	LFK	NLR	NLFK	LFK	NLR	NLFK	LFK	NLR	NLFK	LFK	NLR	NLFK	

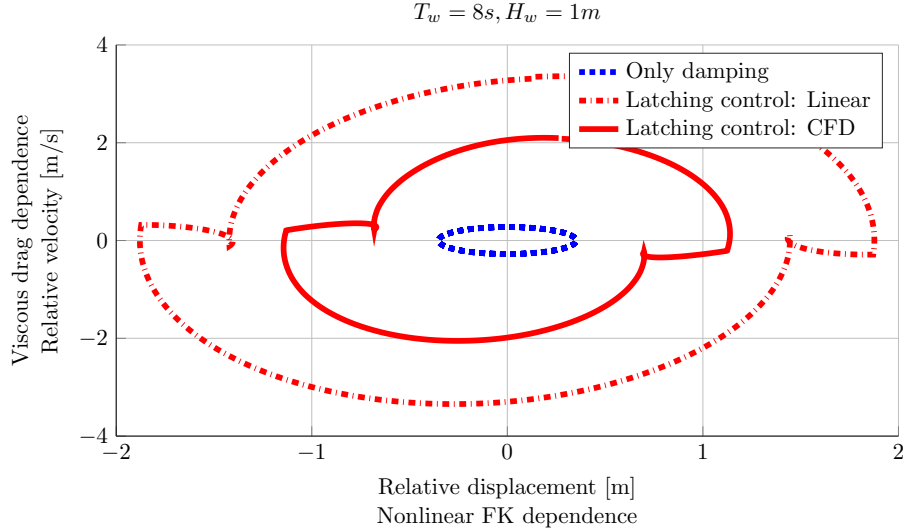


Figure 6.8: Steady state operational space for a regular wave with period $T_w = 8s$ and height $H_w = 1m$. For the uncontrolled case (PTO acting as a simple damper), only one curve is shown since all models substantially overlap. Conversely, under controlled conditions, the fully-linear and fully-nonlinear responses are significantly different and enlarged with respect to the uncontrolled case.

relative displacement is presented on a second vertical axes, in order to evaluate the phase between the response and the forces.

In order to highlight the differences due to modelling only, the linear FK force calculation has been applied to the operational space given by the nonlinear model. Finally, the latching interval is shaded (in red), to indicate that external hydrodynamic forces actually have no influence on the device motion, since the latching mechanism is preventing any body motion. Such intervals are those where the largest relative displacement and, consequently, the largest differences between linear and nonlinear FK forces are found. Conversely, the device velocity is zero, with a correspondingly null viscous drag force.

On the other hand, the regions where the device is free to move, and therefore sensitive to modelling errors, are the regions where the highest velocities and smallest relative displacements are achieved. As a consequence, differences between linear and nonlinear FK forces are smaller, whereas viscous drag, which is completely absent in the linear model, has its strongest influence on the device.

An alternative way of analysing how each force component influences the system's dynamics is to consider its instantaneous relative importance: at every time instant, a force ratio is defined as the fraction between the absolute value of the particular force component, and the sum of the absolute values of all the force components on the right hand side of the equation of motion (6.1). Absolute values are used in order to bound the ratios between 0 and 1; otherwise, due to phase differences, each ratio could be larger than 1, positive or negative. Fig. 6.11 shows such FK and viscous drag ratios, for regular waves with T_w 8s, for four different values of H_w , where the FK ratio is the sum of the static FK ratio and dynamic FK ratio. As in Fig. 6.10, the latched intervals are shaded (in red).

Considering the free response interval (where the body is not latched and free to move), as the viscous drag ratio increases (due to increasing velocities), the FK ratio decreases. Moreover, as H_w increases, the viscous drag ratio increases, making the FK ratio decrease as a consequence. In contrast, the linear FK ratio increases with H_w , since viscous drag is absent in the fully-linear model.

Figure 6.11 shows the continuous variation in the different force ratios throughout

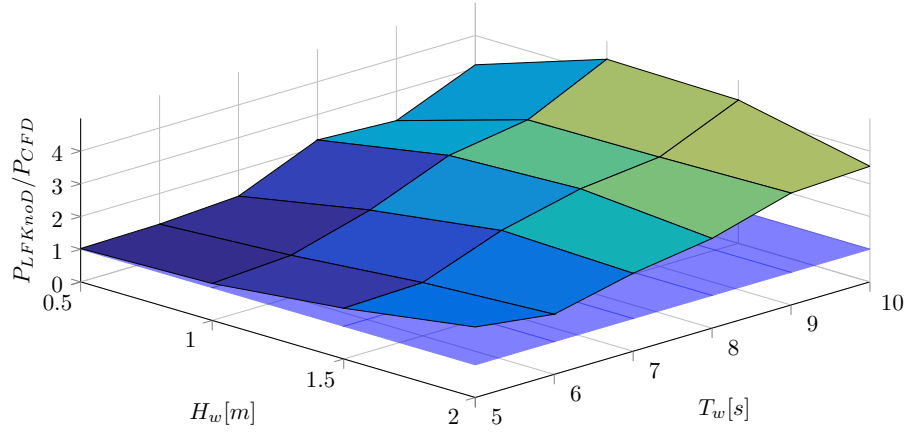


Figure 6.9: Ratio between the predicted power outputs according to the fully-linear model (LFKnoD) and the fully-nonlinear model (CFD). The translucent plane indicates the unity ratio, which corresponds to maximum fidelity.

one period of motion. In order to have a more global view, the range of variation (from minimum to maximum) of such ratios are shown in Fig. 6.12, for all the sea conditions considered in this study. Note that the minimum FK ratio occurs at the maximum of the drag ratio and, likewise, the maximum FK ratio (almost 100%) occurs at the minimum of the drag ratio (equal to zero).

The maximum viscous drag ratios and the minimum linear FK ratios increase as H_w increases, whereas the nonlinear FK ratio bounds remain relatively constant. Furthermore, the difference between the linear and nonlinear representation of FK forces is significant only at the lower bound, varying from a minimum of 9% (at T_w 5s, H_w 0.5m), to a maximum of 28% (at T_w 10s, H_w 2m).

As a final remark, consider that the FK ratio, plotted in Figs. 6.11 and 6.12, is the sum of the absolute values of the static and dynamic FK ratios, in order to be consistent with the equation of motion in (6.1). Furthermore, such a choice enhances the clarity and readability of Figs. 6.11 and 6.12. Recognising that these two operations don't commute, consider now an interchange of the order of summation and absolute value: first compute the total FK force, as the sum (with sign) of its static and dynamic components, and afterwards take the absolute value. Since F_{FK_s} and F_{FK_d} are not in phase, as shown in Chapter 5, they partially cancel out. Consequently, the minimum values of the total FK force ratio drop drastically, reaching values of about 1-2%. Likewise, the maximum viscous drag ratios considerably increase, between 1.8 and 2.5 times the values shown in Fig. 6.12.

6.7 Conclusions

The choice of an appropriate mathematical model for wave energy converters is not straightforward, and needs to define an appropriate compromise of accuracy and computational cost to satisfy the specific requirements of the application the model is intended for.

This chapter analyzes the performance of nine mathematical models, when a device is operating in the power production region, eight of which are based on potential theory, with different modelling options for FK and viscous drag forces, while the ninth model is based on CFD. The models have been evaluated according to accuracy and computational time indexes.

Overall, it can be broadly concluded that Froude-Krylov and viscous drag nonlinearities are insignificant for uncontrolled small heaving floating devices, operating at wave periods

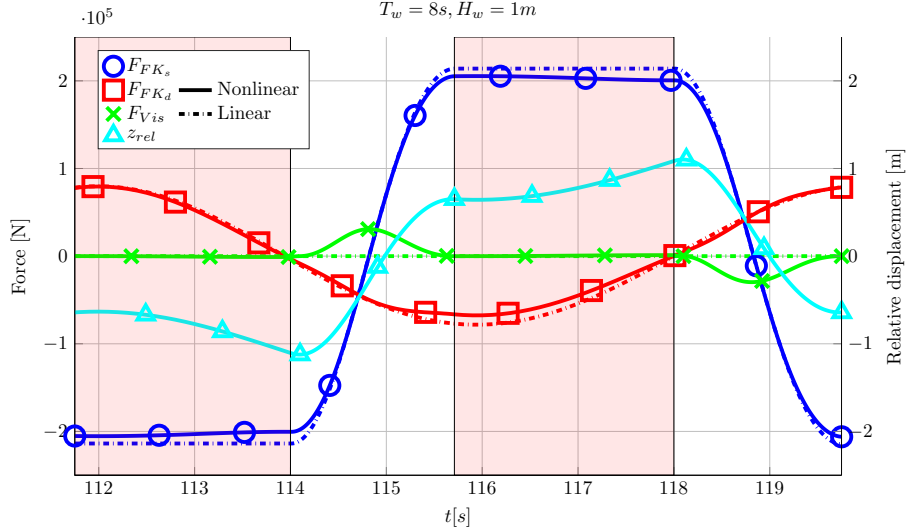


Figure 6.10: Relative displacement z_{rel} , Froude-Krylov and viscous drag forces for one period of the steady response for a wave with period $T_w = 8s$ and height $H_w = 1m$, according to NLFKaD model. Linear force calculations have been applied to displacement and velocity obtained with the nonlinear model in order to compare modelling differences only.

away from resonance; therefore, linear models can be preferred. Nevertheless, a control strategy is likely to be included in a real WEC application, since the primary objective of a wave energy converter is to maximize power absorption.

Results suggest that, under latching control conditions, viscous forces are large enough to reduce the body's displacement to such an extent that a linear description of FK forces becomes quite accurate. However, such a result is substantially dependent on the latching control strategy, which is aggressive enough to generate large velocities, and locks the device motion when FK nonlinearities are more relevant. Different control strategies are likely to indicate a different relative importance of viscous and FK nonlinearities.

In general, accurate models do not necessarily imply accurate results, and vice versa: multiple sources of modelling errors interact, in a constructive or destructive way, in order to produce the total error – and accuracy – of the model. In particular, for the specific case study considered in this chapter, it is found that modelling errors due to the linear representation of both F_{FK_s} and F_{FK_d} partially cancel out (LFK model), so that the total error is lower than the case where only a dynamic FK modelling error is present (NLR model), but greater than the case where no FK modelling error is present (NLFK models).

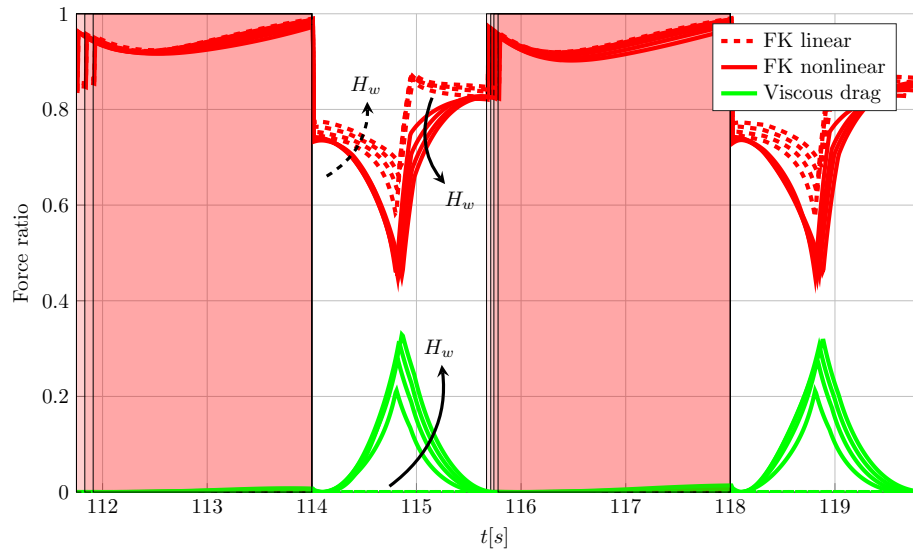


Figure 6.11: Froude-Krylov and viscous drag force ratios for a wave with T_w 8s and four H_w , according to NLFKaD model. Linear force calculations have been applied to displacement and velocity obtained with the nonlinear model in order to compare modelling differences only.

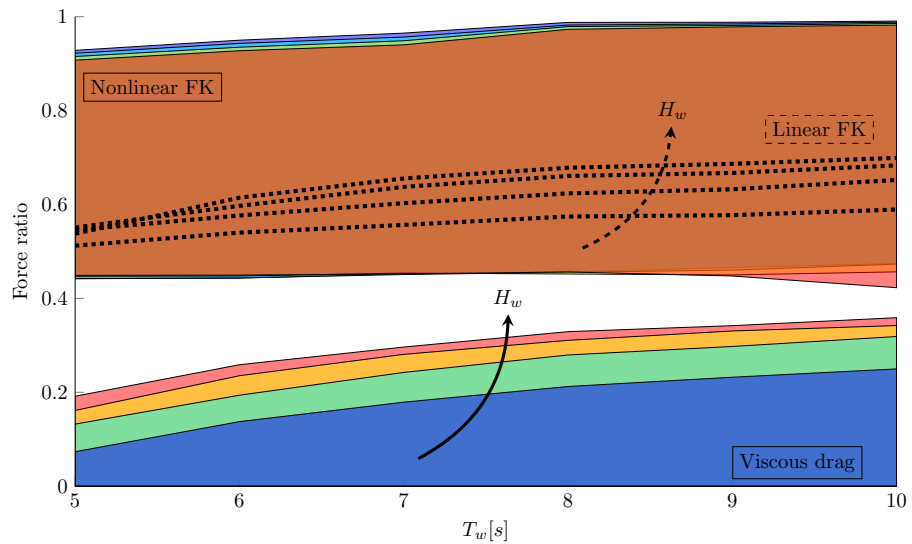


Figure 6.12: Ranges of variation (from minimum to maximum) of Froude-Krylov and viscous drag ratios.

Consistency of viscous drag identification tests for wave energy applications

7.1 Motivation

Chapter 6 demonstrates the importance of including viscous effects in the mathematical model, especially when aggressive control strategies are implemented. Viscous drag forces in mathematical models for wave energy converters are usually modelled by means of a term based on the Morison equation. Due to large relative velocities, induced by control strategies in order to increase power absorption, viscous losses can have a high impact on the model accuracy and, in turn, on model-based power optimization control strategies. Despite the importance of reliable estimation of the drag coefficient in the Morison equation, much inconsistency and low trustworthiness is found in the literature, both concerning the values themselves, and the identification methods. Indeed, drag identification for wave energy applications is particularly challenging, mainly due to the device dimensions, characteristic flow regimes, large motion and, in particular, the presence of the free surface. An ideal identification test would be able to replicate the full complexity of the flow, and concurrently to isolate viscous forces from other forces and nonlinear effects. This chapter seeks to discuss the inherent challenges to drag identification, in the context of wave energy applications. In addition, different identification techniques are implemented, evaluated, and compared, with regard to the estimation of the drag coefficient for a floating heaving point absorber.

7.2 Introduction

Accurate modelling of the interaction between wave energy converters and the surrounding fluid is not trivial, and viscous effects should be carefully taken into consideration, as discussed in Chapter 6. [60] shows that, under *uncontrolled* conditions, viscous drag forces are negligible for HPAs. However, real wave energy systems generally include a control strategy, and while, in HPAs, viscous forces may be relatively small, compared to nonlinear FK forces, as discussed in Chapter 5, viscous effects may become important under *controlled* conditions. This is shown to be particularly true, as shown in Chapter 6, when latching control is applied, which is an aggressive discrete controller, exaggerating the device velocity and, therefore, enhancing viscous effects. Furthermore, modelling nonlinearities is crucial for the control strategy to achieve maximum power extraction: despite viscous drag introduces losses, the optimal control forces are much more effective if they take into account such losses in the optimization strategy, as shown in [178].

The most common way of including viscous drag effects in mathematical models for

WECs is through a Morison-like term [60], based on the Morison equation [97]. The Morison equation was introduced in the 50s, for describing forces on cables of oil platforms and, afterwards, it has been applied in the wave energy field, to describe viscous effects. Despite the fact that several decades have passed, there is still some inconsistency in the literature about drag coefficient values for wave energy applications. As an example, drag coefficients for a flap-type device found in the literature vary from 1.9 [31] to 8 [111]. Likewise, the drag coefficient for the Wavestar device [66], which is a piercing heaving sphere, is 0.2 according to [179], 0.5 according to [180], and 1.0 according to [111]. Furthermore, once the drag coefficient is chosen, there is still some uncertainty about the value itself, since often a sensitivity analysis is performed, with variation from zero to twice the value, as in [111].

In addition, there is no consensus with regard to which drag coefficient estimation technique should be used. Either the standard literature about viscous drag forces, from outside the wave energy field, is used (constant flow around a fully-submerged body), as in [181], or specific tests are performed, in real or numerical wave tanks. Considering a piercing HPA, [60] carries out harmonic prescribed motion tests with a fully-submerged device. A variation of such an approach is proposed in this study, with the addition of a sawtooth motion (triangle wave) displacement profile, instead of harmonic. [179] performs radiation experiments instead, so that two fluid phases are considered (water and air), and the free surface is modelled. Finally, the drag coefficient can also be identified from the response of the device, subject to incoming waves [13].

Inaccuracies in the drag coefficient estimation process, for wave energy applications, are due to the flow conditions reproduced in the experiment, which are often not consistent with, and/or descriptive of, the actual flow around a WEC responding to waves, especially under controlled conditions. Indeed, wave energy applications are particularly challenging, due to the characteristic dimensions of the devices, the presence of the free surface (two fluid phases, non-constant wetted surface, radiation and diffraction forces), large displacements and velocities induced by the control strategy and, overall, a complex fluid flow around the body.

Five different identification experiments (single phase constant flow, single phase harmonic and sawtooth prescribed motion, radiation tests, and wave response) are implemented in this chapter and compared, discussing their appropriateness and applicability in the context of wave energy applications. OpenFOAM [154] is the CFD software used for the three-dimensional numerical simulations, to extract the hydrodynamic force acting on the device, as in Chapter 3. The drag coefficient is then evaluated by means of a least-square curve fitting against the Morison equation.

7.3 Flow around a wave energy converter

Uncertainties and low trustworthiness of the drag coefficient for WECs are mainly consequences of the complex and challenging fluid flow around a device, in its operating conditions. In this chapter a piercing HPA is considered as an example, based on the Wavestar device [66]. The geometry is a half submerged sphere of 5m diameter, and a latching control strategy is implemented.

In general, WECs are large bodies, therefore experimental tests in real wave tanks are usually performed at small scale. An inherent consequence of scaling is the change of flow regime, which is typically laminar at small scale, while turbulent at full scale [171]. Such scalability issues may be overcome by using numerical wave tanks in a CFD environment. However, reliable numerical modelling of turbulence in CFD is a challenging task, requiring time and user experience [182]. Some of the main issues are discussed in Sect. 7.4.1.

Apart from the geometry, the flow regime around the device is determined by the relative velocity of the fluid with respect to the body. Indeed, a dimensionless number,

representative of the flow regime, is the Reynolds number [168], which is defined, for a fixed body fully-submerged in a fluid with constant velocity V_0 , as:

$$Re = \frac{V_0 L_c}{\nu} \quad (7.1)$$

where L_c is the characteristic length of the body (the diameter in the case of a sphere), and ν is the kinematic viscosity. However, due to the action of waves, WECs are typically oscillating; therefore, V_0 refers to the maximum relative velocity achieved during the oscillation [168]. Another relevant dimensionless number, used to characterize the flow around oscillating bodies, is the Keulegan-Carpenter (KC) number [168], defined for fixed fully-submerged bodies in harmonic flow, as:

$$KC = \frac{2\pi A_0}{L_c} \quad (7.2)$$

where A_0 is the amplitude of motion of the fluid particles.

An effective identification experiment should reproduce Re and KC numbers consistent with the flow around a WEC, in its operating conditions. In particular, it is important to consider the response of the device under controlled conditions, since the operational space of relative amplitude and relative velocity is considerably enlarged, as shown, for example, in Fig. 6.8 of Chapter 6.

The response of the HPA, under controlled conditions, is studied for a set of regular wave conditions, with wave periods ranging from 5s to 10s, and wave heights ranging from 0.5m to 2m. The resulting KC numbers are found to lie between 0.56 and 3.11, while Re numbers are between $3.56 \cdot 10^6$ and $1.79 \cdot 10^7$. Since the laminar-turbulent transition of a sphere is at a Re of about 10^6 [182], the resulting flow can be considered to be highly turbulent.

Nevertheless, note that the definition of Re and KC numbers, as well as standard viscous drag theory (outside the wave energy field), refers to fully-submerged bodies. On the contrary, (floating) wave energy applications have to deal with the presence of two fluid phases (water and air), and the dynamical changes of the free surface elevation, making Re and KC numbers less representative of the resulting complex flow regime.

When a piercing device is considered, the wetted surface of the body is continuously changing, and consequently the magnitude of the hydrodynamic force, including the viscous drag force. Furthermore, forces related to the deformation of the free surface elevation come into play, namely radiation and diffraction forces. Highly nonlinear effects may arise, especially when the controller induces large amplitudes of motion, including air bubbles trapped in the fluid close to the surface of the body, splashes, and water jets. As an example, Fig. 6.7, in Chapter 6, shows how the latching control strategy causes large variations of the wetted surface of a heaving sphere.

An ideal drag identification test would be able to replicate the full complexity of the flow around the device, and concurrently isolate viscous forces. Unavoidably, as the flow complexity increases, more nonlinear effects and interactions occur, making the isolation of the viscous drag force more challenging. Several different identification tests exist which, based on different choices and assumptions, compromise some fidelity of flow replication, in order to attempt to isolate the drag force. Five different drag coefficient identification techniques are described and compared in Sect. 7.4.

7.4 Identification techniques

The dynamics of a heaving floating WEC can be described, as discussed in Chapter 6, in the linear potential theory framework [45], by Newton's second law:

$$m\ddot{\mathbf{z}} = \mathbf{F}_{FK_{st}} + \mathbf{F}_{FK_{dy}} + \mathbf{F}_D + \mathbf{F}_R + \mathbf{F}_{PTO} + \mathbf{F}_{vis} \quad (7.3)$$

Usually, \mathbf{F}_{vis} is based on the Morison equation [97], which was introduced in the '50s to describe wave forces on cables of offshore structures, and is used to model the *total* force acting on fixed small bodies, compared to the wave length:

$$\mathbf{F}_{Mor} = -\frac{1}{2}\rho C_d A_d |\mathbf{V}_0| \mathbf{V}_0 - \rho (1 + C_m) V_d \dot{\mathbf{V}}_0, \quad (7.4)$$

where ρ is the fluid density, C_d is the drag coefficient, C_m is the inertia coefficient, A_d is the characteristic area, \mathbf{V}_0 is the undisturbed flow velocity, and V_d the volume of displaced fluid.

Consequently, the literature outside the wave energy field, concerning the Morison equation, often refers to cylindrical (cable-like) small bodies, with the consequent *Re* and *KC* numbers. Conversely, in wave energy applications, only the velocity term of equation (7.4) is used to describe viscous effects acting on large bodies, considering the relative velocity between the velocity of the floater $\dot{\mathbf{z}}$ and the undisturbed flow velocity [60]:

$$\mathbf{F}_{vis} = -\frac{1}{2}\rho C_d A_d |\dot{\mathbf{z}} - \mathbf{V}_0| (\dot{\mathbf{z}} - \mathbf{V}_0), \quad (7.5)$$

Note that the characteristic area is the projection of the instantaneous wetted surface onto a plane normal to the motion. Since equation (7.5) is proportional to C_d , and to the relative velocity squared, the viscous force is more sensitive to changes of velocities, rather than C_d . Therefore, even though C_d typically decreases with larger velocities [168], the overall viscous force increases.

In order to identify the drag coefficient C_d in (7.5), specific experiments are performed, in real or numerical wave tanks, and the total force acting on the body is measured. Then, \mathbf{F}_{vis} is isolated from other (eventually present) forces, and C_d is estimated as the one which minimizes the error between the measure and the model, using, for example, a least squares approach, as shown in [60].

Experiments are designed in order to replicate (to some extent) the flow surrounding the device, in its operating conditions, and concurrently allow the viscous drag force to be isolated from other hydrodynamic forces. Major flow characteristics, discriminating between different estimation techniques, regard the number of fluid phases (one –fully-submerged body–, or two –floating body–), the relative flow (constant, harmonic, sawtooth), and the body motion (fixed, prescribed, dynamic response). Finally, it is important to use the identification tools in conjunction with large displacements and velocities (hence *KC* and *Re*), appropriate to wave energy applications, which may be different from other applications.

In this chapter, the drag coefficient is identified for a floating heaving sphere, subject to latching control. The following approaches are considered and compared:

- (A) Fully-submerged, fixed body, constant flow: see Sect. 7.4.1
- (B) Fully-submerged, prescribed motion, harmonic flow: see Sect. 7.4.2
- (C) Fully-submerged, prescribed motion, sawtooth flow: see Sect. 7.4.3
- (D) Floating, prescribed motion, harmonic flow (radiation test): see Sect. 7.4.4
- (E) Floating, dynamic response: see Sect. 7.4.5

The geometry studied is a 5m diameter sphere which, when the free surface is modelled (approaches (D) and (E)), has its centre at the still water level. CFD simulations, for approaches (A) to (D), have been performed using 24 cores, each one carrying an Intel

(R) Xeon (R) CPU E5-2440 0 @ 2.40GHz processor. Simulations for approach (E) are more computationally demanding; therefore, they have been performed on a high-performance computing cluster, made available by the Irish Centre for High-End Computing (ICHEC) [177].

7.4.1 Fully-submerged, fixed body, constant flow

Established viscous drag theory refers to bodies immersed in a single fluid (usually air or water), subject to constant unidirectional flow. The Re number is defined for such flow conditions, and it determines the point of passage from laminar to turbulent flow, which happens at a Re number of around 10^6 for a sphere. One main phenomenon involved in the viscous drag force is the point of flow detachment, which moves upstream around the surface of the sphere, as the Re number increases [182].

A constant flow around a fixed body is a complex, but well-known process, and a significant amount of literature deals with experimental tests or CFD numerical simulations. Achieving accurate results with CFD numerical tools requires time and user experience, but broad guidelines are available in the literature [183]. In particular, accurately estimating hydrodynamic forces at high Re numbers requires an appropriate description of turbulences and vortices close to the surface of the body. An important role is played by the flow solver: large eddy simulation (LES) solvers should be preferred to Reynolds averaged simulation (RANS) solvers, since they are able to solve turbulent flows more accurately. The k- model has been implemented in this study, as it is common practice in the wave energy field [80]. However k- and SST- k- models are valid alternatives.

Another crucial parameter is the thickness of the boundary layer, namely the distance of the first mesh cell from the body surface. The quality of the boundary layer mesh is evaluated by means of a dimensionless parameter, called y^+ , which should be between 40 and 200, when wall functions are used [183]. The y^+ number is defined as follows:

$$y^+ = \sqrt{\frac{\tau_w}{\rho}} \frac{y}{\nu} \quad (7.6)$$

where τ_w is the wall shear stress, and y the distance from a wall adjacent cell to the wall. However, there are also other important factors to be evaluated in order to assess the quality of the mesh and of the boundary layer (e.g. aspect ratio, expansion ratio, skewness, etc. [184]). In general, the mesh discretization should always be evaluated through convergence studies.

However, such guidelines are less representative for oscillatory flows and/or two fluid phases, so more care must be used in the simulation set up. Indeed, with oscillatory flows, the fluid velocity is reversing, so the flow is never steady, and y^+ values are constantly changing. Furthermore, the Re number is less representative of the flow regime, because reversing velocities may cause the creation of further vortices, even at Re values lower than 10^6 [168]. Moreover, the point of flow detachment moves back and forth around the sphere surface, as the velocity changes magnitude and direction. Finally, the eventual presence of two fluid phases makes the notion of flow detachment more blurred.

Despite such major differences in the flow characteristics, having only a constant unidirectional flow around a fixed body provides perfect isolation of the drag force term, which is indeed the only force acting on the body, since acceleration and free surface forces are absent. However, the drag coefficient must be evaluated at very high Re numbers (up to about $2 \cdot 10^7$), which are required by wave energy applications, as discussed in Sect. 7.3. Identifying a value for C_d in such very turbulent conditions is not straightforward, due to vortex induced vibrations [185], which cause high-frequency forced oscillations.

Figure 7.1 shows, indeed, the drag force in laminar and turbulent conditions, at Re of 10^5 and 10^7 , respectively. In CFD simulations, initial conditions consider a constant

flow velocity throughout the fluid domain. The same constant velocity is imposed on the inlet and outlet boundaries, while the lateral boundaries have a slip velocity condition. Therefore, the slow transients, in Fig. 7.1a, depends on the perturbation that the velocity field undergoes, due to the presence of the body, and the drag coefficient (in laminar flow) can be identified by the steady state force. Conversely, Fig. 7.1b shows high frequency fluctuations of the drag force in extremely turbulent conditions, which make the identification of the drag coefficient troublesome. As a matter of fact, the data in the literature usually refers to experiments for Re numbers up to $2 \cdot 10^6$, just above the drag crisis limit.

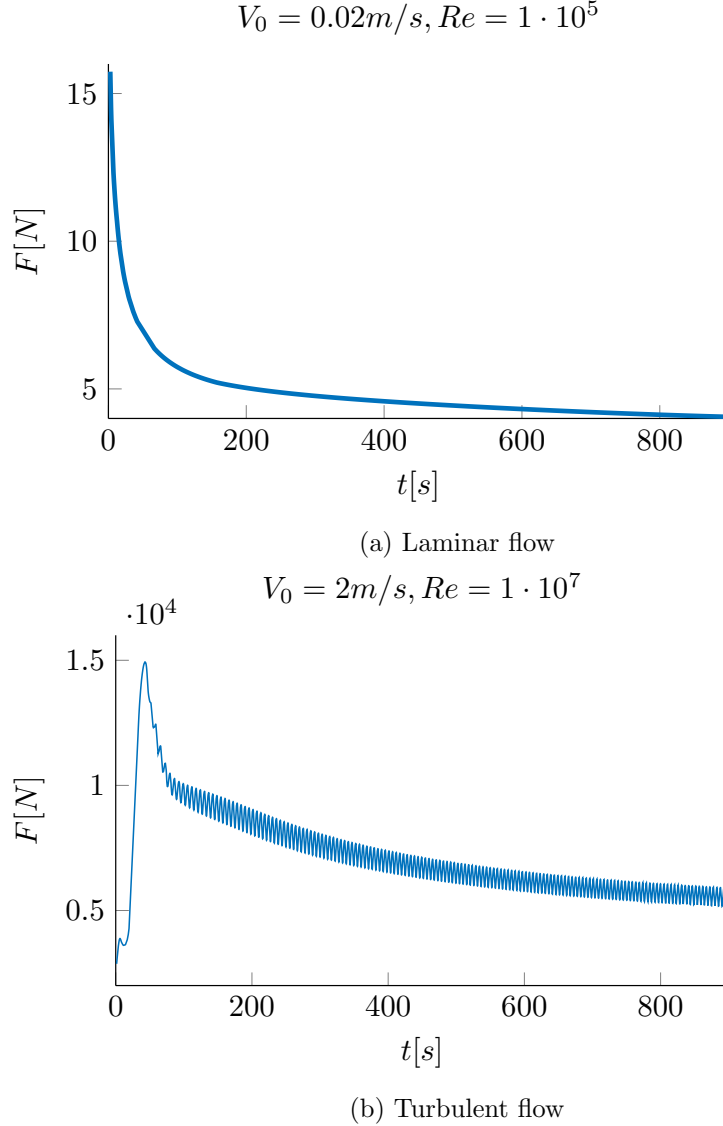


Figure 7.1: Fluid force on a fixed sphere, 5m diameter, fully-submerged in a flow with constant velocity V_0 .

Such a long transient, with constant unidirectional flow, is clearly inconsistent with the oscillatory flow around a WEC, especially at large Re numbers, so that the identification test (A) is largely considered unrepresentative. Therefore, option (A) is not considered in the comparison hereafter.

7.4.2 Fully-submerged, prescribed motion, harmonic flow

The device is fully immersed in calm water, and it is driven to follow a harmonic trajectory, so that the relative flow between the fluid and the body is known. Due to the absence of

Table 7.1: Harmonic prescribed motion amplitudes and periods, for a fully-submerged sphere (5m diameter) in calm water, and resulting Reynolds and Keulegan-Carpenter numbers.

$Re \cdot 10^6$	$A[m]$				
	0.5	1	1.5	2	
3	5.24	10.5	15.7	20.9	
$T[s]$	6	2.62	5.24	7.85	10.5
	9	1.75	3.49	5.24	6.98
	12	1.31	2.62	3.93	5.24
KC	0.63	1.26	1.88	2.51	

the free surface, the only hydrodynamic forces acting on the surface depend on acceleration and velocity; therefore, the two coefficients of the Morison equation (7.4) are identified, namely C_d and C_m .

Compared with the constant flow approach, discussed in Sect. 7.4.2, while the oscillatory (rather than constant) flow is more representative of the intended WEC application, the presence of two force components (rather than one) makes the identification of the drag coefficient more challenging. Indeed, the results is that the inertial term of equation (7.4) is predominant, making the total force less sensitive to the velocity term. As a consequence, small variations in the total force, due to the CFD numerical set up, cause significant variations in the drag coefficient identification. In such a context, convergence studies are particularly relevant. The background mesh has been selected iteratively, in order to achieve y^+ values within the range [40, 200], as suggested in [183]. Furthermore, the convergence of the amplitude of the total hydrodynamic force acting on the device has been checked. The same method has been applied for all identification approaches. The final computational time of each CFD simulation, for approach (B), is about 300 times larger than the simulation time.

A fully-submerged sphere (5m in diameter) is studied, forced to follow a set of 16 harmonic trajectories, with 4 equispaced periods T , from 3s to 12s, and 4 equispaced displacement amplitudes A , from 0.5m to 2m, as shown in Table 7.1. The resulting Re and KC numbers are tabulated in Table 7.1. The most extreme condition (T of 3s, A of 2m), with the largest velocity, Re , and KC numbers, is inspired by the operational conditions of a floating sphere, under latching control conditions, as shown in Chapter 6: the maximum relative displacement between the free surface elevation and the body is equal to the radius of the device (2.5m); furthermore, as a result of the latching control strategy, the device is left free to move from a peak to a trough, or vice versa, in a period of time similar to the natural period of the device (about 3.2s).

In the identification tests, the prescribed motion (position, velocity, and acceleration) of the body is harmonic, and the resulting force acting on the body is proportional to the body's acceleration and the velocity squared, consistent with (7.4), since the velocity of the still water is zero. Following a least squares approach, C_m and C_d are identified such that the error between the force measured in CFD and the Morison force, in (7.4), is minimized. While C_m is largely constant, equal to 0.5, large variations are found for C_d , whose values are tabulated in Table 7.2.

7.4.3 Fully-submerged, prescribed motion, sawtooth flow

On the one hand, experiments with constant flow, discussed in Sect. 7.4.1, have the advantage of having only the velocity term of the Morison equation, but at the price of unidirectional flow. On the other hand, harmonic prescribed motion experiments, discussed in Sect. 7.4.2, have the advantage of modelling a more representative (bidirectional) oscil-

Table 7.2: Estimated drag coefficients, using harmonic prescribed motion for a fully-submerged sphere in calm water, with respect to the case study tabulated in Table 7.1.

C_d		$A[m]$			
		0.5	1	1.5	2
$T[s]$	3	0.29	0.19	0.15	0.10
	6	0.27	0.17	0.14	0.14
	9	0.29	0.18	0.15	0.14
	12	0.31	0.20	0.16	0.15

Table 7.3: Estimated drag coefficients, using sawtooth prescribed motion for a fully-submerged sphere in calm water, with respect to the case study tabulated in Table 7.1.

C_d		$A[m]$			
		0.5	1	1.5	2
$T[s]$	3	0.06	0.05	0.05	0.04
	6	0.09	0.06	0.06	0.05
	9	0.12	0.08	0.07	0.06
	12	0.14	0.09	0.08	0.07

latory flow, but with the drawback of having both the acceleration and velocity terms of the Morison equation to identify concurrently.

A novel identification test is herein proposed, in the attempt of reproducing only the advantages of the two previous methods, without the related disadvantages. A triangle wave (or sawtooth) motion is imposed on the device, so that the flow is bidirectional, while maintaining a constant velocity (apart from the edges of the sawtooth, where the velocity changes sign). The same case study as in Sect. 7.4.2, tabulated in Table 7.1, is considered. The resulting drag coefficients are tabulated in Table 7.3.

Comparing the results using harmonic and sawtooth prescribed motions, in Tables 7.2 and 7.3, respectively, one can notice the same overall trend is followed, with larger drag coefficients at smaller Re numbers. On the other hand, drag coefficients identified using the sawtooth motion experiments are smaller.

7.4.4 Floating, prescribed motion, harmonic flow

A further degree of complexity is added to the identification experiment, with the objective of a more accurate reproduction of the flow conditions around the operating WEC. In particular, vertical harmonic prescribed motions are imposed on a floating body in calm water. Notwithstanding the advantage of having an experimental set-up more similar to the intended WEC application, modelling the free surface introduces other forces (radiation and restoring forces), and nonlinear effects, as described in Sect. 7.3, making the isolation and identification of the viscous drag force more challenging. Furthermore, the CFD computational domain must include numerical beaches, in order to absorb radiated waves. Consequently, the computational time of each CFD simulation is about 900 times longer than the simulation time, which itself is 3 times longer than the time required for approaches (B) and (C).

While the radiation force for heaving point absorbers can be assumed to be linear [45], the restoring force presents relevant nonlinearities, due to the non-constant cross sectional area of the sphere. The nonlinear restoring force is computed as the balance between the weight of the device and the integral of the static pressure over the instantaneous wetted surface. Furthermore, the non-uniform cross sectional area also affects A_d in the viscous force, in (7.5). Equation (7.3) is therefore used to compute the total force, which is compared with the measurement from CFD simulations. The same case study, as

Table 7.4: Estimated drag coefficients, using harmonic prescribed motion for a floating sphere in calm water, with respect to the case study tabulated in Table 7.1.

C_d		$A[m]$			
		0.5	1	1.5	2
$T[s]$	3	0.35	0.24	0.15	0.06
	6	0.44	0.41	0.34	0.32
	9	0.98	0.69	0.45	0.41
	12	1.19	1.01	0.65	0.46

in Sect. 7.4.2, tabulated in Table 7.1, is considered. The resulting drag coefficients are tabulated in Table 7.4.

Despite significant variability, larger estimations of the values for the drag coefficients are overall obtained, in comparison with the results of Tables 7.2 and 7.3. Such differences are justified by the influence of other forces and nonlinear effects, introduced by the free surface. Estimations of C_d are particularly sensitive to modelling errors of the restoring force, which is the largest hydrodynamic force, several times larger than radiation and viscous forces, as discussed in Chapter 5.

7.4.5 Floating, dynamic response

Finally, the dynamic response of the floating device to incoming waves, using a latching control strategy, is considered. On the one hand, the advantage is that none of the characteristics of the flow around a controlled WEC, discussed in Sect. 7.3, are neglected. On the other hand, dealing with the full complexity of such a flow makes the isolation of the viscous drag force very challenging. Indeed, several different forces contribute to the motion of the device, as shown in equation (7.3), which are likely to be nonlinear, due to the presence of large motion, induced by the control strategy.

As a result, the estimated drag coefficient, which minimizes the error between the mathematical model and CFD measurements, is actually a descriptor of all the unmodeled effects/nonlinearities, as well as modelling errors and inaccuracies, as opposed to a descriptor of the drag force only. Therefore, such a drag coefficient may be misleading and inappropriate if used to evaluate viscous effects in isolation. Nevertheless, if the objective is to fill the gap between the partially nonlinear potential flow mathematical model and the fully-nonlinear CFD model, regardless of the nature or source of the difference, the information incorporated in the drag coefficient can be used effectively to reduce modelling errors, and increase the accuracy of the results. Therefore, the notion of *equivalent* drag coefficient is introduced, which highlights the fact that nonlinearities, other than viscous drag, may be included in the coefficient itself. Similarly, [127, 186] include all nonlinear viscous effects present in the CFD simulation into a representative *linear* damping term, identified from a free decay experiment [127], or adaptively during WEC operation [186]. However, care needs to be taken with this approach, since the identified drag coefficients are representative only for the particular experimental conditions.

Nonlinear static and dynamic FK forces are included, while radiation and diffraction forces are considered linear, since the wave length is much longer than the diameter of the floating buoy [45]. As in Chapter 6, a set of regular wave conditions are taken into account, with 6 equispaced wave periods T_w , from 5s to 10s, and 4 equispaced wave heights H_w , from 0.5m to 2m. A zero-threshold latching control strategy is implemented [176], as in Chapter 6. KC (between 0.56 and 3.11), and Re (between $3.56 \cdot 10^6$ and $1.79 \cdot 10^7$) numbers are evaluated according to relative displacement and velocity, respectively, obtained in CFD simulations. All the details of the numerical set-up and the computational time required by the CFD simulations are given in Chapter 6.

Table 7.5: Estimated drag coefficients, using the dynamical response to regular waves of a floating sphere, under latching control conditions.

C_d	$H_w[m]$			
	0.5	1	1.5	2
5	0.05	0.05	0.33	0.47
6	0.06	0.13	0.18	0.19
$T_w[s]$ 7	0.29	0.46	0.49	0.33
8	0.97	0.81	0.66	0.54
9	0.88	0.89	0.73	0.59
10	1.34	1.43	1.15	0.79

While, according to the prescribed motion approaches (B) to (D), drag coefficients are identified using force signals, the *equivalent* drag coefficient is evaluated here by means of motion responses instead. The value of C_d is identified such as to minimize the least squares error between the vertical displacement computed in CFD, and that computed using the equation of motion (7.3). The resulting drag coefficients, tabulated in Table 7.5, vary significantly for different wave conditions, and extend over a wider range of values than those obtained with fully-submerged harmonic and sawtooth prescribed motion experiments, tabulated in Tables 7.2 and 7.3, respectively. On the other hand, a similar range of values is obtained with the floating harmonic prescribed motion test, tabulated in Table 7.4. Therefore, it can be implied that free surface-related nonlinearities are significantly affecting the identification of the drag coefficient.

With such variability of the equivalent drag coefficient for different wave conditions, sensitivity analysis is important to evaluate the impact of the viscous drag term and, in particular, of errors in the choice of C_d . For each of the optimal drag coefficients in Table 7.5, nine equispaced relative variations are applied, from -100% to $+100\%$ (-100% , -75% , -50% , -25% , 0% , $+25\%$, $+50\%$, $+75\%$, and $+100\%$), so from zero to twice the optimal value. The relative error in power production estimation is used as a sensitivity index, considering, for each wave condition, the model using the optimal drag coefficient as a benchmark. Results are shown in Fig. 7.2, where positive relative errors represent power overestimation. Four sections are highlighted, for the four wave heights, and in each section, the wave period increases from left to right.

Clearly, as C_d increases, larger power losses cause the estimated produced power to decrease. Overall, relative errors are increasing with the wave period, being relatively small for short waves, no matter the value of the drag coefficient, indicating little relevance of viscous forces for wave conditions with low energy content (which cause smaller motion and less nonlinearity).

Furthermore, neglecting viscous forces (first curve from top, in Fig. 7.2) causes significant errors, and considerable improvements are achieved already with a drag coefficient four times smaller than the optimal one (second curve, in Fig. 7.2). In general, overestimation of the drag coefficient is preferable to underestimation, since the curves for negative relative errors are much closer to zero than for the positive curves.

Despite the importance of studying variations in the drag coefficient for different wave conditions, a one single value must be chosen, since WECs operate in more realistic irregular sea states. Therefore, a single constant value is used for all the considered wave conditions, and the mean relative error in estimated power is computed. The drag coefficient, which minimizes the absolute value of the mean relative error across all the wave conditions is selected, equal to 0.6, as shown in Fig. 7.3. Moreover, it can be seen that the steepness of the curve decreases as C_d increases, confirming that overestimation of the drag coefficient is preferred. Such a result (better to overestimate than underestimate C_d) is consistent with sensitivity studies performed in [187, 188], for example.

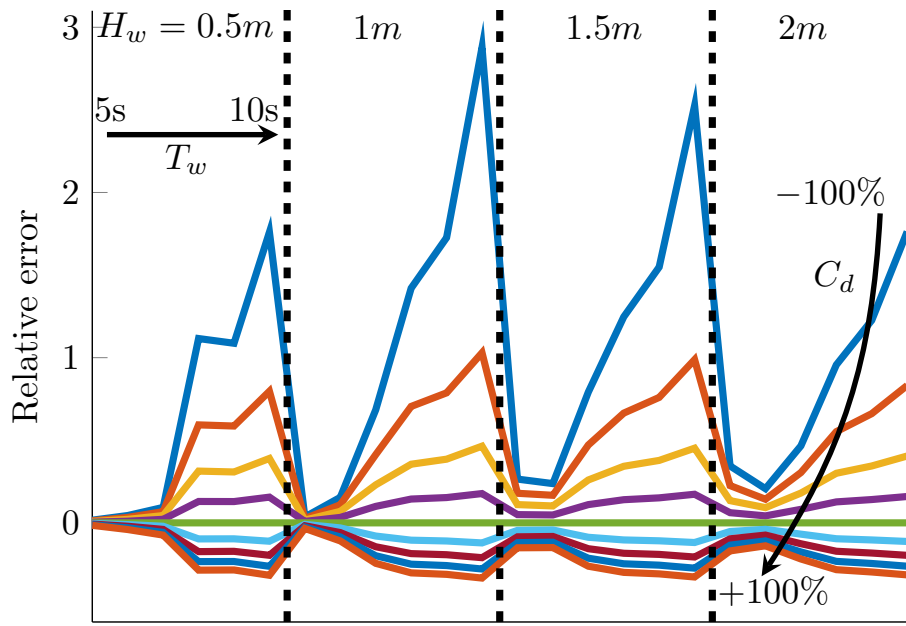


Figure 7.2: Sensitivity analysis on the relative error on the power prediction, varying the drag coefficient from -100% to $+100\%$ of the optimal value at each wave condition. Four sections are highlighted, for the four wave heights. In each section, the wave period is increasing from left to right.

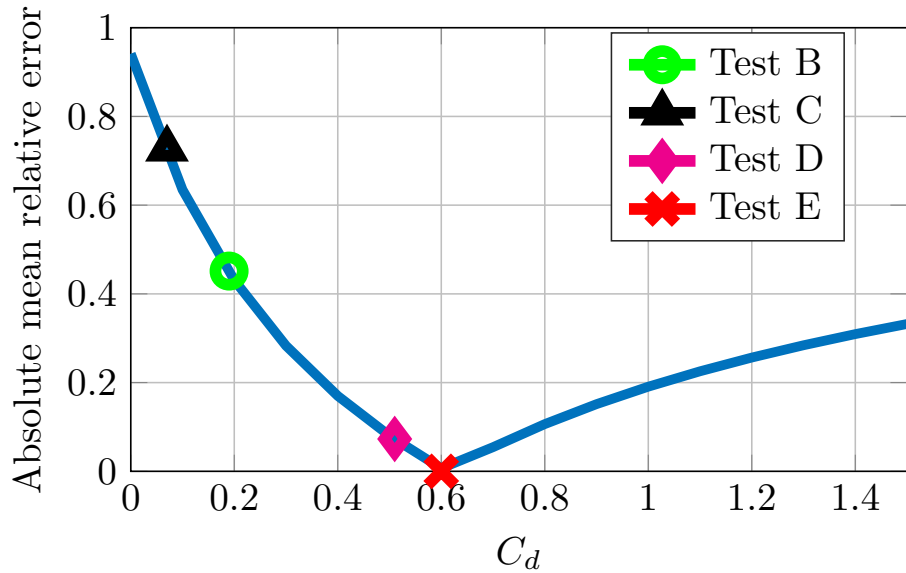


Figure 7.3: Absolute mean relative error for a constant drag coefficient across all the considered wave conditions. The markers refers to the mean values identified according to different approaches, as discussed in the sections 7.4.2 to 7.4.5.

Table 7.6: Absolute mean relative error for the mean drag coefficient, identified according different tests.

	C_d	Absolute mean relative error
No drag	0	94.1%
Sect. 7.4.2	0.19	45.1%
Sect. 7.4.3	0.07	72.6%
Sect. 7.4.4	0.51	7.3%
Sect. 7.4.5	0.60	0%

By way of comparison, the average drag coefficients, according to each of the identification tests, tabulated in Tables 7.2 to 7.4, are shown in Fig. 7.3, and summarized in Table 7.6. Note that they are smaller than the optimal value and, in particular, the drag coefficient increases as the flow becomes more complex: the smallest C_d (0.07) is found with the sawtooth motion, which has a constant velocity. The fully-submerged harmonic motion (velocity and acceleration terms to be identified) returns an average C_d of 0.19. Finally, the radiation test, which includes velocity, acceleration, and free surface effects, gives an average C_d of 0.51. Therefore, it can be speculated that the more complex the flow, the larger the dissipation (due to both viscous drag and other nonlinear effects), and the larger the equivalent drag coefficient.

7.5 Conclusion

Controlled wave energy devices are likely to show nonlinear behaviour, especially due to exaggerated motion, induced by the control strategy, in order to increase power absorption. Therefore, appropriate modelling of nonlinearities, such as viscous drag losses, is crucial for model accuracy, as well as the effectiveness of the control strategy. However, due to the high complexity of the flow around WECs (with large oscillating motion in a multiphase fluid field), estimation of the drag coefficient of the device is challenging, evidenced by uncertainty and inconsistency in the literature material.

Drag identification tests must define a proper compromise between pertinence of the flow reproduction, and simplicity of isolation of the drag term. Pros and cons of five different identification approaches are discussed in this chapter, comparing their performance when applied to a floating heaving point absorber, under latching control conditions. In general, it is shown that defining a single representative and comprehensive drag coefficient is a difficult task, due to significant variability in the results, both within and across the different approaches.

On the one hand, the wide range of relative velocities and displacements, experienced by a WEC in its operating (controlled) conditions, causes actual variations of the drag coefficient. On the other hand, as the flow becomes more complex, different sources of nonlinearity, as well as modelling errors, may interfere with the isolation of the viscous drag force, affecting the identification, and causing “apparent” variations of the drag coefficient. As a result, an *equivalent* drag coefficient is identified, which incorporates effects other than pure viscous drag. Nevertheless, rather than identifying viscous drag forces, the actual final objective, usually, is to fill the accuracy gap between mathematical models and the physical system, for which such an *equivalent* drag coefficient seems to be more effective.

However, such significant variations of the value of the drag coefficient, across different operational conditions, suggest that the functional structure of the Morison equation may not be the most representative one. Different model structures may be evaluated, using data-driven modelling techniques, as the ones described in Sect. 2.4.3.

Finally, despite the large variations in the identified drag coefficient, it is shown that, even with a non-optimal drag coefficient, errors are drastically reduced if a viscous drag term is included in the mathematical model. Furthermore, in case of uncertainty, sensitivity studies show that it is preferable to choose a larger rather than smaller drag coefficient, since overestimation is less detrimental than underestimation.

Relevance of pressure field accuracy for nonlinear Froude-Krylov force calculations

8.1 Motivation

Previous chapters have focused on nonlinear Froude-Krylov force computation, but using the linear pressure field representation. However, one of the sources of nonlinearity in fluid-body interactions is the wave field itself. Different wave models exist, among which are linear Airy's theory, Wheeler's stretching approach, the nonlinear Rienecker-Fenton method, and higher order spectral methods, all of which achieve a different compromise of accuracy and complexity. The impact of the accuracy of such wave theories strongly depends on the specific device (operating principle, power production region or survivability mode), and installation site (water depth, occurrences of each sea state in the scatter diagram of the installation site). This chapter evaluates the performance of different wave field representations, firstly in absolute terms and, secondly, in relation to the associated computation of nonlinear Froude-Krylov forces, for different wave energy devices, in regular and irregular sea states. It is shown that Wheeler stretching offers a good accuracy/complexity compromise, for WECs operating in the power production region.

8.2 Introduction

Nonlinearities in fluid-body interactions depend on:

- (i) The free surface elevation
- (ii) The pressure field distribution
- (iii) Geometric nonlinearities

Points (i) and (ii) concern the modelling of the wave field, which is the energy source, while point (iii) concerns the computation of the hydrodynamic forces acting on the body. Computation of nonlinear FK forces, as discussed in Chapter 4, is based on the integration of the undisturbed incident *pressure field* (nonlinearity (ii)) onto the instantaneous wetted *surface* of the device (nonlinearity (iii)), defined by the displacement of the device and the *free surface elevation* (nonlinearity (i)). Although Chapter 4 focuses on geometric nonlinearities only, the accuracy of nonlinear FK force calculations is also directly related to the accuracy of the pressure field model. Likewise, the complexity of the pressure formulation has a significant influence on the computational effort required to compute nonlinear FK forces. Therefore, this chapter purports to discuss the relevance of the accuracy and complexity of pressure field representation for nonlinear FK force calculations.

In the last decade, nonlinear FK models have gradually become more popular in the wave energy field [91, 62, 32, 46, 189]. However, the vast majority of such models just consider the pressure representation from first-order linear Airy’s theory. Different degrees of accuracy (at different complexity costs) can be achieved in modelling the wave field. For the basic case of steady (regular) waves, the simplest approach is linear Airy’s theory, followed by several nonlinear wave formulations, including Stokes’ waves (2nd to 4th order), cnoidal waves, and Rienecker-Fenton (RF) waves [38]. Finally, corrections to linear theory, such as Wheeler’s stretching method [39], can be used to improve the results of Airy’s theory, at a negligible additional complexity cost. For irregular waves, higher-order spectral (HOS) formulations are often used, since they can efficiently solve the nonlinear potential problem, as well as the nonlinear propagation problem [190]. The accuracy of such wave theories depends mainly on the water depth, wave steepness, and wave height; therefore, the impact of such nonlinearity strongly depends on the specific device (position of the device with respect to the free surface and the sea bottom, power production region or survivability mode), and installation site (water depth, occurrence of each sea state in the scatter diagram of the installation site).

This chapter discusses the impact that the choice of the wave field representation model has on the accuracy and complexity of the calculation of *nonlinear* FK forces for wave energy devices. Regular and irregular waves are considered, using Airy’s theory, Wheeler stretching, Rienecker-Fenton waves, and HOS methods. Initially, the pressure profile is evaluated and compared, from the free surface to the sea bottom, for a comprehensive set of wave conditions. Secondly, the effect of different pressure field representations on the calculation of nonlinear FK forces for WECs is discussed, considering HPAs and OWSCs as representative devices. While the accuracy of the pressure field representation has already been discussed in the literature (using Wheeler stretching [191, 192], Rienecker-Fenton [38], and HOS [30]), to the best of the author’s knowledge, the present work is the first study considering the impact of the pressure field accuracy on *nonlinear FK force calculations* for wave energy devices.

8.3 Wave theories

The wave theories discussed herein are based on the assumption of a homogeneous, ideal, incompressible fluid, with irrotational motion [144]. Two-dimensional waves are considered in the (x, z) coordinate system, where x is the direction of propagation of the wave, and z is the vertical axis, positive upwards, with the origin at the still water level (SWL), which is at a distance d from the sea bed. Assuming the flow is irrotational, a velocity potential φ can be defined, such that:

$$\mathbf{u} = \nabla\varphi \tag{8.1}$$

where \mathbf{u} is the velocity vector. Since the fluid is assumed incompressible, φ satisfies Laplace’s equation throughout the fluid:

$$\nabla \cdot \mathbf{u} = \nabla^2\varphi = 0 \tag{8.2}$$

The kinematic boundary conditions are satisfied on the flat sea bottom, (8.3a), and on the free surface η , (8.3b):

$$\frac{\partial\varphi}{\partial z} = 0, \quad \text{at } z = -d \tag{8.3a}$$

$$\frac{\partial\varphi}{\partial z} = \frac{\partial\eta}{\partial t} + \frac{\partial\varphi}{\partial x} \frac{\partial\eta}{\partial x}, \quad \text{at } z = \eta \tag{8.3b}$$

Finally, the dynamic boundary condition (Bernoulli's equation) is verified on the free surface:

$$\frac{\partial\varphi}{\partial t} + \frac{p}{\rho} + gz + \frac{|\nabla\varphi|^2}{2} = 0, \quad \text{at } z = \eta, \quad (8.4)$$

where ρ is the water density, g the acceleration due to gravity, and p the total pressure.

The resolution of such a potential problem is different, depending on whether regular or irregular waves are considered. In Sect. 8.3.1, different regular wave theories are discussed, while Sect. 8.3.2 is concerned with irregular sea state representations.

8.3.1 Regular waves

A general analytical solution to the wave velocity potential problem, described by equations (8.1) to (8.4), does not exist. In particular, some further assumptions are needed to solve the free surface boundary conditions (8.3b) and (8.4): Airy's wave theory linearizes such boundary conditions onto the SWL, while Stokes' wave theory, assuming infinite water depth (with respect to the wave length λ), uses a Fourier series of (8.3b) and (8.4), performing a perturbation expansion in terms of a deviation parameter, which increases with the wave steepness. On the other hand, cnoidal wave theory solves the potential problem, assuming that the wave length is much longer than the water depth.

Regions of validity of such wave theories are shown in Fig. 8.1. Note that there are different orders of Stokes' theory, where first order corresponds to linear Airy's theory. The range of applicability of different theories depends on the water depth, the wave length, and the wave height H_w . The boundary between cnoidal and Stokes wave theories is given by an Ursell number (Ur) of 40 [193], where Ur is the ratio between a measure of nonlinearity (H_w/d), and a measure of shallowness (d^2/λ^2). The theoretical limit for the highest wave possible, based on the model of [194], determines the maximum achievable wave height.

Finally, by means of Rienecker-Fenton wave theory [38], it is possible to achieve a numerical solution to the nonlinear potential problem, without any assumption on the wave depth or height. Indeed, [195] shows how well RF waves embrace Stokes' and cnoidal wave theory, in their respective regions of validity. The drawback is that, while there are analytical formulations for calculating the Stokes' and cnoidal waves parameters, the RF approach requires a numerical optimization search for each wave condition.

8.3.1.1 Linear Airy's wave theory

Assuming small wave steepness ($s = H_w/\lambda$), it is possible to linearize the kinematic and the dynamic free surface boundary conditions, shown in (8.3b) and (8.4), respectively, around the SWL, namely at $z = 0$. The solution to the linearized potential problem consists of a harmonic free surface elevation and an exponential dynamic pressure, as follows:

$$\eta = \frac{H_w}{2} \cos(kx - \omega t) \quad (8.5a)$$

$$p = p_{st} + p_{dy} = -\rho g z + \rho g \eta \frac{\cosh k(z+d)}{\cosh kd} \quad (8.5b)$$

where p_{st} and p_{dy} are the static and dynamic pressures, respectively, $k = 2\pi/\lambda$ is the wave number, $\omega = 2\pi/T_w$ is the wave frequency, and T_w the wave period. Note that, at infinite water depth conditions, the dynamic pressure tends to $\rho g \eta e^{kz}$.

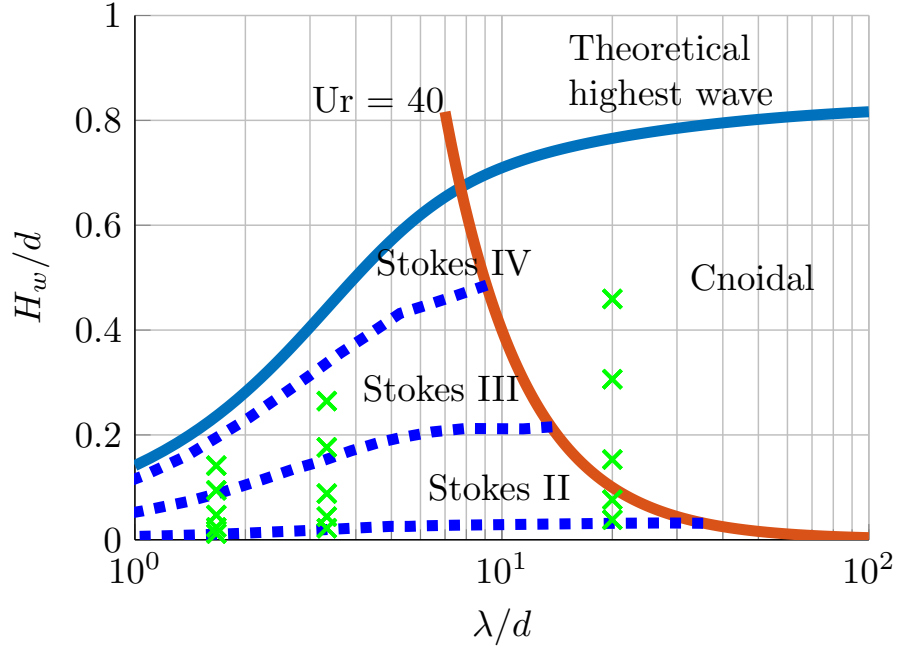


Figure 8.1: Regions of validity of wave theories, based on [123], for different wave lengths λ and wave heights H_w , both normalized with respect to the water depth d . The boundary between cnoidal and Stokes wave theories is given by an Ursell number (Ur) of 40 [193]. The thresholds between consecutive orders of the Stokes wave (dashed lines) are qualitative. The theoretical highest wave possible is based on [194]. The markers on the graph refer to the wave conditions studied in Sect. 8.4.2.

The advantages and disadvantages of Airy’s theory are discussed hereafter. Airy’s theory is mathematically rigorous and consistent with the velocity potential theory framework, shown in (8.1) to (8.4), as long as the linear assumption of small steepness, relative to a unity value, is verified. Therefore, Airy’s theory gives an accurate representation of the wave physics as long as the wave steepness is small. However, in order to compute nonlinear FK forces, pressure specification is required up to the (eventually large positive) free surface elevation, hence introducing modelling errors.

For example, the total pressure p at the free surface ($z = \eta$), according to the boundary condition (8.4), should match atmospheric pressure, therefore equal to *zero*. Assuming, for the sake of argument and simplicity, infinite water depth conditions, it results that, according to Airy’s wave theory, p at the free surface is *not zero*:

$$p = p_{st} + p_{dy} = -\rho g \eta + \rho g \eta e^{k\eta} = \rho g \eta (e^{k\eta} - 1) \quad (8.6)$$

As a consequence of the linearization of the free surface boundary conditions, the total pressure is zero at the SWL ($z = 0$) instead, implying a *modelling error* of the pressure at the actual free surface ($z = \eta$). Equation (8.6) shows that such an error is proportional to $\eta (e^{k\eta} - 1)$, which tends to zero as the wave steepness tends to zero. A similar conclusion can be drawn in generic water depth conditions.

Moreover, such an error depends on the wave number k as well. For regular waves, there is only one k , which is usually small. Conversely, panchromatic waves are characterized by several frequency components. High frequency components, with consequently large wave numbers, are particularly problematic for the calculations of the dynamic pressure at positive z , since the error increases with the exponential of $k\eta$. In fact, for each frequency component, the pressure profile is computed up to the total η , and not just to a single amplitude component. Consequently, exponentials of large k components, up to a positive

large η are causes of large errors. Such an issue is further investigated in Sect. 8.5.

Finally, note that p_{st} is defined in the same way for all methods; therefore, it is not a source of error. Consequently, only p_{dy} will be considered hereafter, when pressure errors are considered. Furthermore, for brevity, the word “pressure” will implicitly refer to p_{dy} , unless explicitly specified.

8.3.1.2 Wheeler’s stretching method

Wheeler’s stretching approach [39] consists of starting from the results obtained with Airy’s theory, and apply a convenient change of coordinates, in order to correct the free surface linearized dynamic boundary condition error. Therefore, in Wheeler’s stretching approach, the total pressure is still computed in a linear way, effectively neglecting the nonlinear term. The vertical coordinate z is substituted with z' , defined as:

$$z' = d \frac{z + d}{\eta + d} - d \quad (8.7)$$

Note that the origin of the stretching is located at the sea bottom, since $z' = z$ at $z = -d$. On the other hand, $z' = 0$ at $z = \eta$, hence the dynamic free surface boundary condition is satisfied, and the (linearized) total pressure at the free surface is zero. Moreover, the issue for high frequency components of panchromatic waves, described in Sect. 8.3.1.1, is resolved. Notwithstanding that the (linearized) dynamic pressure is correct at $z = \eta$, the whole pressure profile is, in general, an approximation, since it is based on a linear stretching of the results from Airy’s theory. Indeed, Wheeler stretching performs a redistribution of the whole potential field in the vertical direction causing, for example, the Laplace condition (8.2) to be violated in the fluid domain.

Therefore, both Wheeler stretching **and** Airy’s theory are approximations. However, the advantage of Wheeler stretching over Airy’s theory is to describe, more realistically, the pressure for $z > 0$, as shown, for example, by [191] and [192]. Nevertheless, to the best of the author’s knowledge, there is no previous study considering how the choice of either Airy’s theory or Wheeler stretching affects the calculations of nonlinear FK forces for different wave energy devices; only the region of fluid where the device operates is relevant, as opposed to the whole pressure profile, from sea bottom to the free surface. Consequently, Wheeler stretching is likely to be particularly effective for floating devices, which operate close to the free surface (where Wheeler stretching is significantly more accurate than Airy’s theory). Further details and discussions are given in Sects. 8.4.2 and 8.5.2.

8.3.1.3 Rienecker-Fenton wave theory

The basis of the Rienecker-Fenton method is to write the analytical solution for the velocity potential φ in a separated variables form:

$$\varphi = \sqrt{\frac{g}{k^3}} \sum_{j=1}^{N_B} B_j \frac{\cosh jk(z + d)}{\cosh jkd} \sin jkx \quad (8.8)$$

where B_j are dimensionless constants for a particular wave, and N_B is a finite integer which, according to [38], should be chosen between 10 and 20. In order to achieve the same level of accuracy, less steep waves would require less Fourier terms, implying a smaller value of N_B . In this study, the highest number of components ($N_B = 20$), suggested by [38], has been chosen, which is able to accurately describe the steepest waves [38]. The truncation of the series for finite N_B is the only approximation in this formulation. The values of B_j are found numerically, using Newton’s method [38].

Note that the complexity of the pressure formulation in the RF method is considerably higher than in Airy's theory and Wheeler's stretching method. In fact, once the N_B terms of the potential are obtained, the pressure is computed from Bernoulli's equation (8.4), which requires the computation of derivatives of the potential. On the other hand, since no approximation is introduced into the formulation of the boundary conditions, the wave pressure profile obtained with the RF method is taken as an accuracy benchmark, and used to evaluate Airy's and Wheeler's approaches. Likewise, the RF approach provides an accurate description of the nonlinear free surface elevation, with higher and steeper peaks compared to linear waves. Figure 8.2 shows an example of the free surface elevation, using Airy's theory and the RF model.

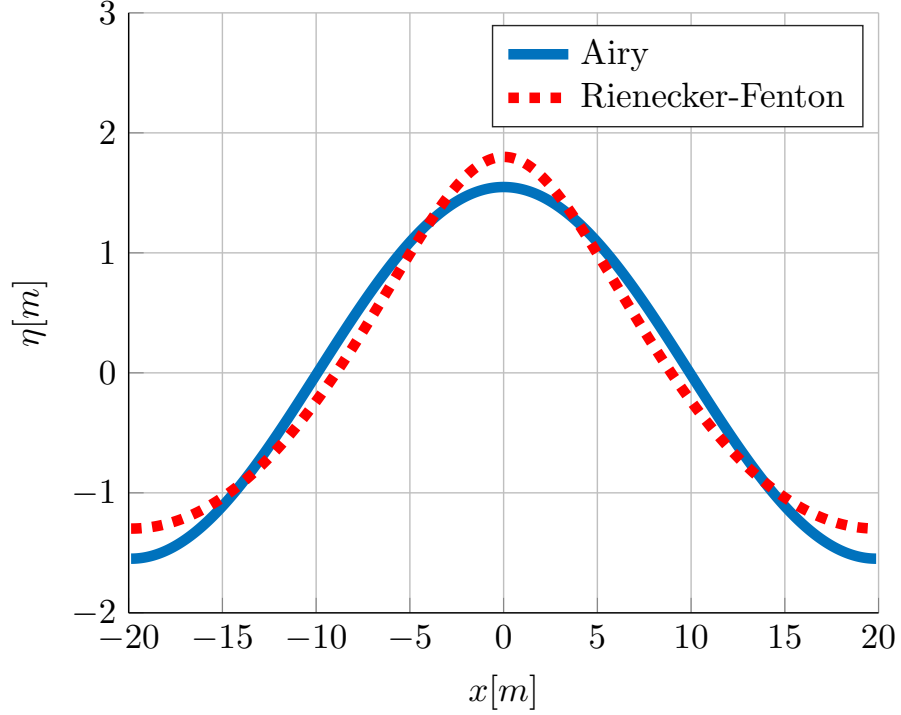


Figure 8.2: Free surface elevation for a regular wave condition with $T = 5s$, $H_w = 3m$, $d = 12m$.

8.3.2 Irregular waves

Irregular sea states are commonly described as a superposition of harmonic components, with frequency-dependent amplitudes and random phases [190]. Consequently, assuming that linear superposition is valid, Airy's theory can be used to define the resulting (linearized) wave pressure field:

$$p_{dy} = \sum_{i=1}^{N_\omega} \rho g A_i \cos(k_i x - \omega_i t + \Phi_i) \frac{\cosh k_i(z+d)}{\cosh k_i d} \quad (8.9)$$

where N_ω is the number of frequency components, A_i , ω_i , and Φ_i are the amplitude, frequency and phase parameters, respectively, and $k_i = 2\pi/\lambda_i$ is the wave number.

As in the regular wave case, for each frequency component, Airy's theory tends to overestimate the pressure at positive displacements (above the SWL), violating the free surface boundary conditions; such an error is proportional to the exponential of $k\eta$, as shown in (8.6) and (8.9). While, in the regular wave case, wave numbers are relatively small, in the irregular case there are quite large k_i , associated with high frequency components of the wave spectrum. The (linearized) dynamic pressure depends linearly on

the wave amplitude, and exponentially on the wave number; therefore, in case of large k_i and positive z , the exponential may dominate over the small amplitude A_i , which are typically associated with high frequency components. Moreover, the pressure profile must be computed up to the total free surface elevation, which may take large positive values. Consequently, due to the *exponential* growth of the error, large inaccuracies are expected, close to the free surface, for large wave heights. Note that such an extreme magnification of pressure errors is present only when *nonlinear* FK forces are considered. Conversely, linear FK force calculation is mathematically consistent with Airy's theory approach, since the pressure integral is computed only up to the SWL ($z=0$), avoiding the exponential growth in pressure error for positive z .

Since errors due to the free surface boundary conditions are especially relevant in the irregular wave case, Wheeler's stretching approach is likely to be particularly effective, since it is designed to verify the linearized free surface dynamic boundary condition at $z = \eta$. As in the regular wave case, the change of variable, defined in (8.7), is applied to the pressure formulation in (8.9). On the other hand, the pressure decay rate, from the free surface to the sea bed, is just an approximation, since it is a simple stretch of Airy's decay. In order to have the correct pressure profile, the full nonlinear boundary problem must be solved.

Furthermore, both Airy's theory and Wheeler stretching assume linear superposition, implying the absence of energy exchange between different frequency components. As a result, the free surface elevation is a Gaussian process, meaning that the probability distribution of the water displacement is symmetric [190] (peaks and troughs, statistically, are of equal width and height). The Gaussianity of a sea state is influenced only by the water depth: the interaction between frequency components is negligible at infinite water depths, more precisely at significant wave heights (H_s) such that $d/H_s \geq 4.17$ [190]. On the contrary, in intermediate/shallow water depths, higher and narrower peaks, and smaller and larger troughs, may be found.

Non-Gaussian processes can be described through the solution of the nonlinear wave propagation problem [196]. The higher-order spectral method is an efficient approach to the solution of both the nonlinear boundary problem and the nonlinear wave propagation problem. In this work, the open-source HOS-Ocean software is used [197]. Section 8.3.2.1 discusses the main features of the method, while full details are given in [196].

8.3.2.1 Higher order spectral method

The HOS scheme is able to iteratively solve for the nonlinear boundary conditions and the nonlinear sea state evolution, taking into account the energy exchange between different frequency components of the free surface spectrum. HOS models have been widely used and validated, modelling nonlinear energy transfer [198], or freak waves, [30, 199], among others.

An efficient solution to the nonlinear potential problem is based on the pseudo-spectral formalism, according to which the velocity potential is expressed through a spectral basis Ψ_m :

$$\begin{aligned}\varphi(x, z, t) &= \sum_{m=1}^N A_m(t) \Psi_m(x, z) \\ &= \sum_{m=1}^N A_m(t) \frac{\cosh k_m (z + d)}{\cosh k_m d} e^{ik_m x}\end{aligned}\tag{8.10}$$

where $k_m = m2\pi/L_x$ are the wave numbers, and L_x is the length of the domain. The HOS scheme is based on the knowledge of the surface quantities η and $\tilde{\varphi} = \varphi(x, \eta, t)$,

which are used to evaluate the vertical velocity at the free surface, $W(x, t)$. The method relies on a Taylor series expansion around $z = 0$, up to the so-called HOS order M :

$$\varphi(x, z, t) = \sum_{m=1}^M \varphi^{(m)}(x, z, t) \quad (8.11a)$$

$$\varphi^{(1)}(x, 0, t) = \tilde{\varphi}(x, t) \quad (8.11b)$$

$$\varphi^{(m)}(x, 0, t) = - \sum_{k=1}^{m-1} \frac{\eta^k}{k!} \frac{\partial^k \varphi^{m-k}}{\partial z^k}(x, 0, t) \quad \text{for } m > 1 \quad (8.11c)$$

Equations (8.11) define a triangular system, which is solved iteratively. The solution is then advanced in time, using a 4th order Runge-Kutta Cash-Carp scheme [196], with an adaptive step size. The kinematics and the fluid pressure within the fluid domain are computed via post-processing from free surface quantities, using the modal coefficients A_m in (8.10). Further details about the HOS scheme and its implementation are available in [196]. [196] also proposes validation of the HOS model for regular waves, effectively comparing HOS results with RF theory.

8.4 Regular wave results

The simplest case of steady (regular) waves is considered first. In Sect. 8.4.1, the accuracy of the pressure profile representation is evaluated for a comprehensive set of wave conditions, from shallow to infinite water depth, and from linear to highly nonlinear waves. Then, in Sect. 8.4.2, two particular devices are chosen, a HPA and an OWSC, as well as a wave scatter diagram for a particular installation site, in order to evaluate the impact that the pressure representation accuracy has on the calculation of nonlinear FK forces.

8.4.1 Pressure profile

The overall objective of the study is to evaluate the influence of nonlinear waves on nonlinear FK forces for wave energy converters. Usually, nonlinear models are formulated in the time domain, so that nonlinearities in the equation of motion can be solved in the time integration scheme. Therefore, a time domain framework for the WEC model is assumed hereafter. The two elements affecting the response of the device are the free surface elevation and the pressure profile. On the one hand, η is just an input to the system; therefore, its complexity does not affect the complexity of the WEC model, since η is evaluated only once. On the other hand, the pressure profile has to be evaluated, and integrated, over the wetted surface of the device, at each time step; therefore, the computational burden of the calculation of nonlinear FK forces is strongly dependent on the complexity of the pressure formulation, though independent of η . Hence, hereafter, a nonlinear η is considered for all wave models. Note that using the undisturbed incident free surface elevation for the calculation of nonlinear FK forces is valid only under the assumption that diffraction and radiation effects are negligible.

The shape of the pressure profile is evaluated for a comprehensive range of wave conditions. Three wave periods, of 5s, 10s, and 15s, are considered, and the corresponding wavelengths are computed, according to the water wave dispersion relation [200]. Three normalized water depths d/λ , of 0.05, 0.3, and 0.6, are considered, respectively defining shallow, intermediate, and infinite water depth conditions [200]. Finally, for each wave condition, five wave heights are studied, corresponding to 5%, 10%, 20%, 40%, and 60% of the theoretical maximum wave height, as defined in [194]. The resulting waves conditions are shown by the ‘x’ markers in Fig. 8.1.

It is worth highlighting that the wave period merely has an effect of scaling the free surface elevation and pressure profiles, by changing the wave length; therefore, the markers in Fig. 8.1 overlap for different values of T_w . Likewise, the normalized pressure profiles for different T , but identical λ/d and H_w/d , overlap.

Figure 8.3 shows two representative examples of pressure profiles, at the wave peak ($z = \eta$), having a wave height equal to 40% of the theoretical maximum wave height. In infinite water depth conditions, the RF pressure profile significantly differs from Airy's profile only at the free surface, converging to almost the same value at the sea bottom, where the dynamic pressure is almost zero, due to the large distance between the wave and the sea bed. Conversely, large errors are found in shallow water conditions, throughout the entire water depth, since the nonlinear influence of the nearby sea bed is significantly changing the pressure decay rate from the free surface to the bottom.

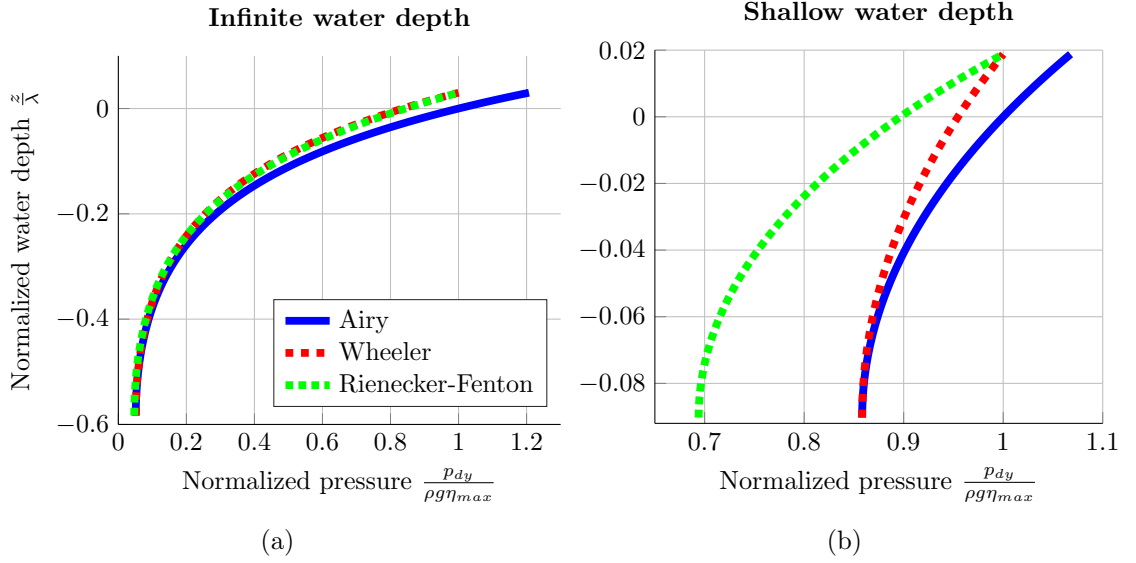


Figure 8.3: Normalized pressure profiles for infinite and shallow water depth conditions, for a wave sample with a wave height equal to 40% of the theoretical maximum wave height.

Wheeler's stretching approach, as explained in Sect. 8.3.1.2, analytically imposes the correct (linearized) boundary condition at the free surface, and linearly stretches the pressure profile from the sea bottom. Indeed, Fig. 8.3 shows that the pressure, according to Wheeler's stretching model, is the same as that from the RF model at the free surface, while is the same as Airy's model at the sea bottom. Consequently, errors in pressure profile modelling for Wheeler's stretching approach are dependent on the pressure error at the sea bottom, which increases with decreasing water depth. Finally, note that the pressure is normalized by $\rho g \eta_{max}$. Consequently, as expected, Airy's theory presents a normalized pressure equal to unity at the SWL. Likewise, the Wheeler stretching and Rienecker-Fenton models show a unity normalized pressure at the actual free surface.

In order to have a more global picture of the errors associated with Airy's theory and Wheeler's stretching model, compared to the RF benchmark model, the mean relative error is computed for all the wave conditions shown by the 'x' markers in Fig. 8.1 as follows:

$$\frac{1}{N} \sum_{n=1}^N \frac{p_{dy}^j(z_n) - p_{dy}^{RF}(z_n)}{p_{dy}^{RF}(z_n)} \quad (8.12)$$

where $p_{dy}^j(z_n)$ is the dynamical pressure computed at point z_n , using model j (either Airy or Wheeler stretching). The relative error is evaluated at N vertical points, from

the sea bottom to the *peak* free surface. Given the variety of water depths considered, and trying to define a depth-independent error index, the same number of points is taken for all the waves. On the other hand, since the pressure decay close to the free surface is faster than in deeper water, with a characteristic exponential decay, the N points are chosen with a logarithmic spacing, so that points are denser close to the free surface, and more widely spread towards the sea bed. Fig. 8.4 plots such relative errors against the wave steepness, which is a representative parameter of the degree of nonlinearity in the wave, as discussed in Sect. 8.3. Finally, note that a positive relative error represents overestimation of the pressure.

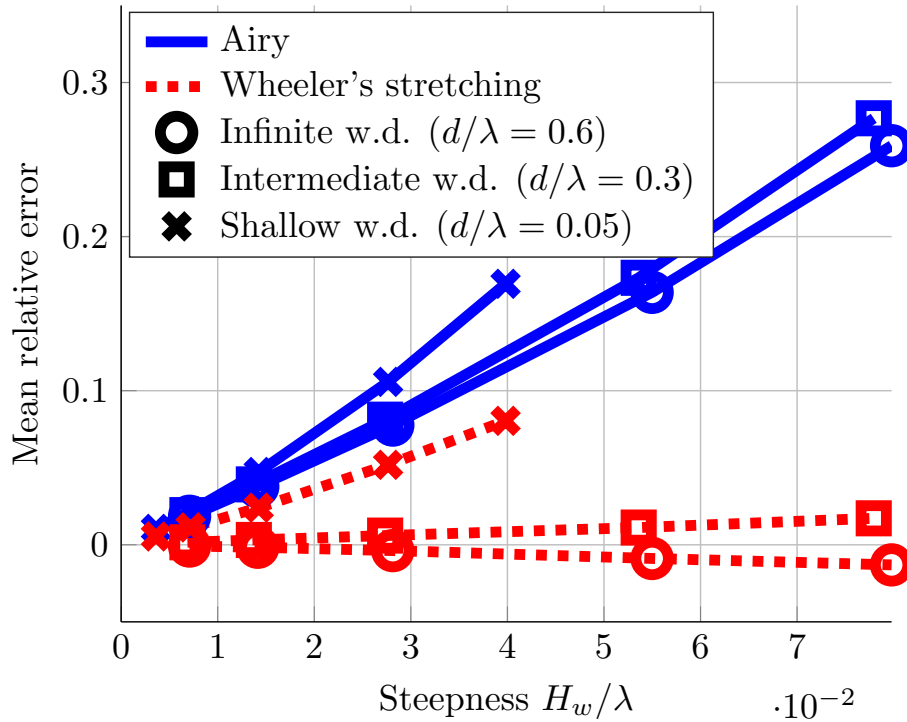


Figure 8.4: Relative errors due to Airy’s theory and Wheeler’s stretching model, compared to the RF benchmark model, for the three water depth (w.d.) conditions. A positive error represents overestimation of the pressure.

In general, Fig. 8.4 shows that the relative error always increases with the wave steepness, associated with the amount of nonlinearity in the wave. Nevertheless, for linear waves (steepness lower than 1%), the relative error is lower than 2% for both models, in all depth conditions. On the other hand, as the wave steepness increases, the curves diverges and the relative error obtained using Airy’s theory reaches a maximum of 28% while, with Wheeler’s stretching approach, the maximum error is less than 2% in intermediate/infinite water depths, and about 8% in shallow water conditions. It is evident that Wheeler’s stretching model always outperforms Airy’s theory; as expected, significant improvements are found at intermediate and infinite water depth conditions, where relative errors are between 12 and 23 times smaller while, at shallow water depths, the relative error is about half.

8.4.2 Pressure integral

The errors, shown in Fig. 8.4, give an *overall* evaluation of the pressure profile representation, from the sea bottom to the free surface, according to Airy’s and Wheeler’s stretching approaches. Nevertheless, as far as nonlinear modelling of wave energy converters is concerned, what is important is the accuracy just in the region of fluid where the device

operates, which affects the accuracy of the computation of the nonlinear FK force.

Consequently, the device operating principle has to be taken into account. On the one hand, piercing heaving point absorbers work in the proximity of the free surface, in either infinite or intermediate water depth conditions. On the other hand, oscillating wave surge converters operate in intermediate/shallow water conditions, spanning almost all the depth from the free surface to the sea bed. Therefore, based on Figs. 8.3 and 8.4, it can be expected that Wheeler's stretching approach can be more effective for HPAs than for OWSCs, since Wheeler stretching errors are particularly small close to the surface, and in infinite or intermediate water conditions.

Inspired by the Wavestar device [66], a spherical HPA is chosen, with a radius of 2.5m, and mass centre at the still water level. The dynamic nonlinear FK force is the integral of the dynamic pressure over the instantaneous wetted surface, which depends on the relative displacement between the device and the free surface elevation. The geometry of the OWSC is based on the Oyster 2 device [170], where the dynamic FK torque is the resulting torque due to the pressure on the front and rear surfaces of the flap. The formulation of nonlinear FK forces for the HPA and the OWSC are given in Chapter 5.

The reason for considering the device geometry is to quantify the importance of the nonlinear pressure profile in the respective water depths where the devices operate. Therefore, with the purpose of temporarily excluding geometric nonlinearities, a zero relative displacement is used for the HPA, and the vertical (rest) position is considered for the OWSC. The dynamic pressure is consequently integrated over half a sphere for the HPA, and over a vertical rectangle of 9m draft, 3m freeboard, and 26m width for the OWSC. The freeboard is taken into account for the evaluation of the wetted surface.

Fig. 8.4 shows how modelling errors significantly increase with the wave steepness. Nevertheless, the occurrence of highly nonlinear waves is likely to be low, depending on the scatter diagram of the installation site. Furthermore, WEC devices are designed to be operative only in a specific range of wave conditions, where physical constraints are respected. Otherwise, for certain wave conditions, the device is not able to produce energy (if waves are not energetic enough), or survivability mode is engaged (if waves are too energetic).

Therefore, for power production assessment studies, the accuracy of the wave representation is important only in the power production region. On the contrary, highly nonlinear and energetic sea states must be considered when maximum structural loads need to be assessed. Nevertheless, more complex fully nonlinear models, like computational fluid dynamics (CFD), are likely to be necessary for such survivability studies and are beyond the scope of this study.

The scatter diagram considered in this study is shown in Fig. 8.5, which refers to the European Marine Energy Centre (EMEC), Orkney, Scotland [35], where the nominal water depth is 50m. The solid line defines the operational region of the OWSC Oyster 800, which covers 86.1% of the total wave occurrences.

A set of regular wave conditions is based on the significant wave heights (H_s) and peak wave periods (T_p) shown in Fig. 8.5. The water depth choice, equal to 13m, is constrained by the OWSC geometry [170]. Nevertheless, the HPA is studied in infinite water depth conditions as well. Varying the water depth condition implies changes in the power content of the scatter diagram, since the transition from deep to shallow water happens with non-negligible power losses. However, in this study, the scatter diagram has been retained unchanged, since the only purpose of considering different water depth conditions is to discuss how the pressure profile changes, due to the proximity (or not) of the sea bottom.

Integrals of the dynamic pressure over the surface of the HPA and the OWSC are computed at the peak of the free surface elevation, in order to highlight nonlinear effects. The computation of such integrals is straightforward for Airy's pressure profile, since algebraic solutions are available. The same algebraic solution can be easily adapted to

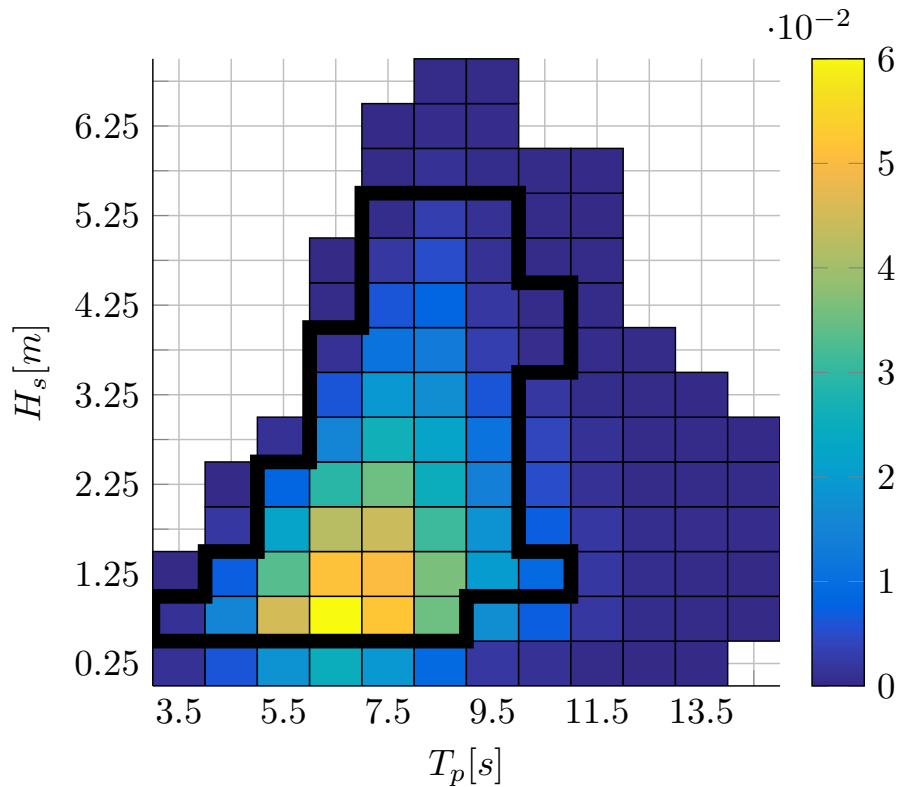


Figure 8.5: Significant wave height H_s , peak wave period T_p scatter diagram at the European Marine Energy Centre (EMEC), Orkney, Scotland. The solid line defines the operational region of the OWSC Oyster800, which covers 86.1% of the total wave occurrences [35].

Wheeler’s stretching pressure profile, since just a change of variable is required. On the contrary, integrating the RF pressure profile is much more complex; given the high number of terms in the RF pressure expression, an algebraic solution does not exist. A trapezoidal numerical integration scheme is then used, iterating the integration until an absolute tolerance lower than 10^{-10} is achieved.

As in Sect. 8.4.2, results obtained using the RF model are used as benchmarks to evaluate Airy’s and Wheeler’s stretching models, whose relative errors are shown in Figs. 8.6 and 8.7, for the HPA and the OWSC, respectively. In both figures, the uppermost surface corresponds to Airy’s model, whereas the lower surface corresponds to Wheeler’s stretching approach, whose errors are always smaller.

Each surface in Figs. 8.6 and 8.7 presents three different shades (grey, red, and green). The outer (grey) surfaces cover the whole scatter diagram. The inner darker (red) shades consider only the wave conditions within the operational region of the scatter diagram, shown in Fig. 8.5, which is the region of interest for power production assessment studies. The inner lighter (green) shades take into account only the wave conditions which pass a significant occurrence threshold, arbitrary set at 1%. Indeed, higher accuracy is required in more probable wave conditions, while larger errors can be accepted for rare wave conditions. The sum of the occurrences over 1% amount to 87%, which is comparable to 86.1% of the whole operational region.

Airy’s theory produces similar errors in both the HPA and the OWSC, up to 36% in the full scatter diagram, up to 28 % in the operational region, and up to 18% in the occurrence threshold region. Conversely, Wheeler’s stretching method performs better for the HPA than the OWSC, with maximum errors of 5% and 20%, respectively. Indeed, HPAs work close to the free surface: in this region of fluid, the (linearized) boundary

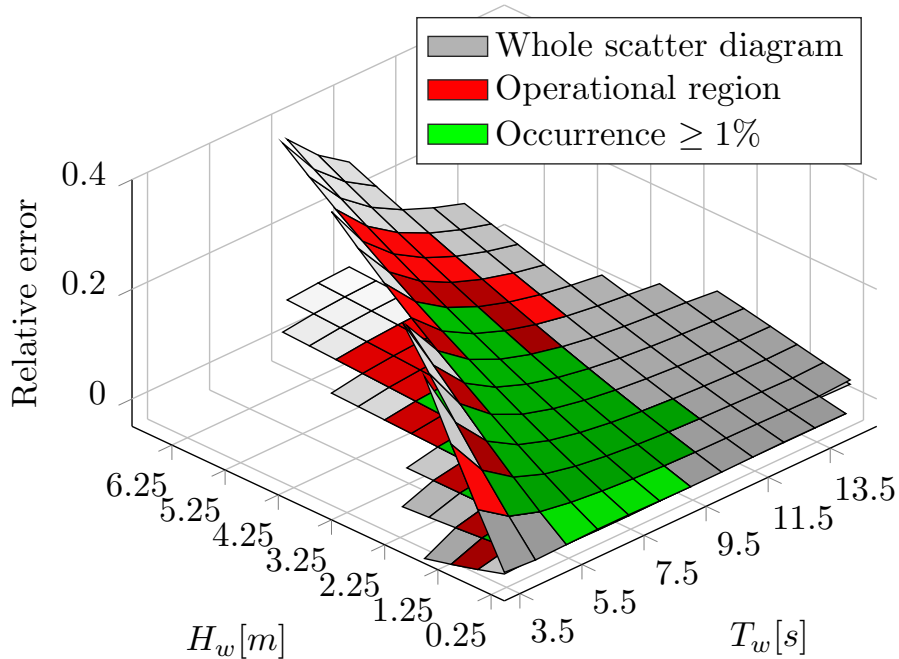


Figure 8.6: Relative error in the pressure integral, using regular waves, for the HPA (water depth of 13 m), using Airy's pressure (on the top), and Wheeler's stretching pressure (on the bottom).

Table 8.1: Maximum errors for the whole scatter diagram, the operational region, and occurrence threshold region, for the HPA and the OWSC. The subscript indicates the water depth for each of the device.

		HPA _∞		HPA ₁₃		OWSC ₁₃	
		Airy	Wheeler	Airy	Wheeler	Airy	Wheeler
Occurrence $\geq 1\%$	(total 87%)	14.1%	-1.0 %	17.3 %	3.1%	18.2 %	9.1 %
Operational boundary	(total 86.1%)	20.6 %	-2.4 %	26.0 %	4.4 %	27.8 %	14.7 %
Whole scatter diagram	(total 100%)	25.1 %	-4.2 %	32.5 %	5.3 %	35.8 %	20.5 %

condition error is zero, thanks to the Wheeler stretching change of coordinates.

Finally, the HPA is studied in an infinite water depth condition as well. Smaller errors are found, compared to the 13 m water depth condition. Airy's theory maximum error drops from 32% to 25%, while the Wheeler stretching maximum error drops from 5% to 4%. A summary of the maximum errors in each of the three regions (whole scatter diagram, operational region, and occurrence threshold region) is tabulated in Table 8.1.

8.5 Irregular wave results

As in Sect. 8.4, the accuracy of the pressure representation is evaluated, for irregular waves, across the whole sea depth, in Sect. 8.5.1, and in relation to nonlinear FK forces on a HPA and an OWSC, in Sect. 8.5.2.

All the 108 sea states in the EMEC scatter diagram, shown in Fig. 8.5, are considered, using JONSWAP spectra with $\gamma = 3.3$ and different H_s and T_p . Constant water depth, of 13m, is assumed, as in Sect. 8.4.2. Note that, even though the HOS software solves the nonlinear wave propagation problem, treating all sea states as potentially non-Gaussian, only 41 sea states, out of 108 (38%), are actually non-Gaussian. Indeed, the remaining 67 sea states can be considered predominantly Gaussian processes, since $d/H_s \geq 4.17$ [190].

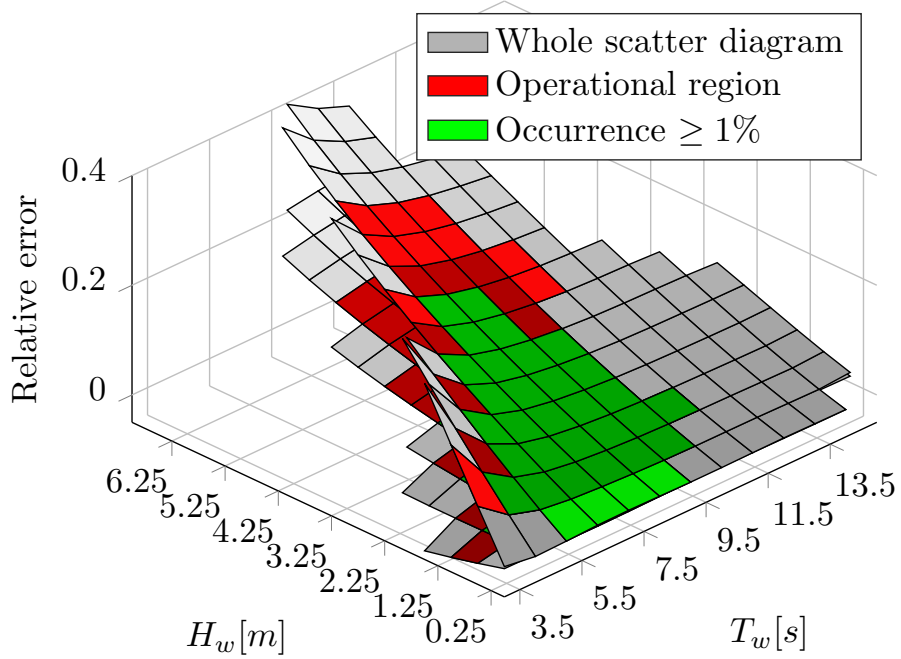


Figure 8.7: Relative error in the pressure integral, using regular waves, for the OWSC, using Airy’s pressure (on the top), and Wheeler’s stretching pressure (on the bottom).

Two-dimensional HOS simulations are run with HOS-Ocean, in a spatial domain 40 times longer than the peak wave length λ_p of the sea state, using $N = 256$ sampling points (see (8.10)), as in [196]. The HOS order M , in (8.11), is chosen equal to 5, based on a convergence study for the steepest sea state ($H_s = 4.75m, T_p = 6.5s$), which is the most challenging to simulate, where the sea state steepness is defined as H_s/λ_p . The convergence test is based on the free surface horizontal velocity at the highest wave crest.

Note that, in the most severe sea state considered, there are chances that some waves break, since the ratio H_s/λ_p is larger than 0.064 [201]. In case of wave breaking, the HOS method may not converge to a solution. [201] gives the most useful guidelines to set-up the HOS model in order to reduce the risk of failure and, in general, to ensure appropriate levels of accuracy. In this work, since only one set of random phases is studied for each sea state, it happens that, by chance, the HOS does not diverge for the one particular realization considered.

Finally, each simulation is run for a duration of 250 times the peak period, in order to guarantee proper nonlinear wave propagation, and to have a representative statistical description of the sea state. The post-processing routine of the HOS code, used to extract the pressure profile in the fluid domain, is performed at $x = 0$, with a sampling rate of 1.28 Hz.

8.5.1 Pressure profile

In order to apply Airy’s theory and Wheeler’s stretching method to compute the pressure field distribution, the frequency components (frequency, amplitude and phase) of the free surface elevation are needed, which can be obtained through a fast Fourier transform (FFT). Given the significant length of the time signals ($250 T_p$), at a sampling rate of 1.28 Hz, the FFT of the whole signal would require a very large number of components, which would considerably slow down post-processing calculations. Therefore, the time series are divided into 25 segments, of equal length ($10 T_p$), which is considered appropriate to be representative of the sea state. Apart from the practical advantage, the segmentation is useful in obtaining some statistical information about the mean error computed for each

sea state.

From each segment, a FFT is used to calculate an energy spectrum. Note that such time series are not periodic; consequently, the reconstructed time signal (obtained through an inverse FFT of the energy spectrum) overlaps with the original time series at all the sampling points, except for the very last point. A fair comparison of the three wave modelling approaches (Airy's theory, Wheeler stretching, and HOS), must consider the identical surface elevation in all cases; therefore, the last point is discarded.

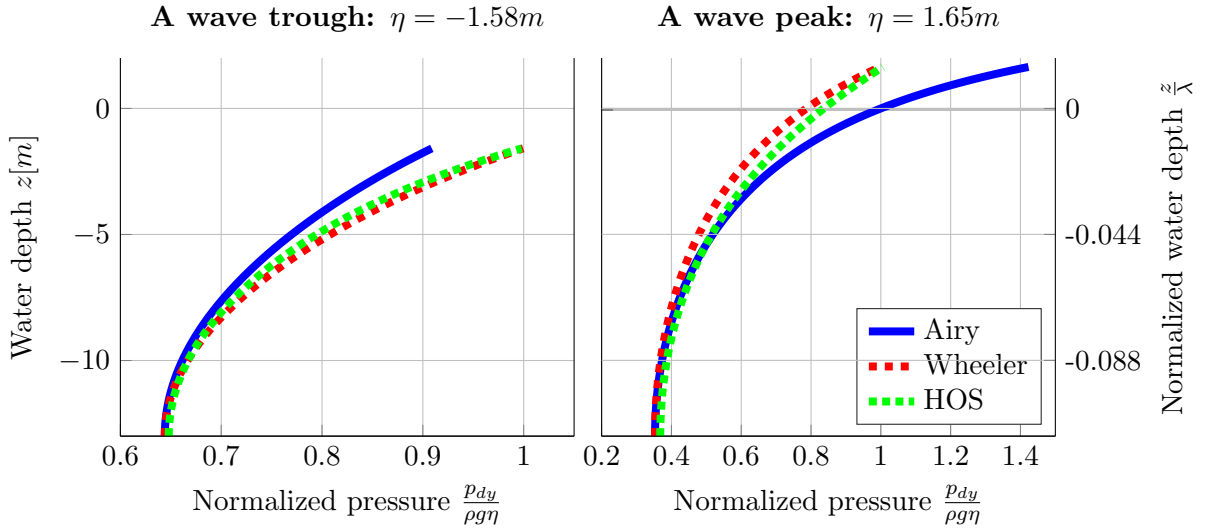


Figure 8.8: Normalized pressure profiles for a sea state with $T_p = 8.5s$ and $H_s = 3.25m$, at 13m water depth, taken at a wave trough (on the left) and a wave peak (on the right), whose absolute value is about half of H_s .

For each point *in time*, the pressure profile is compared, along the complete water depth. Figure 8.8 shows an example of wave profiles for a sea state in the middle of the scatter diagram, with $T_p = 8.5s$ and $H_s = 3.25m$. Both a wave trough and a wave peak are considered, whose absolute value is chosen to be about half of H_s , in order to be representative of the irregular sea state. Note that, similarly to Fig. 8.3, the normalized pressure for Airy's theory is unity at the still water level ($z = 0$), while for Wheeler stretching and the HOS, the normalized pressure is unity at the actual free surface ($z = \eta$).

Some preliminary qualitative considerations are offered concerning the sign of the error, either positive (overestimation), or negative (underestimation), where the HOS pressure profile is taken as a benchmark. On the one hand, at the free surface ($z = \eta$), Airy's theory overestimates the pressure for positive η , but underestimates it for negative η , due to the approximation of the free surface dynamic boundary condition around the SWL. Note that errors for positive η can be particularly large, due to the exponentially increasing pressure, and the relatively large wave number for some frequency components, as discussed in Sect. 8.3.2. On the other hand, Wheeler's stretching approach produces negligible errors at the free surface, which is indeed the objective of the stretching.

At the sea bottom ($z = -d$), it is not possible, in general, to anticipate the sign of the error. Nevertheless, if the water depth tends to infinity, the dynamic pressure tends to zero, for all three methods. Therefore, the pressure profile, according to Airy's theory, would remain always on the same side of the HOS pressure profile (consistently over- or under-estimating), and the sign of Airy's theory error would remain constant across the entire water depth, converging to zero as the depth increases. However, with finite water depth, the pressure at the sea bottom is not negligible, as shown, for example, in Fig. 8.3; hence larger errors are expected, either positive or negative. Therefore, the pressure profile, according to Airy's theory, may intersect the HOS profile, causing a change of sign

of the error as the depth increases. Likewise for Wheeler’s pressure profile, which is just a stretch, centred at the sea bottom, of Airy’s pressure profile.

For quantitative considerations, due to the eventual change of sign of the pressure error across the fluid domain, the absolute error is considered instead, in order to avoid errors of opposite sign cancelling out. The sign of the error, which is lost with such an absolute error, is recovered in Sect. 8.5.2, when the resulting nonlinear FK forces are considered.

The error is normalized by the maximum characteristic pressure of the sea state, defined as $\rho g H_s/2$. For each point in time, the average of all the errors, at different *depths* from the sea bottom to the free surface elevation, is considered. Afterwards, for each data segment, the *time* average is considered:

$$\frac{1}{\rho g H_s/2} \frac{1}{NM} \sum_{m=1}^M \sum_{n=1}^N \left| p_{dy}^j(z_n, t_m) - p_{dy}^{HOS}(z_n, t_m) \right| \quad (8.13)$$

where $p_{dy}^j(z_n, t_m)$ is the dynamic pressure, according to model j , computed at z_n in space, and t_m in time, with $t_1 = 0$ and $t_M = 10T_p$. Consequently, for each sea state, there are 25 estimates of the overall error, from which the mean and the 95% confidence interval (CI) are computed, which are tabulated in Table 8.2. The bold line represents the operational region, as in the scatter diagram in Fig. 8.5. The (cyan) shading of the cells is proportional to the steepness of the sea state.

The mean overall errors, in Table 8.2, are shown in Fig. 8.9 as well, where the horizontal axis represents a progressive enumeration of the sea states, based on a vertical reading of Table 8.2: starting from the first column (constant T_p), the enumeration increases with H_s , until the row is full; then, the enumeration continues to the following column. Consequently, in Fig. 8.9, T_p is constant between two consecutive peaks of the error curves, while H_s increases from left to right. Indeed, as expected, errors increase with increasing values of H_s .

From both Table 8.2 and Fig. 8.9, it can be noticed that, as expected, Wheeler’s stretching always outperforms Airy’s theory. Nevertheless, while large improvements are appreciable for severe sea states, smaller differences are found in milder sea conditions. Therefore, it is important to weight the performance of the two approaches with the probability of occurrence of each sea state, and whether or not the sea state is within the power production region. Consequently, similarly to the regular wave case in Sect. 8.4.2, Fig. 8.9 shows the occurrence curve, a 1% occurrence threshold, and the sea states which are outside the operational region of the device (shaded in red). It is evident that larger errors, as expected, occur for sea states which are outside the operational region, and/or are relatively rare. Nevertheless, even though the performance of Airy’s theory and Wheeler stretching is similar in the operational region, Wheeler stretching is preferred, since it is always more accurate, while maintaining the same (low) complexity of Airy’s theory.

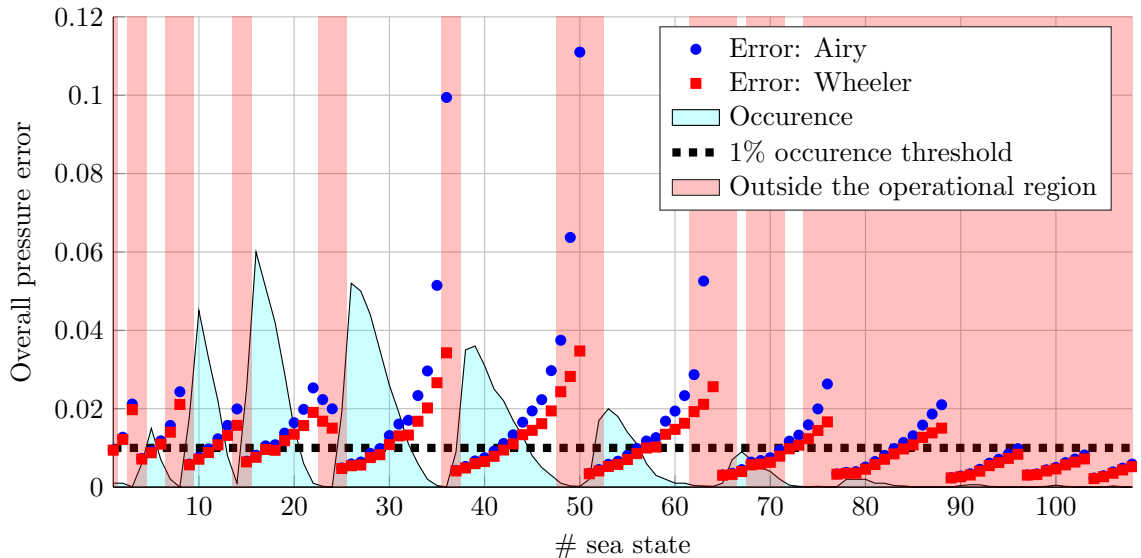


Figure 8.9: Overall pressure error, as in Table 8.2, with a progressive enumeration of the sea states, following the columns of Table 8.2. The occurrence of each sea state is shown, according to the scatter diagram, in Fig. 8.5. The sea states outside the operational region are shaded (in red).

An important variable, which is missing from Fig. 8.9, is the sea state steepness. Indeed, the two sea state parameters, influencing the pressure error, are the sea state steepness and the significant wave height. Fig. 8.10 plots the overall pressure errors of Table 8.2 against sea steepness. Recall that, as explained in Sect. 8.5, for a wave steepness larger than 0.064, wave breaking is possible. The general trends clearly show an increasing error with wave steepness, but there are significant oscillations, especially for Airy’s theory, for large steepness values, which are due to the wave height. In fact, a similarly large steepness can be obtained with a short but small sea state (for example $T_p = 3.5s$ and $H_s = 1.25m$), or a long but high sea state (for example $T_p = 8.5s$ and $H_s = 6.75m$), as shown by the shading of the cells in Table 8.2. Consequently, with almost the same

steepness, much larger errors are obtained for larger H_s . Such variations are particularly evident in Airy's theory approach, since significant errors are obtained for large waves.

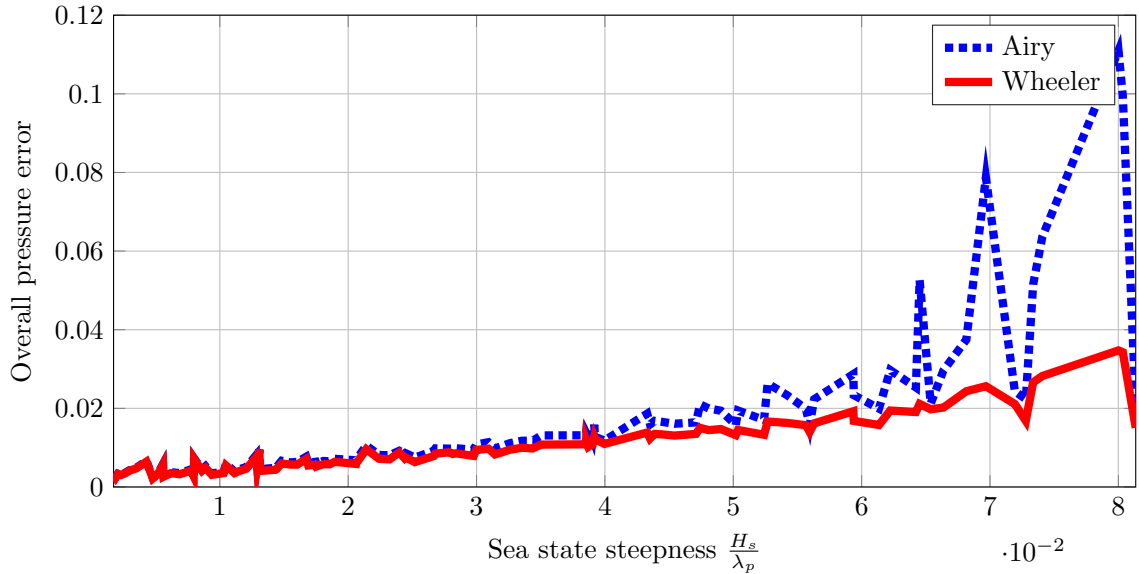


Figure 8.10: Overall pressure error, as in Table 8.2, plotted against the sea state steepness.

8.5.2 Pressure integral

The impact of the dynamic pressure representation accuracy on the nonlinear FK force calculations is investigated, for a hypothetical HPA and an OWSC installed at EMEC, with a water depth of 13m. As in Sect. 8.4.2, the objective is to introduce representative geometries for a HPA and an OWSC, which can highlight the essential differences due to the operating principles. Therefore, on the one hand, the HPA is represented by a half-submerged floating sphere, with 5m diameter, i.e. with the centre of gravity at the free surface elevation. On the other hand, the OWSC is represented by a 26m wide vertical rectangle, with 9m draft and 3m freeboard, which is taken into account for the evaluation of the wetted surface.

Consequently, the HPA is strongly affected by the large errors that Airy's theory produces close to high crests, due to the high frequency components of the spectrum. Conversely, the OWSC is constrained by its limited freeboard; when large waves occur, the OWSC becomes fully submerged, and hence avoids the free surface dynamic boundary condition errors of Airy's theory.

A single estimate of the model accuracy, across the complete time series, would be useful. Since the nonlinear FK force is oscillating, between positive and negative values, the definition of a fair relative error, for each time step, is challenging, due to the changes of sign, and divisions by quasi-zero values. Furthermore, an average over the whole time series should be taken. Rather, the area Γ under the absolute value of the nonlinear FK force (F_{FK}) time series, is considered instead:

$$\Gamma = \int_0^{250T_p} |F_{FK}| dt \quad (8.14)$$

Γ has the advantage of being a single, positive value, characterizing the complete time series, and conveying overall under/overestimation information. An accuracy index is then defined as the ratio between Airy's theory (or Wheeler's stretching) area, and the HOS area. Fig. 8.11 shows such an accuracy index, for the HPA and the OWSC, using

Airy’s theory and Wheeler’s stretching, highlighting which sea states are outside the power production region.

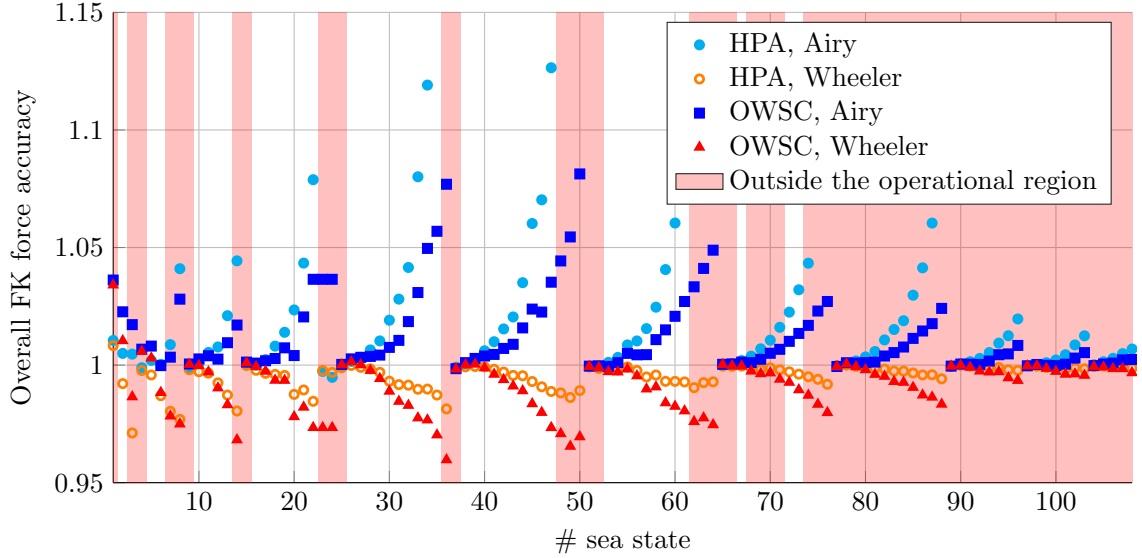


Figure 8.11: Froude-Krylov accuracy index, defined as the ratio between the areas under the absolute value of the nonlinear FK time series, where indices greater than unity represent overestimations of the FK force.

Consistent with Figs. 8.9 and 8.10, Wheeler stretching performs better than Airy’s theory, showing smaller deviations from the unity accuracy index. Furthermore, Wheeler stretching, in general, underestimates the nonlinear FK force, whereas Airy’s theory overestimates it.

Despite the fact that the two devices are subject to the same pressure errors, the essential geometric differences, between the HPA and the OWSC, cause significant variations in the FK force accuracy. Indeed, Airy’s theory performs worse for the HPA, in particular for quite extreme sea states (errors up to 2.01). Note that, in order to improve the readability of Fig. 8.11, the upper limit of the vertical axis is set to 1.15, excluding HPA Airy’s errors for the six most extreme sea states. In any case, such sea states are outside the power production region.

Such results for the HPA, with irregular waves, contrast with those for regular waves, shown in Figs. 8.6 and 8.7. Airy’s theory is affected by two errors: the free surface dynamic boundary condition error and the entire pressure profile error. Due to their dimensions and positions in the fluid domain, the HPA is mainly affected by the free surface error, whereas the OWSC by the pressure profile error. In the irregular wave case, the free surface dynamic boundary condition error can become particularly large, due to high frequency components, as discussed in Sect. 8.5.1, which are absent in the regular wave case.

Conversely, since Wheeler stretching resolves the dynamic boundary condition error, it is affected only by the pressure profile error. Therefore, consistent with the results for regular waves, Wheeler stretching is more accurate for the HPA than the OWSC, even with irregular waves, since the HPA is located in a smaller region of fluid, close to the free surface, where Wheeler’s representation is most accurate.

8.6 Conclusion

The accuracy of nonlinear hydrodynamic models for wave energy converters is directly influenced by the fidelity of the wave field representation. However, accuracy improvements have to be weighted by the increase in complexity and computational cost, required to

implement more accurate wave models. Using regular and irregular waves, this study considers four different modelling approaches, namely linear Airy's theory, Wheeler's stretching approach, the Rienecker-Fenton method (only for regular waves), and a higher-order spectral method (only for irregular waves). In particular, the focus of the study is on the impact of the accuracy of the pressure field representation on *nonlinear* Froude-Krylov force calculations.

The entire pressure profile is evaluated for a comprehensive range of wave conditions, both regular and irregular. Modelling error magnitudes depend on the water depth, wave steepness, and wave height. In all cases, Airy's theory produces larger errors than Wheeler stretching, especially with irregular sea states, due to the relatively high frequency components of the wave spectrum.

As far as WEC nonlinear models are concerned, only the region of fluid where the device operates is relevant for the final accuracy of the results. On the one hand, Figs. 8.6 and 8.7 show that, when regular waves are considered, smaller errors are produced in HPAs, with respect to OWSCs, for both Airy's theory and Wheeler stretching. On the other hand, Fig. 8.11 shows that, with irregular waves, consistent results are found only for Wheeler stretching, which is more accurate for HPAs. Conversely, Airy's theory performs better for OWSCs than HPAs.

Furthermore, it is important to highlight that the performance of the wave models have to be weighted with the occurrence of each sea condition, according to the scatter diagram of the installation site. A further criterion to consider is the power production region, which is the only one taken into account for power production assessment studies.

Finally, it can be concluded that the Wheeler stretching approach is a convenient wave modelling option for computing nonlinear Froude-Krylov forces for wave energy devices, since it performs well compared to RF/HOS methods, and always performs better than Airy's theory, while maintaining the same level of complexity.

Multi-degree of freedom nonlinear Froude-Krylov force models

9.1 Motivation

Previous chapters consider only single degree of freedom devices, mainly due to their simplicity in modelling and analysis. However, although usually converting energy from only one mode, wave energy converters are, in general, responsive in more than one degree of freedom. Energy exchange, and linear and nonlinear interactions between different DoFs are potentially important aspects to consider, with consequences on the overall device efficiency and survivability, as well as on the effectiveness of any associated control strategy. Therefore, representative multi-DoF mathematical models are required. One remarkable nonlinear phenomenon, that only nonlinear 6-DoF models can articulate, is parametric roll, which is a potentially detrimental effect for wave energy conversion.

9.2 Introduction

The conceptual design of a wave energy converter is strongly driven by what kind of motion the PTO system requires. Standard technologies for generator units are based on single-axis motion, either rotational or translational. Therefore, WECs are usually designed to work in a single-DoF, so that the energy ideally flows from the incoming wave, to one absorbing DoF of the floater, to the PTO system, via a mechanical link, which converts a single-axis motion (the floater's) into another single-axis motion (the PTO's). In such a scheme, any motion of the floater in secondary DoFs (which absorb part of the incoming energy) is not exploitable, therefore effectively causing losses. An alternative would be to use customized PTOs, and/or complex mechanical conversion systems, which would be able to convert energy from ideally all system's modes. However, possible drawbacks of complex PTO solutions are higher manufacturing and maintenance costs.

Consequently, the vast majority of floating wave energy converters are designed to absorb and convert energy from just one DoF. However, under certain conditions, the floater may use part of the incoming energy to excite secondary DoFs. Such an excitation can be linear or nonlinear, external or internal. On the one hand, considering, for example, a point absorber, subject to mono-directional waves, *external* excitation is related to the incoming wave, acting on surge, heave, and pitch DoFs. On the other hand, an *internal* excitation mechanism is potentially provided by parametric resonance, which is a purely nonlinear effect, diverting part of the energy, from externally excited DoFs, to the roll or pitch DoF. Furthermore, certain PTO systems and mooring configurations may increase the complexity of the WEC response, eventually providing additional coupling effects

between DoFs.

Overall, it is of paramount importance for the WEC designer to have representative mathematical models, in order to be aware of the full complexity of the system dynamics, and to conduct well-informed device optimization and control. This chapter purports to extend the nonlinear Froude-Krylov formulation, described in Chapter 4, from 1-DoF to 3-DoF first, up to 6-DoF. The 3-DoF intermediate step is used to discuss nonlinearities in *external* excitations (surge, heave, and pitch). The 6-DoF model is then used to investigate the likelihood and the severity of the eventual *parametric response*. Furthermore, defining and comparing different nonlinear models, at different complexity levels, is useful to select the proper (parsimonious) model for each application. In fact, since parametric resonance is a phenomenon confined to a relatively small frequency range, the 3-DoF model may be the most appropriate for device optimization and control, over a wide range of frequencies, while the 6-DoF model may be preferred for motion simulation.

Such models are hereafter applied to three case studies, inspired by existing WECs, namely the CorPower, Wavebob, and SparBuoy devices, in order to show the applicability to real devices. Such devices are different implementations of the heaving point absorber concept, the CorPower device being a bottom-referenced single body device, the Wavebob a self-reacting 2-body device, and the SparBuoy a floating OWC. Different aspects and implications of using nonlinear FK models are investigated with the different devices:

- CorPower: validation of the modelling approach (Sect. 9.3.3), and effects of parametric roll response (Sect. 9.4.2);
- Wavebob: sensitivity to nonlinearity and modelling errors (Sect. 9.4.3);
- SparBuoy: sensitivity of parametric instability to the drag coefficient, and discussion of practical issues due to long simulations with irregular wave (Sect. 9.4.4).

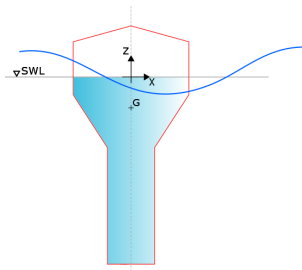
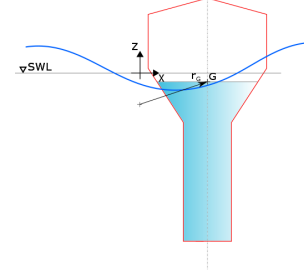
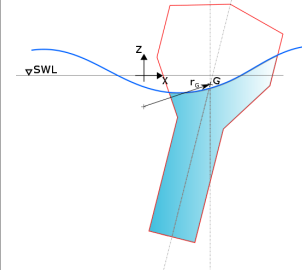
9.3 Three-DoF nonlinear Froude-Krylov model

This section provides an extension of the discussion in Chapter 4, Sections 4.3 and 4.4, in order to define a more general framework for the computation of nonlinear FK forces, in any degree of freedom. Using the same parametrization as in Sect. 4.4, it is possible to analytically describe nonlinear FK forces. In general, FK integrals must be solved numerically using, for example, a trapezoidal rule. However, under certain assumptions, the most important of which is the one of small pitch angles, it is possible to further simplify the problem, and achieve an algebraic solution, which is considerably faster than numerical integration.

Hereafter, LFK is used as the acronym for *linear* FK forces, VFK for the algebraic-nonlinear model (since it assumes a *vertical* geometry for the computation of nonlinear FK forces), and RFK for the numerical-nonlinear model (since it considers a *rotating* geometry). Table 9.1 summarizes the main differences between such modelling approaches. As already widely discussed in Chapter 4, the difference between linear and nonlinear models is the wetted surface considered for calculation of FK forces, either constant (LFK) or instantaneous (VFK, RFK). More interestingly, the difference between VFK and RFK are in the pitch angle (zero or not, respectively), in the intersection between the floater and the free surface (flat or not, respectively), and in the water depth conditions (only infinite depth for VFK).

The application of these three different approaches to FK force calculation (linear, algebraic-nonlinear, and numerical-nonlinear) may depend on the particular purpose the mathematical model is intended for. For preliminary studies, shape optimization, or WEC farm configuration analysis, many iterations are needed; therefore, the requirement for fast

Table 9.1: Summary of the main difference between the three Froude-Krylov modelling approaches for axisymmetric buoys.

	LFK Linear Froude-Krylov (FK)	VFK Algebraic nonlinear FK	RFK Numerical nonlinear FK
Wetted surface $S(t)$	Constant	Instantaneous	Instantaneous
Pitch angle θ	0	0	θ
Free surface $\eta(x, t)$	0	$\eta(t)$	$\eta(x, t)$
Water depth	Generic	∞	Generic
Computational time	+	++	+++
			

calculation prevails over the accuracy requirement. In case of control optimization routines, a higher level of accuracy is of great importance, at a significantly low computational time; therefore, the algebraic-nonlinear approach may be the most appropriate. Finally, a higher degree of accuracy is needed for power production assessment, or to compute maximum loads (for the design of the mechanical properties of the structure and mooring lines). In such cases, the numerical-nonlinear method may be preferred.

Froude-Krylov forces As discussed in Chapter 4, FK forces are computed by integrating the pressure of the undisturbed incident wave field over the instantaneous wetted surface $S(t)$. However, while only heave forces were presented in Chapter 4, the generic expression for forces and torques follows:

$$\mathbf{F}_{FK} = \mathbf{F}_g - \iint_{S(t)} p \mathbf{n} dS \quad (9.1a)$$

$$\mathbf{T}_{FK} = \mathbf{r} \times \mathbf{F}_g - \iint_{S(t)} p \mathbf{r} \times \mathbf{n} dS \quad (9.1b)$$

where $\mathbf{n} = (n_x, n_y, n_z)$ is the unit vector normal to the surface, pointing outwards, $\mathbf{r} = (x, y, z)$ is the position vector, and \times is the cross product.

For a geometry of arbitrary complexity, it is not possible to solve the FK integrals in (9.1a) and (9.1b). Linear boundary-element solvers linearize the problem around the still water level (SWL: $z = \eta = 0$), therefore considering a constant wetted surface. Alternatively, computationally expensive mesh-based approaches, such as LAMSWEC [91], can be used for computing FK forces with respect to the instantaneous wetted surface. For axisymmetric buoys, a convenient parametrization of the wetted surface can ease the calculation of the FK integrals. In particular, computationally efficient algebraic solutions of the FK integrals exist for vertical axisymmetric buoys, as shown in Chapter 4, Section 4.4. However, if the body is also significantly pitching, numerical integration is required.

9.3.1 Algebraic integration

The integrals in (9.1a) and (9.1b) can be rewritten in the cylindrical coordinate system, as already discussed in Chapter 4. The only difference is that the floater is also moving in

surge, while a negligible pitch angle is assumed. Assumptions/conditions for the algebraic integrations are hereafter recalled. The intersection between the free surface elevation and the floater, which defines the upper limit of integration $\varrho_2(\vartheta)$, is assumed constant, and equal to the free surface elevation at the axis of the buoy ($\bar{\eta}$). Such a condition is relatively accurate if the wave length is much longer than the characteristic horizontal dimension of the device at the free surface elevation, which is often the case. Although ϱ_2 is constant, the pressure field does change along the x direction. Moreover, note that buoys much smaller than the wave length are usually not very responsive in pitch, which is consistent with the hypothesis of small rotation.

In order to permit an algebraic solution, the cosine term of the pressure formulation, shown in (4.4), must be replaced with its McLaurin expansion, introducing a small error, as discussed in [15]. One further simplification, needed to achieve an algebraic solution, is to consider the pressure formulation in infinite water-depth. The approximation introduced is normally negligible, given that point absorbers are usually installed in deep-water locations. Finally, for the computation of nonlinear FK forces, it is advantageous to apply Wheeler stretching to the dynamic pressure in equation (4.4) [19]. Therefore, the following pressure, expressed in cylindrical coordinates, is used in the integrals:

$$\begin{aligned}
p = & -\gamma z + \gamma a e^{k_s(z-\bar{\eta})} \\
& (\cos \omega t + k f(\varrho) \cos \vartheta \sin \omega t - \frac{(k f(\varrho) \cos \vartheta)^2}{2} \cos \omega t \\
& - \frac{(k f(\varrho) \cos \vartheta)^3}{6} \sin \omega t + \frac{(k f(\varrho) \cos \vartheta)^4}{24} \cos \omega t + \\
& \frac{(k f(\varrho) \cos \vartheta)^5}{120} \sin \omega t) + o((k f(\varrho) \cos \vartheta)^5)
\end{aligned} \tag{9.2}$$

where $k_s = \frac{kh}{\bar{\eta}+h}$ is the stretched wave number. Although the McLaurin expansion, up to the fifth order, is composed of six terms, only three are non-zero, since odd powers of $\cos \vartheta$ integrate to zero, when $\vartheta \in [-\pi, \pi]$. Clearly, which terms cancel out from (9.2) depends on the degree of freedom of the specific unity vectors considered, which may contain either $\cos \vartheta$ or $\sin \vartheta$. Moreover, note that, for any axisymmetric vertical device, static surge and pitch FK forces are zero, because the integrand contains a $\cos \vartheta$.

The solution of the nonlinear FK integrals for a disc, cylinder, and cone with vertical axis are hereafter presented. In fact, the vast majority of axisymmetric point absorbers can be described as a combination of cylinders and cones. However, the discs (lids), which close the surface of a cylinder, cannot be described using cylindrical coordinates. To this end, polar coordinates are used to describe any closing disc.

Hereafter, superscripts s , h , and p stand for surge, heave, and pitch components, respectively, while FK_{st} and FK_{dy} subscripts stand for static and dynamic FK components, respectively.

9.3.1.1 Cylinder section description

For the lateral surface of a vertical cylinder, characterized by $f(\varrho) = R$, the following results are obtained:

$$\mathbf{e}_\varrho \times \mathbf{e}_\vartheta = R \begin{pmatrix} -\cos \vartheta \\ -\sin \vartheta \\ 0 \end{pmatrix} \tag{9.3}$$

$$\langle \mathbf{r} \times (\mathbf{e}_\varrho \times \mathbf{e}_\vartheta), \mathbf{j} \rangle = -R \varrho \cos \vartheta \tag{9.4}$$

$$F_{FK_{st}}^h = 0 \quad (9.5)$$

$$F_{FK_{dy}}^s = \frac{\gamma\pi R^2 k}{k_s} a \sin \omega t \left(\frac{k^2 R^2}{8} + \frac{k^4 R^4}{192} - 1 \right) \left[e^{k_s(\varrho - \bar{\eta})} \right]_{\varrho_1}^{\varrho_2} \quad (9.6)$$

$$F_{FK_{dy}}^h = 0 \quad (9.7)$$

$$T_{FK_{dy}}^p = \frac{\gamma\pi R^2 k}{k_s^2} a \sin \omega t \left(\frac{k^2 R^2}{8} + \frac{k^4 R^4}{192} - 1 \right) \left[(k_s \varrho - 1) e^{k_s(\varrho - \bar{\eta})} \right]_{\varrho_1}^{\varrho_2} \quad (9.8)$$

9.3.1.2 Disc section description

In order to completely describe a cylinder, the bottom disc, which ‘closes’ the cylinder, must be also considered. For this purpose, polar coordinates are used, as opposed to cylindrical coordinates. The following results are obtained:

$$\begin{cases} x(r, \vartheta) = r \cos \vartheta \\ y(r, \vartheta) = r \sin \vartheta \\ z(r, \vartheta) = h_0 \end{cases}, \quad \vartheta \in [-\pi, \pi) \wedge r \in [0, R] \quad (9.9)$$

$$\mathbf{e}_r \times \mathbf{e}_\vartheta = \begin{pmatrix} \cos \vartheta \\ \sin \vartheta \\ 0 \end{pmatrix} \times \begin{pmatrix} -r \sin \vartheta \\ r \cos \vartheta \\ 0 \end{pmatrix} = r \begin{pmatrix} 0 \\ 0 \\ 1 \end{pmatrix} \quad (9.10)$$

$$\langle \mathbf{r} \times (\mathbf{e}_r \times \mathbf{e}_\vartheta), \mathbf{j} \rangle = -r^2 \varrho \cos \vartheta \quad (9.11)$$

$$F_{FK_{st}}^h = -\gamma\pi R^2 h_0 \quad (9.12)$$

$$F_{FK_{dy}}^s = 0 \quad (9.13)$$

$$F_{FK_{dy}}^h = \gamma\pi R^2 e^{k_s(h_0 - \bar{\eta})} a \cos \omega t \left(1 - \frac{k^2 R^2}{8} + \frac{k^4 R^4}{192} \right) \quad (9.14)$$

$$T_{FK_{dy}}^p = \frac{1}{4} \gamma\pi R^4 k e^{k_s(h_0 - \bar{\eta})} a \sin \omega t \left(\frac{k^4 R^4}{384} + \frac{k^2 R^2}{12} - 1 \right) \quad (9.15)$$

where h_0 is the draft of the disc.

9.3.1.3 Cone section description

Finally, for a vertical cone, whose profile of revolution is defined as $f(\varrho) = m\varrho + q$, the following results stand:

$$\mathbf{e}_\varrho \times \mathbf{e}_\vartheta = (m\varrho + q) \begin{pmatrix} -\cos(\vartheta) \\ -\sin(\vartheta) \\ m \end{pmatrix} \quad (9.16)$$

$$\langle \mathbf{r} \times (\mathbf{e}_\varrho \times \mathbf{e}_\vartheta), \mathbf{j} \rangle = -(m\varrho + q) (\varrho + m(m\varrho + q)) \cos \vartheta \quad (9.17)$$

$$F_{FK_{st}}^h = -2\gamma\pi m \left[m\frac{\varrho^3}{3} + q\frac{\varrho^2}{2} \right]_{\varrho_1}^{\varrho_2} \quad (9.18)$$

$$F_{FK_{dy}}^s = -\gamma\pi ka \sin \omega t [A_s(\varrho) - B_s(\varrho)]_{\varrho_1}^{\varrho_2} \quad (9.19)$$

$$F_{FK_{dy}}^h = \gamma\pi ma \cos \omega t \left[2A_h(\varrho) - \frac{k^2}{2}B_h(\varrho) + \frac{k^4}{32}C_h(\varrho) \right]_{\varrho_1}^{\varrho_2} \quad (9.20)$$

$$T_{FK_{dy}}^p = -\gamma\pi ka \sin \omega t \left[A_p(\varrho) - \frac{k^2}{8}B_p(\varrho) \right]_{\varrho_1}^{\varrho_2} \quad (9.21)$$

where

$$A_s(\varrho) = \frac{e^{k_s(\varrho-\bar{\eta})}}{k_s^3} \left(m^2(k_s^2\varrho^2 - 2k_s\varrho + 2) + 2mqk_s(k_s\varrho - 1) + q^2k_s^2 \right) \quad (9.22)$$

$$B_s(\varrho) = \frac{k^2 e^{k_s(\varrho-\bar{\eta})}}{8k_s^5} \left(m^4(k_s^4\varrho^4 - 4k_s^3\varrho^3 + 12k_s^2\varrho^2 - 24k_s\varrho + 24) + \right. \\ \left. 4m^3qk_s(k_s^3\varrho^3 - 3k_s^2\varrho^2 + 6k_s\varrho - 6) + 6m^2q^2k_s^2(k_s^2\varrho^2 - 2k_s\varrho + 2) + 4mq^3k_s^3(k_s\varrho - 1) + q^4k_s^4 \right) \quad (9.23)$$

$$A_h(\varrho) = \frac{e^{k_s(\varrho-\bar{\eta})}}{k_s^2} (m(k_s\varrho - 1) + k_sq) \quad (9.24)$$

$$B_h(\varrho) = \frac{e^{k_s(\varrho-\bar{\eta})}}{k_s^4} \left(k_s^3q^3 + 3k_sm^2q(k_s^2\varrho^2 - 2k_s\varrho + 2) + 3k_s^2mq^2(k_s\varrho - 1) + m^3(k_s^3\varrho^3 - 3k_s^2\varrho^2 + 6k_s\varrho - 6) \right) \quad (9.25)$$

$$C_h(\varrho) = \frac{e^{k_s(\varrho-\bar{\eta})}}{k_s^6} \left(k_s^5q^5 + 5k_s^4mq^4(k_s\varrho - 1) + 10k_s^2m^3q^2(k_s^3\varrho^3 - 3k_s^2\varrho^2 + 6k_s\varrho - 6) + \right. \\ \left. 10k_s^3m^2q^3(k_s^2\varrho^2 - 2k_s\varrho + 2) + 5k_sm^4q(k_s^4\varrho^4 - 4k_s^3\varrho^3 + 12k_s^2\varrho^2 - 24k_s\varrho + 24) + \right. \\ \left. m^5(k_s^5\varrho^5 - 5k_s^4\varrho^4 + 20k_s^3\varrho^3 - 60k_s^2\varrho^2 + 120k_s\varrho - 120) \right) \quad (9.26)$$

$$A_p(\varrho) = \frac{e^{k_s(\varrho-\bar{\eta})}}{k_s^4} \left(3k_sm^3q \left(k_s^2\varrho^2 - 2k_s\varrho + 2 \right) + k_smq(k_s^2(2\varrho^2 + q^2) - 4k_s\varrho + 4) + k_s^2q^2(k_s\varrho - 1) + \right. \\ \left. m^4(k_s^3\varrho^3 - 3k_s^2\varrho^2 + 6k_s\varrho - 6) + m^2 \left(k_s^3(\varrho^3 + 3\varrho q^2) - 3k_s^2(\varrho^2 + q^2) + 6k_s\varrho - 6 \right) \right) \quad (9.27)$$

$$B_p(\varrho) = \frac{e^{k_s(\varrho-\bar{\eta})}}{k_s^6} \left(k_s^4q^4(k_s\varrho - 1) + k_s^2m^2q^2 \left(k_s^3(6\varrho^3 + 5\varrho q^2) - k_s^2(18\varrho^2 + 5q^2) + 36k_s\varrho - 36 \right) + \right. \\ \left. k_s^3mq^3 \left(k_s^2(4\varrho^2 + q^2) - 8k_s\varrho + 8 \right) + 5k_sm^5q(k_s^4\varrho^4 - 4k_s^3\varrho^3 + 12k_s^2\varrho^2 - 24k_s\varrho + 24) + \right. \\ \left. 2k_sm^3q \left(k_s^4(2\varrho^4 + 5\varrho^2q^2) - 2k_s^3(4\varrho^3 + 5\varrho q^2) + 2k_s^2(12\varrho^2 + 5q^2) - 48k_s + \varrho + 48 \right) + \right. \\ \left. m^4 \left(k_s^5(\varrho^5 + 10\varrho^3q^2) - 5k_s^4(\varrho^4 + 6\varrho^2q^2) + 20k_s^3(\varrho^3 + 3\varrho q^2) - 60k_s^2(\varrho^2 + q^2) + 120k_s\varrho - 120 \right) + \right. \\ \left. m^6(k_s^5\varrho^5 - 5k_s^4\varrho^4 + 20k_s^3\varrho^3 - 60k_s^2\varrho^2 + 120k_s\varrho - 120) \right) \quad (9.28)$$

9.3.2 Numerical integration

Calculating forces for a rotating body requires consideration of the coordinate system in which such forces are going to be represented. In particular, the dynamic equations may be written in an inertial global frame, or in a non-inertial body-fixed frame. Two right-handed frames of reference are therefore considered, as schematically shown in Fig. 9.1: an inertial frame (x, y, z) , with the origin fixed at the SWL, and a non-inertial frame $(\hat{x}, \hat{y}, \hat{z})$, fixed with the body, with the origin at the CoG of the body.

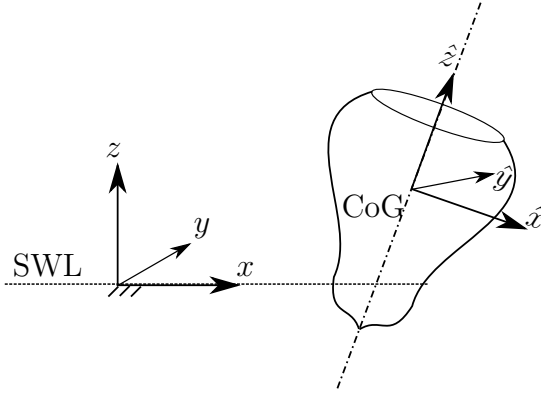


Figure 9.1: Inertial frame (x, y, z) , with the origin at still water level (SWL), and non-inertial frame $(\hat{x}, \hat{y}, \hat{z})$, fixed with the body, with the origin at the centre of gravity (CoG) of the body.

In order to have a constant and minimal inertial matrix, it is usually convenient to employ a frame of reference fixed on the body, and with its origin at the body centre of gravity. Therefore, FK forces, in the body-frame, can be equivalently represented in two ways:

- (a) Formulating and solving the integral in the global frame, then transferring the results to the body-frame.
- (b) Formulating and solving the integral directly in the body-frame.

Option (a) requires the definition of the geometry in the global frame, which can be achieved by applying a rigid rotation matrix to the vertical cylindrical coordinates, such that the geometry pitches at an angle θ about an axis parallel to the y -axis, and passing through the $CoG = (x_G, 0, z_{CoG} + z_G)$, as:

$$\begin{cases} x(\tilde{\rho}, \vartheta) = f\left(\frac{\tilde{\rho}}{\cos\theta}\right) \cos\vartheta \cos\theta + \tilde{\rho} \tan\theta - z_{CoG} \sin\theta + x_G \\ y(\tilde{\rho}, \vartheta) = f\left(\frac{\tilde{\rho}}{\cos\theta}\right) \sin\vartheta \\ z(\tilde{\rho}, \vartheta) = -f\left(\frac{\tilde{\rho}}{\cos\theta}\right) \cos\vartheta \sin\theta + \tilde{\rho} + z_{CoG}(1 - \cos\theta) + z_G \end{cases} \quad (9.29)$$

where x_G and z_G are the body displacements, and z_{CoG} is the position of the CoG at equilibrium, with respect to the SWL, reasonably assuming that the CoG lays on the vertical axis of the axisymmetric buoy. In (9.29), $\tilde{\rho}$ is a temporary parameter, which will be substituted shortly, in order to solve the following problem: with the current formulation of $z(\tilde{\rho}, \vartheta)$, it is not straightforward (or possible, in some cases) to extract the value of the integral limits, $\tilde{\rho}_1$ or $\tilde{\rho}_2$, in order to satisfy an arbitrary condition $z(\tilde{\rho}, \vartheta) = z^*$. In particular, it is impossible to define the value of the top limit $\tilde{\rho}_2$ such that $z^* = \eta = a \cos(\omega t - \chi x(\tilde{\rho}, \vartheta) + \varphi)$.

It is therefore convenient to re-parametrize the surface, using a new parameter, such that $z(\varrho, \vartheta) = \varrho$, so that any arbitrary condition can be easily imposed, just as $\varrho_2 = z^*$.

By applying the substitution $z = \varrho$ in (9.29), the new coordinate system is defined, as follows:

$$\begin{cases} x(\varrho, \vartheta) = f\left(\frac{\xi(\varrho, \vartheta)}{\cos \theta}\right) \cos \vartheta \cos \theta + h(\varrho, \vartheta) \tan \theta - z_{CoG} \sin \theta + x_G \\ y(\varrho, \vartheta) = f\left(\frac{\xi(\varrho, \vartheta)}{\cos \theta}\right) \sin \vartheta \\ z(\varrho, \vartheta) = \varrho \end{cases} \quad (9.30)$$

where $\xi(\varrho, \vartheta)$ is a functional depending on the particular geometry. Typical examples are given:

- Cylinder, with $f(\varrho) = R$:
 $\xi(\varrho, \vartheta) = \varrho + R \cos \vartheta \sin \theta + z_{CoG}(\cos \theta - 1)$
- Cone, with $f(\varrho) = m\varrho + q$:
 $\xi(\varrho, \vartheta) = \frac{\varrho - z_G + q \cos \vartheta \sin \theta + z_{CoG}(\cos \theta - 1)}{1 - m \cos \vartheta \tan \theta}$

Using equation (9.30), the unity vectors \mathbf{e}_ϱ and \mathbf{e}_ϑ can be calculated, and the nonlinear FK integrals can be defined. The main drawback of such a representation (option (a)) in the global frame is related to the complexity of the resulting limits of integrations and the unity vectors \mathbf{e}_ϱ and \mathbf{e}_ϑ , which adversely affects the computational time of the numerical integration.

In contrast, following **option (b)**, the formulation of the unity vectors is as simple as in the vertical case. In fact, the geometry is described in the body-fixed frame $(\hat{x}, \hat{y}, \hat{z})$, with the origin at the centre of gravity of the device, by means of the cylindrical coordinates (ϱ, ϑ) :

$$\begin{cases} \hat{x}(\varrho, \vartheta) = f(\varrho) \cos \vartheta \\ \hat{y}(\varrho, \vartheta) = f(\varrho) \sin \vartheta \\ \hat{z}(\varrho, \vartheta) = \varrho \end{cases}, \quad \vartheta \in [-\pi, \pi) \wedge \varrho \in [\varrho_1, \varrho_2] \quad (9.31)$$

However, in option (b), the pressure $p(x, z, t)$ must be mapped from the global frame onto the body-frame. This is simply done by applying a rigid rotation and translation to the body-frame $(\hat{x}, \hat{y}, \hat{z})$, in order to define the inertial frame (x, y, z) as:

$$\begin{cases} x = \hat{x} \cos \theta + \hat{z} \sin \theta + x_G \\ y = \hat{y} \\ z = -\hat{x} \sin \theta + \hat{z} \cos \theta + z_G + z_{CoG} \end{cases} \quad (9.32)$$

Option (b) is more advantageous than option (a), since the increase in complexity required to define the unity vectors in the global frame (option (a)) is significantly higher than the increase in complexity due to the pressure mapping onto the body-frame (option (b)). Moreover, in the body frame, simplified geometric properties can be exploited; in particular, the surge component of a disc, and the heave component of the lateral surface of a cylinder, are always null in the body frame.

Finally, for both options (a) and (b), the FK force integrals must be solved numerically using, for example, a trapezoidal rule. The computation time depends, apart from the hardware specification of the computing machine (Intel(R) Xeon(R) CPU (E5-1620 v3 @ 3.50 GHz) processor, with 16.0 GB RAM and Windows 7 Professional 64 bit), on the integration scheme utilized, a 2D-quadrature scheme [202], and on the relative and absolute tolerances used to approximate the integral. Furthermore, it is convenient to compute the static and dynamic FK forces together, in order to reduce the number of integrals to be solved. The ultimate extent of the computation time depends also, and most importantly, on the complexity of the geometry. Indeed, real WEC buoys may be a combination of

different sections, typically cylinders and cones, with each section of the buoy requiring an individual integral. However, from the case studies hereafter analyzed, see Sect. 9.4.2 to 9.4.4, it is found that the numerical integration scheme (option (b)) is, on average, about 50 times slower than the algebraic integration, where the computational time of the VFK method is of the order of $1 \cdot 10^{-4}s$. Note that option (a) is about 80 times slower than the algebraic integration, hence 60% slower than option (b).

The consequent run time for computing the response of the device depends on the discrete time solver scheme, the time step, and the simulation duration. Using a constant time step Runge-Kutta scheme, the resulting run time is evaluated in Sects. 9.4.2 to 9.4.4, for 6-DoF models, which will be discussed in Sect. 9.4 (6-DoF models are obviously slower than 3-DoF). For different geometries, and varying the time step as part of a convergence study, the resulting simulation time is found to be between one and three times the simulation time. Therefore, such a method has the potential to run roughly in *real time*, or a little slower, depending on the particular implementation. However, these considerations are for computations performed in Matlab, which is between one and two orders of magnitude slower than lower level coding languages, such as C or Fortran [164]. With C or Fortran implementation, therefore, real time execution is easily achievable. Nevertheless, although the mesh-based LAMSWEC nonlinear FK model is coded in Fortran (which is a significantly faster implementation than Matlab), it has a run time about 10 times longer than the simulation time [91], therefore about one order of magnitude slower than the method proposed in this chapter.

9.3.3 Validation of modelling approach

Several checks have been performed, in order to ensure the code, implementing the nonlinear FK force calculations, to be correct and reliable. The surface of several simple geometries, generated with either the vertical or rotated cylindrical coordinates, has been visually inspected, with particular care taken with regard to the ability to correctly represent the intersection between the rotated buoy and the free surface elevation. All the algebraic calculations have been checked via the symbolic calculation software Mathematica [203], and effectively compared with numerical integration. Furthermore, surface and volume integrals have been computed, in order to calculate the surface and volume of sample geometries (cylinders and cones), either vertical or rotated. Options (a) and (b) for numerical integration have been also effectively compared against each other.

9.3.3.1 Comparison with WAMIT

Linear boundary element method (BEM) codes can be used to validate the static and dynamic FK integrals; for very small motion and wave amplitudes, the nonlinear models should produce results consistent with linear BEM codes. Hereafter, a particular device is taken into account for the computation of FK forces, based on the CorPower device geometry [204], whose shape is shown in Table 9.1. Based on [205], the device dimensions are shown in Fig. 9.2.

The BEM code WAMIT [162] is used to calculate the linear surge, heave, and pitch hydrodynamic stiffness and the linear FK force for the vertical device. The nonlinear static FK forces are calculated with the VFK and RFK methods, using very small displacements in heave and pitch (0.01m and 0.01rad, respectively), while nonlinear dynamic FK forces are computed with waves of different periods T_w , and height $H_w = 0.01m$. The three models (LFK, VFK, and RFK) return identical results, validating the method in linear conditions. Note that, in general, the RFK method converges to the VFK method when the pitch angle is zero.

A second configuration is run in WAMIT, considering the geometry statically rotated by 15° around its centre of gravity, in order to compute the hydrostatic stiffness and

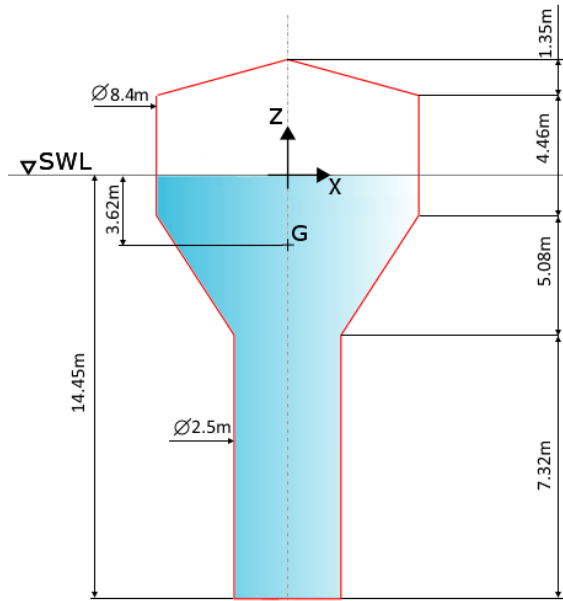


Figure 9.2: Shape and dimensions of the case study buoy for validation of the modelling approach, inspired by the CorPower device.

FK forces, linearized around a non-zero pitch angle, and validate the RFK method for a rotated geometry. Figure 9.3 shows the validation of the dynamic FK force amplitude coefficients and phase lags, with respect to the free surface elevation.

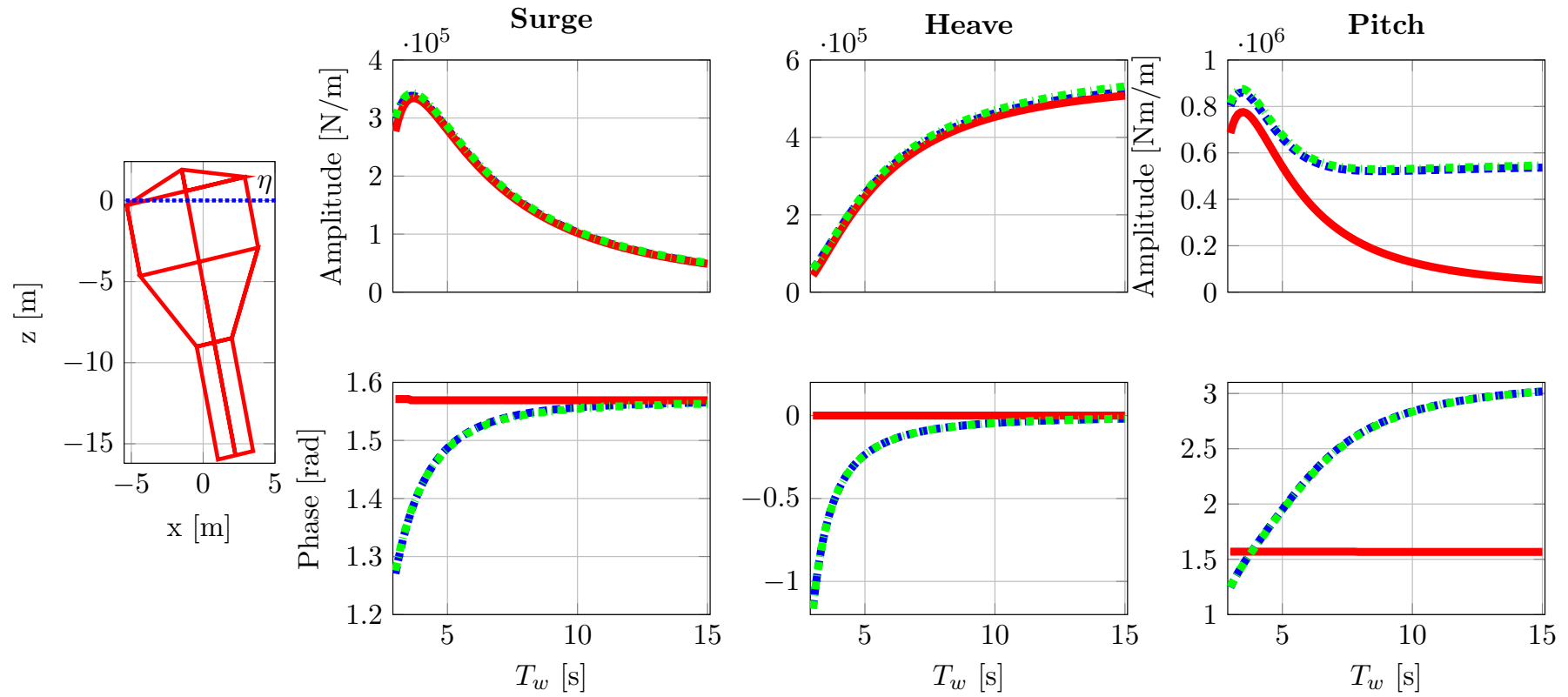


Figure 9.3: Validation, in linear conditions, of the RFK method (■—■), compared with linear results for the CorPower buoy rotated by 15° (■—■). For comparison, the VFK method is presented (—), which refers to a vertical buoy.

On the one hand, LFK and RFK results almost perfectly overlap, both for amplitude and phase. The slight differences are due to an approximation that the BEM code introduces, due to the meshed geometry, as opposed to the actual analytical geometry considered in the RFK method. On the other hand, the VFK curve describes the dynamic forces for the vertical geometry. From the comparison between the VFK and RFK methods, it is interesting to notice that there is a phase difference in all three degrees of freedom. While the phase is constant for the vertical buoy (VFK), it is frequency-dependent for the rotated one (RFK).

Furthermore, it can be noted, from Fig. 9.3, that the amplitudes of surge and heave are almost identical between vertical and rotated geometries, but are significantly different for the pitch torque. Such a difference can be explained by considering the translation forces (surge and/or heave) which contribute to the formation of the pitch torque; for a vertical buoy, the heave forces have, overall, no contribution to the torque, due to the axisymmetric geometry. In fact, the pitch torque profile has the same shape as the surge force profile. Conversely, for a rotated buoy, both surge and heave contribute to the pitch torque which, indeed, resembles the profile of the surge curve for short wave periods (large surge, small heave), and vice versa for long wave periods (small surge, large heave). Similar considerations can also be made for the phase lags, shown in Fig. 9.3.

9.3.4 Comparison with tank tests

Comparing force components for the 3-DoF nonlinear model with WAMIT results, in linear conditions, is a simple way to verify the correctness of the implementation, and to validate the modelling approach. However, conclusions can be drawn only for small relative displacements of the body, with respect to the free surface. A complete validation of the model, particularly with larger waves and device displacements, ideally requires wave tank data. The CorPower device was tested in November 2014 in the wave tank at Ecole Centrale de Nantes, France, and results are published in [205]. Although the author is not in possession of the actual data from the tank, it is possible to reproduce the experimental setup within the mathematical model, and compare results, in order to achieve preliminary validation.

One of the main objectives of the experimental campaign was to test the effectiveness of the WaveSpring (WS) mechanism, which acts as a negative spring. Considering a linear damper (LD) as a power take-off (PTO), two configurations are tested, namely with (LD+WS) or without (LD) WaveSpring. Refer to [205] for full details concerning the experimental setup, and the mathematical model used for the WaveSpring mechanism. Replicating the same experimental conditions, the motion of the device is simulated, as discussed in Sect. 9.4.2, using the RFK model. Results are shown in Fig. 9.4. From the comparison, it can be concluded that the agreement between numerical and experimental results is quite good, in both configurations.

9.3.5 Parametric study

The relative disparity in accuracy between the three methods (LFK, VFK, and RFK) depends on four different factors, two concerning the position of the device (z_G and θ), and two concerning the wave characteristics (H_w and T_w). Consequently, regular waves are considered, in order to study the specific dependence on H_w and T_w . Importantly, larger waves induce larger variations in the wetted surface during the wave cycle, inducing subsequently more significant nonlinearities. However, the LFK and VFK methods converge for small values of z_G ; similarly, the VFK and RFK methods converge for small values of θ . Given the typical oscillatory response of a WEC, the differences between the VFK and RFK models vanish in that part of the response cycle corresponding to a zero

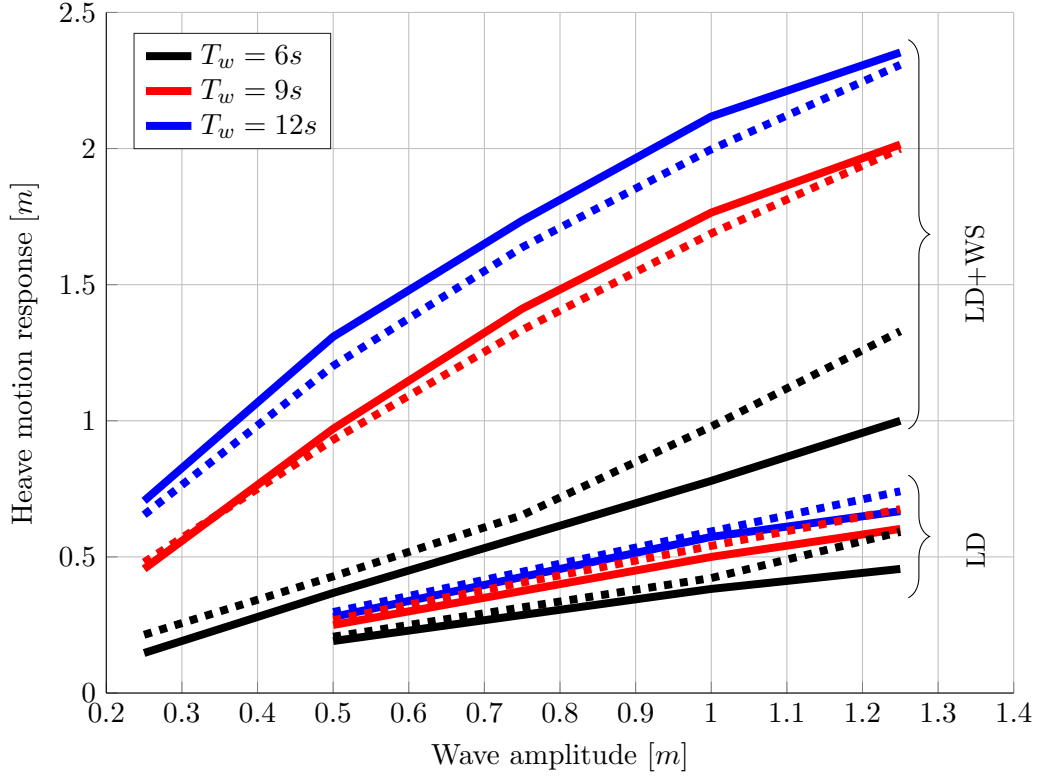


Figure 9.4: Comparison of the heave response to regular waves, obtained in wave tank tests in [205](solid line), and numerical simulations (dashed line), using the RFK model.

crossing, while they are maximal at the peaks and troughs of the oscillation, as might be expected.

In order to understand how linear and nonlinear models vary and differ from each other, and how they individually depend on z_G and θ , surge, heave, and pitch FK forces are computed, for several different regular waves, with the device *fixed* in a particular position. An example comparison is presented in Fig. 9.5. The following ranges are considered: $T_w \in [4s, 15s]$, with $1s$ step; $H_w \in [0.5m, 3m]$, with $0.5m$ step; $z_G \in [-3m, 3m]$, with $0.25m$ step; $\theta \in [-15^\circ, 15^\circ]$, with 1.5° step. In this section, only static FK forces, in the body-frame, are discussed. The effect of dynamic FK forces is taken into account in Sect. 9.4.2, where the full dynamic response to incoming waves is simulated.

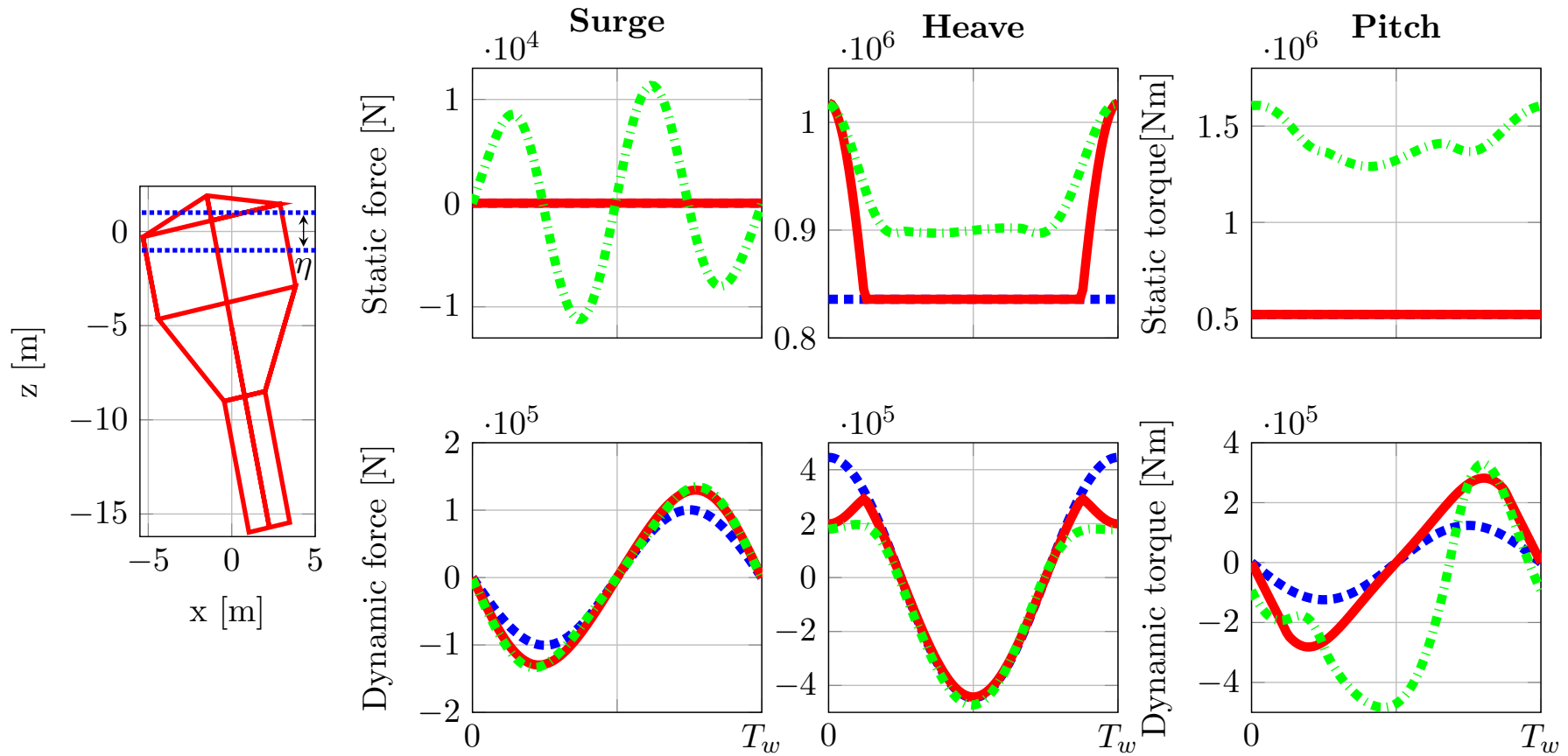


Figure 9.5: Froude-Krylov forces for the CorPower buoy, fixed at $z_G = -1.5\text{m}$ and $\theta = -15^\circ$, as shown in the schematic on the left, subject to a wave with $H_w = 2\text{m}$ and $T_w = 10\text{s}$, according to LFK (—), VFK (—), and RFK (—) models.

The static surge FK force (F_{FKst}^s) is zero for both LFK and VFK models since, for a vertical buoy, regardless of the extent of the instantaneous wetted surface, static pressure contributions at diametrically opposite points cancel out. Note that, in the case of the VFK model, such a result is a consequence of the flat surface elevation assumption. Indeed, using the RFK model for a vertical buoy would return a non-zero F_{FKst}^s , since the actual (not flattened) free surface is considered. For a rotated geometry, F_{FKst}^s is non-zero, since part of the geometry pierces the water and, therefore, does not have a diametrically opposite point. In particular, it can be noted, from Fig. 9.5, that the frequency of F_{FKst}^s is about twice the wave frequency. In fact, F_{FKst}^s is zero twice as often as η is zero: firstly, when η has its peak/trough on the buoy axis, so that p_{st} is symmetric with respect to the $y - z$ plane, and secondly, when η is zero on the buoy axis, so that p_{st} is symmetric with respect to the $x - y$ axis. In both cases, the contributions from diametrically opposite points cancel out. However, such variations are likely to have a small relative importance, since the static surge FK force is always one or two orders of magnitudes smaller than the heave force.

As shown in Fig. 9.5, the static heave FK force (F_{FKst}^h) is linear, for the VFK model, when η intersects the cylinder section, while becoming nonlinear in the cone section, since the cross sectional area is not constant. A more general representation of how F_{FKst}^h varies can be achieved using an ‘equivalent’ stiffness, for each value of z_G , where F_{FKst}^h is divided by z_G . Figure 9.6 shows such an equivalent stiffness for a particular wave, at $\theta = 15^\circ$, and varying z_G . Results for the nonlinear VFK and RFK models are represented by areas, since F_{FKst}^h is not constant.

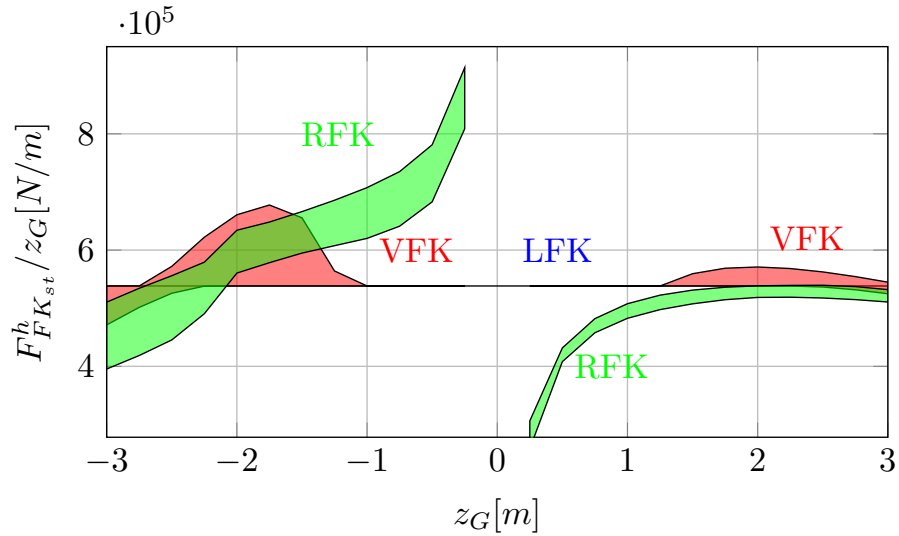


Figure 9.6: Equivalent static heave Froude-Krylov force for the CorPower buoy, rotated by $\theta = -15^\circ$, subject to a wave with $H_w = 2m$ and $T_w = 10s$, according to the LFK, VFK, and RFK models.

The VFK model results coincide with those for the LFK model, for small vertical displacements, since η intersects the buoy only at the cylinder section, while differences are found at larger z_G . Conversely, the RFK model is always nonlinear, since the actual rotated geometry is considered. Note that a larger equivalent stiffness for small z_G does not mean a larger error; in fact, the difference appears larger just because F_{st}^h is divided by a smaller z_G . The nonlinearity/variability of F_{FKst}^h , for both the VFK and RFK models, depends on which buoy section is engaged by η . In particular, larger errors are introduced by the top cone (engaged when z_G is large and negative), which has a more pronounced slope than the bottom cone (engaged when z_G is large and positive), since the rate of change of the cross sectional area of the top cone is greater. Note that similar graphs

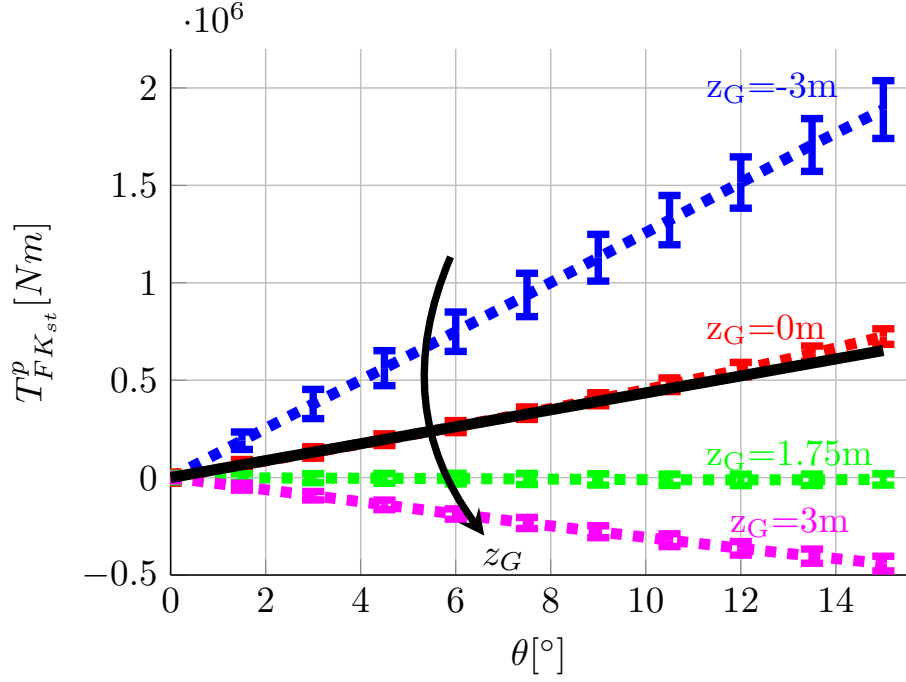


Figure 9.7: Static pitch Froude-Krylov force for the CorPower buoy, subject to a wave with $H_w = 2m$ and $T_w = 10s$, according to LFK and VFK (solid line), and RFK (dashed line) models, for different z_G .

can be drawn for different T_w and H_w . While the equivalent heave stiffness is largely insensitive to the wave period, larger wave heights introduce larger errors, since more significant changes in the wetted surface appear.

Finally, the static pitch FK torque ($T_{FK_{st}}^p$) is considered. Figure 9.7 presents F_{st}^p for different z_G and θ , for a sample wave of $T_w = 10s$ and $H_w = 2m$. Only positive pitch angles are shown, since the results are symmetric with respect to the pitch angle.

Given the variability of nonlinear $T_{FK_{st}}^p$, as shown in Fig. 9.5, the mean torque is presented in Fig. 9.7, along with error bars, whose length is equal to the standard deviation of the static torque, over one wave period. Overall, the variability is quite small, compared to the mean values, apart from a very negative z_G , where the highly nonlinear top cone intersects η . Obviously, the RFK model significantly overlaps with the LFK model for very small z_G , and diverges from it with when the absolute value of either θ or z_G increases. Furthermore, for vertical displacements larger than 1.75m, the static torque changes sign, contriving to drive the buoy away from the equilibrium position, as opposed to acting as a restoring torque, which is the case for a linear model. In fact, for $z \geq 1.75m$, the metacentre falls below the centre of gravity, which is the condition for *pitching instability* [206]. Finally, as in Fig. 9.6, Fig. 9.7 shows a relative insensitivity of $T_{FK_{st}}^p$ to T_w , while larger values of H_w cause slightly smaller absolute mean values of $T_{FK_{st}}^p$, and slightly increased variability.

9.4 Six-DoF nonlinear Froude-Krylov model

While Sect. 9.3 considers only the three degrees of freedom externally excited by the incoming mono-directional wave train, a complete 6-DoF nonlinear FK model is proposed in the present section. Indeed, other DoFs may be activated by the PTO system, moorings, or eventual other ancillary systems, specific to the particular WEC. From a hydrodynamic perspective, the study of the highly-nonlinear phenomenon of parametric resonance is of particular interest, which may open a channel for the incoming energy to flow into DoFs

which are different from the externally excited ones.

A brief critical discussion of parametric excitation is proposed in Sect. 9.4.1, with a particular focus on its causes and consequences, in the particular application case of wave energy converters. Furthermore, available tools to investigate parametric instability are discussed, among which are nonlinear FK approaches [46], justifying the attempt to expand the model of Sect. 9.3 to 6 DoFs. In fact, since parametric excitation depends on time-variant system parameters [207], nonlinear FK models, which consider the *instantaneous* wetted surface, are expected to be able to articulate parametric resonance. Likewise, linear models are unable to capture any parametric motion.

Similarly to Sect. 9.3.2, following the more efficient option (b), the device geometry is defined in the invariant body-fixed frame $(\hat{x}, \hat{y}, \hat{z})$, as shown in (9.31). Finally, since integrals are defined in the body frame, it is necessary to map the pressure from the inertial-frame (where it is defined) onto the body surface. The transformation, from (x, y, z) to $(\hat{x}, \hat{y}, \hat{z})$, is represented by the Euler angle triad (ϕ, θ, ψ) , corresponding to roll, pitch, and yaw angles, respectively, as shown in (9.33).

$$\begin{pmatrix} \hat{x} \\ \hat{y} \\ \hat{z} \end{pmatrix} = \left(\begin{bmatrix} c\psi & -s\psi & 0 \\ s\psi & c\psi & 0 \\ 0 & 0 & 1 \end{bmatrix} \begin{bmatrix} c\theta & 0 & s\theta \\ 0 & 1 & 0 \\ -s\theta & 0 & c\theta \end{bmatrix} \begin{bmatrix} 1 & 0 & 0 \\ 0 & c\phi & -s\phi \\ 0 & s\phi & c\phi \end{bmatrix} \right)^{-1} \begin{pmatrix} x - x_G \\ y - y_G \\ z - z_G - z_{CoG} \end{pmatrix} \quad (9.33)$$

where the operators c and s stand for cosine and sine, respectively. The centre of gravity, in the inertial frame, is at $(0, 0, z_{CoG})'$ at rest, and then moves of $(x_G, y_G, z_G)'$. The 3-2-1 Euler angle sequence is the rotation convention commonly used for marine vehicles, thought of as three sets of rigid rotations [208]. In order to apply a rotation around the origin of the body frame (instead of around the origin of the inertial frame), a translation needs to be applied before and after the rotation, so that the two origins overlap at the moment of the rotation.

Consequently, the integral for $\mathbf{F}_{FK_{dy}}$, for example, becomes:

$$\mathbf{F}_{FK_{dy}} = \iint_{S(t)} p_{dy}(\hat{x}, \hat{y}, \hat{z}) \mathbf{n} dS = \int_{\vartheta_1}^{\vartheta_2} \int_{\varrho_1}^{\varrho_2} p_{dy}(\varrho, \vartheta) \mathbf{e}_\varrho \times \mathbf{e}_\vartheta d\varrho d\vartheta \quad (9.34)$$

9.4.1 Parametric resonance in wave energy converters

Parametric instability consists of an internal excitation mechanism, which feeds part of the incoming energy to secondary DoFs, generating parasitic motion. One well-known example is the appearance of a sustained roll response, whereas the incoming mono-directional wave train is directly exciting the floating body just in the surge, heave, and pitch DoFs. Such a phenomenon is observed in floating bodies, when the roll natural period is around twice the heave/pitch natural period, and it has been widely investigated in shipping and offshore spar-type structure. However, little investigation has been undertaken in the wave energy field [24]. Numerical and experimental studies are available for the pitching SEAREV device [62], the 2-body self-reacting Wavebob heaving device [209], and the floating spar-type oscillating water column device, SparBuoy [48]. Such studies show the detrimental effect of parametric resonance on the WEC performance, since energy is parametrically transferred from the primary mode of motion into other modes. Nevertheless, parametric resonance may be beneficial for certain WECs, some of which could be expressly designed to take advantage of parametric excitation [210, 211, 24].

However, parametric resonance is very often unexpected by wave energy converter designers. In fact, at an early design stage, when significant modifications to the device concept, operating principle, shape, and dimensions take place, overly-simplistic linear

models are commonly used, thanks to their computational convenience. However, parametric resonance, undetectable by linear models, is usually discovered with surprise after initial wave tank tests, at a stage where there is less design freedom, due to the greater level of investment required. Therefore, parametric roll is usually detrimental, and sub-optimal mitigating actions take place, in order to contain the undesired phenomenon. On the contrary, having a computationally viable mathematical model, able to describe nonlinear phenomenon, including parametric resonance, is potentially beneficial for informing the design process with regard to the *real* device dynamics. Furthermore, reliable knowledge of the device dynamics can eventually channel the device design into exploiting nonlinear behaviour, instead of limiting it. In particular, since instability involves an extreme magnification of an initial small perturbation, a dedicated design that takes advantage of parametric resonance is potentially highly beneficial for power production. Likewise, a well-informed control strategy can lead the device into desirable instability, and/or generating conditions for maximum power generation.

Since parametric resonance is due to time-varying system parameters [207], linear models, which take the mean wetted surface into account, are inadequate. On the contrary, it has been shown that parametric instability can be detected by nonlinear FK models, which integrate the static and dynamic pressure of the undisturbed wave field over the *instantaneous* wetted surface. Particular examples, in wave energy applications, are given by the SEAREV [62] and the Wavebob [46] devices, for which parametric resonance is studied with a mesh-based nonlinear FK force model (LAMSWEC) [91], which compares well with wave tank tests, provided an appropriate viscous drag description is included. Nonetheless, the main drawback of mesh-based nonlinear FK models is the computational burden, since they require time-consuming re-meshing routines. However, while mesh-based approaches are likely to be the only option for a geometry of arbitrary complexity, the computationally efficient method proposed in this thesis, particularly in Sect. 9.4, can be applied to axisymmetric devices.

Apart from nonlinear FK models, the classical approach to investigate the likelihood of parametric roll, especially outside the wave energy field, is the Mathieu equation [207], which is a single-DoF unforced equation, with harmonic variations of the stiffness term. According to the Mathieu equation, two conditions for the generation of parametric resonance are defined [210]: 1) the frequency of the excitation is approximately twice or equal to the natural frequency of the secondary system (frequency condition), and 2) the amplitude of the parametric excitation is larger than the damping of the secondary system (threshold condition). Although it can give some insight, such an approach cannot forecast the severity of the eventual parametric response. Furthermore, several significant approximations are needed to reduce the full nonlinear 6-DoF model into a 1-DoF partially linearized model, which would fit into the Mathieu equation structure. In particular, linear and nonlinear coupling effects between the 6-DoF are neglected, and the variations of the stiffness term are assumed to be harmonic, which is not necessarily the case. Furthermore, the definition of the natural period in 6-DoF is more obscure, due to coupling effects. Finally, nonlinear variations in the excitation force are also neglected.

9.4.2 The CorPower-like device

The CorPower device is considered as a first case study, because it is a relatively simple, bottom referenced, single-body, axisymmetric WEC. Further case studies are a self reacting two-body WEC, in Sect. 9.4.3, and a floating oscillating water column WEC, in Sect. 9.4.4.

The 6-DoF nonlinear hydrodynamic model is used to simulate the response of the heaving point absorber to incoming waves. Regular waves are considered, in order to be able to study the effect of the wave height (H_w) and wave period (T_w), independently. Furthermore, since parametric resonance is particularly sensitive to the frequency and

amplitude of the external excitation, it is convenient to study monochromatic waves only. A wide range of wave conditions, based on [205], is considered, with $T_w \in [4, 15]s$, step $0.5s$, and $H_w \in [0.5, 4]m$, step $0.5m$. However, waves steeper than 2% (low period and large height) are excluded.

The case study is a heaving buoy WEC, inspired by the CorPower [204] device, whose shape and dimension, based on [205], are shown in Fig. 9.2. Such a device presents the peculiarity of a pre-tensioning system, used to reduce the weight of the buoy, and the WaveSpring mechanism, which effectively acts as a negative spring [205]. The motion of the device is described by Newton's second law, in vectorial form, for 6 DoFs, written in the body-fixed frame of reference:

$$M\ddot{\mathbf{x}} = \mathbf{f}_{FK_{st}} + \mathbf{f}_{FK_{dy}} + \mathbf{f}_d + \mathbf{f}_{rad} + \mathbf{f}_{vis} + \mathbf{f}_{Cor} + \mathbf{f}_{mor} + \mathbf{f}_{pre} + \mathbf{f}_{WS} + \mathbf{f}_{PTO}, \quad (9.35)$$

where M is the inertial matrix, $\mathbf{x} = (\hat{x}, \hat{y}, \hat{z}, \phi, \theta, \psi)$ is the state vector in the body-fixed frame, \mathbf{f} is the generalized force vector, composed of 3 forces and 3 torques. The other force components in (9.35) are \mathbf{f}_d , the diffraction force, \mathbf{f}_{rad} , the radiation force, \mathbf{f}_{vis} , the viscous force, \mathbf{f}_{Cor} , the Coriolis force, \mathbf{f}_{mor} , the mooring force, \mathbf{f}_{pre} the pretension force, \mathbf{f}_{WS} the WaveSpring force, and \mathbf{f}_{PTO} the power take-off force. Note that \mathbf{f}_{pre} , \mathbf{f}_{WS} , and \mathbf{f}_{PTO} act on the axis of the device, therefore along \hat{z} . The common expression for \mathbf{f}_d , \mathbf{f}_{rad} , \mathbf{f}_{vis} , and \mathbf{f}_{Cor} are used [208], where \mathbf{f}_d is computed through the diffraction impulse response function, \mathbf{f}_{rad} through a state space representation of the radiation convolution integral [148], and \mathbf{f}_{vis} through a Morison-like equation [18]. Note that, in general, viscous effects can present coupling between different DoFs; however, uncoupled viscous forces are here considered, consistent with [205]. Furthermore, \mathbf{f}_{mor} and \mathbf{f}_{pre} are linearly proportional to displacement, while \mathbf{f}_{PTO} is assumed to be linearly proportional to velocity (i.e. linear damping control).

The important numerical parameter values used in the model are based on [205, 22], and summarized in Table 9.2, where K_{mor} is the mooring stiffness, K_{pre} the pretension stiffness, B_{PTO} the PTO damping coefficient, C_d the drag coefficient vector, and T_n the natural period vector. The WaveSpring mechanism, which is composed of three pneumatic cylinders, is modelled as in [189], assuming an adiabatic compression of the working fluid in the chambers of the cylinders. It follows that \mathbf{f}_{WS} is computed as:

$$\mathbf{f}_{WS} = N_c p_{WS} A_{WS} \hat{z} \sqrt{L_{WS,0}^2 + \hat{z}^2}, \quad (9.36)$$

where N_c is the number of cylinders (3), A_{WS} the active area of the cylinder ($0.1489m^2$), $L_{WS,0}$ the initial length of the cylinder (4m), and p_{WS} is the pressure in the chambers, defined as

$$p_{WS} = p_{WS,0} V_{WS,0}^{\gamma_a} / V_{WS}^{\gamma_a} \quad (9.37)$$

where V_{WS} is the volume of the cylinder chamber, γ_a the constant adiabatic index (1.4), and the subscript 0 indicates initial conditions.

9.4.2.1 Results for the CorPower-like device

The pitch response of the device, comparing the linear and nonlinear 6-DoF models, is shown in Fig. 9.8, considering, for clarity, only waves of height $2m$. Similar results are found for waves of different heights, with increasing nonlinear effects as the wave becomes higher, therefore steeper and more energetic.

Overall, the pitch response predicted by the nonlinear model is significantly larger, especially for periods close to the pitch resonant period (low periods), and close to the surge resonant period (long periods), which is coupled with pitch. The increase in the

Table 9.2: Model parameters, based on [205, 22].

	Surge/Sway	Heave	Pitch/Roll
M	$7.513 \cdot 10^5 kg$	$7.513 \cdot 10^5 kg$	$2.36 \cdot 10^6 kgm^2$
K_{mor}	$7.2 \cdot 10^4 N/m$	$2 \cdot 10^4 N/m$	$9.5 \cdot 10^5 Nm/m$
K_{pre}	-	$5.17 \cdot 10^5 N/m$	-
B_{PTO}	-	$2.44 \cdot 10^6 Ns/m$	-
C_d	0.35	0.35	1
T_n	13s	6.5s	7.5s

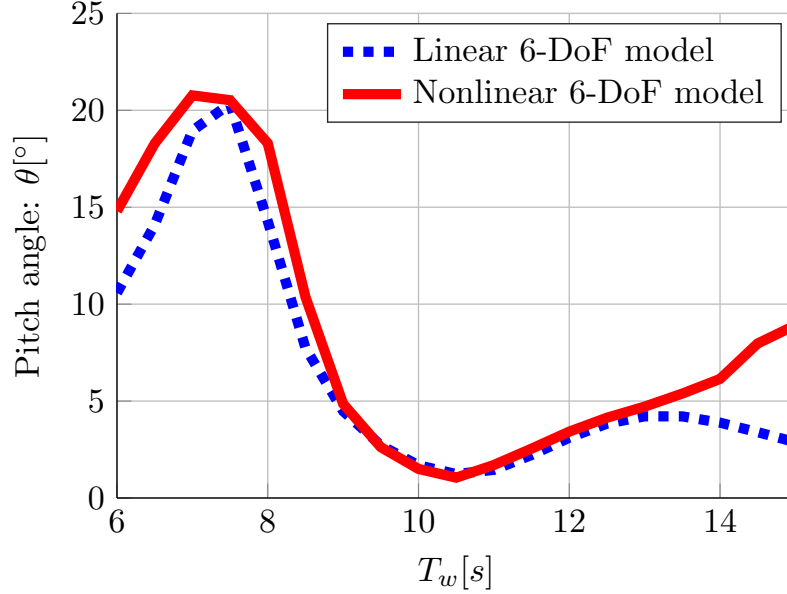


Figure 9.8: Amplitude of the pitch response of the CorPower device, subject to regular waves of height $2m$, according to linear and nonlinear Froude-Krylov 6-DoF models.

pitch response can be partially explained by variations in the hydrostatic restoring torque in pitch, due to fluctuations of the metacentric height, as discussed in Sect. 9.3.5.

The roll response is now considered, shown in Fig. 9.9. Note that the motion of the device is studied for an initial roll displacement of 0.1° , as suggested in [209], in order to provide some initial energy in the roll DoF. Since the external force is null in this DoF, the roll mode can only be internally excited, requiring some nonlinear mechanism for exchanging energy between different DoFs. Furthermore, in order to generate significant roll responses, parametric resonance must occur. In fact, when a system resonates, it magnifies negligible fluctuations from the equilibrium position into infinitely large motion, if the system is undamped, or until damping limitations are met.

The conditions for parametric resonance depend on the excitation amplitude and period, H_w and T_w , respectively, as explained in Sect. 9.3.5. Figure 9.9 clearly shows how parametric roll appears after a certain amplitude threshold is exceeded. The main periods where parametric roll is excited are in the range $7.5 - 8s$, where the maximum roll amplitude is about 8° . Smaller parametric roll responses are found at $11.5s$ and $9.5s$.

In WECs with a large roll natural period, for example [209] (T_n about $20s$), parametric resonance happens at wave periods about half the roll natural period, therefore T_w of about $10s$. Conversely, for the CorPower device, the roll T_n is quite small (about $7.5s$); therefore, waves with $T_w = \frac{1}{2}T_n$ are too small, and outside the target production region. However, since T_n is small in roll, parametric resonance mainly occurs at about $T_w = T_n$, as shown in Fig. 9.9.

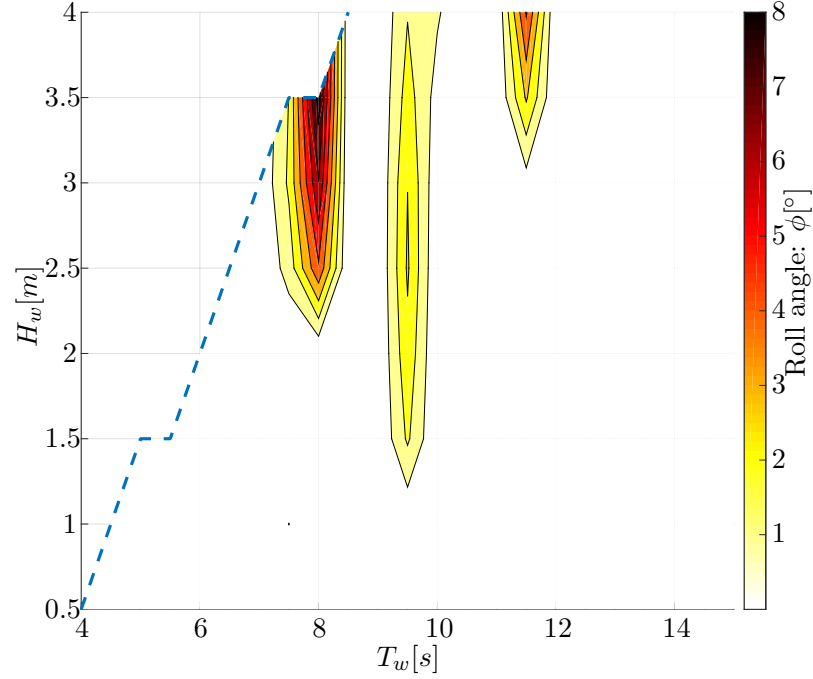


Figure 9.9: Maximum roll angle, due to parametric resonance, according to the 6-DoF nonlinear Froude-Krylov model, for the CorPower-like device.

The response in roll, for the wave condition with the largest roll amplitude ($T_w = 8s$, $H_w = 3.5m$) is shown in the phase graph $(\phi, \dot{\phi})$, and fast Fourier transform (FFT), in Fig. 9.10. The frequency components of the FFT are normalized against the wave frequency ω_w . The limit cycle response is quite simple, dominated by a normalized frequency of unity. Such a response confirms that $T_w = 8s$ is the main wave frequency where parametric roll is directly excited. Furthermore, non-zero mean values and super-harmonics are evident.

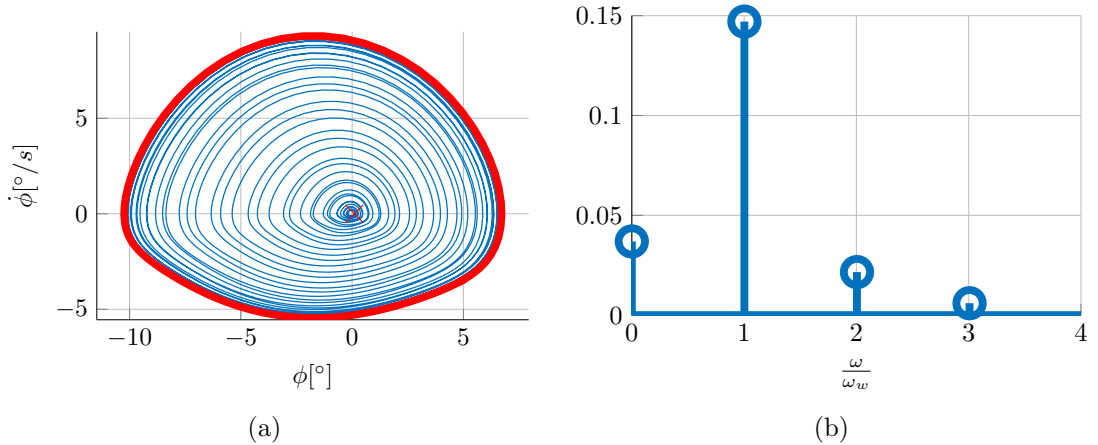


Figure 9.10: Phase graph $(\phi, \dot{\phi})$ (left figure), and FFT (right figure), for the wave condition with $T_w = 8s$ and $H_w = 3.5m$, for the CorPower-like device. In the top left figure, the cross indicates the initial condition $(\phi = 0.1^\circ, \dot{\phi} = 0^\circ)$, while the external solid line represents the limit cycle response.

Figure 9.9 shows that the secondary frequency where parametric roll is excited is at

$T_w = 11.5s$. The phase diagram and FFT of the roll response to a wave of $T_w = 11.5s$ and $H_w = 4m$ is shown in Fig. 9.11. It can be noted that the limit cycle response is topographically more complex. Furthermore, the FFT graph shows that sub-harmonics are generated. The dominant normalized frequency is 1.5, which corresponds to a period of $7.5s$, which is exactly the roll natural period. Therefore, it can be inferred that parametric roll at $T_w = 11.5s$ is caused, in an indirect way, by the roll natural period.

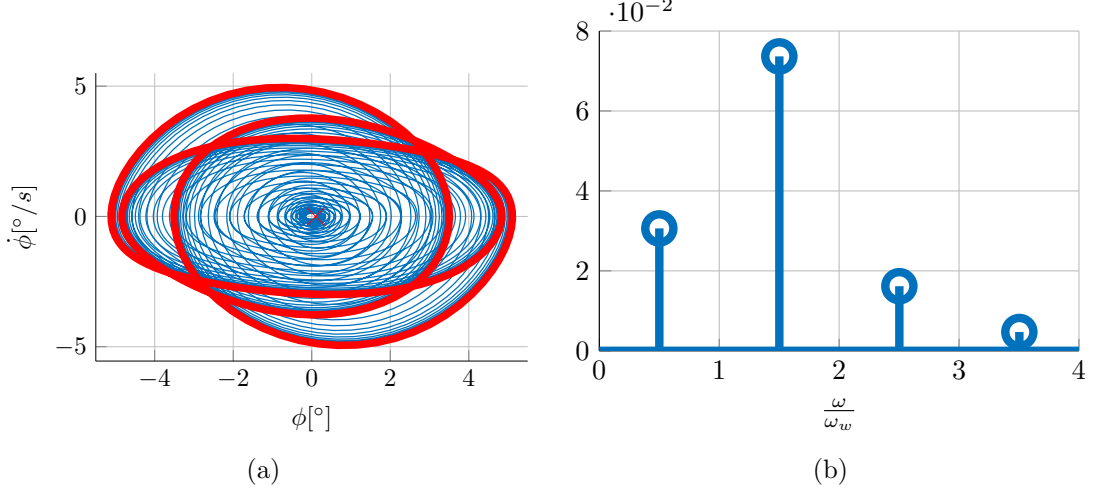


Figure 9.11: Phase graph $(\phi, \dot{\phi})$ (left figure), and FFT (right figure), for the wave condition with $T_w = 11.5s$ and $H_w = 4m$, for the CorPower-like device. In the top figure, the cross indicates the initial condition $(\phi = 0.1^\circ, \dot{\phi} = 0^\circ)$, while the external solid line represents the limit cycle response.

Finally, the consequences of pitching instability and parametric roll on energy absorption are investigated. In particular, neglecting one or more DoFs can affect power production estimation. For the case of a heaving buoy, such as that studied in this section, a 1-DoF linear model should predict the same power capture as a 6-DoF one, since heave is linearly uncoupled from all the other modes. Conversely, nonlinear models take nonlinear coupling effects into account; therefore, there could be differences between models with different numbers of DoFs. In order to include, selectively, pitching nonlinearities, and parametric resonance, 1-(only heave), 3-(surge-heave-pitch), and 6-DoF models are compared. Figure 9.12 shows the power production estimated with such models.

Obviously, for small wave heights, the three models overlap, since nonlinear effects are minimal. For higher waves, the 3-DoF model produces, overall, more power in heave than the 1-DoF model, apart from wave periods close to $8s$, where a significant power drop is found. Hence, it can be inferred that the power differences are due to the presence of the pitching motion, which is nonlinearly coupled with heave, as shown in [22]. While pitch angles up to about 15° (for T_w greater than $9s$, as shown in Fig. 9.8) benefit power conversion, large pitch angles appear to be detrimental (ϕ up to about 22° , at T_w of about $7.5s$, as shown in Fig. 9.8).

Small differences are found between the 3-DoF and the 6-DoF models, indicating that, for the CorPower device, the influence of parametric roll on power production is effectively negligible. Indeed, though present, the parametric roll angles are relatively small. However, for the wave condition where the roll angle is maximal (8° , at $T_w = 8s$, and $H_w = 3.5m$), the power difference, although small, is not negligible.

In order to provide a clearer representation of the power production under- or over-estimation, Fig. 9.13 shows the ratio between the power estimated with the 6-DoF model, compared to the power estimated with the 1-DoF model. Consistent with Fig. 9.12, modest overestimation is found for large wave periods, with peaks of $+5\%$. However,

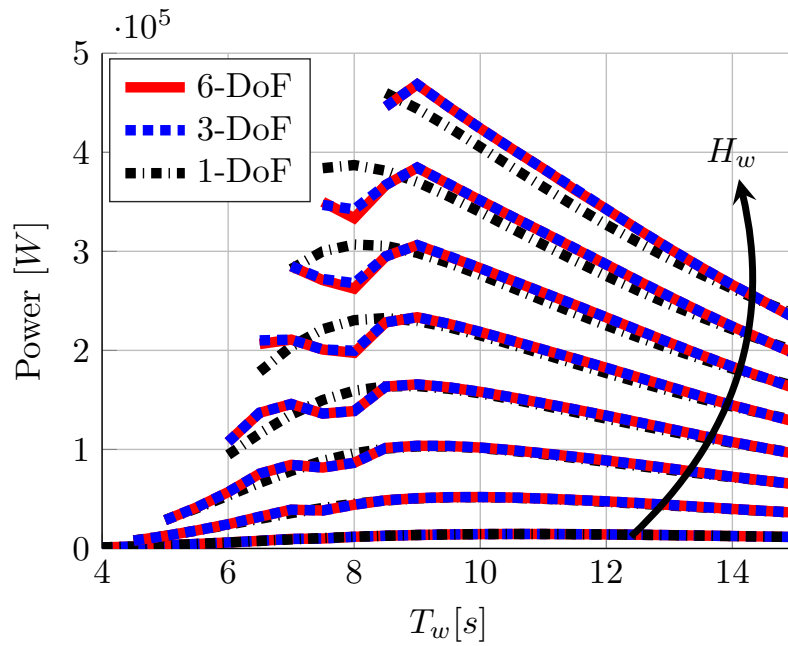


Figure 9.12: Power estimation, according to the 1-, 3-, and 6-DoF nonlinear Froude-Krylov models, for the CorPower-like device.

larger excursions are found at T_w between 6s and 9s, with up to +16% overestimation at around $T_w = 7s$, and up to -15% for $T_w = 8s$.

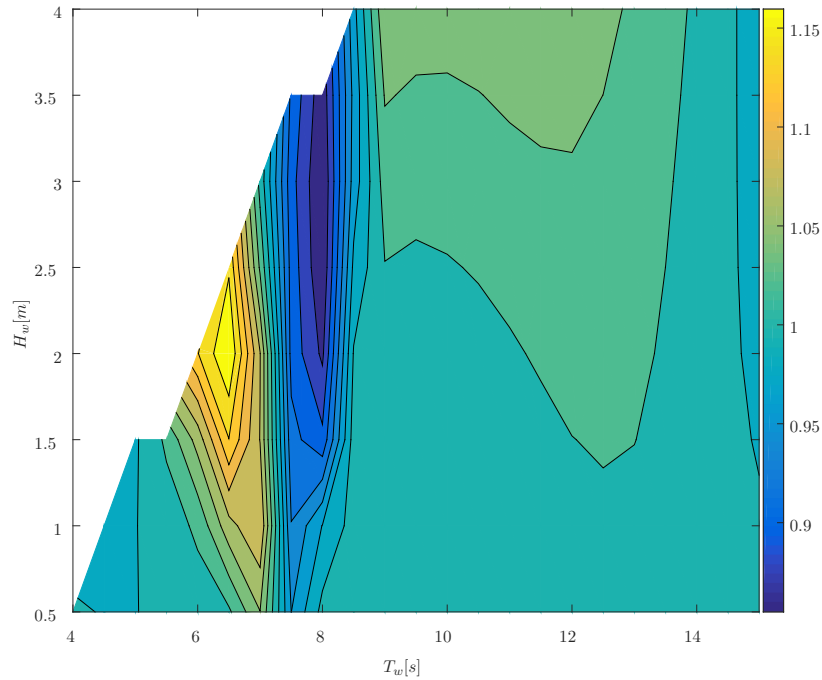


Figure 9.13: Power production estimation ratio, between the 6-DoF and the 1-DoF model, for the CorPower-like device.

9.4.3 The Wavebob-like device

A simplified version of a the Wavebob device, at 1:17 prototype scale, is now considered as a case study, since [46] demonstrates, through tank tests and a mesh-based nonlinear FK model, peculiar parametric instability for the Wavebob device, with negative consequences

on the efficiency. The simplified Wavebob-like WEC is a self-reacting heaving device, with a cylindrical spar (radius $0.3m$, draft $3.5m$), moving inside a cylindrical torus (outer radius $0.62m$, inner radius $0.36m$, draft $0.35m$). Since the real Wavebob device has a ballast system at the bottom of the spar, it has been assumed that two thirds of the weight of the spar is uniformly distributed in the bottom half of it. The centre of gravity and inertia properties are computed accordingly. A linear mooring system is considered attached to the spar. The PTO, which acts between the two bodies, extracting energy from the relative heave motion, is modelled as a linear damper. Finally, as in [46], the 12 DoFs (6 DoFs for each body) are reduced to 7, considering heave for both bodies (\hat{z}_s and \hat{z}_t , respectively, for the spar and the torus), and the remaining five DoFs (surge \hat{x} , sway \hat{y} , roll ϕ , pitch θ , and roll ψ) for the whole system, considered as a single body. Note that, for simulation, a small initial roll and pitch angle position (0.007rad) has been employed, as suggested by [46], in order to provide some initial energy in these DoFs. If not excited, either internally or externally, such small angles quickly decrease to zero; conversely, the roll angle increases only when parametric resonance occur.

The geometry has been simplified because of the intention to study mainly those nonlinearities related to pitch and roll motion. In fact, if the cylinder and cylindrical torus were to be constrained to a purely heaving motion, their response would be essentially linear, due to their constant cross sectional area [59]. Conversely, when large pitch/roll angles appear, even such geometries are subject to nonlinearities in the FK forces.

The choice of a self-reacting type of device is driven by the fact that such devices are particularly prone to parametric resonance, caused by time-varying system parameters. In the case of the considered WEC, leading causes of parametric instability are the variation of the metacentre, and of centre of gravity, due to pitch and relative heave motion, and to variations in the wetted surface. Furthermore, the Mathieu-type of instability is well-known to appear, after a certain wave amplitude threshold, at an exciting frequency twice the pitch natural frequency [207]. Due to the typical long spar of a system like the Wavebob, the pitch natural frequency is usually low. Consequently, some of the wave excitation frequencies, normally experienced in nominal power production conditions, are likely to be twice the pitch natural frequency, meeting the frequency requirement of the Mathieu equation.

However, for a fully coupled nonlinear 7-DoF model, the notion of a single natural frequency in pitch is quite blurred, as explained in Sect. 9.4.1, making the condition on the frequency less meaningful. Nevertheless, as shown in [46], parametric instability is a frequency dependent phenomenon. Therefore, as is commonplace in the literature concerning parametric resonance, regular waves are primarily considered, to give frequency-resolved insight. Given the threshold condition, parametric roll also depends on wave amplitude. Since FK nonlinearities mainly depend on wave steepness, defined as the ratio between the wave height and wave length, the wave amplitude is chosen so that a constant steepness of 2% is produced, which is at the upper edge of the region of validity of linear Airy's waves. Therefore, the set of analyzed wave conditions is unidimensional, with a one-to-one relationship between wave frequency (ω_w) and wave height (H_w).

9.4.3.1 Results for the Wavebob-like device

The optimization of the PTO damping coefficient B_{PTO} has been performed for each wave condition. Both the linear FK and the nonlinear FK models are considered, in order to highlight eventual differences in the optimal parameters, and therefore the sensitivity of the controller to modelling errors. The resulting optima are shown in Fig. 9.14. The two sets of B_{PTO} optima are hereafter referred to as B_L and B_{NL} , indicating which model is used to compute them, either the linear FK model or the nonlinear FK model, respectively.

Significant differences are only found in the range of frequencies between 2.5 and 3rad/s.

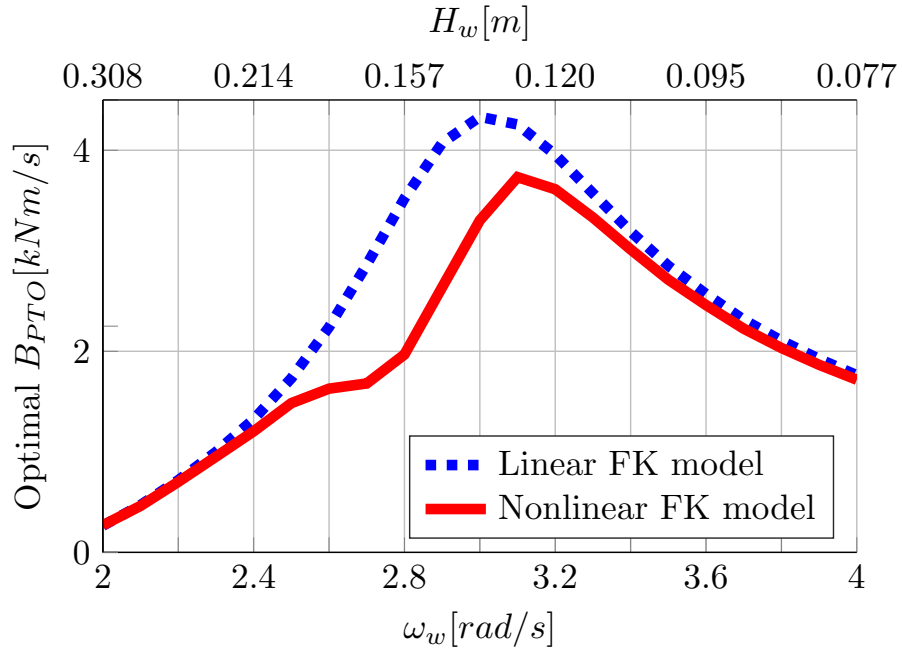


Figure 9.14: Optimal power-take off damping coefficient B_{PTO} for each wave condition, according to the linear and nonlinear FK models, for the Wavebob-like device.

It is reasonable to infer that such differences are strictly related to parametric resonance in the roll DoF which, as shown in Fig. 9.15, is generated over the same frequency range.

Obviously, since in the linear FK model there is no excitation mechanism in the roll DoF, the resulting roll motion is inherently zero. On the contrary, in the nonlinear FK model, an internal excitation mechanism is activated, due to parametric resonance, at those frequencies which lead the roll DoF into instability. In Fig. 9.15, both sets of PTO optima are used, from Fig. 9.14, obtained using the linear and nonlinear models. A significant dependence on the PTO damping coefficient can be noticed: on the one hand, the larger the PTO damping, the larger the roll response; on the other hand, the frequency range, where parametric roll appears, is generally insensitive to B_{PTO} , even though the frequency of the roll peak response changes from 2.8rad/s, with lower damping, to 2.7rad/s, with higher damping.

Therefore, it is interesting to undertake a more comprehensive study of the relation between the parametric roll excitation, and the PTO damping coefficients. Figure 9.16 shows the peak roll response for different wave conditions, and for different B_{PTO} values, ranging from 0 to about twice the maximum optimal PTO value, from Fig. 9.14. Consistent with Fig. 9.15, and in agreement with results shown by [46], it is found that the parametric roll response significantly increases with B_{PTO} , reaching peaks of 11.3° . Similarly, the frequency range for parametric instability widens as B_{PTO} increases, with the peak frequency for maximum roll motion slightly tending towards larger frequencies. Such behaviour is due to a progressively stiffening system, as the PTO resistance grows [46].

Figure 9.16 has important consequences both in the power production region, for the control strategy, and in the survivability mode. In fact, in case of extreme events, a natural tendency to avoid harm to the WEC might be to significantly increase the PTO damping, in order to limit the relative motion between the spar and the torus, and avoid end stop striking. However, what Fig. 9.16 shows is that, for large B_{PTO} values, parametric roll increases further, possibly causing severe structural damage.

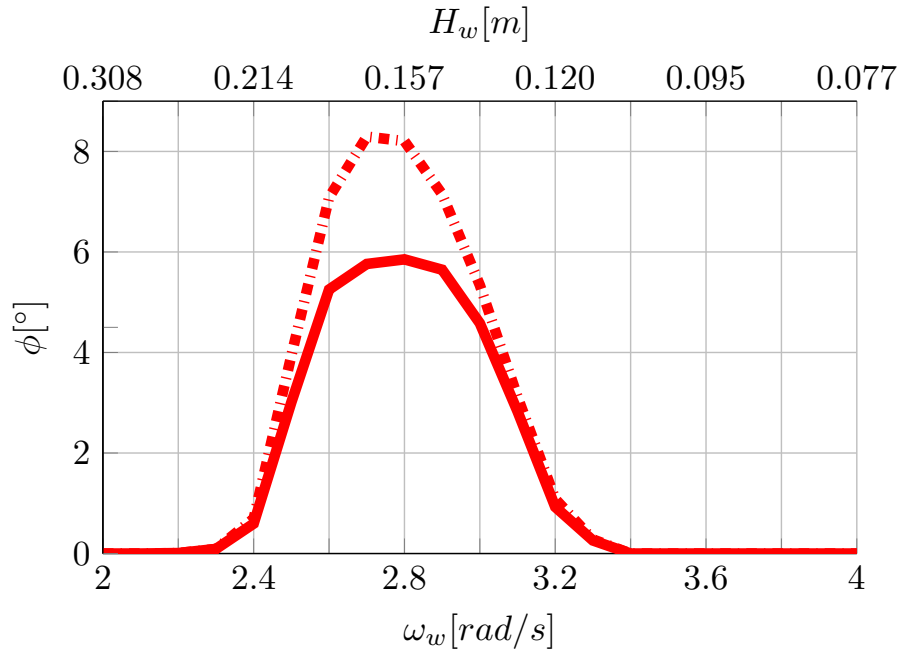


Figure 9.15: Maximum roll angle, for each wave condition, according to the nonlinear FK model, using optima computed with the linear (dashed-dotted line) and nonlinear FK model (solid line), for the Wavebob-like device, as shown in Fig. 9.14.

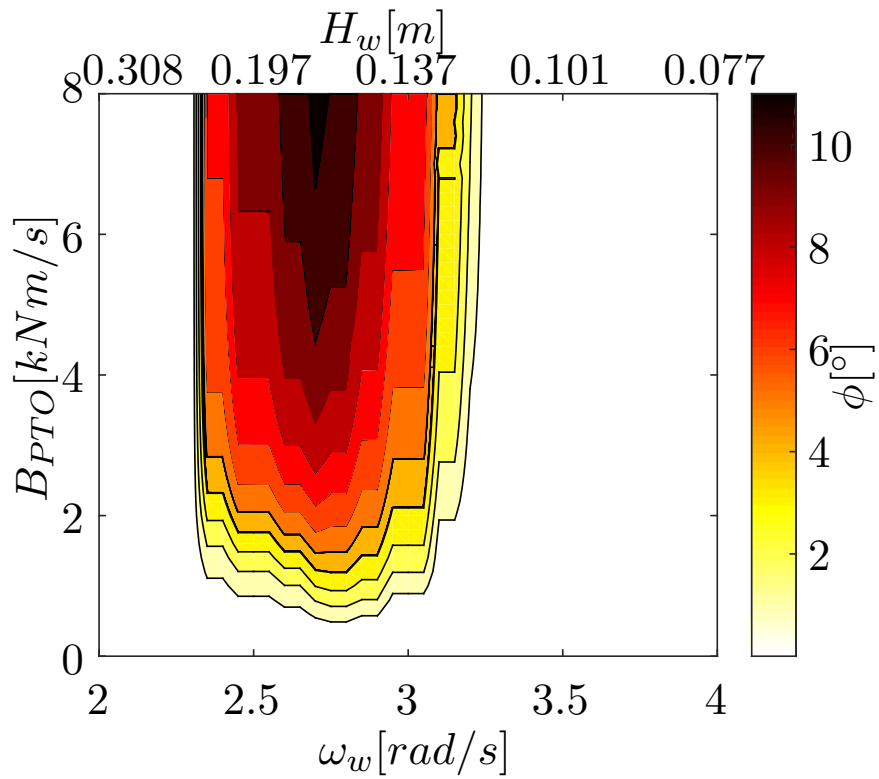


Figure 9.16: Sensitivity analysis on the maximum roll angle, for different wave conditions and PTO damping coefficients, for the Wavebob-like device.

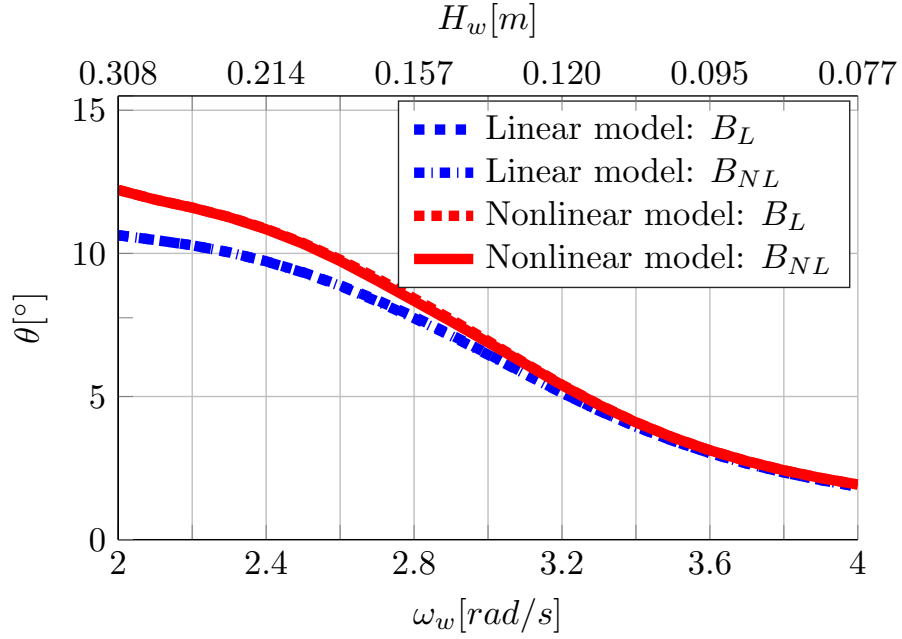


Figure 9.17: Maximum pitch angle, for each wave condition, according to the linear and nonlinear FK model, using optima computed with the linear and nonlinear FK model, for the Wavebob-like device, as shown in Fig. 9.14.

Apart from the parametric instability of the roll DoF, the pitch DoF is also parametrically excited. While roll is completely neglected in a linear FK model, pitch is excited in both models. Therefore, Fig. 9.17 shows the maximum pitch response, using both the linear and nonlinear FK models, each of them using the two sets of PTO damping optima, B_L and B_{NL} , from Fig. 9.14, for a total of four curves.

Little dependence on the PTO parameters, and consequently on the roll motion, is found, since the curves for each model, using the two sets of B_{PTO} parameters, substantially overlap. In contrast, a significant difference between the two models can be appreciated, with the nonlinear FK model forecasting larger pitch motion, especially at low wave frequencies. The nonlinear FK model is more responsive in pitch, mainly because of the changes in the metacentric height. In particular, the pitch hydrostatic stiffness decreases as the metacentre moves down and, if it eventually falls below the centre of gravity, the restoring force becomes negative, leading to instability [206].

Finally, power output prediction, for both linear and nonlinear models, and using the two sets of PTO parameters, is considered, and shown in Fig. 9.18. Differences within the same model, using different PTO optima, are obviously concentrated in the range of frequencies between 2.5 and 3 rad/s, where parametric roll is excited. Overall, the power produced according to the nonlinear FK model is lower than in the linear FK model, mainly due to the larger pitch motion, as shown in Fig. 9.17. Indeed, larger differences in power estimation are found at low wave frequencies, where larger errors are obtained in the pitch motion prediction.

The lower efficiency with the nonlinear FK model can be explained with reference to Figs. 9.15 and 9.17; roll and pitch motions are both larger in the nonlinear FK model, while the energy of the incoming wave is the same. Therefore, in order to excite such DoFs, and produce larger oscillations, some energy is diverted from the principal (heave) PTO axis, where the energy is harvested, and fed into to the secondary roll/pitch axes, where no PTO conversation takes place. Such a mechanism is particularly evident for parametric roll, and shown in Fig. 9.19, which presents the envelope of the squared-

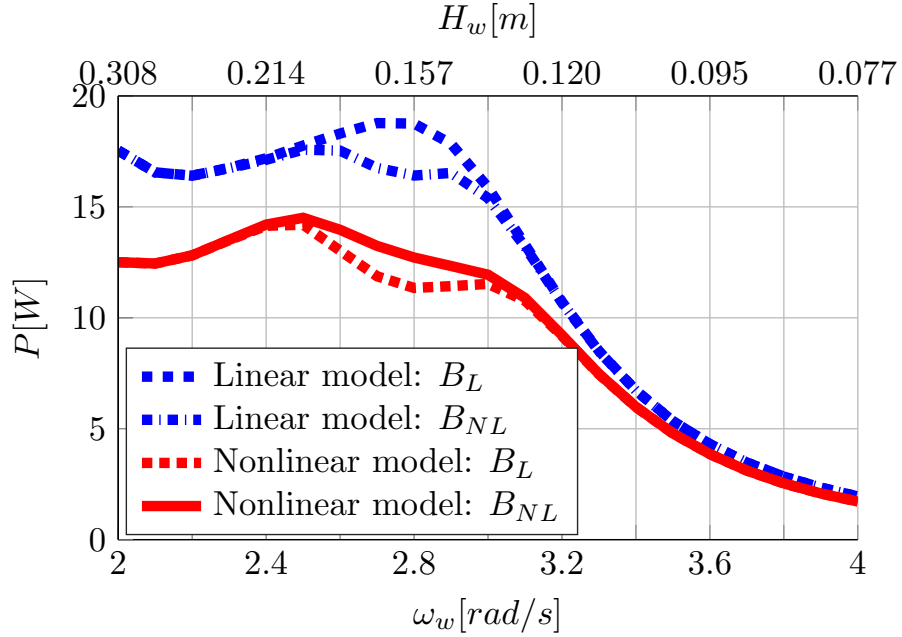


Figure 9.18: Power produced, for each wave condition, according to the linear and nonlinear FK model, using optima computed with the linear and nonlinear FK model, for the Wavebob-like device, as shown in Fig. 9.14.

velocity time traces, for relative heave, and roll motion. Note that the squared-velocity is a more representative quantity of the energy absorbed, which is extracted in the relative heave DoF, while wasted in the roll DoF. Figure 9.19 shows that the energy content in the relative heave motion is larger when the roll motion is still negligible (left part of the time trace); conversely, the gradual increase in parametric roll causes a decrease in relative heave, until steady state is reached (right part of the time trace). Therefore, it is evident that, due to parametric resonance, part of the energy is diverted from relative heave to roll, as schematically represented by the wavy arrow in Fig. 9.19.

9.4.4 The SparBuoy-like device

The last case study considered is inspired by the SparBuoy prototype device [48], which is a floating OWC, extracting energy from the relative motion between a hollow spar buoy and the water column contained within. A 1:100 scale prototype is considered, for which wave tank experiments have highlighted parametric resonance [48]. Shape and dimensions of the floater are represented in Fig. 9.20, while Table 9.3 tabulates relevant physical quantities (z_g the center of gravity, z_b the center of buoyancy, m the mass of the floater, I the roll/pitch inertia, and T_n the natural period). Moorings are modelled, in surge and sway, as linear restoring coefficients, chosen in order to match the natural period, given in [48].

Moorings forces are renown to potentially play an important role in parametric resonance generation, as discussed in [212]. However, since the purpose of the present study is to show the ability of the nonlinear model to articulate *hydrodynamically* induced parametric roll, the mooring model has been extremely simplified.

The SparBuoy device can be modelled as a two-body system, considering the floater in 6-DoF, with an additional heaving DoF for the water column, effectively modelled as a weightless rigid piston [213]. The hydrodynamic coefficients are computed with the boundary element method software WAMIT, using generalized modes for the moonpool

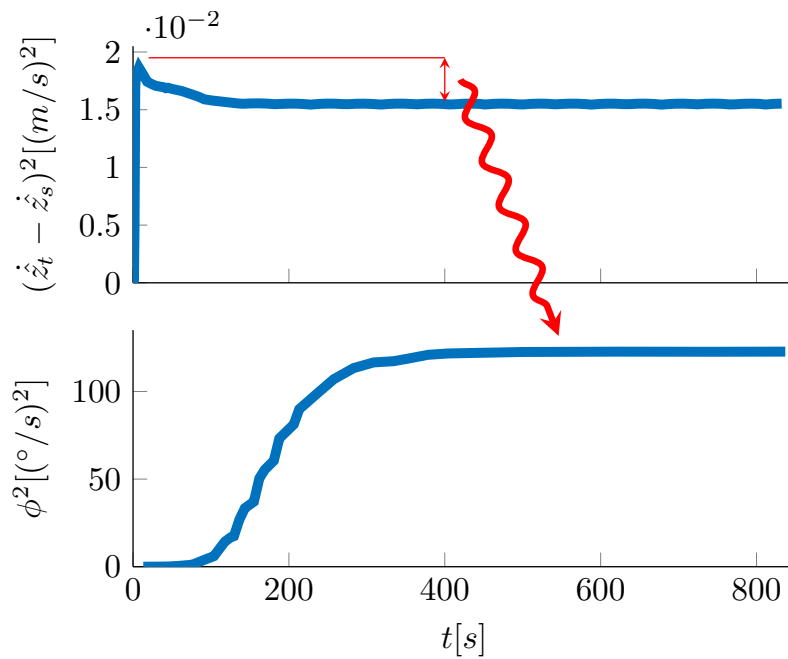


Figure 9.19: Envelope of the time traces for the squared-velocity in relative heave (top), and roll (bottom), using the nonlinear optimum at $\omega_w = 2.8rad/s$, for the Wavebob-like device. The wavy arrow schematically represents the energy diverted, due to parametric resonance, from the relative heave to the roll DoF.

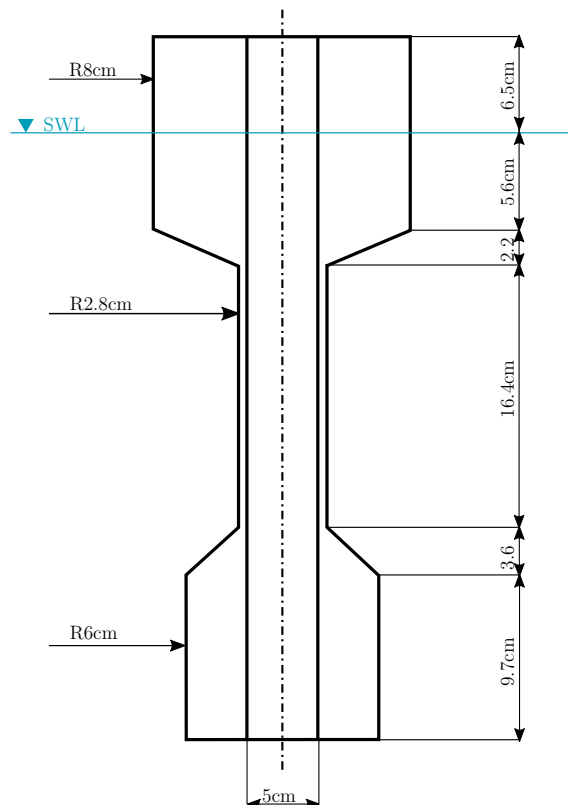


Figure 9.20: Shape and dimensions of the SparBuoy-like device, at 1:100 prototype scale.

free surface [162].

A linear turbine is considered, for which the ratio between the pressure difference in

Table 9.3: Physical properties of the SparBuoy-like device, at 1:100 prototype scale. Coordinates given in the inertial frame.

			Surge		Roll
			Sway	Heave	Pitch
z_g	[m]	-0.205			
z_b	[m]	-0.168			
m	[kg]	2.395			
I	[kg/m ²]	0.00733			
T_n	[s]		12.7	0.89	1.35

the chamber and the flow rate is constant (k_{PTO}). Ignoring air compressibility effects, it follows that the force interchanged between the water column and the floater is [214]:

$$F_{PTO} = \pm k_{PTO} A_{wc}^2 (\dot{\mathbf{x}}(3) - \dot{\mathbf{x}}(7)), \quad (9.38)$$

where A_{wc} is the cross sectional area of the water column, $\dot{\mathbf{x}}$ is the heave velocity of the floater ($\dot{\mathbf{x}}(3)$) and the water column ($\dot{\mathbf{x}}(7)$), respectively. The symbol \pm means that F_{PTO} acts on the two bodies with opposite sign. The turbine coefficient k_{PTO} is optimized for each wave conditions, using the linear model, in order to maximise the power capture [214].

With the aim of defining a parsimonious model, nonlinear computation of FK forces are applied only to floater's heave, roll, and pitch DoFs, since surge and sway is of little value in terms of accuracy, compared to the other DoFs for a point absorber [22].

The response of the device is studied in both monochromatic waves, in Sect. 9.4.4.1, and panchromatic waves, in Sect. 9.4.4.2. In particular, a practical implementation issue, related to long simulations with irregular wave conditions, is discussed, and solved in Sect. 9.4.4.2.

9.4.4.1 Monochromatic waves results

Parametric instability appears when two conditions are satisfied: the amplitude of the excitation is larger than the damping of the secondary DoF, and the frequency of external excitation is about twice the natural frequency of the parametrically excited DoF. Therefore, in order to study the amplitude and the frequency conditions, separately, simulations have been performed using a dense grid of wave conditions, with 11 wave heights, equally spaced between 0.005m and 0.0150m, and 76 wave periods, equally spaced between 0.5s and 2s.

Dissipation mechanisms, in the roll DoF, are the radiation damping, and viscous drag losses (which are modelled as an additional linear loss, proportional to velocity). Due to the lack of available information to determine an accurate viscous drag coefficient, it is firstly set to zero, and then a sensitivity analysis is performed. The resulting maximum roll response, without drag, is shown in Fig. 9.21

As predicted by theory [207], and consistent with experimental results [48], parametric roll is localized at wave periods equal to, or half of, the roll natural period, while elsewhere the roll response is null. Likewise, it can be noted that parametric instability emerges after an amplitude threshold is passed, namely for a 0.009m high wave, at $T_w = 0.5T_n$.

Further insight can be gained by analysing the spectral energy content of the response of the device, both in roll and pitch. Considering, for the sake of argument, a representative wave height of 0.01m, the Fourier transform is computed for all wave periods, as shown in the waterfall plots in Fig. 9.22 and Fig. 9.23, for roll and pitch, respectively. Both the Fourier frequency components (ω), and the excitation frequencies (ω_e), are normalized by the roll natural period (ω_n). Note that results shown in Figs. 9.22 and 9.23 are consistent

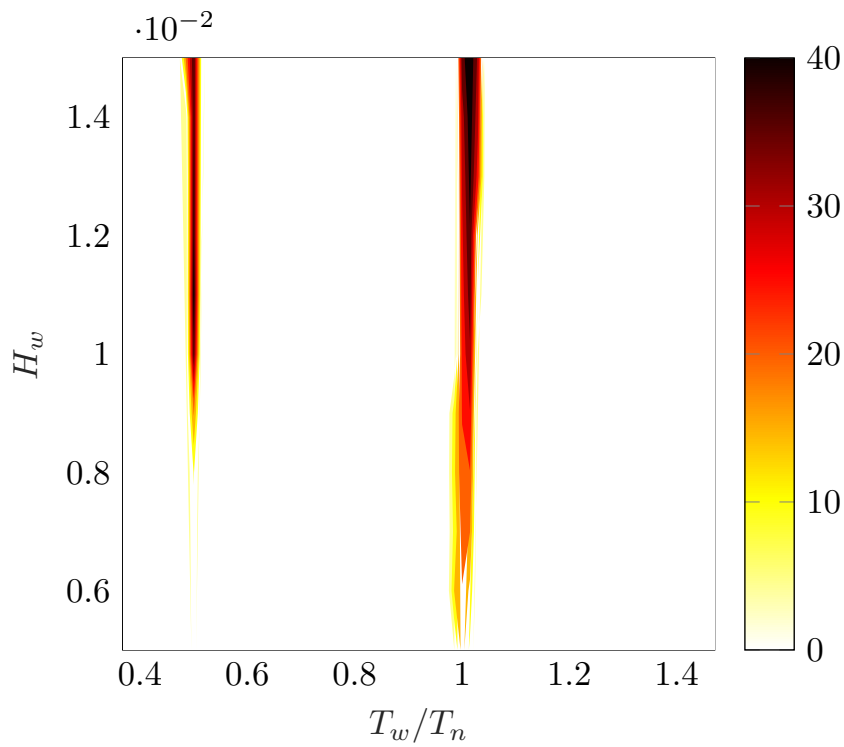


Figure 9.21: Maximum roll response, in degrees, without viscous drag, for the SparBuoy-like device. Wave periods are normalized by the roll natural period.

with similar results obtained for the Wavebob device, using the LAMSWEC mesh-based approach [46].

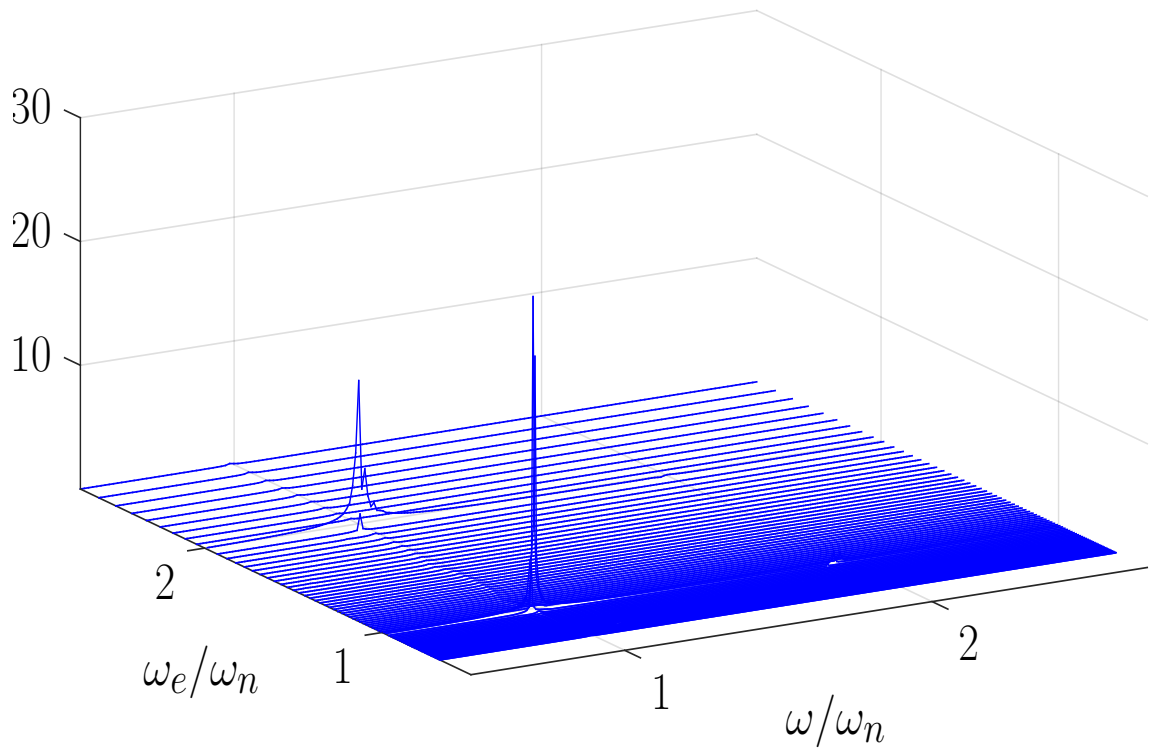


Figure 9.22: Magnitude of the Fourier transform of the roll response, in degrees, at different excitation frequencies ω_e , with wave amplitude of $0.01m$ for the SparBuoy-like device. Both frequencies are normalized by the roll natural frequency (ω_n).

Considering Fig. 9.22, it is clear that the roll response is non-zero only for normalized excitation frequencies of 1 and 2, and the spectrum has an evident peak at the normalized frequency component of 1. In fact, while the roll degree of freedom is never externally excited, parametric resonance activates an internal excitation mechanism at integer multiples of the normalized excitation frequency.

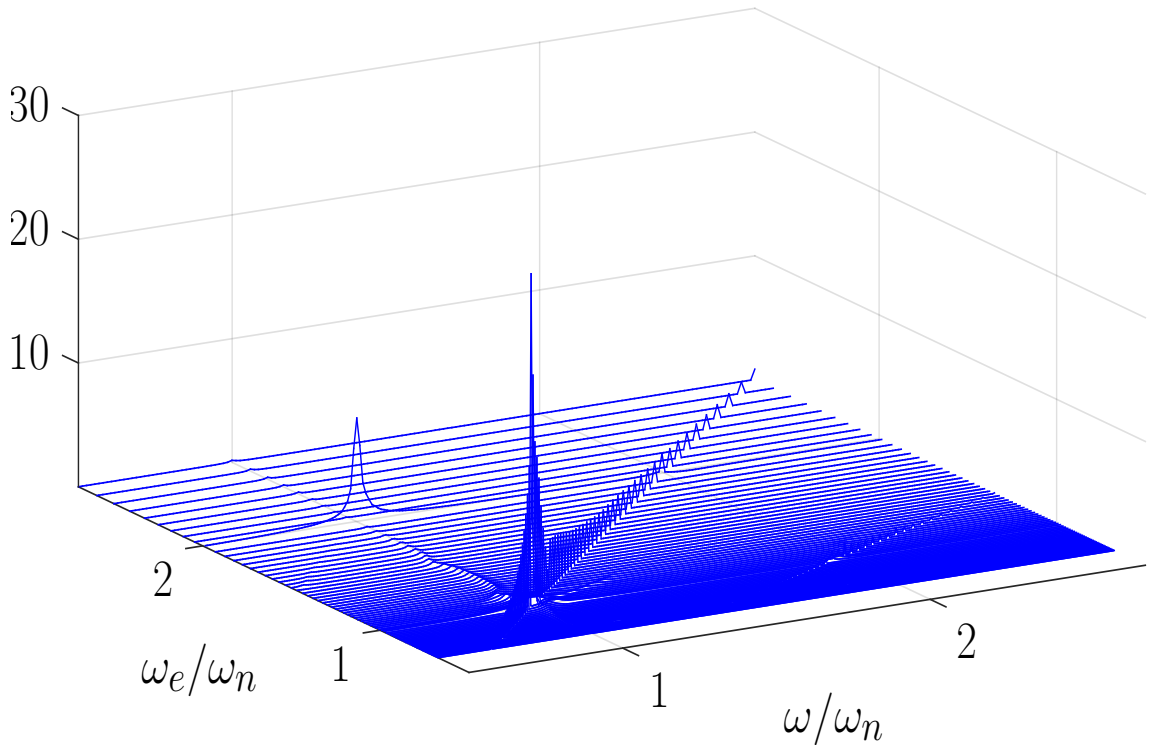


Figure 9.23: Magnitude of the Fourier transforms of the pitch response, in degrees, at different excitation frequencies ω_e , with wave amplitude of $0.01m$ for the SparBuoy-like device. Both frequencies are normalized by the roll natural frequency (ω_n).

Conversely, since waves are externally exciting the device in the pitch DoF, the response spectrum shows a peak at the same excitation frequency; indeed, Fig. 9.23 shows that peaks align along the bisector of the horizontal plane (direction $\omega = \omega_e$). Looking at the plot from a direction perpendicular to the direction of the bisector (where $\omega = -\omega_e$), one can recognize the typical shape of the first-order pitch response. However, for a normalized excitation frequency of 2, when parametric roll occurs, a peak in the pitch spectra is generated at the pitch natural frequency.

Figures 9.21 to 9.23 demonstrate that the proposed modelling method is able to articulate parametric instability. However, Although the likelihood of, and the conditions for, parametric instability generation are well described by the model, the severity of the parametric response is overestimated. In fact, although the model considered in this study has simplified mooring and PTO systems, with respect to that tested in [48], making the comparison less relevant, the maximum roll response obtained in the wave tank was about 21° , about half of that given by the model (about 40° , as shown in Fig. 9.21). Such a result is definitely consistent with the absence of viscous drag loss in the model for rotational DoFs. A similar issue is found, for example, in [62], where the LAMSWEC (mesh-based nonlinear FK) method is applied to the SEAREV device, without modelling viscous drag effects.

Therefore, in order to discuss the influence of viscous drag on the generation of parametric instability, a sensitivity study is performed. Considering a wave at half the pitch natural period ($0.68s$), and $H_w = 0.01m$, 11 linear drag coefficients are tested, equally

spaced between 0 and $0.01Nms$. The resulting amplitudes of the steady state responses are shown in Fig. 9.24, while the time traces are shown in Fig. 9.25, where each area represents the envelop of the time trace, using one drag coefficient.

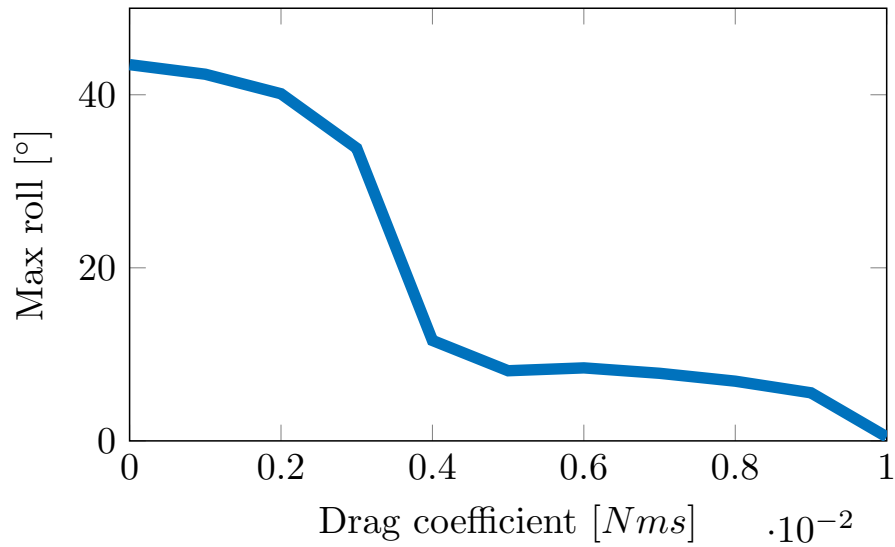


Figure 9.24: Amplitudes of the steady state roll responses, for a wave with $T_w = 0.68s$ and $H_w = 0.01m$, for 11 linear drag coefficients, equally spaced between 0 and $0.01Nms$.

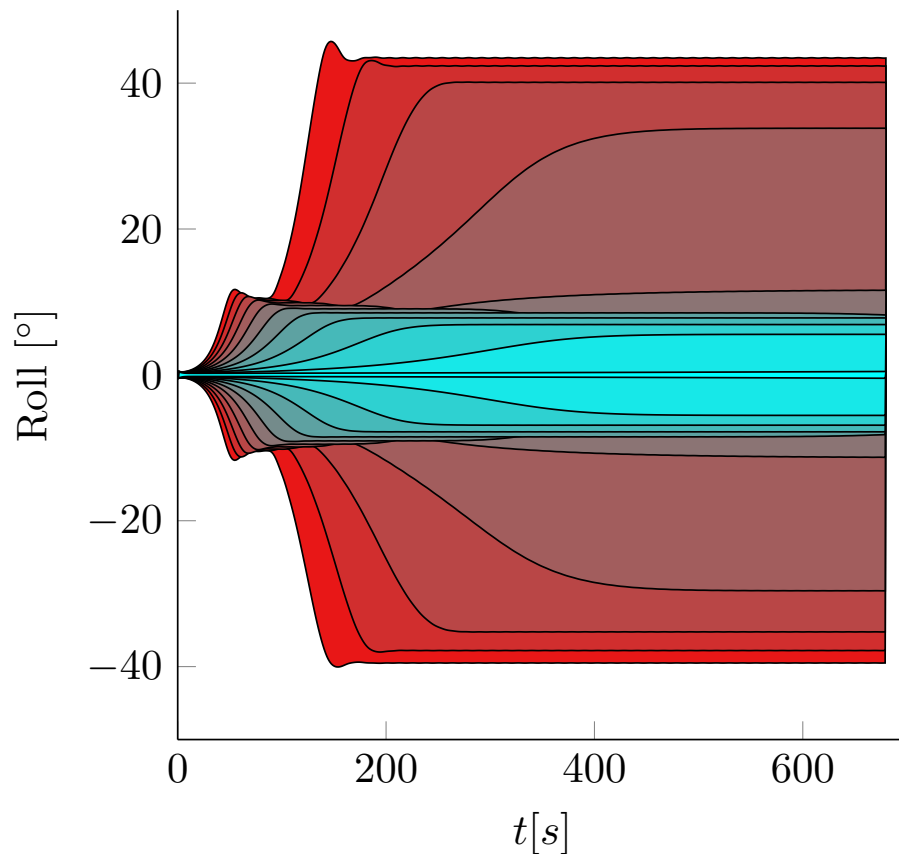


Figure 9.25: For a wave with $T_w = 0.68s$ and $H_w = 0.01m$, for 11 linear drag coefficients, equally spaced between 0 and $0.01Nms$, each area corresponds to the envelop of the roll response time traces. As drag increases, roll response decreases.

As expected, larger linear drag coefficients cause the roll response to diminish, until it

largely disappears for a drag coefficient of $0.01Nms$. In fact, one of the usual expedients adopted, in order to avoid parametric roll, is to increase viscous dissipation, for example through additional fins attached to the main floater body [48]. However, Fig. 9.25, which plots $1000T_w$ -long simulations, also shows that the transient time for building-up steady parametric roll significantly increases with the drag coefficient. Consequently, a very long transient, in regular wave conditions, would obviate the significance of parametric resonance in real sea conditions: given the panchromatic nature of irregular waves, there would be insufficient time to generate a sustained parametric response. Therefore, it is important to investigate the conditions for parametric resonance also in (realistic) irregular sea states, as will be carried out in Sect. 9.4.4.2.

9.4.4.2 Panchromatic waves results

From the discussion so far, it is clear that parametric resonance is an extremely frequency-dependent phenomenon. Regular waves steadily excite the device at the same frequency, facilitating the progressive build-up of parametric instability, when the excitation frequency is equal to, or twice, the resonant frequency in pitch/roll. However, real waves are panchromatic, so conditions for parametric excitation are weaker. In fact, comparing regular and irregular wave tank experiments, [215] shows that the roll response is more widely spread across the frequency range, but with lower maxima, although larger wave heights are used. Indeed, since parametric excitation is localized in a very narrow frequency window, a sustained parametric response is harder to achieve in the presence of a panchromatic wave process, as opposed to monochromatic excitation at the exact parametric resonant frequency.

Therefore, in order to verify the likelihood of a parametric response, with statistical reliability of the results, very long simulations/experiments are usually performed, in order to allow the device to escape the static equilibrium of a zero roll angle. As an example of ‘very long’, wave tank experiments for the SparBuoy device, in [215], last for about 1000 times the peak period, and a significant roll response is achieved only after $600 T_p$. While relatively long experimental tests do not usually represent a substantial issue, numerical simulations may be affected, as a consequence of a combination of the Nyquist sampling criterion (imposing the bandwidth from the sampling rate [216]) and the condition for aperiodic realisation generation (imposing the frequency step from the realisation length [217]): assuming a sampling frequency of 1.28Hz (commonly implemented in wave data-buoys) a very long (aperiodic) time window (say $T = 1000T_p$) imposes a tiny frequency step ($1/T$) for correct realisation of the free surface elevation, hence an excessive number of frequency components (up to 4000). Having so many frequency components is not a significant problem for linear models, since all forces are computed offline. On the contrary, time-domain nonlinear models are likely to compute nonlinear forces online, according to the actual relative position between the free surface elevation and the device. Nonlinear FK models are particularly adversely temporally affected by the number of spectral components, since they have to consider the two-dimensional pressure field (both x - and z - dependence).

This is especially true for the 6-DoF numerical integration FK model which, while roughly achieving real time computation with regular waves, becomes much slower when an excessive number of frequency components are included. A quantification of such a decline in computational performance is given in Fig. 9.26, which shows the increase in computational time for the calculation of FK forces, using N_ω components (t_{N_ω}), with respect to the regular wave case limit, where only one frequency component is used (t_1). Starting from a $1000T_p$ -long realisation of an irregular sea spectrum, 500 equally spaced time samples of a $10T_p$ -long section are considered, in order to reduce the uncertainty regarding the computational time (which depends on the value of the integrals, with respect

to relative and absolute tolerances, as well as the computing machinery). Consequently, equally-spaced N_ω components are selected from within the bandwidth of the original process, with $N_\omega \in [1, N_\omega^{max}]$, where N_ω^{max} is the total number of components of the full process (4300). Note that $N_\omega = 1$ correspond to a single frequency component, i.e. a regular wave.

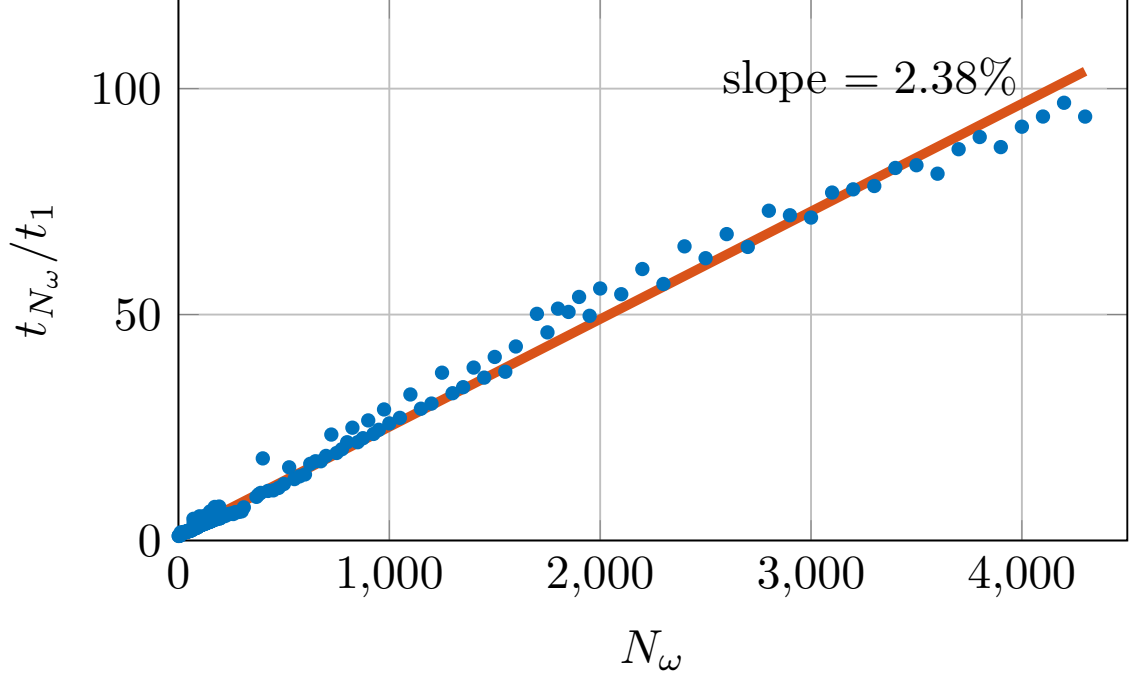


Figure 9.26: Increase in computational time t_{N_ω} , relative to the monochromatic limit t_1 , for the numerical computation of nonlinear Froude-Krylov forces, with panchromatic waves, using N_ω spectral components.

Figure 9.26 shows an approximately linear increase in the relative computation time with the number of spectral components, with an interpolating line slope of 2.38%. In particular, Fig. 9.26 proves that using all the components of the original spectrum represents an important practical issue, since the computation time may increase by up to a factor of 100. Such a significant slowdown would conflict with one of the main advantages of the modelling approach proposed in this chapter, which is computational efficiency.

However, despite the fact that many frequency components are required to generate a statistically random long realisation (in time), the *local* (in space, at a given time) wave and pressure fields are likely to be much less complex, therefore needless of such a refined discretization in the frequency domain. In fact, numerical integration is performed, at each time step, using the wave and pressure fields in the (relatively small) spatial region where the device is sitting. Therefore, at every time instant, t_0 , a computationally cheaper reduced model is sought (offline), which can efficiently and accurately describe the pressure field in the local body location, i.e. in the $x - z$ domain where the device is expected to operate.

Two approaches for the identification of the local pressure field are hereafter examined, namely a fitting approach and a FFT-based approach. According to the fitting approach, the parameters (α_i) of an alternative structure (\tilde{p}) are chosen so that the error with respect to the actual pressure field is minimized. The most convenient structure is found to be the following:

$$\tilde{p} = \alpha_0 + \sum_{i=1}^{\widetilde{N}_\omega} \left[\alpha_i \cos(k_i x) + \alpha_{i+\widetilde{N}_\omega} \sin(k_i x) \right] \frac{\cosh k_i(z+d)}{\cosh k_i d} \quad (9.39)$$

where \widetilde{N}_ω is the number of frequency components of the reduced representation, selected within the bandwidth of the original process, in order to obtain equally-spaced levels of spectral energy; in this way, the spectrum is used to inform the definition of the fitting structure. The primary merit of the representation in (9.39) is that, while resembling the original pressure field representation, in (8.5b), it is linear in the parameters, leading to a simple least-squares quadratic optimization problem, easy to solve analytically. Note that \widetilde{N}_ω is a variable defining both the accuracy of the fit, and the size of the reduced model, since the number of parameters is $2\widetilde{N}_\omega + 1$.

Accurate results are achievable, provided that the fitting grid size and density is properly chosen. However, such a choice would require a convergence study, and the evaluation of the model's accuracy outside the fitting grid. Since the second option (FFT-based) is found to be less arbitrary and less sensitive to the parameter choices, the fitting approach has been discarded.

According to the FFT-based approach, at each time step, say t_0 , the FFT of the free surface elevation is computed over a time window, centred on t_0 . The frequency-domain components are then used to compute the free surface elevation $\hat{\eta}$, and pressure field \hat{p} , at $t = t_0$, and over a spatial domain local to the device. Since such components are used just at $t = t_0$, the non-periodicity at the extremes of the time window is irrelevant.

However, since different wave components travel at different speed, the accuracy of the reconstructed field (in space) depends on the length of the time window, as well as the length of the spatial domain. Note that the sampling frequency and the length of the time window defines the number of frequency components of the identified model. The length and depth of the considered spatial domain is roughly defined by the expected operational space spanned by the device.

On the one hand, such an identification method implies a negligible overhead, thanks to efficient algorithms for FFT computation. On the other hand, a considerable speed up in computational time is achieved, since accurate results are easily obtained with less than 100 components (see Fig. 9.27), as opposed to several thousand.

In order to define the error index, shown in Fig. 9.27, consider a spatial domain $x \in [-0.15m, 0.15m]$ and $z \in [-0.20m, \eta]$, selected according to the dimensions of the device, shown in Fig. 9.20; from a $1000T_p$ -long realisation of a JONSWAP spectrum with $T_p = 0.68s$, $H_s = 0.02m$, and $\gamma = 3.3$, a portion is selected, taking 201 time samples, at the sampling frequency of 1.28Hz, centred at the highest peak of η (100 samples at each side), which are sufficient to give a significant description of the possible range of errors. At each time instant, the mean of the absolute value of the normalized relative error, between the identified \hat{p} and the original p , is computed over the spatial domain. Figure 9.27 shows the consequent maximum and average errors, in time, depending on the number of components \widetilde{N}_ω of the reduced representation, showing that very accurate results can be achieved already with $\widetilde{N}_\omega = 50$. Note that, given the 2.38% increase rate of the computational time with \widetilde{N}_ω , shown in Fig. 9.26, $\widetilde{N}_\omega = 85$, for example, would just double the computational time, with respect to the computation for a regular wave, while producing a negligible error, as shown in Fig. 9.27. This compares favourably with a 100-fold increase in computation, in the absence of model reduction.

Finally, using the FFT-based reduction method, the response of the SparBuoy device is studied for a comprehensive range of sea states, based on JONSWAP spectra, with T_p ranging from 0.5s to 1.6s, with a 0.02s step, and H_s ranging from 0.005m to 0.025m, with a 0.005m step, considering $500T_p$ -long realisations. Note that larger waves are considered, with respect to the regular wave case, since parametric excitation is weaker, due to the

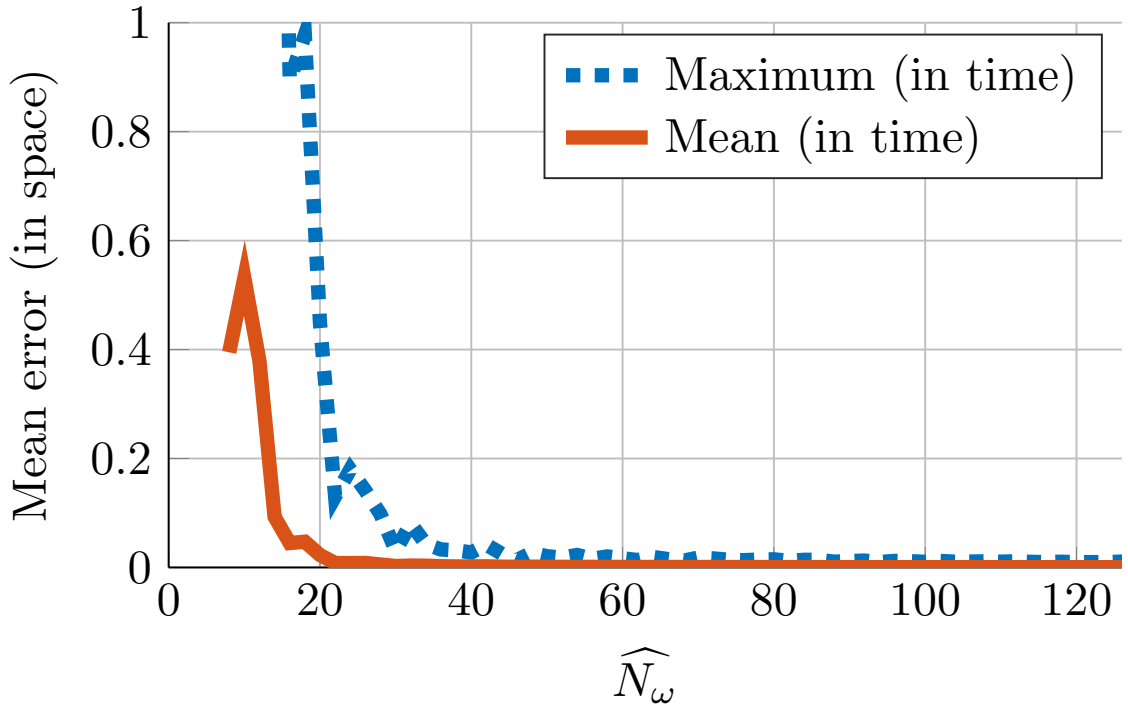


Figure 9.27: Maximum and mean error, using the FFT-based approach for pressure representation reduction, with respect to the number of spectral components.

panchromatic nature of the incoming waves. This approach is consistent with experimental tests in [215], where maximum significant wave heights, with irregular waves, are larger than the maximum wave heights of the regular waves.

As in Sect. 9.4.4.1, no viscous drag is initially included, so a sensitivity analysis, with regard to the viscous drag coefficient, is subsequently performed. An example of the parametric roll response of the device is shown in Fig. 9.28, for the sea state which generates the most dramatic roll motion, i.e. $T_p = 0.68s$ and $H_s = 0.025m$. Furthermore, Fig. 9.29 presents the maxima of the roll responses for all the considered sea states, comparable to Fig. 9.21.

As expected, although with larger significant wave heights, the roll response with irregular waves is smaller than with regular waves. Furthermore, the frequency range where parametric resonance appears, while still centred at T_p/T_n of values 0.5 and 1, is wider, due to the panchromatic nature of the excitation. However, Fig. 9.29 only shows the maximum roll response, while it is interesting to also consider the standard deviation, in order to provide a more significant evaluation of the overall behaviour of the system. Figure 9.30 shows a cross section of the map in Fig. 9.29, at $H_s = 0.025m$. In the region where parametric roll is significant, the maximum response is between 2.5 and 5 times the standard deviation.

Finally, as for Fig. 9.24, a sensitivity analysis is performed, shown in Fig. 9.31, in order to evaluate the degree of which viscous drag affects the eventual parametric excitation of the device, for the sea state of maximum parametric response ($T_p = 0.68s$, $H_s = 0.025m$). Comparing Fig. 9.31 to Fig. 9.24, similar trends are found but, although larger waves are used in irregular conditions, a smaller roll response is obtained. Such information has the potential to inform the design process, suggesting an ideal viscous drag coefficient in the roll DoF, achieved for example with lateral fins, as in [215], such that parametric roll is largely avoided.

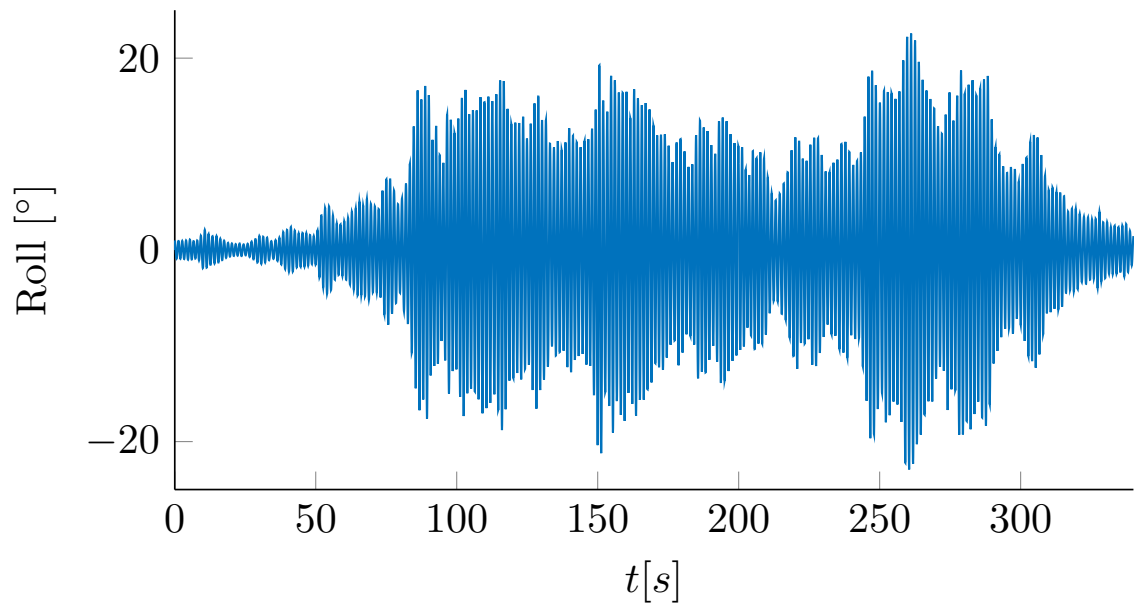


Figure 9.28: Parametric roll response of the SparBuoy-like device, without viscous drag, with $T_p = 0.68s$ and $H_s = 0.025m$

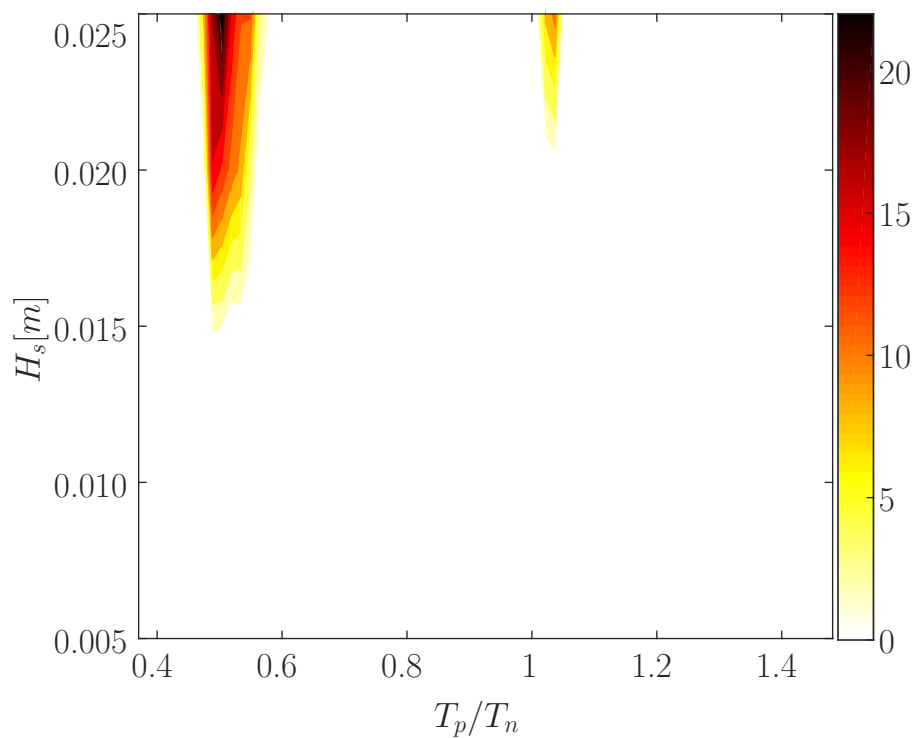


Figure 9.29: Maximum roll response, in degrees, without viscous drag, in irregular wave conditions, for the SparBuoy-like device. Wave periods are normalized by the roll natural period.

9.5 Conclusions

Most wave energy converters are designed to absorb and convert energy in only one degree of freedom. However, although simplified single-DoF mathematical models are very useful to describe the overall behaviour of a WEC, they may miss important dynamical aspects of the real response of the device. Nonlinear multi-DoFs models should also be used, in

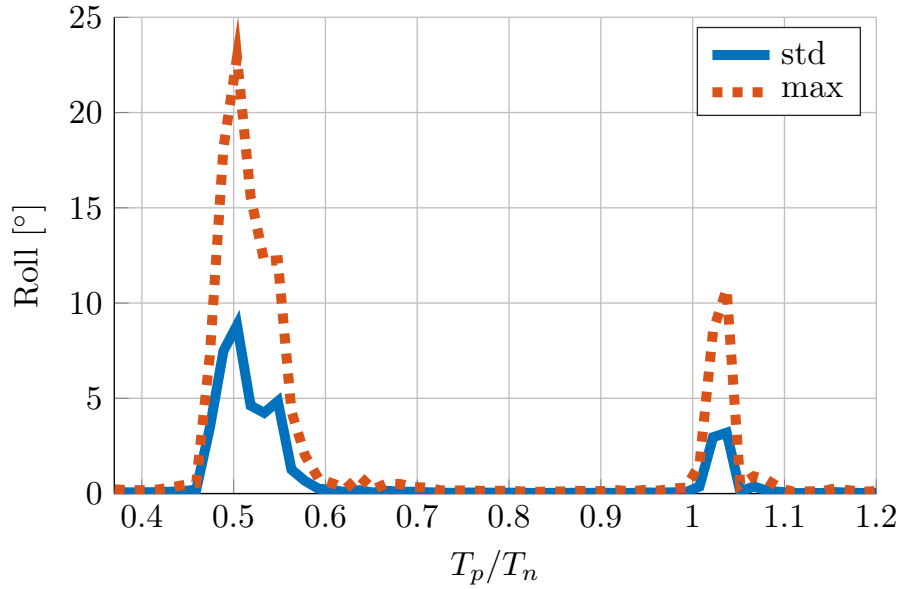


Figure 9.30: Maximum (max) and standard deviation (std) of the roll response, without viscous drag, with $H_s = 0.025m$, for the SparBuoy-like device. Wave periods are normalized by the roll natural period.

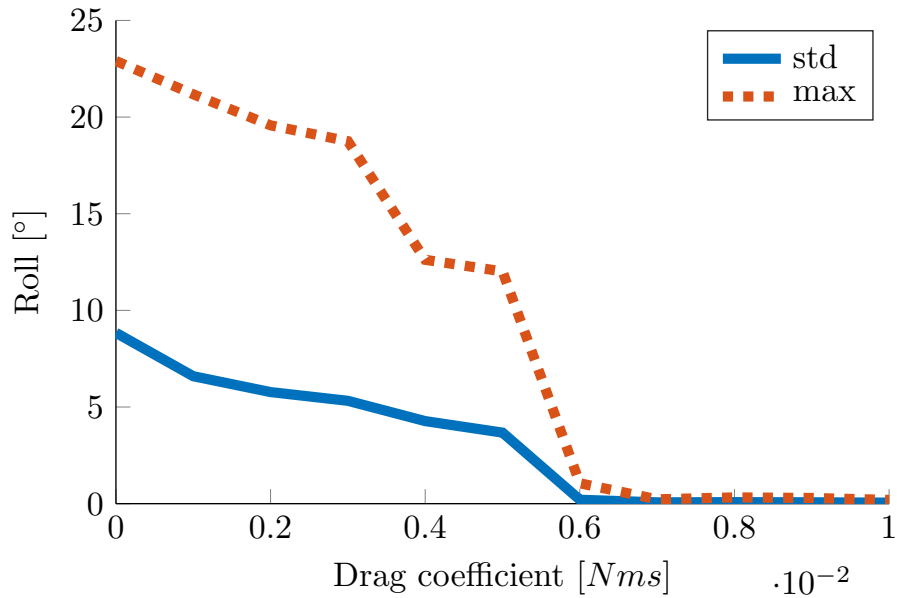


Figure 9.31: Maximum (max) and standard deviation (std) of the roll response, depending on the viscous drag coefficient, with $T_p = 0.68s$ and $H_s = 0.025m$, for the SparBuoy-like device.

order to assess the importance of secondary motion, the effect of linear and nonlinear interaction between DoFs, and the likelihood of parametric resonance. In particular, the impact on design, optimization, control strategy, and survivability should be evaluated, in order to use the most computationally compact suitable model for each application.

In this chapter, the computationally efficient nonlinear Froude-Krylov modelling approach, introduced in Sect. 4 in heave only, is expanded to multi-DoFs, discussing strengths and weaknesses, and introducing two levels of complexity in formulating FK forces, namely requiring algebraic or numerical integration. Furthermore, 3- and 6-DoF models are examined since, with mono-directional waves, only surge, heave, and pitch are excitable;

however, if parametric resonance appears, also sway and roll motions are activated.

Considering three WEC prototypes (CorPower, Wavebob, and SparBuoy), as opposed to academic case studies, different aspects of multi-DoFs modelling are highlighted. Non-linearities introduce perturbations in the system parameters, which directly affect the motion of the device and, ultimately, power absorption. Moreover, optimization of control parameters is shown to be sensitive to both nonlinearities (modelling errors), and interactions between the DoFs, affecting not only power extraction, but also the potential survivability of the device. Finally, nonlinear models able to articulate nonlinearities in many DoFs, including, for example, generation of parametric resonance, can be effectively used to take design decisions, such as the determination of an appropriate drag coefficient to avert excessive parametric response. While the number of tank tests is inherently limited by duration and costs of the experimental campaign, computationally efficient numerical models can be run extensively, covering a wide range of design scenarios, leading to more informed design and tests.

Conclusions and future work

Contemporary wave energy technologies need to perform a substantial leap from externally funded research to sustainable industrial competition in the energy market. Economic viability is the imperative prerequisite, which can only be achieved by reducing costs and/or increasing productivity. Both objectives require *mathematical models* to be accurate and reliable, which often mean *nonlinear*, as widely discussed in this thesis. High confidence in motion and loads prediction, thanks to accurate models, is beneficial for an appropriate definition of operational costs, a precise planning of maintenance and calculation of residual lifetime of components, and an effective design of the structural properties of the system. In fact, rough estimations of the system dynamics can lead to either over-sizing, hence a more expensive device, or down-sizing, hence reduced lifespan and risk of unexpected failures. In general, linear models tend to be overoptimistic about energy absorption, as shown in Fig. 4.9 in Chapter 4, considerably overestimating, for example, the maximum torque and power the generator must withstand, hence the size and price of the machine. As a further example, Chapter 9 shows how an accurate nonlinear model can be precious to assist strategical decisions regarding the survivability of the WaveBob device: on the one hand, trusting linear model results, the best option to survive to extreme events would be increasing the PTO damping coefficient as much as possible, in order to avoid end stop striking between the spar and the torus; on the other hand, a more accurate nonlinear model demonstrates (see Fig. 9.16) that large PTO damping causes an increase in parametric roll response (completely neglected by linear models), which can possibly cause severe structural damage. Similarly, the whole design of moorings is substantially different in case where the device is supposed to respond in roll (as the nonlinear model predict), or not (as the inaccurate linear model would suggest). Therefore, accurate mathematical models can enhance a well informed design, not only reducing costs, but also improving the device dynamics and performance. Chapter 9 proposes a further example, considering the SparBuoy device, where the ability of the model to articulate parametric roll has major consequences on the device design. In fact, parametric resonance is a detrimental effect for the system efficiency, which should therefore be limited; thanks to a computationally efficient nonlinear model, a sensitivity analysis to the drag coefficient can be performed (see Figs. 9.24 and 9.30), in turn leading to a modification of the basic design, including appropriate lateral fins.

An essential tool for increasing the productivity of a wave energy device is the *control strategy*, whose main purpose is usually to exaggerate the motion in order to maximize power absorption, as shown, for example, in Fig. 6.8 in Chapter 6. However, the effectiveness of model-based control strategies (the most common type of controllers for WECs) is often extremely *sensitive to modelling errors*, so that accurate mathematical models are crucial for obtaining decent performance. In fact, Chapters 3, 4, and 9 show how variable the optimized control parameters are, when models of different accuracy are used for the

optimization (see Figs. 3.5, 4.7 and 4.8, and 9.14). Inevitably, control parameters, optimal according to a particular model, generate suboptimal power when implemented in other models (see Fig. 9.18) and, by extension, in the real system. Therefore, the performance of the control strategy in the real system much relies on the representativeness of the model used for the optimization.

As a remark, note that the usual approach to control design and optimization is to assume the system as invariant, and attempt to maximize its performance without changing its principal geometric and hydrodynamic characteristics. However, it is potentially beneficial to consider the system as a further variable of the control optimization, as opposed to a static input. In this way, an overall optimized performance can be obtained through a synergetic concurrent design of both device and controller. Objectives other than power maximization can particularly benefit from this approach, such as the definition of physical constraints or sizing of different components. However, such a holistic approach to device optimization is viable only at early design stages, when the device design is still very flexible. In particular, referring to the TRL-TPL matrix, shown in Fig. 1.2, the objective is to increase the overall performance of the system (increase TPL), when investments and marginal expenditures are still low (low TRL). Nevertheless, the success of such a design strategy is highly dependent on the ability of mathematical models to be representative of the behaviour of the real full-scale device, as discussed in Chapter 1.

However, accuracy is not the only influential aspect of a mathematical model. An equally crucial feature is the required computational time, which is often limiting the area of applicability of the model, since many iterations (e.g. for optimization studies) or real-time calculations (e.g. for model-based controllers) may be required. Unfortunately, computational time and accuracy are often mutually contrasting factors, so that an appropriate compromise should be defined, that suits the purpose the model is intended to be used for. Although very popular, due to their computational convenience, linear models can often be very imprecise, when applied to WECs under controlled conditions (note that controlled conditions should be the normality, if economic viability is to be achieved). In fact, the linear assumption of small motions is not respected when the control strategy exaggerates the motion, in order to increase power absorption. Linear models are effectively used in classic ocean engineering, where the usual objective is to stabilize the floater; conversely, the objective of a WEC is the opposite, namely to resonate with the wave and maximize the response, so that classical modelling approaches may become inadequate. Chapters 4 and 6 show how accurate linear models are in absence of a control strategy, with negligible error, and virtually no difference between linear and nonlinear models (see Fig. 6.5); in contrast, when the controller enlarges the displacement-velocity operational space, linear models become unrepresentative, even leading to unrealistic results (see Fig. 4.5) and overoptimistic power productions (see Fig. 6.9). On the other hand, the inclusion of nonlinearities is likely to improve the fidelity of the mathematical model, usually at the price of an additional computational burden (see Fig. 6.6).

A plurality of nonlinear modelling approaches exists, as discussed in Chapter 2, starting from potential theory-based models, to Navier-Stokes-based software, and to models identified from data. According to the particular fidelity/computational requirements of the intended study, a *parsimonious* model should be selected, which is the one that includes only relevant nonlinearities, in the most computationally efficient way, in order to achieve an appropriate level of accuracy. However, mostly due the large variety of WEC concepts and operational conditions, there is no a single “best” model for each application, so that individual cases should be assessed independently. This thesis focuses on potential theory-based models in the power production region, namely in mild, medium wave conditions, while extreme events (likely to require CFD simulations) are neglected. Chapter 5 particularly deals with major hydrodynamic differences between two common WEC types, heaving point absorbers and oscillating wave surge converters, mainly show-

ing that Froude-Krylov force nonlinearities are much more relevant in HPAs than OWSCs, as shown in Fig. 5.9.

Modelling *nonlinear FK forces* requires the integration of the undisturbed incident pressure field onto the instantaneous wetted surface of the device. For geometries of arbitrary complexity, computationally expensive mesh-based approaches are the only option. However, based on the assumption of *axisymmetric* point absorbers, Chapters 4 and 9 propose computationally efficient analytical representation of nonlinear FK integrals, which achieve the same accuracy of mesh-based approaches (see Fig. 6.6), at a fraction of the computational time (about 1/10 for the 6-DoFs models considered in Chapter 9). Furthermore, Chapter 8 suggests that, for the computation of nonlinear FK forces, using the *Wheeler’s stretching* method is a pragmatic and efficient way to take into account nonlinearities in the pressure field distribution: the major advantage of applying Wheeler’s stretching is the elimination of the linearized free surface boundary condition error, which is particularly detrimental in irregular wave conditions. In general, Chapter 8 argues that the relevance of the accuracy of representation of the nonlinear pressure field distribution is not only influenced by the severity of the sea conditions, but also by the water depth, and the region of the fluid the device occupies.

Chapter 6 suggests that, while diffraction and radiation forces are small and mostly linear for HPAs, viscous drag is potentially a relevant nonlinearity, especially when large velocities are induced by an aggressive control strategy, such as latching control. However, the selection of the drag coefficient is troublesome since, in the wave energy field literature, there are several, at times inconsistent, values and identification techniques. In Chapter 7, it is argued that such uncertainties are related to the inherent challenges wave energy applications offer, as opposed to the traditional viscous drag theory, mainly due to the presence of the free surface. In fact, drag identification tests must define a proper compromise between pertinence of the flow reproduction, and simplicity of isolation of the drag term. Comparing different identification tests, it is found that the drag coefficient depend on the identification experiment, and increases with the complexity of the flow, as shown in Fig. 7.3. Hence, the concept of “*equivalent drag coefficient*” is introduced, as a term that aims to include all unmodelled nonlinearities, in order to increase the overall accuracy, as opposed to describe drag effects only. Finally, it is suggested that, in case of uncertainties, it is pragmatically preferable to overestimate the drag coefficient.

10.1 Future work

The research presented in this thesis highlights several direction for further work:

- Perform a thorough validation of the nonlinear FK force model, using complete experimental data from wave tank tests, under controlled conditions.
- Include accurate nonlinear models for mooring dynamics, using, for example, available open-source software, such as MoorDyn [218] or Moody [219]. Indeed, moorings may have an important role in inducing parametric roll responses and, in general, affecting the device dynamics.
- Improve the computing performance of the nonlinear FK force model, translating the code from Matlab to a lower level coding language (Python, Fortran, C), and/or parallelize the computation of FK integrals.
- Apply model order reduction techniques to the nonlinear FK force model, in order to further reduce the computational time, making the model a viable option for model-based control strategies and estimation of the incoming wave excitation force.

Bibliography

- [1] A. Pecher, J. Peter, and K. Editors, *Ocean Engineering & Oceanography 7 Handbook of Ocean Wave Energy*. Springer International Publishing, 2016.
- [2] European Commission, “20 20 20 by 2020 - Europe’s climate change opportunity. Communication from the Commission to the European Parliament, the Council, the European Economic and Social Committee and the Committee of the Regions,” 2008.
- [3] European Commission, “Energy roadmap 2050, impact assessment and scenario analysis,” tech. rep., 2011.
- [4] J. Cruz, *Ocean wave energy. Current status and future perspectives*. Springer-Verlag, 2008.
- [5] J. H. Todalshaug, *Modelling an phase control of wave-energy converters*. PhD thesis, NTNU, 2010.
- [6] S. H. Salter, “Wave Power,” *Nature*, vol. 249, pp. 720–724, jun 1974.
- [7] C. J. Fitzgerald, “Technology Readiness Level Definitions,” *Private communication, Ireland*, 2011.
- [8] J. Weber, “WEC Technology Readiness and Performance Matrix finding the best research technology development trajectory,” in *International Conference on Ocean Energy*, (Dublin), 2012.
- [9] M. Penalba, G. Giorgi, and J. V. Ringwood, “Mathematical modelling of wave energy converters: a review of nonlinear approaches,” *Renewable and Sustainable Energy Reviews*, vol. 78, pp. 1188–1207, 2017.
- [10] M. Penalba, G. Giorgi, and J. V. Ringwood, “A Review of Non-Linear Approaches for Wave Energy Converter Modelling,” in *Proceedings of the 11th European Wave and Tidal Energy Conference*, (Nantes), 2015.
- [11] G. Giorgi and J. V. Ringwood, “Implementation of latching control in a numerical wave tank with regular waves,” *Journal of Ocean Engineering and Marine Energy*, vol. 2, no. 2, pp. 211–226, 2016.
- [12] J. Davidson, C. Windt, G. Giorgi, R. Genest, and J. V. Ringwood, *Evaluation of energy maximising control systems for wave energy converters using OpenFOAM*. 2017.
- [13] G. Giorgi and J. V. Ringwood, “Nonlinear Froude-Krylov and viscous drag representations for wave energy converters in the computation/fidelity continuum,” *Ocean Engineering*, vol. 141, no. April, pp. 164–175, 2017.

- [14] G. Giorgi, M. Penalba, and J. V. Ringwood, “Nonlinear Froude Krylov Force Representation for Heaving Buoy Wave Energy Converters,” in *Proceedings of the 3rd Asian Wave and Tidal Energy Conference*, (Singapore), 2016.
- [15] G. Giorgi and J. V. Ringwood, “Computationally efficient nonlinear Froude–Krylov force calculations for heaving axisymmetric wave energy point absorbers,” *Journal of Ocean Engineering and Marine Energy*, vol. 3, no. 1, pp. 21–33, 2017.
- [16] G. Giorgi and J. V. Ringwood, “Comparing nonlinear hydrodynamic forces in heaving point absorbers and oscillating wave surge converters,” *Journal of Ocean Engineering and Marine Energy*, vol. 4, no. 1, pp. 25–35, 2018.
- [17] G. Giorgi, M. Penalba, and J. V. Ringwood, “Nonlinear hydrodynamic force relevance for different wave energy converter types,” in *Proceedings of the 3rd Asian Wave and Tidal Energy Conference*, (Singapore), pp. 154–162, 2016.
- [18] G. Giorgi and J. V. Ringwood, “Consistency of viscous drag identification tests for wave energy applications,” in *12th European Wave and Tidal Energy Conference*, (Cork), 2017.
- [19] G. Giorgi and J. V. Ringwood, “Relevance of pressure field accuracy for nonlinear FroudeKrylov force calculations for wave energy devices,” *Journal of Ocean Engineering and Marine Energy*, vol. 4, no. 1, pp. 57–71, 2018.
- [20] G. Giorgi and J. V. Ringwood, “Importance of nonlinear wave representation for nonlinear Froude-Krylov force calculations for wave energy devices,” in *Proceedings of the 12th European Wave and Tidal Energy Conference*, (Cork), 2017.
- [21] G. Giorgi and J. V. Ringwood, “Analytical Formulation of Nonlinear Froude-Krylov Forces for Surging-Heaving-Pitching Point Absorbers,” in *ASME 2018 37th International Conference on Ocean, Offshore and Arctic Engineering*, (Madrid), 2018.
- [22] G. Giorgi and J. V. Ringwood, “Analytical representation of nonlinear Froude-Krylov forces for 3-DoF point absorbing wave energy devices,” *Ocean Engineering*, vol. 164, no. 2018, pp. 749–759, 2018.
- [23] G. Giorgi and J. V. Ringwood, “A Compact 6-DoF Nonlinear Wave Energy Device Model for Power Assessment and Control Investigations,” *IEEE Transactions on Sustainable Energy*, 2018.
- [24] J. Davidson, T. Kalmar-Nagy, G. Giorgi, and J. V. Ringwood, “Nonlinear rock and roll - Modelling and control of parametric rresonances in wave energy devices,” in *Proceedings of the 9th Vienna International Conference on Mathematical Modelling*, (Vienna), 2018.
- [25] G. Giorgi and J. V. Ringwood, “Articulating Parametric Nonlinearities in Computationally Efficient Hydrodynamic Models,” in *Proceedings of the 11th IFAC Conference on Control Applications in Marine Systems, Robotics, and Vehicles*, (Opatija), 2018.
- [26] G. Giorgi and J. V. Ringwood, “Parametric motion detection for an oscillating water column spar buoy .,” in *Proceedings of the 3rd International Conference on Renewable Energies Offshore RENEW*, (Lisbon), 2018.
- [27] A. F. Falcão, “Modelling and Control of Oscillating-Body Wave Enrgy Conberters with Hydraulic PTO and Gas Accumulator,” *Ocean Engineering*, vol. 34, pp. 2021–2032, 2007.

- [28] A. Babarit, M. Guglielmi, and A. H. Clément, “Declutching control of a wave energy converter,” *Ocean Engineering*, vol. 36, no. 1213, pp. 1015–1024, 2009.
- [29] G. Bacelli and J. V. Ringwood, “Nonlinear Optimal Wave Energy Converter Control with Application to a Flap-Type Device,” in *Preprints of the 19th World Congress, The Intl. Federation of Automatic Control (IFAC)*, (Cape Town), pp. 7696–7701, 2014.
- [30] G. Ducrozet, F. Bonnefoy, D. Le Touzé, and P. Ferrant, “3-D HOS simulations of extreme waves in open seas,” *Natural Hazards and Earth System Sciences*, vol. 7, no. 1, pp. 109–122, 2007.
- [31] M. A. Bhinder, A. Babarit, L. Gentaz, and P. Ferrant, “Effect of Viscous Forces on the Performance of a Surging Wave Energy Converter,” in *Proceedings of the 22nd International and Polar Engineering Conference*, (Rhodes), pp. 545–549, 2012.
- [32] A. Mérigaud, J.-C. Gilloteaux, and J. V. Ringwood, “A nonlinear extension for linear boundary element methods in wave energy device modelling,” in *ASME 2012 31st International Conference on Ocean, Offshore and Arctic Engineering*, (Rio de Janeiro), pp. 615–621, 2012.
- [33] P. C. Vicente, A. F. Falcão, and P. A. Justino, “Nonlinear Dynamics of a Tightly Moored Point-Absorber Wave Energy Converter,” *Ocean engineering*, vol. 59, pp. 20–36, 2013.
- [34] A. H. Clément, “Non-linearities in wave energy conversion,” in *4th Maynooth university wave energy workshop*, (Maynooth), 2015.
- [35] L. O’Boyle, K. Doherty, J. van’t Hoff, and J. Skelton, “The Value of Full Scale Prototype Data-Testing Oyster 800 at EMEC, Orkney,” in *Proceedings of the 11th European Wave and Tidal Energy Conference*, (Nantes), 2015.
- [36] D. E. Reeve, Y. Chen, S. Pan, V. Magar, D. Simmonds, and A. Zacharioudaki, “An investigation of the impacts of climate change on wave energy generation: The Wave Hub, Cornwall, UK,” *Renewable Energy*, vol. 36, no. 9, pp. 2404–2413, 2011.
- [37] Sea Power, “Seapower Platform Power Matrix.” Available at <http://www.seapower.ie/wp-content/uploads/Seapower-Powermatrix.png>, 2016.
- [38] J. D. Fenton, “Nonlinear wave theories,” *the Sea*, vol. 9, no. Part A, pp. 3–25, 1990.
- [39] J. Wheeler, “Method for Calculating Forces Produced by Irregular Waves,” *Journal of Petroleum Technology*, vol. 22, no. 03, pp. 359–367, 1970.
- [40] W. J. Pierson and L. Moskowitz, “Aproposed spectral form for fully developed wind seas based on the similarity theory of S.A. Kitaigorodskii,” tech. rep., U.S. Naval Oceanographic Office, 1963.
- [41] K. Hasselmann, T. P. Barnett, E. Bouws, H. Carlson, D. E. Cartwright, K. Enke, J. A. Ewing, H. Gienapp, D. E. Hasselmann, P. Kruseman, A. Meerburg, P. Muller, D. J. Olbers, K. Richter, W. Sell, and H. Walden, “Measurements of wind-wave growth and swell decay during the joint north sea wave project (JONSWAP),” tech. rep., Deutsches Hydrographisches Institut, Hamburg, 1973.
- [42] C. L. Bretschneider, “Wave variability and wave spectra for wind generated gravity waves,” Tech. Memo 118, Beach Erosion Board, US Army Corps of Engineering, Washington DC, 1959.

- [43] M. K. Ochi and E. N. Hubble, “Six-parameter wave spectra,” *Coastal Engineering*, pp. 301–328, 1976.
- [44] N. E. Huang, Z. Shen, S. R. Long, M. C. Wu, H. H. Shih, Q. Zheng, N.-C. Yen, C. C. Tung, and H. H. Liu, “The empirical mode decomposition and the Hilbert spectrum for nonlinear and non-stationary time series analysis,” *Proceedings of the Royal Society of London A: Mathematical, Physical and Engineering Sciences*, vol. 454, no. 1971, pp. 903–995, 1998.
- [45] J. Falnes, *Ocean waves and oscillating systems*. Cambridge University Press, 2002.
- [46] K. R. Tarrant and C. Meskell, “Investigation on parametrically excited motions of point absorbers in regular waves,” *Ocean Engineering*, vol. 111, pp. 67–81, 2016.
- [47] A. Babarit and A. H. Clément, “Application of the optimal command method to the control of the SEAREV wave energy converter: A study on the influence of time constants on the efficiency of the latching control,” in *European Control Conference*, (Budapest), pp. 3737–3742, IEEE, 2009.
- [48] R. P. F. Gomes, J. D. C. Malvar Ferreira, S. Riberio de Silva, J. C. Henriques, and L. M. C. Gato, “An experimental study on the reduction of the dynamic instability in the oscillating water column spar buoy,” in *Proceedings of the 12th European Wave and Tidal Energy Conference*, (Cork), 2017.
- [49] N. N. Moiseyev and V. V. Rumyantsev, *Dynamic stability of bodies containing fluid*, vol. 6. Springer Science & Business Media, 2012.
- [50] A. Henry, P. Schmitt, T. W. Whittaker, A. Rafiee, and F. Dias, “The characteristics of wave impacts on an oscillating wave surge converter,” in *The Twenty-third International Offshore and Polar Engineering Conference*, pp. 101–110, International Society of Offshore and Polar Engineers, 2013.
- [51] L. Johanning, G. Smith, and J. Wolfran, “Mooring Design Approach for Wave Energy Converters,” *Journal of Engineering for the Maritime Environment*, vol. 220, no. 4, pp. 159–174, 2006.
- [52] P. C. Vicente, A. F. Falcão, and P. A. Justino, “Non-linear Slack-Mooring Modelling of a Floating Two-Body Wave Energy Converter,” in *Proceedings of the 9th European Wave and Tidal Energy Conference*, (Southampton), 2011.
- [53] L. Johanning, G. Smith, and J. Wolfran, “Measurements of static and dynamic mooring line damping and their importance for floating WEC devices,” *Ocean Engineering*, vol. 34, no. 14-15, pp. 1918–1934, 2007.
- [54] Orcina-Ltd., “OrcaFlex Software.” <http://orcina.com/>, 2014.
- [55] L. Johanning, G. Smith, and J. Wolfran, “Interaction between mooring line damping and response frequency as a result of stiffness alteration in surge,” in *Proceedings of the ASME 2006 25th International Conference on Offshore Mechanics and Arctic Engineering*, (Hamburg), 2006.
- [56] D. Bull and P. Jacob, “Methodology for creating nonaxisymmetric WECs to screen mooring designs using a Morison Equation approach,” *OCEANS 2012 MTS/IEEE: Harnessing the Power of the Ocean*, 2012.
- [57] R. P. F. Gomes, J. C. Henriques, L. M. C. Gato, and A. F. Falcão, “Testing of a small-scale floating OWC model in a wave flume,” in *International Conference on Ocean Energy*, (Dublin), 2012.

- [58] J. Kapell, *Analysis of the Inner Flow in the Wave Energy Converter WaveTube*. PhD thesis, KTH School of Industrial Engineering and Management, 2012.
- [59] M. Penalba, A. Mériçaud, J. C. Gilloteaux, and J. V. Ringwood, “Influence of non-linear FroudeKrylov forces on the performance of two wave energy points absorbers,” *Journal of Ocean Engineering and Marine Energy*, vol. 3, no. 3, pp. 209–220, 2017.
- [60] M. A. Bhinder, A. Babarit, L. Gentaz, and P. Ferrant, “Assessment of viscous damping via 3d-cfd modelling of a floating wave energy device,” in *Proceedings of the 9th European Wave and Tidal Energy Conference*, (Southampton), 2011.
- [61] L. Tao and D. Dray, “Hydrodynamic performance of solid and porous heave plates,” *Ocean Engineering*, vol. 35, no. 10, pp. 1006–1014, 2008.
- [62] A. Babarit, H. Mouslim, A. H. Clément, and P. Laporte-Weywada, “On the numerical modelling of the nonlinear behaviour of a wave energy converter,” in *Proceedings of the ASME 2009 28th International Conference on Ocean, Offshore and Arctic Engineering*, (Honolulu), 2009.
- [63] A. Henry, “Determination of Non-linear Damping Coefficients of bottom- hinged Oscillating Wave Surge Converters Using Numerical Free Decay Tests,” tech. rep., Queen’s University Belfast, 2014.
- [64] Y. Torre-Enciso, I. Ortubia, L. I. de Aguilera, and J. Marqués, “Mutriku wave power plant: from the thinking out to the reality,” in *Proceedings of the 8th European Wave and Tidal Energy Conference*, (Upsala), pp. 319–329, 2009.
- [65] A. F. Falcão, J. C. Henriques, and J. J. Cândido, “Dynamics and optimization of the OWC spar buoy wave energy converter,” *Renewable Energy*, vol. 48, pp. 369–381, 2012.
- [66] Wavestar, “Wavestar A/S, available at <http://wavestarenergy.com/>,” 2016.
- [67] J. Fiévez and T. Sawyer, “Lessons Learned from Building and Operating a Grid Connected Wave Energy Plant,” in *Proceedings of the 11th European Wave and Tidal Energy Conference*, (Nantes), 2015.
- [68] M. Mekhiche and K. A. Edwards, “Ocean power technologies power buoy: system-level design, development and validation methodology,” in *Proceedings of the 2nd Marine Energy Technology Symposium*, (Seattle), 2014.
- [69] A. H. Clément, A. Babarit, J.-C. Gilloteaux, C. Josset, and G. Duclos, “The SEAREV wave energy converter,” in *Proceedings of the 6th Wave and Tidal Energy Conference*, (Glasgow), 2005.
- [70] T. Mäki, T. Mucha, and M. Vuorinen, “Waveroller one of the leading technologies for wave energy conversion,” in *4th International Conference on Ocean Energy*, (Halifax), 2014.
- [71] M. Penalba and J. V. Ringwood, “A Review of Wave-to-Wire Models for Wave Energy Converters,” *Energies*, vol. 9, no. 7, p. 506, 2016.
- [72] A. F. Falcão, “Wave energy utilization: A review of the technologies,” *Renewable and Sustainable Energy Reviews*, vol. 14, no. 3, pp. 899–918, 2010.
- [73] A. F. Falcão and J. C. Henriques, “Oscillating-water-column wave energy converters and air turbines: A review,” *Renewable Energy*, vol. 85, pp. 1391–1424, 2016.

- [74] M. Jelali and A. Kroll, *Hydraulic servo-systems: modelling, identification and control*. Springer Science & Business Media, 2012.
- [75] T. O. Andersen, R. H. Hansen, and A. H. Hansen, “Simulation of Utilisation of Pressure Propagation for Increased Efficiency of Secondary Controlled Discrete Displacement Cylinders,” in *Fluid Dynamic and Mechanical & Electrical Control Engineering*, vol. 233 of *Applied Mechanics and Materials*, pp. 3–6, Trans Tech Publications, 2012.
- [76] R. H. Hansen, *Design and control of the powertake-off system for a wave energy converter with multiple absorbers*. The Faculty of Engineering and Science, Aalborg University, 2013.
- [77] R. Crozier, *Optimisation and Comparison of Integrated Models of Direct-Drive Linear Machines for Wave Energy Conversion*. PhD thesis, The University of Edinburgh, 2013.
- [78] R. Crozier, H. Bailey, M. Mueller, E. Spooner, P. McKeever, and A. McDonald, “Analysis, design and testing of a novel direct-drive wave energy converter system,” in *In proceedings of european wave and tidal energy conference*, (Southampton), 2011.
- [79] A. H. Hedjripour, A. P. Callaghan, and T. E. Baldock, “Generalized transformation of the lattice Boltzmann method for shallow water flows,” *Journal of Hydraulic Research*, vol. 54, no. 4, pp. 371–388, 2016.
- [80] C. Windt, J. Davidson, and J. V. Ringwood, “High-fidelity numerical modelling of ocean wave energy systems: A review of computational fluid dynamics-based numerical wave tanks,” *Renewable and Sustainable Energy Reviews*, vol. 93, no. April, pp. 610–630, 2018.
- [81] R. Temam, *Navier-Stokes equations: theory and numerical analysis*, vol. 343. American Mathematical Soc., 2001.
- [82] K. Tanizawa, “The state of the art on Numerical Wave Tank,” in *Proceedings of 4th Osaka Colloquium on Seakeeping Performance of Ships*, (Osaka), pp. 95–114, oct 2000.
- [83] J. Wackers, B. Koren, H. C. Raven, A. van der Ploeg, A. R. Starke, G. B. Deng, P. Queutey, M. Visonneau, T. Hino, and K. Ohashi, “Free-Surface Viscous Flow Solution Methods for Ship Hydrodynamics,” *Archives of Computational Methods in Engineering*, vol. 18, no. 1, pp. 1–41, 2011.
- [84] H. K. Versteeg and W. Malalasekera, *An Introduction to Computational Fluid Dynamics*, vol. M. 1995.
- [85] S. M. El-Behery and M. H. Hamed, “A comparative study of turbulence models performance for separating flow in a planar asymmetric diffuser,” *Computers and Fluids*, vol. 44, no. 1, pp. 248–257, 2011.
- [86] S. Chakraborti, “Physical Model Testing of Floating Offshore Structures,” in *Dynamic Positioning Conference*, (Houston), 1998.
- [87] P. Schmitt, T. W. Whittaker, D. Clabby, and K. Doherty, “The opportunities and limitations of using CFD in the development of wave energy converters,” in *Marine & Offshore Renewable Energy*, pp. 89–97, 2012.

- [88] P. Ferrant, L. Gentaz, C. Monroy, R. Luquet, G. Dupont, G. Ducrozet, B. Alessandrini, E. Jacquin, and A. Drouet, “Recent Advances Towards the Viscous Flow Simulation of Ships Manoeuvring in Waves,” in *23rd International Workshop on Water Waves and Floating Bodies*, (Jeju), 2008.
- [89] B. Alessandrini and G. Delhommeau, “Simulation of three-dimensional unsteady viscous free surface flow around a ship model,” *International journal for numerical methods in fluids*, vol. 19, no. 4, pp. 321–342, 1994.
- [90] R. Sampath, N. Montanari, N. Akinci, S. Prescott, and C. Smith, “Large-scale solitary wave simulation with implicit incompressible SPH,” *Journal of Ocean Engineering and Marine Energy*, vol. 2, no. 3, pp. 313–329, 2016.
- [91] J.-C. Gilloteaux, *Mouvements de grande amplitude d’un corps flottant en fluide parfait. Application à la récupération de l’énergie des vagues*. PhD thesis, Ecole Centrale de Nantes-ECN, 2007.
- [92] M. Penalba, A. Mérigaud, J.-C. Gilloteaux, and J. V. Ringwood, “Nonlinear Froude-Krylov force modelling for two heaving wave energy point absorbers,” in *Proceedings of the 11th European Wave and Tidal Energy Conference*, (Nantes), 2015.
- [93] Š. Malenica, E. R. Taylor, J. B. Huang, R. E. Taylor, and J. B. Huang, “Second-order water wave diffraction by an array of vertical cylinders,” *Journal of Fluid Mechanics*, vol. 390, pp. 349–373, 1999.
- [94] L. Letournel, *Développement d’un outil de simulation numérique basé sur l’approche Weak-Scatterer pour l’étude des systèmes houlomoteurs en grands mouvements*. PhD thesis, Ecole Centrale de Nantes, 2015.
- [95] S. T. Grilli, P. Guyenne, and F. Dias, “A Fully Non-Linear Model for Three-Dimensional Overtuning Waves over an Arbitrary Bottom,” *International Journal for Numerical Methods in Fluids*, vol. 35, no. June 2000, pp. 829–867, 2001.
- [96] L. Letournel, P. Ferrant, A. Babarit, G. Ducrozet, J. C. Harris, M. Benoit, and E. Dombre, “Comparison of fully nonlinear and weakly nonlinear potential flow solvers for the study of wave energy converters undergoing large amplitude motions,” in *Proceedings of the ASME 2014 33rd International Conference on Ocean, Offshore and Arctic Engineering*, (San Francisco), American Society of Mechanical Engineers, 2014.
- [97] J. Morison, J. Johnson, and M. P. O. Brien, “Experimental Studies of Forces on Piles,” *Coastal Engineering*, pp. 340–370, 1950.
- [98] S. Beatty, B. J. Buckham, and P. Wild, “Experimental comparison of self-reacting point absorber WEC designs,” in *Proceedings of the 10th European Wave and Tidal Conference, EWTEC*, (Aalborg), 2013.
- [99] J. V. Ringwood, J. Davidson, and S. Giorgi, “Optimising numerical wave tank tests for the parametric identification of wave energy device models,” in *Proceedings of the ASME 2015 34th International Conference on Ocean, Offshore and Arctic Engineering*, (St. John’s, Newfoundland, Canada), 2015.
- [100] L. Ljung, *System Identification: Theory for the User*. Pearson Education, 1998.
- [101] O. Nelles, *Nonlinear System Identification: From Classical Approaches to Neural Networks and Fuzzy Models*. Engineering online library, Springer, 2001.

- [102] R. K. Pearson and M. Pottmann, “GrPa-box identification of block-oriented nonlinear models,” *Journal of Process Control*, vol. 10, no. 4, pp. 301–315, 2012.
- [103] R. K. Pearson and B. A. Ogunnaike, *Identification and control using Volterra models*. Springer Science & Business Media, 2002.
- [104] J. Davidson, S. Giorgi, and J. V. Ringwood, “Numerical Wave Tank Identification of Nonlinear Discrete Time Hydrodynamic Models,” *Renewable Energies Offshore*, p. 279, 2015.
- [105] S. Giorgi, J. Davidson, and J. V. Ringwood, “Identification of wave energy device models from numerical wave tank data - Part 2: Data-based model determination,” *IEEE Transactions on Sustainable Energy*, vol. 7, no. 3, pp. 1020–1027, 2016.
- [106] A. Rafiee and J. Fiévez, “Numerical Prediction of Extreme Loads on the CETO Wave Energy Converter,” in *Proceedings of the 11th European Wave and Tidal Energy Conference*, (Southampton), 2015.
- [107] S. Beatty, M. Hall, B. J. Buckham, P. Wild, and B. Bocking, “Experimental and numerical comparisons of self-reacting point absorber wave energy converters in regular waves,” *Ocean Engineering*, vol. 104, pp. 370–386, 2015.
- [108] E. Renzi, K. Doherty, A. Henry, and F. Dias, “How does Oyster work? the simple interpretation of Oyster mathematics,” *European Journal of Mechanics, B/Fluids*, vol. 47, no. June 2012, pp. 124–131, 2014.
- [109] Y. Wei, T. Abadie, A. Henry, and F. Dias, “Wave interaction with an Oscillating Wave Surge Converter. Part II: Slamming,” *Ocean Engineering*, vol. 113, pp. 319–334, 2016.
- [110] Y. Wei, A. Rafiee, A. Henry, and F. Dias, “Wave interaction with an oscillating wave surge converter, Part I: Viscous effects,” *Ocean Engineering*, vol. 104, pp. 185–203, 2015.
- [111] A. Babarit, J. H. Todalshaug, M. J. Muliawan, A. Kurniawan, T. Moan, and J. Krokstad, “Numerical benchmarking study of a selection of wave energy converters,” *Renewable Energy*, vol. 41, pp. 44–63, 2012.
- [112] D. Halamay and A. Simmons, “Reserve Requirement Impacts of Large-Scale Integration of Wind, Solar and Ocean Wave Power Generation,” *IEEE Transactions on Sustainable Energy*, vol. 2, pp. 1–7, jul 2011.
- [113] F. Fusco, G. Nolan, and J. V. Ringwood, “Variability reduction through optimal combination of wind/wave resources - an Irish case study,” *Energy*, vol. 35, no. 2010, pp. 314–325, 2010.
- [114] X. Yang, Y. Song, G. Wang, and W. Wang, “A Comprehensive Review on the Development of Sustainable Energy Strategy and Implementation in China,” *IEEE Transactions on Sustainable Energy*, vol. 1, pp. 57–65, jul 2010.
- [115] A. Babarit and A. H. Clément, “Optimal latching control of a wave energy device in regular and irregular waves,” *Applied Ocean Research*, vol. 28, pp. 77–91, 2006.
- [116] M. Greenhow, J. H. Rosen, and M. Reed, “Control strategies for the clam wave energy device,” *Applied ocean research*, vol. 6, no. 4, pp. 197–206, 1984.

- [117] P. Nebel, “Maximizing the efficiency of wave-energy plant using complex-conjugate control,” *Proceedings of the Institution of Mechanical Engineers, Part I: Journal of Systems and Control Engineering*, vol. 206, no. 4, pp. 225–236, 1992.
- [118] S. H. Salter, “Power conversion systems for ducks,” in *Proceedings of International Conference on Future Energy Concepts, London, Institution of Electrical Engineers*, vol. 171, pp. 100–108, jan 1979.
- [119] K. Budal, J. Falnes, A. Kyllingstad, and G. Oltedal, “Experiments with point absorbers,” in *Proceedings of First Symposium on Wave Energy Utilization, Gothenburg, Sweeden*, pp. 253–282, 1979.
- [120] F. Kara, “Time domain prediciton of power absorption from ocean waves with latching control,” *Renewable Energy*, vol. 35, no. 2010, pp. 423–434, 2010.
- [121] G. Bacelli, J.-C. Gilloteaux, and J. V. Ringwood, “A Predictive Controller for a Heaving Buoy Producing Potable Water,” in *Proceedings of the European Control Conference*, (Budapest), 2009.
- [122] N. Faedo, S. Olaya, and J. V. Ringwood, “Optimal Control, MPC and MPC-Like Algorithms for Wave Energy Systems: An Overview,” *IFAC Journal of Systems and Control*, vol. 1, pp. 37–56, 2017.
- [123] B. Le Méhauté, *An Introduction to Hydrodynamics and Waterwaves*. Springer Science & Business Media, 2014.
- [124] T. Bjarte-Larsson and J. Falnes, “Laboratory experiment on heaving body with hydraulic power take-off and latching control,” *Ocean Engineering*, vol. 33, no. 2006, pp. 847–877, 2006.
- [125] M. Durand, A. Babarit, B. Pettinotti, O. Quillard, J. L. Toularastel, and A. H. Clément, “Experimental validation of the performances of the SEAREV Wave Energy Converter with real time latching control,” in *Proceedings of the 7th European Wave and Tidal Energy Conference*, (Porto), 2007.
- [126] G. Clauss, C. E. Schmittner, and R. Stuck, “Numerical Wave Tank - Simulation of extreme waves for the investigation of structural responses,” in *Proceedings of the ASME 24th International Conference on Offshore Mechanics and Artic Engineering*, vol. 3, (Halkidiki), pp. 785–792, jun 2005.
- [127] J. Davidson, S. Giorgi, and J. V. Ringwood, “Linear parametric hydrodynamic models for ocean wave energy converters identified from numerical wave tank experiments,” *Ocean Engineering*, vol. 103, pp. 31–39, 2015.
- [128] R. E. Hoskin and N. Nichols, “Latching control of a point absorber,” in *n.k.nichols, 1986, The Fluid Engineering Centre*, (Bedford), pp. 317–330, 1986.
- [129] M. Greenhow and S. White, “Optimal heave motion of some axisymmetric wave energy devices in sinusoidal waves,” *Applied Ocean Research*, vol. 19, no. 3-4, pp. 141–159, 1997.
- [130] K. Tanizawa and A. H. Clément, “Report of the 2nd Workshop of ISOPE Numerical Wave Tank Group: Benchmark Test Cases of Radiation Problem (Brest, May1999),” in *Proceedings of the 10th International Offshore and Polar Engineering Conference*, vol. III, (Seattle), pp. 175–184, 2000.
- [131] M. A. Afshar, “Numerical wave generation in OpenFOAM,” Master’s thesis, Chalmers University of Technology, 2010.

- [132] M. Cathelain, *Modelling of a floating object in heave motion using a numerical wave tank in OpenFOAM*. PhD thesis, École centrale de Nantes, 2013.
- [133] J. Palm, C. Eskilsson, G. M. Paredes, and L. Bergdahl, “CFD simulation of a moored floating wave energy converter,” in *In proceedings of the 10th European Wave and Tidal Energy Conference*, (Aalborg), 2013.
- [134] P. Schmitt, S. Bourdier, T. W. Whittaker, D. Sarkar, E. Renzi, F. Dias, K. Doherty, and J. van’t Hoff, “Hydrodynamic Loading of a Bottom Hinged Oscillating Wave Surge Converter,” in *Proceedings of the 22nd International Offshore and Polar Engineering Conference*, (Rhodes), jun 2012.
- [135] T. Vyzikas, E. Ransley, M. Hann, D. Magagna, D. M. Greaves, D. Simmonds, V. Margar, and D. Conley, “Integrated numerical modeling system for extreme wave events at the Wave Hub site,” in *Proceedings of ICE Conference on Coasts, Marine Structures and Breakwaters*, (Edinburgh), 2013.
- [136] N. G. Jacobsen, D. R. Fuhrman, and J. Fredsøe, “A wave generation toolbox for the open-source CFD library: OpenFoam,” *International Journal for Numerical Methods in Fluids*, vol. 70, no. 9, pp. 1073–1088, 2012.
- [137] C. Hirt and B. Nicholis, “Volume of fluid (vof) method for the dynamics of free boundaries,” *Journal of Computational Physics*, vol. 39, pp. 201–225, nov 1979.
- [138] G. Giorgi and J. V. Ringwood, “NWT latching control algorithm and user manual,” in <http://www.eeng.nuim.ie/coer/research-projects/>, 2016.
- [139] J. Falnes and P. M. Lillebekken, “Budal’s latching-controlled-buoy type wave-power plant,” in *Proceedings of the 5th European Wave Energy Conference*, vol. 1720, (Cork), pp. 233–244, 2003.
- [140] J. V. Ringwood and S. Butler, “Optimisation of a wave energy converter,” in *Proceedings of IFAC Conference on Control Applications in Marine Systems*, (Ancona), 2004.
- [141] B. Teillant, J.-c. Gilloteaux, and J. V. Ringwood, “Optimal Damping Profile for a Heaving Buoy Wave Energy Converter,” in *Proceedings IFAC Conference on Control Applications in Marine Systems*, (Rostock), pp. 393–398, 2010.
- [142] A. Babarit, G. Duclos, and A. H. Clément, “Comparison of latching control strategies for a heaving wave energy device in random sea,” *Applied Ocean Research*, vol. 26, no. 5, pp. 227–238, 2004.
- [143] J. H. Todalshaug, T. Bjarte-Larsson, and J. Falnes, “Optimum reactive control and control by latching of a wave-absorbing semisubmerged heaving sphere,” in *Proceedings of ASME 21th International Conference on Offshore Mechanics and Artic Engineering*, vol. 4, (Oslo), pp. 415–423, jun 2002.
- [144] J. N. Newman and L. Landweber, *Marine Hydrodynamics*, vol. 45. The MIT Press, 1978.
- [145] W. Cummins, “The impulse response function and ship motion,” *Schiffstechnik*, no. 9, pp. 101–109, 1962.
- [146] T. F. Ogilvie, “Recent progress toward the understanding and prediction of ship motions,” in *Proc. of the 5th Symposium on Navan Hydrodynamics*, vol. ACR-112 of ONR, (Bergen), pp. 3–79, 1964.

- [147] E. R. Jefferys, “Device characterisation,” tech. rep., In Count. B. (Ed.) *Power from Sea Waves*. Academic Press, London. pp. 413-438, 1980.
- [148] R. Taghipour, T. Perez, and T. Moan, “Hybrid frequency-time domain models for dynamic response analysis of marine structures,” *Ocean Engineering*, vol. 35, pp. 685–705, may 2007.
- [149] T. Perez and T. I. Fossen, “A {M}atlab Toolbox for Parametric Identification of Radiation-Force Models of Ships and Offshore Structures,” *Modelling, Identification and Control*, vol. 30, no. 1, pp. 1–15, 2009.
- [150] F. Fusco and J. V. Ringwood, “Suboptimal Casual Reactive Control of Wave Energy Converters Using a second Order System model,” in *Proceedings of the 21st International Offshore and Polar Engineering Conference*, (Maui), 2011.
- [151] M. G. Safonov, R. Y. Chiang, and D. J. N. Limebeer, “Optimal Hankel model reduction for nonminimal systems,” *Automatic Control, IEEE Transactions on*, vol. 35, pp. 496–502, apr 1990.
- [152] J. Davidson, M. Cathelain, L. Guillemet, T. Le Huec, and J. V. Ringwood, “Implementation of an OpenFOAM Numerical Wave Tank for Wave Energy Experiments,” in *Proceedings of the 11th European Wave and Tidal Energy Conference*, (Nantes), 2015.
- [153] E. Mansard and E. Funke, “The measurement of incident and reflected spectra using a least squares method,” *Ocean En*, pp. 154–172, 1980.
- [154] OpenFOAM Foundation, “Boundary Conditions,” *CFL 3D Mannual*, no. February, pp. 79–122, 2013.
- [155] P. K. Kundu, I. M. Cohen, and D. R. Dowling, *Fluid Mechanics*. Academic Press; 5th edition, 2011.
- [156] G. Bacelli and J. V. Ringwood, “Numerical optimal control of wave energy converters,” *Sustainable Energy, IEEE Transactions on*, vol. 6, no. 2, pp. 294–302, 2015.
- [157] J. C. Henriques, M. F. Lopes, R. P. F. Gomes, L. M. C. Gato, and A. F. Falcão, “On the annual wave energy absorption by two-body heaving WECs with latching control,” *Renewable Energy*, vol. 45, pp. 31–40, 2012.
- [158] R. H. Hansen and M. M. Kramer, “Modelling and control of the Wavestar prototype,” *Proceedings of the 9th European Wave and Tidal Energy Conference*, 2011.
- [159] A. H. Clément and P. Ferrant, *Nonlinear Water Waves: IUTAM Symposium, Tokyo Japan, August 25–28, 1987*, ch. Superharmo, pp. 423–433. Berlin, Heidelberg: Springer Berlin Heidelberg, 1988.
- [160] M. Guerinel, A. S. Zurkinden, M. Alves, and A. Sarmiento, “Validation of a partially nonlinear time domain model using instantaneous froude-krylov and hydrostatic forces,” in *Proceedings of the 10th European Wave and Tidal Energy Conference*, (Aalborg), Technical Committee of the European Wave and Tidal Energy Conference, 2013.
- [161] A. Babarit, “ACHIL3D v2.011 User Manual,” no. February, pp. 1–21, 2010.
- [162] M. I. T. WAMIT Inc., “User Manual Wamit,” 2014.

- [163] G. Nolan, J. V. Ringwood, W. Leithead, and S. Butler, “Optimal damping profiles for a heaving buoy wave-energy converter,” in *Proceedings of the 15th International Offshore and Polar Engineering Conference*, vol. 1, (Seoul), pp. 477–485, 2005.
- [164] F. F. Wendt, Y.-H. Yu, K. Nielsen, K. Ruehl, T. Bunnik, I. Touzon, B. W. Nam, J. S. Kim, K.-H. Kim, and C. E. Janson, “International Energy Agency Ocean Energy Systems Task 10 Wave Energy Converter Modeling Verification and Validation,” in *Proceedings of the 12th European Wave and Tidal Energy Conference*, (Cork), Technical Committee of the European Wave and Tidal Energy Conference, 2017.
- [165] M. Folley, A. Henry, and T. W. Whittaker, “Contrasting the hydrodynamics of heaving and surging wave energy converters,” *Proceedings of the 11th European Wave and Tidal Energy Conference*, 2015.
- [166] K. S. Lok, T. J. Stallard, P. K. Stansby, and N. Jenkins, “Optimisation of a clutch-rectified power take off system for a heaving wave energy device in irregular waves with experimental comparison,” *International Journal of Marine Energy*, vol. 8, pp. 1–16, 2014.
- [167] G. H. Keulegan and L. H. Carpenter, *Forces on cylinders and plates in an oscillating fluid*. US Department of Commerce, National Bureau of Standards, 1956.
- [168] B. Molin, *Hydrodynamique des structures offshore*. Editions Technip, 2002.
- [169] P. W. Bearman, M. J. Downie, J. M. R. Graham, and E. D. Obasaju, “Forces on cylinders in viscous oscillatory flow at low Keulegan-Carpenter numbers,” *Journal of Fluid Mechanics*, vol. 154, no. 7, pp. 337–356, 1985.
- [170] Aquamarine, “Aquamarine Power, available at [http://http://www.aquamarinepower.com/](http://www.aquamarinepower.com/),” 2016.
- [171] V. Heller, “Scale effects in physical hydraulic engineering models,” *Journal of Hydraulic Research*, vol. 49, no. 3, pp. 293–306, 2011.
- [172] T. W. Whittaker, D. Collier, M. Folley, M. Osterried, A. Henry, and M. Crowley, “The development of Oyster: a shallow water surging wave energy converter,” in *Proceedings of the 7th European Wave and Tidal Energy Conference*, (Porto), pp. 11–14, 2007.
- [173] D. Clabby, *Wave Energy Conversion at Prototype and Model Scales*. PhD thesis, 2014.
- [174] P. Schmitt and B. Elsäßer, “The application of Froude scaling to model tests of Oscillating Wave Surge Converters,” *Ocean Engineering*, vol. 141, no. June, pp. 108–115, 2017.
- [175] D. I. Forehand, A. E. Kiprakis, A. J. Nambiar, and A. R. Wallace, “A Fully Coupled Wave-to-Wire Model of an Array of Wave Energy Converters,” *Sustainable Energy, IEEE Transactions on*, vol. 7, no. 1, pp. 118–128, 2016.
- [176] A. F. Falcão, “Phase control through load control of oscillating-body wave energy converters with hydraulic PTO system,” *Ocean Engineering*, vol. 35, no. 3, pp. 358–366, 2008.
- [177] ICHEC, “Irish Centre for High-End Computing (ICHEC),” 2016.

- [178] G. Bacelli, R. Genest, and J. V. Ringwood, “Nonlinear control of flap-type wave energy converter with a non-ideal power take-off system,” *Annual Reviews in Control*, vol. 40, pp. 116–126, 2015.
- [179] A. S. Zurkinden, F. Ferri, S. Beatty, J. P. Kofoed, and M. M. Kramer, “Non-linear numerical modeling and experimental testing of a point absorber wave energy converter,” *Ocean Engineering*, vol. 78, pp. 11–21, 2014.
- [180] M. M. Jakobsen, *Wave-Structure Interactions on Point Absorbers - an experimental study*. PhD thesis, Aalborg University, 2015.
- [181] P. Schmitt, *Investigation of the near flow field of bottom hinged flap type wave energy converters*. PhD thesis, Queen’s University Belfast, 2013.
- [182] A. Ooi, “OpenFOAM validation for high Reynolds number flows,” tech. rep., University of Melbourne, 2012.
- [183] J. H. Ferziger and M. Peric, *Computational methods for fluid dynamics*. AIP, 1997.
- [184] D. Mavriplis, *Handbook of Computational Fluid Mechanics*. Academic Press London, 1996.
- [185] B. R. Munson, D. F. Young, and T. H. Okiishi, *Fundamentals of fluid mechanics*. John Wiley & Sons, 1990.
- [186] J. Davidson, R. Genest, and J. V. Ringwood, “Adaptive control of a wave energy converter simulated in a numerical wave tank,” in *Proceedings of the 12th European Wave and Tidal Energy Conference*, (Cork), 2017.
- [187] A. C. M. O’ Sullivan and G. Lightbody, “The Effect of Model Inaccuracy and Move-blocking on the Performance of a Wave-to-wire Wave Energy Converter , under Economic Predictive Control,” in *Proceedings of the 12th European Wave and Tidal Energy Conference*, (Cork), 2017.
- [188] A. C. O’Sullivan and G. Lightbody, “The Effect of Viscosity on the Maximisation of Electrical Power from a Wave Energy Converter under Predictive Control,” *IFAC-PapersOnLine*, vol. 50, no. 1, pp. 14698–14704, 2017.
- [189] M. Guerinel, E. Jansson, J. H. Todalshaug, and M. Jesmani, “Modelling Alternatives for a Heaving Point Absorber with and without Stiffness Modulation,” in *Proceedings of the 12th European Wave and Tidal Energy Conference*, (Cork), pp. 1190–(1–8), 2017.
- [190] M. K. Ochi, *Ocean waves: the stochastic approach*, vol. 6. Cambridge University Press, 2005.
- [191] S. X. Du, D. A. Hudson, W. G. Price, and P. Temarel, “Implicit expressions of static and incident wave pressures over the instantaneous wetted surface of ships,” *Proceedings of the Institution of Mechanical Engineers, Part M: Journal of Engineering for the Maritime Environment*, vol. 223, no. 3, pp. 239–256, 2009.
- [192] G. Clauss, S. Kosleck, F. Sprenger, and F. Boeck, “Adaptive stretching of dynamic pressure distribution in long-and short-crested sea states,” in *ASME 2009 28th International Conference on Ocean, Offshore and Arctic Engineering*, no. December 2015, pp. 333–343, American Society of Mechanical Engineers, 2009.
- [193] T. Hedges, “Regions of validity of analytical wave theories,” in *ICE Proceedings Water Maritime and Energy*, vol. 112, pp. 111–114, 1995.

- [194] J. M. Williams, “Limiting gravity waves in water of finite depth,” *Philosophical Transactions of the Royal Society of London A: Mathematical, Physical and Engineering Sciences*, vol. 302, no. 1466, pp. 139–188, 1981.
- [195] R. J. Sobey, P. Goodwin, R. J. Thieke, and R. J. Westberg Jr, “Application of Stokes, cnoidal, and Fourier wave theories,” *Journal of waterway, port, coastal, and ocean engineering*, vol. 113, no. 6, pp. 565–587, 1987.
- [196] G. Ducrozet, F. Bonnefoy, D. Le Touzé, and P. Ferrant, “HOS-ocean: Open-source solver for nonlinear waves in open ocean based on High-Order Spectral method,” *Computer Physics Communications*, vol. 203, pp. 245–254, 2016.
- [197] G. Ducrozet, “Open-source release of HOS-Ocean,” in <https://github.com/LHEEA/HOS-ocean/wiki>, 2017.
- [198] M. Tanaka, “Verification of Hasselmann’s energy transfer among surface gravity waves by direct numerical simulations of primitive equations,” *Journal of Fluid Mechanics*, vol. 444, pp. 199–221, 2001.
- [199] A. Sergeeva and A. Slunyaev, “Rogue waves, rogue events and extreme wave kinematics in spatio-temporal fields of simulated sea states,” *Natural Hazards and Earth System Sciences*, vol. 13, no. 7, pp. 1759–1771, 2013.
- [200] R. G. Dean and R. A. Dalrymple, *Water Wave Mechanics for Engineers and Scientists*, vol. 7. 1999.
- [201] G. Ducrozet, F. Bonnefoy, and Y. Perignon, “Applicability and limitations of highly non-linear potential flow solvers in the context of water waves,” *Ocean Engineering*, vol. 142, pp. 233–244, 2017.
- [202] L. F. Shampine, “Matlab program for quadrature in 2D,” *Applied Mathematics and Computation*, vol. 202, no. 1, pp. 266–274, 2008.
- [203] Mathematica, “Wolfram mathematica,” in <http://www.wolfram.com/matavailable>, 2017.
- [204] CorPower, “CorPower Ocean AB, available at <http://www.corpowerocean.com/>,” 2017.
- [205] J. H. Todalshaug, G. S. Asgeirsson, E. Hjálmarsson, J. Maillet, P. Möller, P. Pires, M. Guérinel, and M. F. Lopes, “Tank testing of an inherently phase-controlled wave energy converter,” *International Journal of Marine Energy*, vol. 15, pp. 68–84, 2016.
- [206] A. Biran and R. L. Pulido, *Ship hydrostatics and stability*. Butterworth-Heinemann, 2013.
- [207] T. I. Fossen and H. Nijmeijer, *Parametric resonance in dynamical systems*. Springer, 2012.
- [208] T. I. Fossen, *Handbook of marine craft hydrodynamics and motion control*. John Wiley & Sons, 2011.
- [209] K. R. Tarrant, *Numerical Modelling of Parametric Resonance of a Heaving Point Absorber Wave Energy Converter*. PhD thesis, Trinity College Dublin, 2015.
- [210] R. Galeazzi and K. Y. Pettersen, *Parametric resonance in dynamic systems, Controlling parametric resonance: induction and stabilization of unstable motions*. Springer, 2012.

- [211] B. Orazov, *A novel excitation scheme for an ocean wave energy converter*. PhD thesis, University of California, Berkeley, 2011.
- [212] J. Davidson and J. V. Ringwood, “Mathematical modelling of mooring systems for wave energy converters - A review,” *Energies*, vol. 10, no. 5, 2017.
- [213] J. C. Henriques, J. C. Portillo, L. M. C. Gato, R. P. F. Gomes, D. N. Ferreira, and A. F. Falcão, “Design of oscillating-water-column wave energy converters with an application to self-powered sensor buoys,” *Energy*, vol. 112, pp. 852–867, 2016.
- [214] W. Sheng, R. Alcorn, and A. Lewis, “Hydrodynamics of OWC wave energy converters,” *Renewable Energies Offshore*, pp. 489–496, 2015.
- [215] J. D. C. Malvar Ferreira, “Experimental study of the dynamic instability in the oscillating water column spar buoy,” Tech. Rep. July, Instituto Superior Tecnico, University of Lisbon, 2016.
- [216] R. Basman, *Probability and Statistics: The Harald Cramer Volume*. JSTOR, 1962.
- [217] A. Mérigaud and J. V. Ringwood, “Free-Surface Time-Series Generation for Wave Energy Applications,” *IEEE Journal of Oceanic Engineering*, vol. 43, no. 1, pp. 19–35, 2018.
- [218] M. Hall and A. Goupee, “Validation of a lumped-mass mooring line model with DeepCwind semisubmersible model test data,” *Ocean Engineering*, vol. 104, pp. 590–603, 2015.
- [219] J. Palm, *Mooring dynamics for wave energy applications*. PhD thesis, Chalmers University of Technology, 2017.